

**Development of a Snow Water Equivalent (SWE) Algorithm over First-  
Year Sea Ice using *In-Situ* Passive Microwave Radiometry**

By

Alexandre Langlois

A Thesis submitted to the Faculty of Graduate Studies of  
The University of Manitoba  
in partial fulfilment of the requirements of the degree of

DOCTOR OF PHILOSOPHY

Centre for Earth Observation Science  
Clayton H. Riddell Faculty of Environment, Earth and Resources  
Department of Environment and Geography  
University of Manitoba  
Winnipeg

Copyright © 2007 by Alexandre Langlois

**THE UNIVERSITY OF MANITOBA**  
**FACULTY OF GRADUATE STUDIES**  
\*\*\*\*\*  
**COPYRIGHT PERMISSION**

**Development of a Snow Water Equivalent (SWE) Algorithm over First-Year Sea Ice using  
*In-Situ* Passive Microwave Radiometry**

**BY**

**Alexandre Langlois**

**A Thesis/Practicum submitted to the Faculty of Graduate Studies of The University of  
Manitoba in partial fulfillment of the requirement of the degree**

**DOCTOR OF PHILOSOPHY**

**Alexandre Langlois© 2007**

**Permission has been granted to the University of Manitoba Libraries to lend a copy of this thesis/practicum, to Library and Archives Canada (LAC) to lend a copy of this thesis/practicum, and to LAC's agent (UMI/ProQuest) to microfilm, sell copies and to publish an abstract of this thesis/practicum.**

**This reproduction or copy of this thesis has been made available by authority of the copyright owner solely for the purpose of private study and research, and may only be reproduced and copied as permitted by copyright laws or with express written authorization from the copyright owner.**

## ABSTRACT

The Arctic is thought to be an area where we can expect to see the first and strongest signs of global scale climate variability and change. We have already begun to see a reduction in: i) the aerial extent of sea ice at about 3 percent per decade and ii) ice thickness at about 40 percent. At the current rate of reduction we can expect a seasonally ice-free Arctic by midway through this century given the current changes in thermodynamic processes controlling sea ice freeze-up and decay. Many of the factors governing the thermodynamic processes of sea ice are strongly tied to the presence and geophysical state of snow, yet snow on sea ice remains poorly studied.

In this dissertation, I present results from a snow water equivalent algorithm development study over first-year sea ice from the Canadian Arctic Shelf Exchange Study (CASES) overwintering mission in 2003-2004. The analysis provides the current state of knowledge pertaining to the geophysical, thermodynamic, and dielectric properties of snow on sea ice. A detailed analysis is first provided on snow thermophysical properties and the existing linkages with passive microwave scattering and emission mechanisms in a temporal evolution pattern. Results show that winter snow thickness has a significant impact on thermophysical properties as well as the seasonal surface energy balance. Winter thermodynamic processes such as desalination and snow metamorphism are more important than previously expected and their control on brightness temperatures through the dielectric properties can be significant. The known/found linkages between snow thermophysical properties and passive microwaves are employed to retrieve snow water equivalent (SWE). Predictions are significant throughout the season over evolving snow thickness with a  $R^2$  of 0.95 with *in-situ* measured data. The developed algorithm is applied to

satellite remote sensing and predicted SWE values statistically agree with *in-situ* validation measurements for two AMSR-E pixels located in the Franklin Bay region.

**Keywords:** Climate Change, Arctic, Snow, Sea Ice, Geophysical Properties, Surface Energy Balance, Seasonal Evolution, Passive Microwave, Remote sensing.

## **Acknowledgements**

It is impossible to neither realize nor expect the amount of work required in a PhD dissertation without undertaking such adventure. Even though my name is the only one on the cover page, this work would have been impossible without support, direct or indirect, of numerous colleagues, partners, family and friends. Moving away from home to undertake a PhD in a new language was quite a challenge, but an absolute positive experience that I would start all over again...or maybe not.

First, I need to thank deeply David Barber not only for guidance as a supervisor, but also for his patience with my true excitement about science that pulled me off-track numerous times. To share his experience was extremely beneficial professionally and personally. He also gave me the opportunity to be involved in the ArcticNet coordination which will help me greatly in my career. I would also like to thank Tim Papakyriakou for tremendous help throughout the thesis, and also as guidance on my first field season that was quite a storm to swim in. I would also like to thank my internal/external advisor Lotfollah Shafai and my external advisor Thorsten Markus for very helpful comments that helped polished the final version of the dissertation. On that note, I acknowledge Ryan Galley, Bob Hodgson, Christina Blouw, Teresa Fisico, Owen Owens, Phil Hwang, John Iacozza from the University of Manitoba and Mark Christopher Fuller, Kris Konig, John Kudlak and the crew of the Amundsen for tremendous field assistance.

Special thanks go to CJ Mundy whose patience, help and friendship helped me immensely throughout my PhD. Many thanks to the support staff at the Centre for Earth Observation Science, especially to Dave Moss crop whose support and friendship will be greatly missed.

Funding for my PhD came from grants to David Barber for the CASES NSERC network, ArcticNet, the Canada Foundation for Innovation (CFI), the Canada Research Chair program (CRC), the Canadian Space Agency and the Polar Continental Shelf Project. Additional funding also came from the Northern Scientific Training Program (NSTP) from whom I acknowledge year-to-year support for fieldwork.

Outside of the university world, I could not omit to thank the Wombats RFC rugby club for a priceless support and generosity beyond imagination. It was a life lesson to have such great friends, you all make my departure extremely difficult. I could never payback the club for what they gave me and Roxanne, perhaps leaving with a smile and those couple lines in my PhD dissertation will prove how much I appreciated, but I am afraid it will never be enough. Long live the Wombats.

Évidemment, je dois à tout prix remercier ma famille pour un support inconditionnel tout au long de l'aventure. Tout d'abord merci à Serge et Deirdre pour me pousser au meilleur de moi-même et d'avoir rendu l'aventure universitaire financièrement possible. Du fond du cœur je vous dis merci et espère être à la hauteur. Roxanne, je suis sans mot pour exprimer ma gratitude envers ton support aveugle. Tu m'a suivi dans l'aventure manitobaine même si à ton arrivée je suis partis pour vivre un de mes rêves: l'Arctique. Sans toi je n'y arriverais jamais, merci, merci, merci. Merci à mes précieux amis, j'en ai trop pour mentionner leurs noms à tous. Cependant je dois remercier l'AES de Sébastien Matton et Philippe Solomon-Côté de qui j'ai appris énormément depuis mon arrivée dans le monde universitaire en 1998. Merci les boys, on se revoit bientôt!

## **Dedication**

Cette thèse est dédiée à ma famille : Serge, Deirdre et Roxanne, merci pour un support inconditionnel tout au long de l'aventure, et à la toute nouvelle venue Frédérique, merci de m'avoir fait réaliser à nouveau ce qui compte vraiment...

*Un homme ne peut guère reconnaître l'insuffisance de son savoir jusqu'à ce qu'il commence à étudier, et lorsqu'il enseignera, il apprendra qu'il y a encore beaucoup de problème non résolus.*  
(Proverbe chinois)

# Table of Contents

Abstract .....	i
Acknowledgements .....	iii
Dedication .....	v
Table of content .....	vi
List of tables .....	xiii
List of figures .....	ix
<b>1.0. Introduction .....</b>	<b>1</b>
<b>1.1. Rationale .....</b>	<b>1</b>
<b>1.2. Objectives .....</b>	<b>7</b>
<b>1.3. Thesis Outline .....</b>	<b>11</b>
<b>2.0. Background .....</b>	<b>16</b>
<b>2.1. Ocean and Atmospheric Circulation .....</b>	<b>16</b>
<b>2.2. Surface Energy Balance of the OSA .....</b>	<b>17</b>
<b>2.3. Snow Formation and Accumulation .....</b>	<b>19</b>
<b>2.4. Snow Properties .....</b>	<b>21</b>
<i>2.4.1. Thermophysical Properties .....</i>	<i>21</i>
2.4.1.1. Thermal Conductivity .....	21
2.4.1.2. Thermal Diffusivity .....	23
2.4.1.3. Specific Heat and Heat Capacity .....	24
<i>2.4.2. Electrical Properties .....</i>	<i>26</i>

2.4.3. <i>Snow Surface Energy Balance</i>	28
<b>2.5. Snow Processes</b>	<b>30</b>
2.5.1. <i>Heat Transfer</i>	30
2.5.1.1. Conduction	30
2.5.1.2. Vapor Diffusion	32
2.5.1.3. Convection	34
2.5.1.4. Advection	38
2.5.2. <i>Metamorphism</i>	39
2.5.2.1. Dry Snow (Temp. gradient)	39
2.5.2.2. Dry Snow (Equilibrium)	40
2.5.2.3. Wet Snow	43
2.5.3. <i>Snow Aeolian Processes</i>	45
<b>2.6. Microwave Emission and Scattering</b>	<b>48</b>
<b>2.7. Snow Processes and Microwave Signatures</b>	<b>54</b>
2.7.1. <i>Fall</i>	54
2.7.2. <i>Winter</i>	58
2.7.2.1. Cooling Period	58
2.7.2.2. Warming Period	62
2.7.3. <i>Spring</i>	64
<b>2.8. Summary</b>	<b>67</b>
<b>3.0. Data and Methods</b>	<b>70</b>
<b>3.1. Study Site</b>	<b>70</b>
<b>3.2. Meteorological Observations</b>	<b>73</b>

<b>3.3. Micrometeorological Data</b>	.....	73
<b>3.4. Snow Physical Properties</b>	.....	74
3.4.1. <i>Snow Sampling</i>	.....	74
3.4.2. <i>Vertical Profile Characterization</i>	.....	79
<b>3.5. Snow Electrical Properties</b>	.....	80
<b>3.6. Microwaves Data</b>	.....	84
3.6.1. <i>Surface Based Radiometer Data</i>	.....	84
3.6.2. <i>Satellite Based Data</i>	.....	87
3.6.2.1. Atmospheric Corrections.....	.....	89
3.6.2.2. Sea Ice Roughness	.....	90
3.6.2.2.1. Polarization Ratio and Gradient Ratio	.....	90
3.6.2.2.2. Active Microwave Backscattering Coefficient	.....	91
<b>3.7. Summary</b>	.....	93
<b>4.0. Seasonal Time Scales</b>	.....	<b>94</b>
<b>4.1. Snow Thickness and Air Temperature Evolution.....</b>	.....	94
<b>4.2. Cooling Period</b>	.....	96
4.2.1. <i>Met. Observations, Vapor Pressure and Energy Fluxes</i>	.....	96
4.2.2. <i>Snow</i>	.....	99
4.2.2.1. Thin Snow	.....	99
4.2.2.1.1. Physical	.....	99
4.2.2.1.2. Electrical	.....	101
4.2.2.2. Thick Snow	.....	103
4.2.2.2.1. Physical	.....	103

4.2.2.2.2. Electrical .....	105
4.2.3. <i>In-Situ Passive Microwaves</i> .....	107
4.2.3.1. Thin Snow (30-40°) .....	107
4.2.3.2. Thick Snow (55-70°) .....	108
<b>4.3. Warming Period</b> .....	110
4.3.1. <i>Met. Observations, Vapor Pressure and Energy Fluxes</i> .....	110
4.3.2. <i>Snow</i> .....	111
4.3.2.1. Thin Snow .....	111
4.3.2.1.1. Physical .....	111
4.3.2.1.2. Electrical .....	112
4.3.2.2. Thick Snow .....	113
4.3.2.2.1. Physical .....	113
4.3.2.2.2. Electrical .....	114
4.3.3. <i>In-Situ Passive Microwaves</i> .....	114
4.3.3.1. Thin Snow (30-40°) .....	114
4.3.3.2. Thick Snow (55-70°) .....	115
<b>4.4. Conclusion and Discussion</b> .....	115
4.4.1. <i>Physical Properties</i> .....	115
4.4.1.1. Thin Snow .....	115
4.4.1.2. Thick Snow .....	118
4.4.2. <i>Electrical Properties</i> .....	120
4.4.2.1. Thin Snow .....	120
4.4.2.2. Thick Snow .....	121

4.4.3. <i>Passive Microwave Linkages</i> .....	121
4.4.3.1. Thin Snow (30-40°) .....	121
4.4.3.2. Thick Snow (55-70°) .....	122
<b>4.5. Conclusions</b> .....	<b>125</b>
4.5.1. <i>Snow Properties</i> .....	125
4.5.2. <i>Passive Microwaves</i> .....	126
<b>5.0. Diurnal Time Scales</b> .....	<b>128</b>
<b>5.1. Low-Pressure Disturbances (LPDs)</b> .....	<b>129</b>
5.1.1. <i>Background</i> .....	129
5.1.2. <i>Overview during CASES</i> .....	131
<b>5.2. Results from the Case Study</b> .....	<b>132</b>
5.2.1. <i>Meteorological Observations</i> .....	133
5.2.2. <i>Snow</i> .....	135
5.2.2.1. Thin Snow .....	135
5.2.2.1.1. Physical and Electrical Properties .....	135
5.2.2.1.2. Heat/Mass Transfer and Snow Metamorphism .....	138
5.2.2.2. Thick Snow .....	141
5.2.2.2.1. Physical and Electrical Properties .....	141
5.2.2.2.2. Heat/Mass Transfer and Snow Metamorphism .....	144
5.2.3. <i>In-Situ Passive Microwaves</i> .....	147
5.2.3.1. Thin Snow .....	147
5.2.3.2. Thick Snow .....	147
<b>5.3. Discussion</b> .....	<b>148</b>

5.3.1. <i>Thin Snow Processes</i> .....	148
5.3.2. <i>Thick Snow Processes</i> .....	150
5.3.3. <i>Snow Properties and <math>T_b</math> Variations</i> .....	152
<b>5.4. Conclusion</b> .....	153
<b>6.0. Development of a Snow Water Equivalent Algorithm from</b>	
<b><i>In-Situ Data</i></b> .....	<b>155</b>
<b>6.1. Algorithm Development</b> .....	155
6.1.1. <i>Thin Snow (30-40 °)</i> .....	156
6.1.2. <i>Thick Snow (55-70 °)</i> .....	158
6.1.3. <i>Seasonally Evolving Snow Thickness (53 °)</i> .....	160
<b>6.2. Comparison</b> .....	165
6.2.1. <i>In-Situ Algorithms</i> .....	165
6.2.2. <i>Satellite Algorithms</i> .....	167
<b>6.3. Discussion and Conclusions</b> .....	169
6.3.1. <i>Seasonally Thin and Thick Snow Algorithms</i> .....	169
6.3.2. <i>Evolving Snow Algorithm</i> .....	171
<b>7.0. Satellite Remote Sensing of Snow Water Equivalent</b> .....	<b>173</b>
<b>7.1. SWE Algorithms</b> .....	173
7.1.1. <i>In-situ Meteorological Tower</i> .....	174
7.1.2. <i>MODIS</i> .....	175
7.1.3. <i>NARR</i> .....	175
<b>7.2. Results and Discussion</b> .....	176
7.2.1. <i>Air Temperatures</i> .....	176

7.2.2. AMSR-E $T_b$	178
7.2.3. SWE Predictions	179
7.2.3.1. Smooth Ice Snow Water Equivalent Data	182
7.2.3.2. Rough Ice Snow Water Equivalent Data	183
<b>7.3. Roughness Analysis</b>	<b>188</b>
7.3.1. Passive Microwaves	188
7.3.2. Active Microwaves	191
<b>7.4. Conclusions</b>	<b>196</b>
7.4.1. Ice Roughness vs Passive and Active Microwaves	196
7.4.2. Scaling Effects on SWE Predictions	197
<b>8.0. Summary and Conclusions</b>	<b>200</b>
<b>8.1. Thesis summary</b>	<b>200</b>
<b>8.2. Limitations</b>	<b>206</b>
8.2.1. Field Sampling	206
8.2.2. Surface Based Radiometer	208
<b>8.3. Future Work</b>	<b>209</b>
8.3.1. Data Collection and Modeling	209
8.3.2. Remote Sensing	210
<b>8.4. Closing Comments</b>	<b>210</b>
<b>Literature Cited</b>	<b>212</b>
<b>Appendix A</b>	<b>238</b>

## **List of Tables**

<b>Table-3.1:</b> Snow thickness temporal evolution for SBR incidence angles between 30 and 70° .....	87
<b>Table-5.1:</b> Sampling times (local ship time) for thin/thick snow covers and surface based radiometer (SBR) measurements .....	135
<b>Table-6.1:</b> Correlation coefficient between air, surface, snow/ice interface temperatures and temperature gradient with 19 and 37 GHz for a) C1 and C2 periods and b) C3 and C4 periods .....	163
<b>Table-7.1:</b> Basic SWE statistical data calculated from smooth ice snow thickness data .....	182
<b>Table-7.2:</b> Basic SWE statistical data calculated from rough ice snow thickness data .....	184

## List of Figures

### CHAPTER 1:

<b>Figure-1.1:</b> Schematic of snow properties and processes linkages with microwave radiometry .....	10
--	----

### CHAPTER 2:

<b>Figure-2.1:</b> Surface energy balance of snow over first-year sea ice (adapted from Hanesiak, 2001) .....	29
<b>Figure-2.2:</b> Heat conduction from one snow grain to another .....	31
<b>Figure-2.3:</b> Heat conduction through a) fresh-wetted and b) brine-wetted snow grains .....	32
<b>Figure-2.4:</b> Vapor flow path length with regards to a) large and b) small grain size .....	33
<b>Figure-2.5:</b> Thermal convection within the snow cover (adapted from Sturm and Johnson, 1991) .....	35
<b>Figure-2.6:</b> a) Turbulence pumping under unstable atmospheric conditions over a smooth snow surface and b) flow pumping under rough snow surface (modified after Power <i>et al.</i> , 1985; Granberg, 1998) .....	38
<b>Figure-2.7:</b> Snow grain bonding through dry snow equilibrium metamorphism .....	42
<b>Figure-2.8:</b> The joint density of snow grains where A and B have a N-values of 4 and 3 respectively (adapted from Arons and Colbeck, 1995) .....	43
<b>Figure-2.9:</b> Scaled snow grain micro-photographs for a) size and b) structure calculations .....	47
<b>Figure-2.10:</b> Snow drifts over a) smooth and b) rough first-year sea ice .....	48
<b>Figure-2.11:</b> Geometry of microwave propagation through a layered snowpack .....	51
<b>Figure-2.12:</b> Schematic fall snow physical processes .....	58
<b>Figure-2.13:</b> Temporal evolution of daily average air temperatures during the CASES study. The cooling and warming periods are separated by the coldest day .....	59
<b>Figure-2.14:</b> Schematic winter snow physical processes .....	61

<b>Figure-2.15:</b> Spring melt over first-year sea ice (adapted from Gogineni, 1992)	65
---	----

**CHAPTER 3:**

<b>Figure-3.1:</b> Canadian Arctic Shelf Exchange Study (CASES) overwintering mission location	71
<b>Figure-3.2:</b> Sampling sites locations around the ship (ship located beside area A)	72
<b>Figure-3.3:</b> Snow grain photography in the ship's cold laboratory	76
<b>Figure-3.4:</b> Schematic of conducted SWE transects over smooth first-year sea ice	79
<b>Figure-3.5:</b> Surface Based Radiometer calibration results for May 6 <sup>th</sup> 2004	85
<b>Figure-3.6:</b> Surface based radiometer (SBR) mounted on the C.C.G.S. Amundsen	86
<b>Figure-3.7:</b> Surface based Radiometer (SBR) measurements geometry before a) and after b) day 6	86
<b>Figure-3.8:</b> AMSR-E pixel location within Franklin Bay, N.W.T.	88
<b>Figure-3.9:</b> ScanSAR images taken on a) day 358 and b) day 24. The top two images are at 6 km resolution, and the bottom two at 11.6 km resolution	92

**CHAPTER 4:**

<b>Figure-4.1:</b> Temporal evolution of snow thickness at a) thin snow and b) thick snow sites	95
<b>Figure-4.2:</b> Temporal evolution of daily averaged a) air temperature, b) wind speed and c) cloud amount	96
<b>Figure-4.3:</b> Temporal evolution of vapor pressure for a) thin and b) thick snow covers	97
<b>Figure-4.4:</b> Temporal evolution of daily averaged a) net, b) downwelling shortwave, c) upwelling shortwave, d) downwelling longwave and e) upwelling longwave radiation	98
<b>Figure-4.5:</b> Temporal evolution of snow a) grain size, b) grain ratio, c) density, d) temperature, e) salinity and f) brine volume for thin snow covers	100

<b>Figure-4.6:</b> Temporal evolution of a) permittivity and b) dielectric loss for 19, 37 and 85 GHz for thin snow covers .....	102
<b>Figure-4.7:</b> Temporal evolution of snow grain a) size and b) ratio (major axis/minor axis) for thick snow covers .....	103
<b>Figure-4.8:</b> Temporal evolution of snow a) density and b) temperature for thick snow covers .....	104
<b>Figure-4.9:</b> Temporal evolution of snow a) salinity and b) brine volume for thick snow covers .....	105
<b>Figure-4.10:</b> Temporal evolution of a) permittivity and b) dielectric loss for 19, 37 and 85 GHz for thick snow covers .....	106
<b>Figure-4.11:</b> Temporal evolution of brightness temperatures the a) vertical and b) horizontal polarizations at 19, 37 and 85 GHz over thin snow covers .....	107
<b>Figure-4.12:</b> Temporal evolution of brightness temperatures the a) vertical and b) horizontal polarizations at 19, 37 and 85 GHz over thick snow covers .....	109
<b>Figure-4.13:</b> Temporal evolution of a) temperature gradient ( $^{\circ}\text{C}\cdot\text{cm}^{-1}$ ), b) vapor pressure gradient ( $\text{kPa}\cdot\text{cm}^{-1}$ ) and c) snow wetness for thin snow covers .....	117
<b>Figure-4.13:</b> Temporal evolution of a) temperature gradient ( $^{\circ}\text{C}\cdot\text{cm}^{-1}$ ), b) vapor pressure gradient ( $\text{kPa}\cdot\text{cm}^{-1}$ ) and c) snow wetness for thick snow covers .....	119

## CHAPTER 5:

<b>Figure-5.1:</b> Temporal evolution of hourly a) atmospheric pressure, b) air temperature, c) relative humidity, d) wind speed, e) wind direction and f) cloud amount .....	134
<b>Figure-5.2:</b> Temperature profiles measured throughout the diurnal study for a) thin and b) thick snow covers .....	137
<b>Figure-5.3:</b> Vertical profiles of thin snow a) salinity and b) brine volume temporal evolution .....	137
<b>Figure-5.4:</b> Thin snow modeled a) permittivity and b) dielectric loss temporal evolution .....	138
<b>Figure-5.5:</b> Thin snow calculated a) thermal conductivity, b) specific heat and c) thermal diffusivity temporal evolution .....	140
<b>Figure-5.6:</b> Thin snow grain size and vapor pressure temporal evolution .....	141

<b>Figure-5.7:</b> Vertical profiles of thick snow a) salinity and b) brine volume temporal evolution .....	143
<b>Figure-5.8:</b> Thick snow modeled a) permittivity and b) dielectric loss temporal evolution .....	144
<b>Figure-5.9:</b> Thick snow calculated a) thermal conductivity, b) specific heat and c) thermal diffusivity temporal evolution .....	145
<b>Figure-5.10:</b> Thick snow grain size and vapor pressure temporal evolution .....	146
<b>Figure-5.11:</b> Temporal evolution of passive microwave brightness temperatures for the vertical and horizontal polarizations at 19 GHz (a and b), 37 GHz (c and d) and 85 GHz (e and f) .....	148

## CHAPTER 6:

<b>Figure-6.1:</b> Comparison between the modeled and measured SWE values (a) and the temporal evolution of the variation (b) for thin snow covers .....	158
<b>Figure-6.2:</b> Comparison between the modeled and measured SWE values (a) and the temporal evolution of the variation (b) for thick snow covers .....	160
<b>Figure-6.3:</b> Relationship between brightness temperatures ( $53^\circ$ ) and evolving snow water equivalent (SWE) for a) 19 GHz and b) 37 GHz .....	161
<b>Figure-6.4:</b> Temporal evolution of snow thickness (cm) at $53^\circ$ of incidence angle .....	162
<b>Figure-6.5:</b> Correlation between measured and modeled snow water equivalent (SWE) at $53^\circ$ of incidence angle .....	164

## CHAPTER 7:

<b>Figure-7.1:</b> Temporal evolution of a) meteorological tower, MODIS and NARR air temperatures and b) the differences between MODIS and NARR data with respect to the meteorological tower (considered as reference) .....	178
<b>Figure-7.2:</b> Temporal evolution of atmospherically corrected AMSR-E brightness temperatures in both vertical and horizontal polarizations .....	179
<b>Figure-7.3:</b> Temporal evolution of predicted SWE using air temperature data from the NARR re-analysis and AMSR-E brightness temperatures .....	181

<b>Figure-7.4:</b> Temporal evolution of SWE predictions for modeled p_Min and p_Max (black and gray lines), and measured at the smooth SWE transects sites (dots)	.....183
<b>Figure-7.5:</b> Temporal evolution of SWE predictions for modeled p_Min and p_Max, and measured at the rough snow thickness transects sites	.....185
<b>Figure-7.6:</b> Temporal evolution of a) polarization ratio at 18 GHz and b) the gradient ratio between 18 and 36 GHz for both p_Min and p_Max. In c) a scatter plot of the polarization ratio and gradient ratio	.....189
<b>Figure-7.7:</b> ScanSAR images taken on a) day 358 and b) day 24. The top two images are at 6 km resolution, and the bottom two at 11.6 km resolution (p_Min at top right, and p_Max at bottom left)	.....191
<b>Figure-7.8:</b> Mean backscatter values for p_Min and p_Max at a) 6 km and b) 11.6 km of resolution	.....193
<b>Figure-7.9:</b> Standardized backscatter values for both p_Min and p_Max relative to the surrounding area (see Figure-3.9) at a) 6 km and b) 11.6 km resolutions	.....194

# CHAPTER 1: INTRODUCTION

## 1.1. Rationale

The first and strongest signs of global climate variability and change have been observed in the Arctic over the past three decades (ACIA, 2004) due to a variety of strong climate related feedbacks (Francis *et al.*, 2005; Rothrock and Zhang, 2005). Patterns in sea ice areal extent and thickness show a statistically significant trend towards negative anomalies throughout the period 1979 to 2000 (Barber and Hanesiak, 2004). Spatial sea ice depletion of approximately 7.8 % per decade since the 1970s has decreased the total sea ice coverage by more than 1.3 million km<sup>2</sup> (Stroeve *et al.*, 2005). Furthermore, significant decrease in sea ice thickness was measured in both first-year and multi-year ice with a 32 % decrease in thick ice volume between 1958 and 1997 (Yu *et al.*, 2004). Both spatial and thickness reductions in sea ice can have a significant impact on global-scale climate variability due to their control on atmospheric circulation patterns (Gerdes, 2006) such as the North Atlantic Oscillation (Polyakov *et al.*, 2003).

The ocean-sea ice-atmosphere (OSA) interface plays a critical role in the exchange of energy and mass across the surface and thus plays a central role in how the marine cryosphere responds to climate change. A detailed examination of the observed climate states of the snow in particular is required given recent evidence of a rapidly depleting ice cover (e.g., Deser *et al.*, 2000; Hilmer and Lemke, 2000; Wadhams and Davis, 2000; Francis *et al.*, 2005; Stroeve *et al.*, 2005) with a potential summer ice-free Arctic by mid-century (e.g., Flato and Boer, 2001; Barber and Hanesiak, 2004). Of primary concerns are the spatial and temporal scales of snow variability in the Arctic (Barber *et al.*, 1995; Sturm *et al.*, 2006; Markus *et al.*, 2006a) and the scarcity of existing annual snow datasets over first-year sea ice coupled with ancillary measurements of heat

and mass transfers, energy fluxes as well as microwave scattering and emission data. Furthermore, current sea ice models, have lingering uncertainties due to strong assumptions with regards to snow cover (Martin *et al.*, 2005) and improved information on snow properties is required. Of the snow on sea ice work, almost all of the previous studies have focused on the spring to summer transition rather than the important fall to winter, or winter to spring transition. An accelerated hydrological cycle, as modeled under an increased CO<sub>2</sub> and aerosol scenario (Boer *et al.*, 2000), would increase the amount of snowfall during the winter period given the expected climatology of sea ice covered oceans (Flato and Boer, 2001), and better ways to quantify snow over sea ice has yet to be developed.

Snow is arguably the most important element of the OSA as it controls both conductive and radiative exchanges across this interface (e.g., Powell *et al.*, 2005). In particular, snow regulates heat and mass transfers between the atmosphere and the ocean due to its low thermal conductivity ( $k_s$ ) and diffusivity ( $v_s$ ) (Arons and Colbeck, 1995; Sturm *et al.*, 2002), playing a dominant role in the surface energy balance (SEB) (Moritz and Perovich, 1996; Frei and Robinson, 1999; Jordan and Andreas, 1999; Sturm *et al.*, 2002; Eicken, 2003; Dethloff *et al.*, 2006). Consequently, changes in snow physical and thermal properties (hereinafter referred as thermophysical properties) can substantially alter the OSA surface energy balance (e.g., Welch and Bergmann, 1989; Barber *et al.*, 1998; Mundy *et al.*, 2005) as well as the timing of annual freezing/melting of sea ice (Ledley, 1991; Flato and Brown, 1996; Boer *et al.*, 2000).

Studies of conductive and diffusive transfers in snow covered sea ice (e.g., Eicken *et al.*, 1995; Sturm *et al.*, 2002; Albert, 2002; Zhekamukhova, 2004) have shown that snow physical

properties control thermal conduction and diffusion. The thermal conductivity of snow is computed from statistical models relating  $k_s$  to snow density ( $\rho_s$ ) and is directly proportional to thermal diffusivity, a fundamental parameter in metamorphic processes (e.g., Mellor, 1977; Colbeck, 1993; Albert, 2002). *In-situ* measurements of  $k_s$  by Sturm *et al.*, (2002) ranged between 0.078 to 0.290  $\text{W}\cdot\text{m}^{-1}\cdot\text{K}^{-1}$  with a bulk average of 0.14  $\text{W}\cdot\text{m}^{-1}\cdot\text{K}^{-1}$ , noting that air movements, snow structure and density play important roles in heat and mass transfers. Snow thermal diffusivity can be calculated from density, specific heat ( $c$ ) and thermal conductivity (Oke, 1987) however; limited work was conducted *in-situ*. Bartlett *et al.*, (2004) highlighted the control of  $v_s$  on snow basal layer temperature, controlling the temperature gradient. Both  $k_s$  and  $v_s$  are variable on both diurnal and seasonal scales strengthening the need in understanding how snow physical properties such as density and grain morphology affect thermodynamic processes.

Seasonal snow density values have been widely published (e.g., Mellor, 1977; Vowinkel and Orvig, 1970; Barber *et al.*, 1994; Sturm *et al.*, 1997; Warren *et al.*, 1999), but detailed snow grain morphology observations are limited. Previous research have shown that kinetic growth grains dominate the basal layers and more rounded grains typically occur within upper layers of the snow cover (e.g., Grenfell and Maykut, 1977; Barber *et al.*, 1995; Sturm *et al.* 2002; Flanner and Zender, 2006). A lack of information on snow geometry variation and evolution has led to the realization that improved observations are needed to correctly parameterize heat and mass transfers within the snow cover (Wu *et al.*, 1999; Massom *et al.*, 2001; Sturm *et al.*, 2002; Eicken, 2003).

Energy fluxes also have a dominant influence on snowpack thermophysical properties evolution including metamorphism and water phase transitions (Barber *et al.*, 1994). Net shortwave radiation ( $K^* = K\downarrow - K\uparrow$ ) is highly influenced by the presence or absence of snow over sea ice. The high albedo ( $\alpha$ ) of snow significantly reduces absorbed downwelling shortwave ( $K\downarrow$ ) radiation and fresh snowfall can significantly increase the surface albedo, particularly in the near infrared portions of the spectrum (Li *et al.*, 2001). Radiative transfer of shortwave energy is also dominated by grain size and shape as well as the amount of liquid water within the snow (e.g., Warren, 1982; Zhou and Li, 2002). The presence of small amounts of water in liquid phase can have a dramatic effect on increasing shortwave transmission within naturally occurring snow on sea ice (Yang *et al.*, 1999) by decreasing the albedo and increasing thermal conductivity (e.g., Eicken, 2003). The net longwave flux ( $L^* = L\downarrow - L\uparrow$ ) is determined by the temperature and humidity profile in the lower atmosphere and the surface temperature of the snow (Hanesiak *et al.*, 1999). The open ocean, melt ponds and melting snow of spring and summer will increase cloud fraction, increasing the amount of downwelling longwave radiation during the summer (Barber and Thomas, 1998). Sensitivities to melt onset from cloud fraction, base height and phase transitions in the snow are the topic of contemporary research outside of the scope of this dissertation (e.g., Curry *et al.* 1996; Xin and Barber, 2005).

Microwave remote sensing has proved to be a useful tool to estimate snow thickness (i.e. snow water equivalent, SWE) remotely from space due to its relative transparency to clouds and darkness (e.g., Ulaby *et al.*, 1986; Golden *et al.*, 1998), and the high sensitivity of microwave emission to the changes in dielectric properties of snow (i.e. the changes in thermophysical properties). Extensive work estimating snow thickness using passive microwave radiometry

from satellite remote sensing has been conducted since the 1980s (e.g., Cavalieri and Comiso, 2000). Many of these studies have examined the relationship between SWE and passive microwave brightness temperature ( $T_b$ ) over land (e.g., Chang *et al.*, 1982, 1987; Kunzi *et al.*, 1982; Comiso *et al.*, 1989; Walker and Goodison, 1993; Tait, 1998; Pulliainen and Hallikainen, 2001, Walker and Silis, 2002; Derksen *et al.*, 2005), however accurate methods have yet to be developed over first-year sea ice. Limited work on snow depth distribution over sea ice (e.g., Comiso *et al.*, 1989; Markus and Cavalieri, 1998; Markus *et al.*, 2006a) showed fairly good agreement between estimated and measured data. Amongst the difficulties, we denote vertical, diurnal and seasonal changes in snow physical properties (e.g., Barber *et al.*, 1994; Sturm *et al.*, 2002) due to metamorphic processes that can alter microwave emission (e.g., Grenfell and Lohanick, 1985; Armstrong *et al.*, 1993; Lohanick, 1993). Furthermore, the precision of the SWE estimation is also affected by the changes in the liquid water content in snow, which readily modifies the snow emissivity (Drobot and Barber, 1998).

Some studies looked specifically at SWE over first-year sea ice using data from surface based passive microwave radiometers (Drobot and Barber, 1998; Barber *et al.*, 2003) and results showed that 37 GHz was the most appropriate frequency to estimate SWE in snow depth averaging 20 cm. Other work using spaceborne brightness temperatures data looked at the gradient ratio between 19 and 37 GHz to estimate snow thickness accounting for the fraction of open water within the satellite pixel (Cavalieri and Comiso, 2004; Markus *et al.*, 2006b). However no detailed winter analysis on snow thickness variations nor the impact of thermophysical processes on passive microwaves signatures have yet been conducted.

One of the main challenges in SWE retrieval studies over sea ice relates to spatial heterogeneity (e.g., Sturm *et al.*, 2006). For instance, brightness temperatures from the Advanced Microwave Scanning Radiometer for Earth Observing System (AMSR-E) include emission contributions from different surface features (smooth ice, rough ice, open water) found in a pixel of 12.5 x 12.5 km (e.g., Mäkynen and Hallikainen, 2005) that can potentially affect SWE predictions. Hence, the impact of ice roughness on existing algorithms needs to be addressed qualitatively and quantitatively.

With increasing ice roughness, the scattering increases and the polarization effect is expected to decrease (e.g., Matzler, 1987; Eppler, 1992). Hence, the discrimination between smooth ice and ice ridges is possible due to the strong polarization effect of a layered snowpack (e.g., Garrity, 1992). Previous results from Kurvonen and Hallikainen (1996) showed good detection of deformed ice and old level ice using a combination of high (94 GHz) and low (24 or 34 GHz) airborne brightness temperature data. Furthermore, Mäkynen and Hallikainen (2005) investigated the effect of ice deformation on the passive microwaves polarization ratio (PR) and gradient ratio (GR) for different types of snow covers. Their results showed that the polarization ratio decreases with increasing ice roughness for both dry and moist snow but they had no success in discriminating all ice types. The combination of passive microwave brightness temperatures along with synthetic aperture radar (SAR) backscatter information could improve sea ice roughness information and very few studies have looked into this issue.

Despite upcoming challenges addressing snow global scale variability, microwave snow remote sensing has proven to be the best tool for the development of SWE retrieval algorithms and

efforts are required given the actual changes that are occurring in the Arctic. Therefore, snow on sea ice remains a high priority for field, modeling and process related studies pertaining to sea ice and climate change (IPCC, 2001).

## 1.2. Objectives

The main objective of my dissertation is to develop a snow water equivalence (SWE) algorithm over first-year sea ice using passive microwave radiometry. To meet this goal, an acute comprehension on the seasonal evolution of Arctic snow cover dynamic and thermodynamic processes with regards to atmospheric conditions is required. Furthermore, the existing linkages between these processes and passive microwave scattering and emission mechanisms are of primary importance in order to meet the challenges of passive microwave remote sensing over sea ice described above (Figure-1.1).

I eluded to existing 'science gaps' that need to be addressed in order to retrieve SWE over first-year sea ice using spaceborne remote sensing. Four main objectives arise from this statement:

**Objective 1:** To understand the temporal evolution of snow thermodynamic and dynamic processes. More specifically, I want to:

- a) evaluate the winter seasonal evolution (long term),*
- b) evaluate short-term changes associated with daily atmospheric pressure variations (short term),*

*c) understand the seasonal and diurnal dynamic and thermodynamic processes within the snow cover,*

*d) identify the forcing agents and understand their impact on the surface energy balance.*

**Objective 2:** To understand the effect of these snow temporal evolution processes on microwave signatures. Specific objectives are to:

*a) understand the impact of snow seasonal evolution on passive microwave signatures,*

*b) understand the impact of snow short-term changes on passive microwave signatures,*

*c) evaluate the impact of polarization and incidence angles on these changes on both short and long term scales.*

**Objective 3:** To develop snow water equivalence (SWE) algorithms using passive microwave radiometry from *in-situ* measurements. Specific objectives are to:

*a) understand the effect of frequency, polarization and incidence angle in SWE predictions,*

*b) investigate different algorithms for both thin and thick snow covers at different incidence angles,*

*c) validate these algorithms with existing in-situ and satellite products,*

*d) develop a SWE algorithm valid over a wide range of snow thickness at incidence angle used by satellites (53-54 °).*

**Objective 4:** Apply the algorithms developed in Objective 3 to passive microwave satellite data.

Specifically, I want to:

- a) apply the SWE algorithm developed in objective 3d to AMSR-E satellite data,*
- b) to validate the predictions with in-situ snow thickness distribution data,*
- c) to evaluate the potential of qualifying ice roughness using passive and active microwave remote sensing,*
- d) to evaluate the effect of surface roughness on the SWE predictions using passive and active microwave data.*

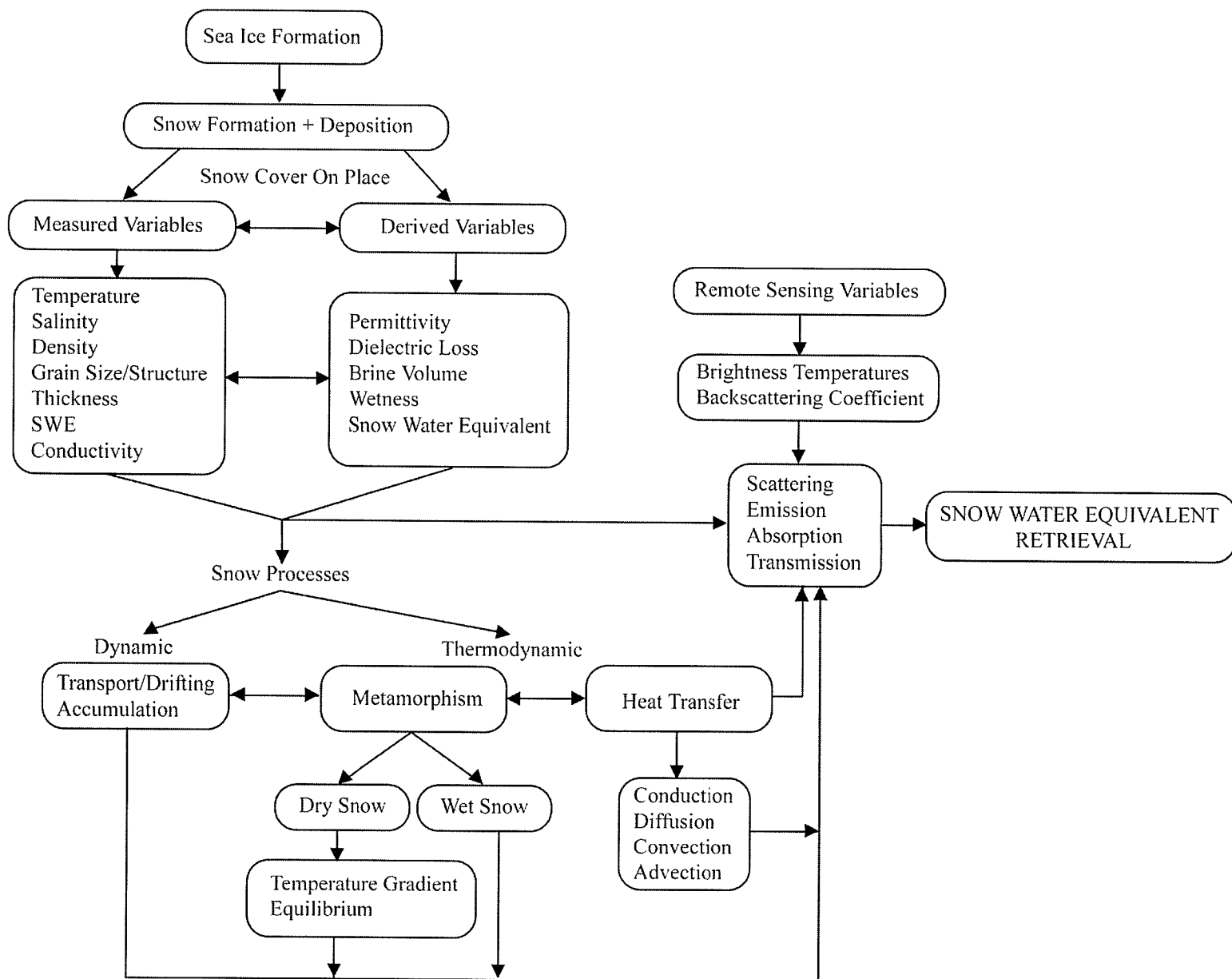


**Figure-1.1:** Schematic of snow properties and processes linkages with microwave radiometry.

### 1.3. Thesis Outline

Each of the objectives mentioned above are addressed in research papers highlighted in this dissertation. The dissertation consists of 8 chapters, each addressing specific objectives. I provide the references for the research papers I have submitted and published (Manuscripts 1 to 6) throughout my PhD at the end of this section.

In Chapter 2, I provide a summary of the current state of knowledge pertaining to the geophysical, thermodynamic, and dielectric properties of snow on sea ice. I first give a detailed description of snow thermal properties such as thermal conductivity, diffusivity, specific heat, heat capacity and how snow geophysical/electrical properties are affected by seasonal surface energy balance. I also review the different microwave emission and scattering mechanisms associated with different seasonal snow processes. Finally, I discuss the annual evolution of the Arctic system through snow thermodynamic (heat/mass transfer, metamorphism) and aeolian processes, with linkages to microwave remote sensing that have yet to be defined from an annual perspective in the Arctic.

In Chapter 3 I provide a general overview of the main study site located in Franklin Bay, N.W.T throughout the Canadian Arctic Shelf Exchange Study (CASES) overwintering mission in 2003-2004. I provide a map of the area, a detailed schematic of the sampling sites around the icebreaker and a brief description of the ice conditions in the region. I also provide basic information on the data and instrumentation from the various meteorological and micrometeorological stations that collected weather information and surface energy balance measurements. I also describe the methods related to snow sampling for both field and

laboratory settings as well as details on the dielectric properties modeling. Finally, detailed methodology on the passive microwave data collection is provided for both the *in-situ* surface based radiometer (passive microwaves) as well as for NASA's Advanced Microwave Scanning Radiometer for Earth Observing System (AMSR-E).

In Chapter 4, I present results from two sampling areas (thin and thick snowpacks) showing that differences in snow thickness can substantially change the vertical and temporal evolution pattern of snow thermophysical and electrical properties. I analyze the winter temporal evolution between December 2003 and May 2004 for both sites where snow was sampled 3 times per day, every second day. I present the differences in evolutionary manner between the winter cooling and warming periods leading into spring. I also provide a thorough analysis on the observed linkages between snow properties and passive microwave brightness temperatures for different frequencies, polarization and incidence angles. This chapter fills a 'science gap' in the literature since most of the work over first-year sea ice has been conducted during spring and over shorter periods of time. The analysis presented represents the core dataset for the development of snow water equivalent algorithm presented in Chapters 6 and applied to AMSR-E in Chapter 7.

The seasonal snow temporal evolution from Chapter 4 is followed by a 'short time scale' analysis looking at changes in snow thermophysical properties and the corresponding response of passive microwave brightness temperatures on a daily scale from a case study. In Chapter 5, I show that short-term changes are strongly affected by atmospheric conditions and these variations could potentially affect SWE predictions from space. A case study under a warm front was conducted during CASES and this chapter highlights the effects on thin and thick snow thermophysical and

electrical properties. More of these low-pressure systems are to be expected in the Arctic, and the detection the impact on brightness temperatures needs to be addressed. I first provide the theoretical basis for these systems as well as a review of their occurrence during the CASES study. I then show that the concomitant changes in snow properties are detectable through *in-situ* passive microwave radiometry at 85 GHz. To the best of my knowledge, this was never measured before over first-year sea ice.

In Chapter 6, a SWE algorithm is developed for thin and thick snow using both *in-situ* microwave measurements and snow thermophysical properties from Chapter 4. I investigate the potential of using numerous temperature measurements (air, snow/ice, temperature gradient) as well as different frequencies and polarizations (19, 37, 85 GHz,  $\Delta T_b$ ) into a multiple regression based algorithm. I discuss which product should be used given the validation results from field data and the multiple regression results. I show that the SWE predictions over thin and thick snow are quite accurate, and show very good agreement with the measured data especially during the cooling period. I also investigate the threshold between thin and thick SWE algorithms at Brewster angle ( $53^\circ$ ) for further satellite application (Chapter 7). Results showed that 33 mm represents a good estimate of the threshold that should be employed given the surface based radiometer  $T_b$  temporal behavior. The resulting predictions over evolving snow thickness are significant throughout a large range of air temperatures and snow thickness. I conclude the chapter with a discussion on the limitations and variations of the SWE predictions given the understanding of snow and  $T_b$  linkages provided in Chapters 4 and 5.

In Chapter 7, I provide SWE predictions from AMSR-E brightness temperatures in two pixels located in the study area. I show that the predictions are statistically valid with the *in-situ* snow thickness data for both smooth and rough ice environments. Only the thin snow algorithm was required throughout the study given the AMSR-E brightness temperature values range (SWE < 33 mm). I also discuss the different air temperature products applicable to the algorithm from a comparison with the meteorological tower measurements provided in Chapter 4. A qualitative study of sea ice roughness using both passive and active microwave satellite data shows that the two pixels are rougher than the surrounding areas, but the SWE predictions did not seem to be affected. However, results were inconclusive with regards to the amplitude of the roughness with the studied AMSR-E pixels.

The material in my thesis has been published in the peer reviewed literature, or is currently in review. Each paper makes up a substantive portion of each of the chapters described above. The pertinent journal articles are:

1. **Langlois A., and Barber D.G.** 2007. *Passive Microwave Remote Sensing of Seasonal Snow Covered Sea Ice*. In press September 2007, *Progress in Physical Geography*.
2. **Langlois A, Mundy C.J, and Barber D.G.** 2007. *On the winter evolution of snow thermophysical properties over landfast first-year sea ice*. *Hydrological Processes*, vol. 21, 6, p. 705-716, doi: 10.1002/hyp.6407.
3. **Langlois A., Barber D.G. and Hwang B.J.** 2007. *Development of a winter snow water equivalent algorithm using in-situ passive microwave radiometry over snow covered first-year sea ice*, vol. 106, no. 1, p. 75-88, doi: 10.1016/j.rse.2006.07.018.
4. **Langlois A., Fisco T., Barber D.G. and Papakyriakou T.N.** 2007. *The response of snow thermophysical processes to the passage of a polar low-pressure system and its impact on in-situ passive microwave data: A case study*, Submitted March 2007, *Journal of Geophysical Research*, 2007JC004197.

5. **Langlois A. and Barber D.G.** 2007. *Seasonal Snow Water Equivalent (SWE) Retrieval using In-Situ Passive Microwave Measurements over First-Year Sea Ice*. Accepted July 2007, *International Journal of Remote Sensing*, TRES-PAP-2007-0210.
6. **Langlois A., Scharien, R., Gelsetzer T., Hwang B.J., Iacozza J., Barber D.G. and Yackel J.** 2007. *Estimating Snow Water Equivalent over First-Year Sea Ice using Satellite Microwave Remote Sensing*. Submitted October 2007, *Remote Sensing of Environment*.
7. **Isleifson, D., Langlois, A., Barber, D.G. and Shafai, L.** 2007. *C-Band Scatterometer Measurement of Late Season Multiyear Sea Ice in the Canadian Arctic*. *IEEE Transactions on Geoscience and Remote Sensing*. Submitted, September 2007, TGRS-2007-00547.
8. **Hwang, B.J., Langlois, A., Barber, D.G. and Papakyriakou, T.N.** 2006. *On detection of the thermophysical state of landfast first-year sea ice from microwave emissions during spring melt: Part 1. An in-situ study*, *Remote Sensing of Environment*, In Press, doi:10.1016/j.rse.2007.02.033.
9. **Geldsetzer, T., Langlois, A. and Yackel, J.** 2007. *Permittivity of brine-wetted snow on first-year sea ice at 20 MHz*. *Cold Regions Science and Technology*, Accepted July 2007, CRST-D-07-00040.

I have provided the scientific rationale for my dissertation in this chapter. I have also described the objectives and the structure in which I address these objectives. In the next chapter, I present the scientific background required to understand the context of my thesis. I present information on snow on sea ice from the perspective of geophysics, thermodynamics and dielectrics. I define each of these terms and introduce the notion of thermophysical properties of snow covered sea ice. I also provide a thorough background on how the surface energy balance drives the diurnal and seasonal evolution of thermophysical properties and evaluate how this may affect estimation of passive microwave derived SWE estimates.

## **CHAPTER 2: BACKGROUND**

In this chapter, I provide background material pertaining to first-year sea ice snow thermophysical and electrical properties as well as their linkages with passive and active microwave radiometry. I first provide a general overview of global Arctic atmospheric and ocean circulation patterns (Section 2.1). I then describe the surface energy balance of the OSA and snow formation and accumulation processes (Sections 2.2 and 2.3). Snow properties and processes such as heat transfer, metamorphism and aeolian transport are discussed in Sections 2.4 and 2.5 whereas details on microwave radiative transfer are given in Section 2.6. Finally, I discuss the annual evolution of the Arctic system through those processes along with applications to microwave remote sensing in Section 2.7.

### **2.1. Ocean and Atmospheric Circulation**

The Arctic Ocean is characterized by "semipermanent" patterns of high- and low-pressure systems. These patterns appear in charts of long-term average surface pressure such as the Aleutian Low, Icelandic Low, Siberian High, Beaufort High, and North American High. These systems trigger air mass movement (fronts), whose travel paths goes from areas of high pressure to areas of low pressure. Such air movement is accompanied with changes in temperatures, wind speed/direction, relative humidity and the impact on the SEB can be significant (e.g. Colbeck, 1989).

On a global scale, the Arctic sea ice thickness and extent is also influenced by oceanic circulation. The consequent drifting ice creates pressure ridges and the magnitude of the surface (ridge sails) and bottom (ridge keels) roughness depends on the drift velocity and ice thickness. There are two dominant ocean circulation regimes in the Arctic namely the Beaufort Gyre and the Transpolar Drift that both push the ice against the north coast of Greenland and the Canadian Archipelago (convergence). Consequent to the increasing convergence, the ice thickness can reach 6 to 8 m in the in these regions (Thorndike *et al.*, 1992). On the other hand, divergence creates cracks, leads and polynyas, which in turn have significant impact on the energy exchange across the OSA by increasing the release of latent heat into the atmosphere. Generally, the Arctic environment is known to be convergence-dominated due to the predominance of land in the ocean as it is dominated by divergence in the Antarctic for the opposite reason.

## 2.2. Surface Energy Balance of the OSA

The surface energy balance controls the various thermodynamic and dynamic processes across the OSA interface. From Eicken (2003), the SEB of this interface can be expressed as:

$$SEB_{OSA} = K \downarrow - K \uparrow + L \downarrow - L \uparrow + Q_h + Q_e + Q_c + Q_p + Q_{ms} \quad [\text{eq. 2.1}]$$

In [eq. 2.1],  $K \downarrow$  represents the incoming shortwave solar radiation,  $K \uparrow$  the reflected shortwave radiation,  $L \downarrow$  the incoming longwave radiation,  $L \uparrow$  the upwelling longwave radiation,  $Q_h$  the sensible heat flux,  $Q_e$  the latent heat flux,  $Q_c$  the conductive flux,  $Q_p$  the heat conducted by precipitation and  $Q_{ms}$  the heat flux associated with phase change (although not significant during

the winter). Each of the elements of [eq. 2.1] change seasonally and affect the snow thermophysical properties measured at the surface. The nature of these changes will be given in Section 2.7.

The turbulent fluxes are very sensitive to variations in wind speed, temperature and humidity (seasonally variable) and thus, are related to atmospheric stability. An increase in atmospheric stability is translated by a decrease in turbulent fluxes (e.g., Arya, 1988; Halliwell and Rouse, 1989). For instance, the passage of a warm front (increasing temperature, wind speed and relative humidity) creates strong  $Q_h$  fluxes directed towards the surface ('+'). Such fluxes can occur both above and below 0°C as  $Q_h$  fluxes directed towards the atmosphere ('-') can only occur in temperatures below 0°C (Steffen and DeMaria, 1996). Negative  $Q_h$  fluxes can be measured behind low-pressure systems or during the passage of a cold front where the air temperature decreases rapidly. The  $Q_e$  flux will respond accordingly to surface temperature and relative humidity, which increase will enhance the upward flux density (Launiainen and Vihma, 1990).

Both sensible ( $Q_h$ ) and latent ( $Q_e$ ) heat fluxes can be calculated as:

$$Q_h = \rho_{air} c_{air} \cdot C_{Hz} (\theta_s - \theta_z) V \quad [\text{eq. 2.2}]$$

$$Q_e = \rho_{air} \ell \cdot C_{Ez} (q_s - q_z) V \quad [\text{eq. 2.3}]$$

where  $\rho_{air}$  is the air density,  $c_{air}$  is the specific heat of the air,  $C_{Hz}$  and  $C_{Ez}$  the transfer coefficients,  $\ell$  the latent heat of vaporization,  $(\theta_s - \theta_z)$  and  $(q_s - q_z)$  the difference (surface –

height) in potential temperatures and specific humidity respectively and  $V$  the wind speed (Holtslag and de Bruin, 1988). The details of the SEB specific to snow are given in Section 2.4.3.

### 2.3. Snow Formation and Accumulation

The water molecule is composed of one atom of oxygen and 2 atoms of hydrogen, arranged as H-O-H at an angle of  $104.5^\circ$ . In order to have precipitable water in the atmosphere, saturated conditions are required. Saturation is met when an air mass is lifted into the atmosphere where the colder temperatures decrease the saturation vapor pressure. Condensation then occurs (Hornberger *et al.*, 1998) in presence of condensation nuclei and water droplets will grow according to:

$$F = \frac{\partial m}{\partial t} = 4\pi \cdot r^2 D = \frac{\partial \rho}{\partial R}, \quad [\text{eq. 2.4}]$$

In [eq. 2.4],  $r$  is the radius of the spherical surface and  $D$  the diffusion coefficient of water. These newly formed water droplets need to collide (coalescence) with each other to overcome gravity.

The change of phase from water droplets to ice particles requires sub-zero temperatures and the presence of nucleating agents. The two main nucleation mechanisms namely heterogeneous and homogeneous nucleation can both trigger ice crystal formation. The homogeneous nucleation is a spontaneous process that occurs when ice crystals form from supercooled water droplets at –

40°C. Alternatively, heterogeneous nucleation is divided in three types: deposition of vapor on ice nucleus ( $R > 1000 \text{ \AA}$ ), immersion-freezing when the ice nucleus is imbedded in supercooled droplet ( $R > 100 \text{ \AA}$ ) and contact-collision between the ice nuclei and the supercooled droplets. Once formed, the ice particles will grow from different mechanisms such as: growth from the vapor phase, aggregation and riming. The growth from vapor phase is driven by the greater supersaturation over ice crystals rather than water droplets resulting in a flux from water vapor to ice (growth). The aggregation occurs with the collision and adhesion of ice particles, when growth rate is faster than the vapor phase growth. Finally, riming is by definition the adhesion of supercooled water to the ice crystal.

The progression from ice particles to snowflakes depends on the type of nuclei (Bailey and Hallett, 2002) and the percentage of supersaturation relative to ice. The supersaturation occurs when the relative humidity exceeds 100% in the atmosphere when an air mass is being cooled without condensing (absence of condensation nuclei). The concentration of ice crystals is controlled by supersaturation depletion due to growth (because the vapor pressure decreases with increasing curvature) and an increasing supersaturation due to cooling (Jensen and Pfister, 2005). The nucleation then ceases when enough crystals have nucleated such that the vapor pressure depletion takes over (Koop *et al.*, 2000).

The initial ice crystal has three a-axis (basal plane) that are separated by an angle of  $120^\circ$  in a hexagonal symmetry and one c-axis  $90^\circ$  to the basal plane. The crystals that grow in the a-axis orientation will create the classic planar star-like snow crystals as the ones growing along the c-axis produce columnar structures. With a high supersaturation percentage relative to ice, the

growth of ice crystals will occur where there is an excess in vapor density ( $\text{Weight}_{\text{vapor}} / \text{Weight}_{\text{volume}}$ ) at the edges and corners producing thin crystals such as dendrites and needles. A low supersaturation level tends to produce solid and thicker structures such as plates and prisms. When these crystals fall into the atmosphere towards the surface, they will travel through different temperature and water vapor regimes that might change their shape. They eventually reach the sea ice surface where their properties and accumulation will greatly influence the SEB of the OSA.

## 2.4. Snow Properties

### 2.4.1. Thermophysical

#### 2.4.1.1. Thermal Conductivity

The thermal conductivity,  $k$ , is defined by a quantity of energy (heat) conducted through a media (i.e. snow layer) in response to a temperature gradient (units in  $\text{W}\cdot\text{m}^{-1}\cdot\text{K}^{-1}$ ). The higher the thermal conductivity the easier heat is transferred from one layer to another. In terms of snow,  $k_s$  is mostly affected by snow texture, density and temperature (Mellor, 1977; Colbeck, 1982; Sturm *et al.*, 2002). Snow is a mixture of ice, air and brine and their respective volume fraction ( $V_{\text{ice}}$ ,  $V_{\text{air}}$  and  $V_{\text{brine}}$ ) dictate the thermal conductivity. Based purely on snow density ( $\rho_s$ ), Abel (1893) first suggested a simple approach to calculate  $k_s$  [eq. 2.5] whereas recent results from *in-situ* work in the Beaufort Sea by Sturm *et al.*, (2002) suggested different thermal conductivity calculations for different density ranges [eq. 2.6 and 2.7] where  $k_s$  adjusts better to higher snow densities.

$$k_s = 2.85\rho_s^2 \quad \text{[eq. 2.5]}$$

$$k_s = 0.138 - 1.01\rho_s + 3.233\rho_s^2 \quad \text{for } (156 \leq \rho_s \leq 600 \text{ kg}\cdot\text{m}^{-3}) \quad [\text{eq. 2.6}]$$

$$k_s = 0.023 - 1.01\rho_s + 0.234\rho_s^2 \quad \text{for } (\rho_s < 156 \text{ kg}\cdot\text{m}^{-3}) \quad [\text{eq. 2.7}]$$

Other work by Ebert and Curry (1993) estimated  $k_s$  based on both temperature and density [eq. 2.8]:

$$k_s = 2.845 \cdot 10^{-6} \cdot \rho^2 + 2.7 \cdot 10^{-4} \cdot 2^{\frac{(T_s - 233)}{5}} \quad [\text{eq. 2.8}]$$

where  $T_s$  is the temperature of snow (K). According to the equations above, both density and temperature dictate the thermal conductivity. Typical values of snow thermal conductivity will range between 0.1 and 0.4  $\text{W}\cdot\text{m}^{-1}\cdot\text{K}^{-1}$  (eg, Ebert and Curry, 1993; Sturm *et al.*, 2002) depending on the state of the snowpack (i.e. volume fractions of ice, air and brine).  $V_{air}$  and  $V_{ice}$  govern the density of the snowpack and therefore the thermal conductivity of snow can be examined as the sum of the constituent conductivities of air ( $k_{air}$ ) and ice ( $k_{ice}$ ). The value of  $k_{air}$ , approximately 0.025  $\text{W}\cdot\text{m}^{-1}\cdot\text{K}^{-1}$ , is much lower than  $k_{ice}$ , which varies between 1.6 and 2.2  $\text{W}\cdot\text{m}^{-1}\cdot\text{K}^{-1}$  (McKay, 2000; Pollard and Kasting, 2005).

The effect of temperatures is related to the volume fraction of brine. Warm temperatures will allow a greater value of  $V_{brine}$  within the snowpack where the thermal conductivity of brine,  $k_b$ , is less than of  $k_{ice}$  (eg, Yen, 1981):

$$k_b = 0.4184 \cdot (1.25 + 0.03T + 0.00014T^2), \quad [\text{eq. 2.9}]$$

where  $T$  is the temperature in Celsius (Lange and Forker, 1952). An increasing brine volume will affect  $k_s$  differently based on whether the increase is at the expense of  $V_{air}$  or  $V_{ice}$ . For instance, if the increase is at the expense of grain size (i.e.  $V_{brine} \uparrow, V_{ice} \downarrow$ ), the  $k_s$  decreases due to a lower thermal conductivity for brine volume relative to ice. On the other hand, if brine volume increases at the expense of air, the thermal conductivity is expected to increase (i.e.  $V_{brine} \uparrow, V_{air} \downarrow$ ) due to the higher thermal conductivity of brine relative to air (Papakyriakou, 1999). Since all air, ice and brine volume fractions change vertically and temporally within the snow cover, the  $k_s$  is not constant with depth and time.

#### 2.4.1.2. Thermal Diffusivity

Snow thermal diffusivity,  $v_s$ , also plays an important role in the heat transfer through the snow cover (e.g., Oke, 1987). It defines the ratio of the thermal conductivity to the volumetric heat capacity,  $C_s$  ( $\text{J}\cdot\text{m}^{-3}\cdot\text{K}^{-1}$ ) where  $C_s = \rho_s \cdot c_s$  shown on [eq. 2.10]:

$$v_s = \frac{k_s}{\rho_s \cdot c_s}, \quad [\text{eq. 2.10}]$$

where  $c_s$  represents the specific heat ( $\text{J}\cdot\text{kg}^{-1}\cdot\text{K}^{-1}$ ). A snowpack with a high thermal diffusivity adjusts its bulk temperature quickly to variations in air temperature. Hence, the thermal diffusivity dictates the rate ( $\text{m}^2\cdot\text{s}^{-1}$ ) at which heat is transferred from one layer to another. The effect of density is different in the thermal diffusivity calculations as an increase in  $\rho_s$  decreases  $v_s$  but increases  $k_s$ . However, the high air volume within the snow contributes greater to the thermal conductivity (low values) compared to the inverse effect on heat capacity ( $\rho_s \cdot c_s$ ) in [eq. 2.10] resulting in low  $v_s$  values (Yen, 1981; Sturm *et al.*, 1997). The effect of brine volume will

strongly affect the heat capacity thereby decreasing thermal diffusivity. The presence of brine raises the specific heat (next section) dramatically upwards, to a factor of about 15 (Papakyriakou, 1999). However, this effect is less important in cold temperatures where the distance a temperature change propagates through a salty snow cover increases with cooling temperatures.

Due to its low thermal diffusivity of  $\nu_s \sim 3.9 \times 10^{-7} \text{ m}^2 \cdot \text{s}^{-1}$  (Yen, 1981; Sturm *et al.*, 1997), snow protects the ice from the surface boundary layer temperature oscillations. The effect of air temperature,  $T_{air}$ , variations are more pronounced at the snow surface (air/snow interface) and attenuates at greater depths (e.g., Sturm *et al.*, 1997; Bartlett *et al.*, 2004). The snow-ice interface temperatures,  $T_{si}$ , (proportional to brine volume) are thus largely influenced by the thermal diffusivity and are of primary importance for understanding microwave scattering and emission mechanisms (e.g., Eppler, 1992; Barber *et al.*, 1998).

#### 2.4.1.3. Specific Heat and Heat Capacity

To accurately understand the flow of heat within a given volume, we need to understand the storage of heat. This storage capacity is given by the volumetric heat capacity ( $C_s$ ), which represents the energy absorbed given a corresponding rise in temperature (J/kg·K). The relationship with thermal diffusivity is given in [eq. 2.10] where an increase in  $C_s$  corresponds to a decrease in  $\nu_s$ . Increasing heat capacity means that more energy is required to increase the physical temperature of the volume, therefore less is available for diffusion. A useful term in quantifying the storage of heat is the specific heat ( $c_s$ ), which correspond to the amount of heat

required to increase 1 g of substance (i.e. snow) by 1°C. In saline snow over sea ice, these two terms depend on temperatures and the volume fractions of brine and ice. Doronin and Kheisin (1977) suggested a simplified calculation for snow specific heat (J/kg·K) showed in [eq. 2.11]:

$$c_s = c_{pureice} \left( \frac{M_{ice}}{M} \right) + c_{brine} \left( \frac{M_{brine}}{M} \right) + L_w M_{brine} \left( \frac{\partial V_{brine}}{\partial T} \right) \quad [\text{eq. 2.11}]$$

In [eq. 2.11],  $c_{pureice}$  is the specific heat of pure ice (2113 J/kg·K),  $c_{brine}$  is the specific heat of brine (4217 J/kg·K),  $M_{ice}$  is the mass of pure ice,  $M$  is the total mass,  $M_{brine}$  is the mass of brine,  $L_w$  is the latent heat of fusion (transferred through water vapor from sublimation to diffusion and deposition) and  $\partial V_{brine}/\partial T$  is gradient of brine volume change around a given temperature. Therefore, the specific heat of saline snow will increase with increasing temperature due to increasing brine volume (Ono, 1966). As from [eq. 2.11], volume fractions of both will control snow heat capacity over first-year sea ice where linkages with snow density and brine volume can be made. Hence, a very saline basal snow layer will hinder heat flow to a point where the incoming heat wave will be partially or completely blocked (e.g., Fukusako, 1990).

Furthermore, the latent heat associated with any phase change from melting and/or freezing at the basal layer of the snowpack (brine rich) will impact on the specific heat of the snow cover (Asur, 1958; Eicken, 2003). The large amount of brine allows for more water to be present through the layer at temperatures below the freezing point with a very high specific heat as mentioned before. Brine rich layers need more energy to increase the volume temperature and inversely, more energy needs to be released in order to freeze. However, the temperature variations at the basal

layer (dictating phase change) are controlled by snow diffusivity, which in turned is strongly linked to thickness as discussed previously.

#### 2.4.2. *Electrical Properties*

When an electromagnetic wave penetrates through a volume, the applied electrical field ( $E$ ) causes the movement of charge carriers and the alignment of the dipolar molecule such as  $H_2O$  (Jonscher, 1996; Baker-Jarvis, 2000). When  $E$  is removed, the molecules reorient back to their initial stable arrangement. That reorientation mechanism requires time, referred to here as ‘relaxation time’ (Logsdon and Laird, 2004) and is of primary importance in determining the dielectric constant of a medium. The dielectric constant ( $\epsilon$ ) is composed of the permittivity ( $\epsilon'$ ) and dielectric loss ( $\epsilon''$ ). The permittivity represents the ability of a medium to transmit an incident energy and the dielectric loss refers to the extinction of that same energy. The dielectric constant is related to the refraction index where the wave propagation depends on the intensity of the electrical field in terms of depth ( $E_z$ ), the initial intensity ( $E_0$ ) and a propagation factor ( $\gamma$ ):

$$E_z = E_0 \exp(-\gamma z) \quad [\text{eq. 2.12}]$$

The complex propagation constant (propagation factor in eq. 2.12) can be expressed as:

$$\gamma = A + j\beta \quad [\text{eq. 2.13}]$$

where  $A$  is the absorption (energy transformation) constant and  $\beta$  the phase constant (Tsang *et al.*, 1985). These two terms are related to the dielectric constant by:

$$\alpha = k_0 \operatorname{Im}\{\sqrt{\varepsilon}\}, \quad [\text{eq. 2.14}]$$

$$\beta = k_0 \operatorname{Re}\{\sqrt{\varepsilon}\}, \quad [\text{eq. 2.15}]$$

where  $k_0$  is the wave number in free space and  $\varepsilon$  the dielectric constant. These terms are related to the extinction ( $K_e$ ), absorption ( $K_a$ ) and scattering ( $K_s$ ) coefficients such that  $K_e = K_a + K_s$ . The absorption loss corresponds to the transformation of the initial electromagnetic power into heat as the scattering loss corresponds to the ‘deviation’ from the initial propagation direction dictated by particles size and structure. From  $K_e$ , it is possible to retrieve the penetration depth that corresponds to the depth ( $\delta_p$ ) at which the integration of all  $K_e$  over  $dz = 1$  such that:

$$\int_0^{\delta_p} K_e(z) dz = 1 \quad [\text{eq. 2.16}]$$

Hence, the dielectric constant obeys the Debye equations and depends upon frequency and temperature such as:

$$\varepsilon = \varepsilon' + j\varepsilon'', \quad [\text{eq. 2.17}]$$

Snow over first-year sea ice is considered either dry or wet where different dielectric calculations are required using the Polder-Van Santen approach. The details of the dielectric calculations are described fully in Chapter 3.

### 2.4.3. Snow Surface Energy Balance

The surface energy balance is composed of a radiative and a turbulent term (including phase transition energy), which are in equilibrium with regards to the conservation of energy. The behavior of snow properties changes seasonally under the influence of evolving surface boundary layer conditions. I explained earlier in [eq. 2.1] the various elements of the *SEB* for the *OSA* interface whereas I focus here on snow within the *OSA* interface. The radiative budget of a relatively shallow snowpack  $Q^*_{snow}$  (typical of first-year sea ice) can be described as [eq. 2.18] (Male and Granger, 1981):

$$Q^*_{snow} = Q^* - Q^*_{is} = K^* + L^* - Q^*_{is} = K \downarrow - K \uparrow + L \downarrow - L \uparrow - Q^*_{is} \quad [\text{eq. 2.18}]$$

In [eq. 2.18],  $Q^*$ ,  $K^*$  and  $L^*$  represent the net all-wave, net shortwave (solar) and net longwave radiation budgets of the snow volume. Both  $K^*$  and  $L^*$  have incoming and upwelling components ( $\downarrow$  and  $\uparrow$ ), where the incoming radiation (to the surface) has a '+' sign as the upwelling (away from the surface) has a '-' in [eq. 2.18]. The term  $Q^*_{is}$  represents the net radiation budget available at the snow/sea ice interface, which is essentially composed of a shortwave downwelling and upwelling components ( $K_{is}\downarrow - K_{is}\uparrow$ ). The surface albedo ( $\alpha$ ) represents the ability of the surface to reflect incoming shortwave radiation through a ratio between reflected and incoming radiation such that:

$$\alpha = \frac{K \uparrow}{K \downarrow} \quad [\text{eq. 2.19}]$$

Adding the turbulent portion, the surface energy balance over snow ( $SEB_{snow}$ ) can be described by the following equations and Figure-2.1 (Hanesiak, 2001):

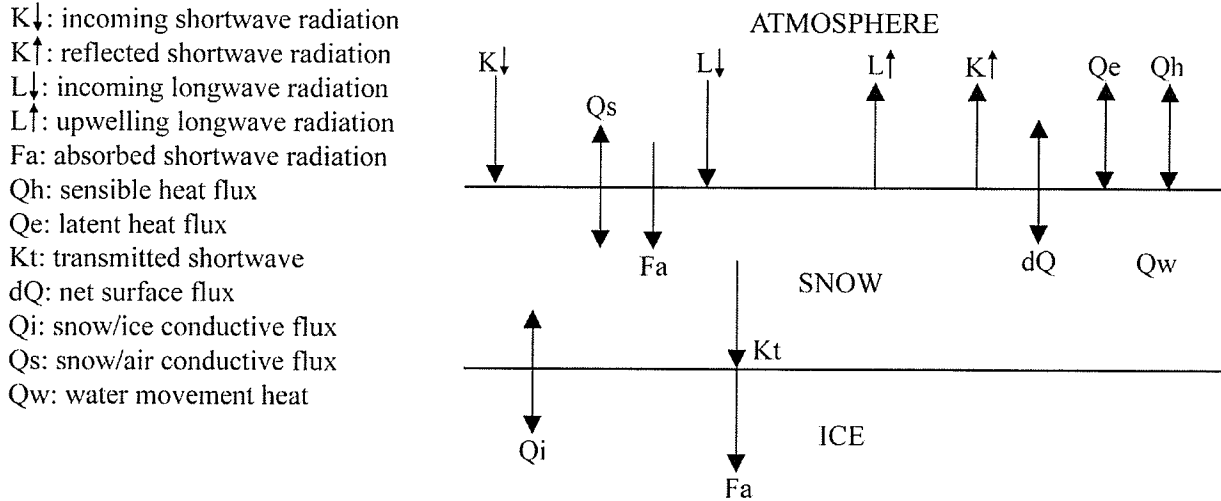


**Figure-2.1:** Surface energy balance of snow over first-year sea ice (adapted from Hanesiak, 2001).

$$\partial Q_{net\_atm} + Q_i - Q_s + F_a + Q_{ms} + Q_w = 0, \quad [\text{eq. 2.20}]$$

$$\partial Q_{net\_atm} = Q^* + Q_h + Q_e, \quad [\text{eq. 2.21}]$$

where  $Q_i$  the conductive heat flux at the snow/ice interface,  $Q_s$  the conductive heat flux at the snow/air interface,  $F_a$  the absorbed solar radiation  $F_a = K\downarrow - K\uparrow$  for both snow and ice interface in Figure-2.1),  $Q_{ms}$  the phase transition energy,  $Q_w$  the heat flux associated with liquid water flow and  $Q_c$  ( $Q_c = k_s \cdot \delta T / \delta z$ ) the total conductive flux at the snow/air interface. Both turbulent and

radiative portions of the surface energy balance evolve throughout the year and detailed analysis of this evolution is provided later in Section 2.7.

## 2.5. Snow Processes

### 2.5.1. Heat Transfer

Heat can be transferred through snow by conduction, diffusion, convection and advection mechanisms. Latent heat is transferred after phase change (such as condensation and sublimation) along with water vapor as the sensible heat is carried by airflow. Therefore, it is necessary to understand these different processes in order to assess the controlling factors on temperature gradients (Albert and McGilvary, 1992). For *conduction*, a contact is required along with a temperature gradient (i.e. snow grains) where heat migrates between and within the snow grains. *Diffusion* occurs in the gas phase where vapor moves through the air pores within the snow. *Convection* corresponds to a vertical movement of heat in response to either temperature gradient (sensible heat flux) or a change of phase/state (latent heat flux). Finally, *advection* of heat will occur during convection processes, but very little is known regarding its contribution to snow heat budget.

#### 2.5.1.1. Conduction

Thermal conductivity was introduced in Chapter 1 where we described the different snow properties affecting the ability to conduct heat through a snow layer. Heat conduction can occur from one grain to another, within the grain itself and from grain to water (in melting snow). The

conduction of heat between the grains requires contact for heat to be transferred and we refer as the thermal contact conductance coefficient ( $h_{c-snow}$ ) the thermal conductivity between to snow grains in contact. When two snow grains are in contact, heat will flow from the hotter grain to the colder grain (i.e. along the temperature gradient). Between the snow grains (Figure-2.2), the temperature will drop due to a phenomenon known as thermal contact resistance ( $1/h_{c-snow}$ ), which is a ratio between the temperature drop over the heat flow (Hollman, 1997).

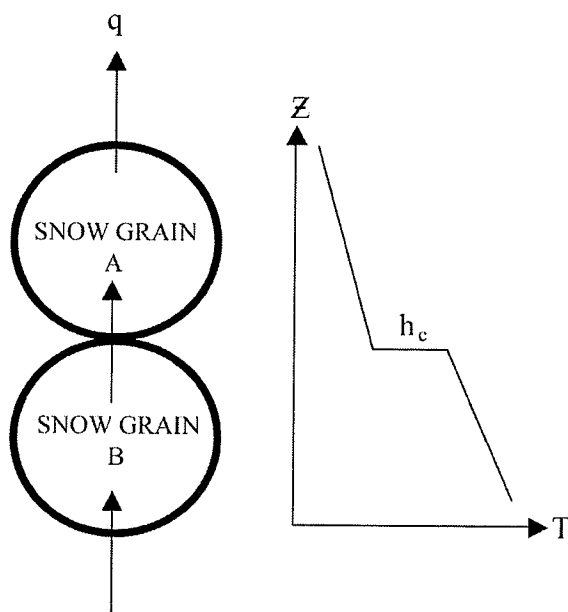


**Figure-2.2:** Heat conduction from one snow grain to another.

The heat flow is related to the thermal conductivity of each grain such as:

$$q = -k \cdot \frac{dT}{dz} + J(L + C_s(T_0 - T)) \quad [\text{eq. 2.22}]$$

where  $q$  is the heat flux ( $\text{J}\cdot\text{m}^{-2}\cdot\text{s}^{-1}$ ),  $k$  the thermal conductivity ( $\text{W}\cdot\text{m}^{-1}\cdot\text{K}^{-1}$ ),  $dT/dz$  the temperature gradient ( $\text{K}$ ) according to Fourier's law,  $J$  the vapor flux ( $\text{g}\cdot\text{m}^{-2}\cdot\text{s}^{-1}$ ),  $L$  the latent heat ( $\text{J}\cdot\text{g}^{-1}$ ) and  $C_s$  the heat capacity ( $\text{J}\cdot\text{kg}^{-1}\cdot\text{K}^{-1}$ ). The conduction of heat can also occur between a snow grain and its surrounding liquid water in the case of melting snow. The same mechanisms occur whereas heat flow from the warmer water into the colder snow grain. However, the process will be different whereas the liquid water is 'brine rich' or mostly fresh. Brine has a much higher thermal conductivity than freshwater, therefore heat transfer will be stronger in a brine 'wetted' environment (Figure-2.3 a and b).

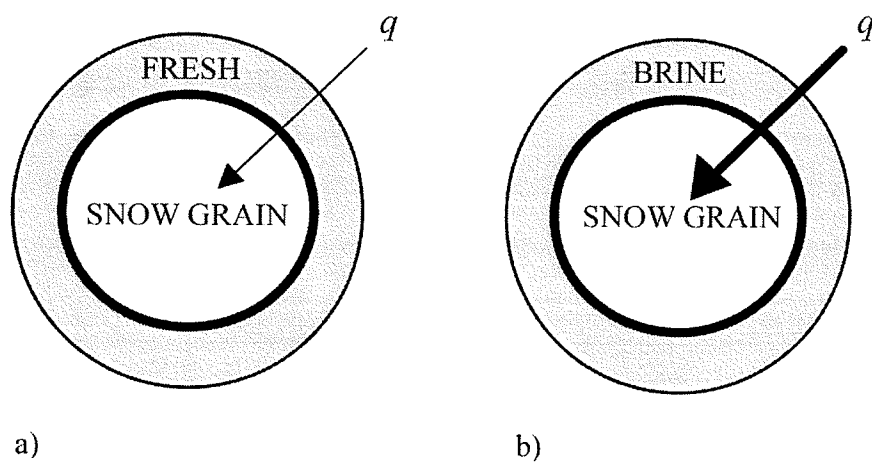


**Figure-2.3:** Heat conduction through a) fresh-wetted and b) brine-wetted snow grains.

#### 2.5.1.2. Vapor Diffusion

The vapor diffusion for snow is of primary importance due to its control over metamorphic processes such as kinetic grain growth. Vapor diffusion is the transport of vapor that takes place after sublimation and the mass is then redistributed elsewhere in the snowpack by deposition

along a given temperature gradient (vapor density gradient) assuming saturation (temperature gradient metamorphism). Vapor diffusion takes place within the air pores (Figure-2.4a and b) in the snowpack and is strongly related to density and grain size whereas the increasing grain size increases the flow path length (e.g., Colbeck, 1993; Sturm and Johnson, 1991). With the absence of convection, the diffusion of vapor through air can occur such as:

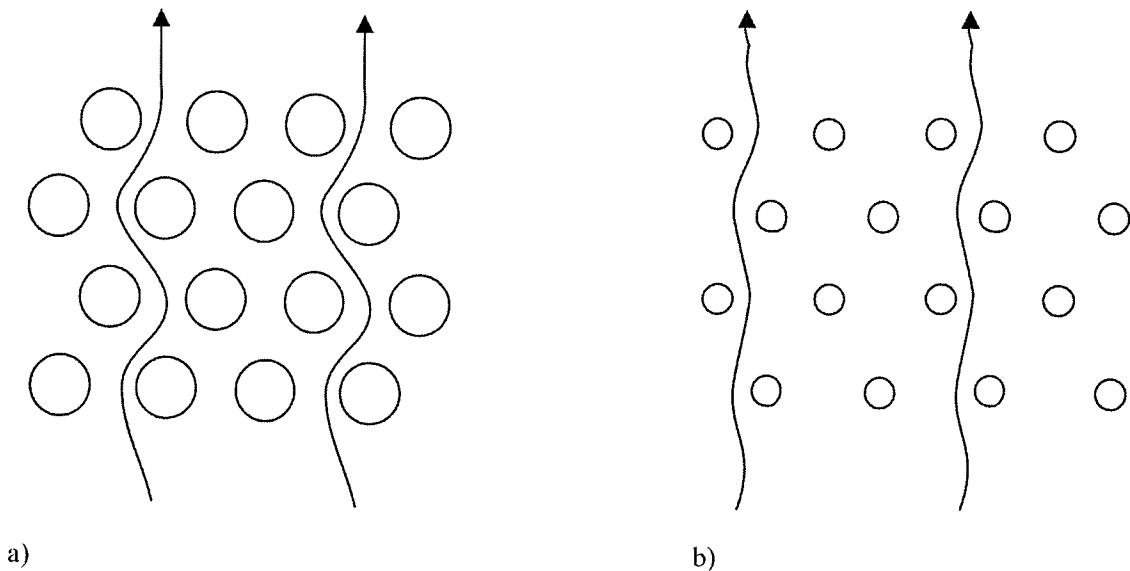


**Figure-2.4:** Vapor flow path length with regards to a) large and b) small grain size.

With the absence of convection, the diffusion of vapor through air can be explained by Fick's law such as:

$$J = -D \cdot \frac{\partial \rho}{\partial z}, \quad [\text{eq. 2.23}]$$

where  $J$  is the vapor flux ( $\text{g}\cdot\text{m}^{-2}\cdot\text{s}^{-1}$ ),  $D$  the diffusivity of water vapor ( $\text{mm}^2\cdot\text{s}^{-1}$ ) in air and  $\partial\rho/\partial z$  the vapor density gradient. The upward mass deposition (metamorphism) decreases the vapor

flux, however, the heat flux is expected to increase due to the release of latent heat from condensation. Vapor flux values have been published (Nikolenko, 1988) where  $J$  ranges between 0.16 and 0.64  $\text{g}\cdot\text{m}^{-2}\cdot\text{s}^{-1}$  with temperatures between  $-30$  and  $0$  °C.

### 2.5.1.3. Convection

Convection in the snow begins with air instability and can affect crystal growth direction and the rates at which the bottom of the snowpack will warm or cool (e.g., Brun *et al.*, 1987; Sturm *et al.*, 2002). The convection can be either ‘free’ or ‘forced’ whereas the former is driven by temperature gradient and unstable boundary conditions and the latter is driven by pressure gradient from wind disturbances (Albert and McGilvary, 1992). Both ‘free’ and ‘forced’ convections can be found under natural conditions. Free convection (hereinafter referred as thermal convection) occurs when spatially variable air and snow/ice interface temperatures creates horizontal temperature deviations (Figure-2.5) that would not occur in diffusive heat transport (Sturm and Johnson, 1991).

A number of criteria have been investigated for thermal convection to occur within the snowpack and its effect on vapor diffusion. Studies have looked in the Rayleigh number ( $Ra$ ) that determines the air instability (Zhekamukhov and Shukhova, 1999), where a critical value is calculated (critical Rayleigh number,  $Ra_c$ ) at which convection is most likely to occur (e.g., Akitaya, 1974; Turcotte and Shubert, 1982). The  $Ra$  can be calculated such as:

$$Ra = \frac{gB(\rho c)_f \Delta T h \kappa_i}{\alpha k_m} \quad [\text{eq. 2.24}]$$

where  $g$  is the acceleration of gravity,  $B$  is the isobaric coefficient for thermal expansion,  $(\rho c)_f$  is the volumetric heat capacity,  $\Delta T$  is the temperature gradient across the layer,  $h$  is the layer thickness,  $\kappa_f$  is the thermal diffusivity,  $\omega$  is the viscosity and  $k_m$  the thermal conductivity (Zhekamukhova, 2004).

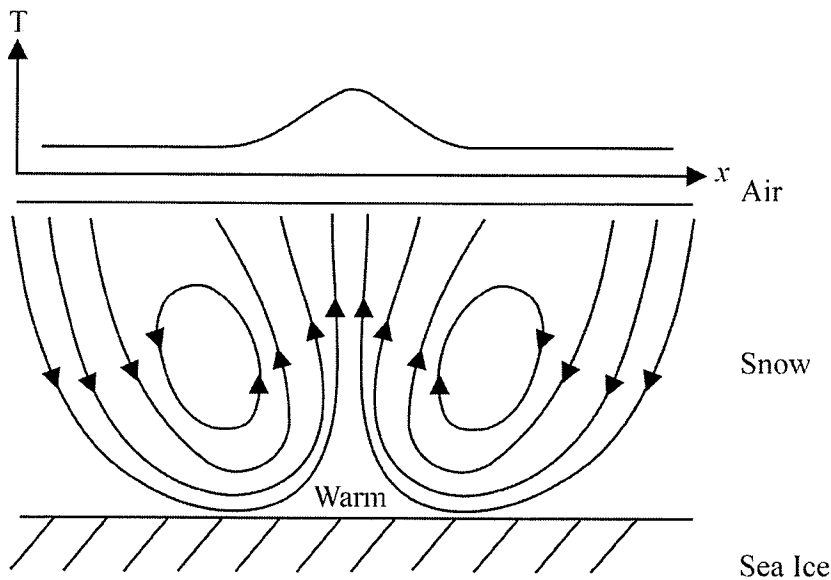


**Figure-2.5:** Thermal convection within the snow cover (adapted from Sturm and Johnson, 1991).

Numerous laboratory experiments attempting to trigger convection in artificial snow covers with stable boundary conditions concluded that ‘extreme’ conditions were necessary such as temperature gradient up to  $500 \text{ }^\circ\text{C}\cdot\text{m}^{-1}$  (Palm and Tveitereid, 1979; Rees and Riley, 1989). Results showed that convection was not likely to occur (Brun *et al.*, 1987) since the  $Ra$  values fell well below  $Ra_c$ . However, Sturm and Johnson (1991) found evidence for snow convection despite of  $Ra$  values below  $Ra_c$ . They attributed this to the unstable boundary conditions that are found in natural snow covers. Furthermore, recent results by Zhekamukhov and Zhekamukhova (2002) and Zhekamukhova (2004) suggest that the high vapor diffusion values from Fedoseeva

and Fedoseev, (1988) within the snow (sometimes higher than within the air) are attributed to convection.

Snow thermal convection is function of the permeability of the media, which is proportional of the fractional volume of air. Therefore, the convection could be reduced by snow transport such as saltation that reduces the size of snow grains (i.e. decreasing the size of air pores). Speculations exist regarding the effect of convection on snow grain size and structure. Results showed that convection enhances vapor transport (Trabant and Benson, 1972) affecting the structure of the grains (Colbeck, 1983; Keller and Hallett, 1982; Sturm and Johnson, 1991), but the impact on the growth remains unclear. Langlois *et al.*, (2007c) found enhanced vapor transport under a low-pressure disturbance and snow grain size increased accordingly. However, the sampling scheme could not confirm whether this process was a result of convection. Sturm (1991) found that thermal convection could increase snow thermal conductivity by a factor of 2 or 3, but still relatively little is known about the subject. The velocity of the convective flow can be measured using two methods, namely the flux gradient method and the heat and mass transport method (Sturm and Johnson, 1991). The first method assumes a one-dimension heat and flow for average values of vapor flux  $J$ , with typical values ranging between 0.2 and 1.3  $\text{mm}\cdot\text{s}^{-1}$ . The second method assumes the common assumption of saturation within the snow (e.g., Giddings and LaChapelle, 1962; de Quervain, 1972) and typical values vary between 0.2 and 2  $\text{mm}\cdot\text{s}^{-1}$ .

Forced convection in snow is known also known as ‘wind pumping’ occurs when wind disturbances create variations in surface pressure that can affect airflow within the snow (Colbeck, 1989). Diffusion and convection are enhanced by these variations, which in turn affect heat transfer and snow metamorphism (Clarke *et al.*, 1987). Wind pumping is a process by which surface pressure variations will force intranival (within snow volume) air convection (Colbeck, 1989) that gives rise to two types of wind pumping: turbulence and flow pumping (Waddington *et al.*, 1996). The resulting air convection depends on the air density stratification above the snow surface. Turbulence pumping occurs during unstable condition such as low-overcast periods where the air stratification is neutral; therefore mechanical turbulences (updrafts) are dominant at the surface (Figure-2.6a).

Flow pumping (Figure-2.6b) is associated with surface features like dunes or ridges where crests have low pressure (outflow of air) and the troughs have high pressure (inflow of air). Both types can have significant impacts on heat, moisture and mass transfers through the snow (Clarke *et al.*, 1987; Clarke and Waddington, 1991; Colbeck 1989). The outflow areas create an air movement from the warmer bottom towards the colder surface (oversaturation) as the inflow causes an air migration from the colder surface towards the warmer bottom (undersaturation).

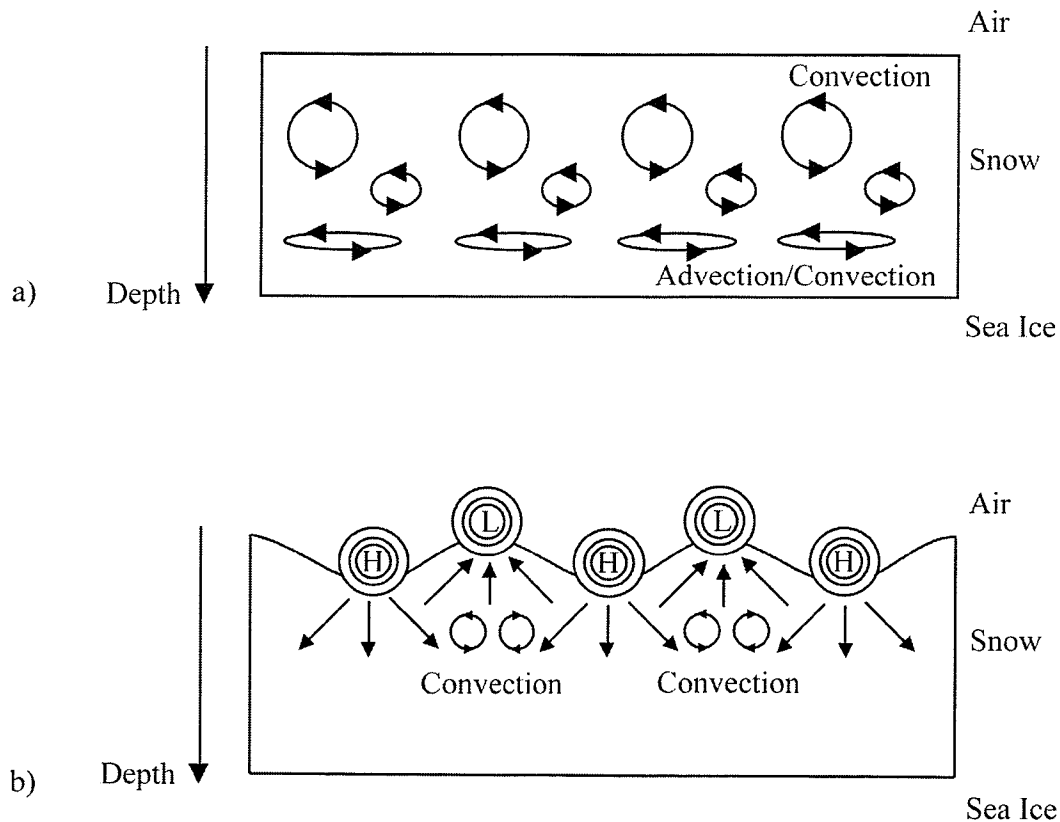


**Figure-2.6:** a) Turbulence pumping under unstable atmospheric conditions over a smooth snow surface and b) flow pumping under rough snow surface (modified after Power *et al.*, 1985; Granberg, 1998).

#### 2.5.1.4. Advection

The concept of warm air advection over snow has been widely studied for some time (e.g., Treidl, 1970; Marsh, 1999; Granger and Essery, 2004) due to its impact on snow properties (Wei *et al.*, 2001), but I will limit my discussion to the thermal advection within the snow cover. Few studies have investigated the advection of air and associated heat and mass transfer within a layered snow cover (Albert and Shultz, 2002), but the concept over sea ice is still in its infancy (Sturm *et al.*, 2002). By definition, advection is the horizontal transfer/movement (ventilation) of air and moisture within a certain volume (snow). The interstitial ventilation transport is triggered

by pressure variations caused by wind such as wind pumping (Gjessing, 1977; Waddington *et al.*, 1996) and affects heat flow within the snowpack (e.g., McConnell *et al.*, 1998). The resulting temperature profile is known to be the balance between both diffusive and advective processes. Such heat transfer mechanism is concentrated in the bottom of the snowpack where the large fractional volume of air increases snow permeability (Colbeck, 1989) (Figure-2.6a).

### 2.5.2. *Metamorphism*

#### 2.5.2.1. Dry Snow (Temperature Gradient Metamorphism)

The temperature gradient metamorphism rises from the temperature difference between snow grains in the vertical direction whereas the warmer grains (bottom of snowpack) act as the source of mass (vapor) and the colder grains (middle and top of snowpack) as a sink (e.g., Colbeck, 1983; Gubler, 1985). Large elongated grains are found (isotropic) typically at the bottom of the snow cover forming what is referred to as 'hoar layer'. Large temperature gradients (i.e. large vapor pressure gradients) result from the heat released by the ocean and growing sea ice at the bottom of the snowpack and the colder near-surface snow protected by its high albedo. The largest temperature gradients are found at night, or in the middle of winter where the incoming solar radiation is minimal (e.g., Barber *et al.*, 1995; Langlois *et al.*, 2007a). The vapor pressure is directly proportional to the temperature, and decreases from about 0.6 kPa at  $-2\text{ }^{\circ}\text{C}$  to approximately 0.1 kPa at  $-25\text{ }^{\circ}\text{C}$  (e.g., Bergen, 1968; Palm and Tveitereid, 1979). The vapor is 'pushed' upward and condensation occurs at the bottom of the grains (downward growth) (de Quervain, 1972). Such grain growth increases the fractional volume of air (decrease in number density), which low thermal conductivity and diffusivity increase the temperature gradient

accelerating the initial grain growth (e.g., Izumi and Huzioka, 1975; Colbeck, 1997; Sturm and Benson, 1997). Previous studies looking at physical values of vapor fluxes from one layer to another were successful over land (Trabant and Benson, 1972; Sturm and Benson, 1997), but further study is required for snow on sea ice.

#### 2.5.2.2. Dry Snow (Equilibrium Metamorphism)

In absence of a significant temperature gradient (anisotropic) ranging between  $0.1$  and  $0.3^{\circ}\text{C}\cdot\text{m}^{-1}$  (Colbeck, 1985; Sturm *et al.*, 2002) the bottom grains are at equilibrium with water vapor at a higher density than the upper grain. The rather large specific area of the snow grain provides a lot of energy to induce microscale heat and mass transfer (e.g., Bader *et al.*, 1939; Colbeck, 1982). The structure of the snow grain will change (diminishing the specific surface area) where the mass is redistributed on and between snow grains following micro shape-dependent vapor pressure gradients. Furthermore, intergranular bonding (sintering) occurs where the concave areas are heated by a release of latent heat of condensation while the convex areas are cooled by evaporation and sublimation. The mass will then migrate from the sharp-edged extremities (higher vapor pressure) to the surrounding concave (lower vapor pressure) areas (Figure-2.7) (Bader and Kuroiwa, 1962; Colbeck, 1993).

Hence, convex-small curvature parts of the ice crystals have a higher vapor pressure ( $p_s$ ) according to Kelvin's equation (e.g., Flanner and Zender, 2006):

$$p_s(r, T) = p_{eq} \exp\left(\frac{2\psi}{R_v T \rho_i r}\right), \quad [\text{eq. 2.25}]$$

where  $p_{eq}$  is the saturation vapor pressure over planar surface,  $\psi$  the surface tension of ice,  $R_v$  the specific gas constant for vapor,  $T$  the temperature,  $r$  the particle's radius and  $\rho_i$  the density of ice. Furthermore, the combined strong temperature gradient and wind pumping can also generate variations in microscale temperature and vapor pressure that can accelerate the process. Small amounts of water in liquid phase, available within the snowpack during the winter period, is usually concordant with isolated peaks in temperatures that decrease  $\delta T/\delta_L$ . With small  $\delta T/\delta_L$ , no vapor is expected to move upward despite the presence of small amount of liquid water (Sturm and Benson, 1997; Langlois *et al.*, 2007a).

The same mechanism can be applied on a smaller scale to calculate the mass flux from one grain to another. The flux is proportional to the curvature of the grain through the surface saturation vapor pressure. Zhang and Schneibel (1995) modeled the sintering flux, although work is very limited on this matter (Colbeck, 1997). Previous work found the flux may be greater in natural conditions when compared to modeled values, which are due to other processes accelerating vapor flow such as wind pumping (Keeler, 1969). However, Zhang and Schneibel (1995) approximated the flux going away from the convex surface ( $J_S$ ) to the influx at the boundary concave surface ( $J_B$ ) with the following equations (Figure-2.7):

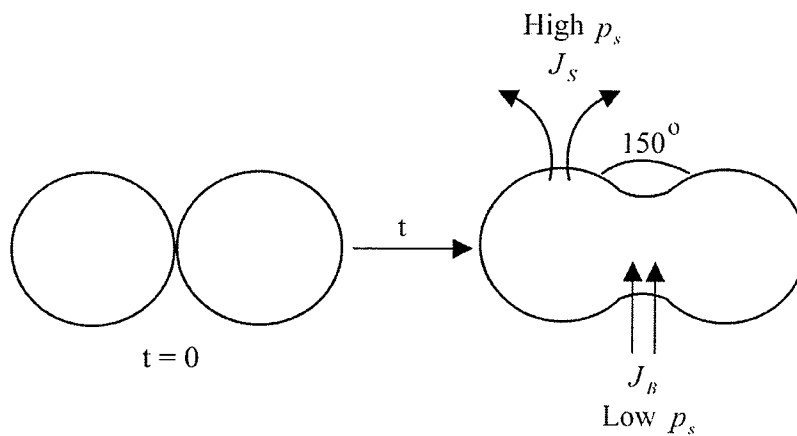
$$J_s = \frac{\delta_s D_s \gamma}{kT} \cdot \frac{\partial K}{\partial s} \quad [\text{eq. 2.26}]$$

where  $\delta_s$  is the surface diffusivity width,  $D_s$  the coefficient of surface diffusion,  $\gamma$  the surface free energy for the solid–vapor surface,  $k$  the Stephan-Boltzmann's constant,  $T$  the temperature,  $K$  the

curvature and  $s$ , the length of the curvature. For the influx at the grain boundary, a similar equation applies:

$$J_B = \frac{\delta_B D_B \gamma}{kT} \cdot \frac{\partial \sigma}{\partial y} \quad [\text{eq. 2.27}]$$

where the flux is integrated over a stress acting on the boundary ( $\sigma$ ) along the radial distance along the boundary ( $y$ ).



$$J_B = \frac{\delta_B D_B \gamma}{kT} \cdot \frac{\partial \sigma}{\partial y}$$

$$J_s = \frac{\delta_s D_s \gamma}{kT} \cdot \frac{\partial K}{\partial s}$$

$$p_s(r, T) = p_{eq} \exp\left(\frac{2\gamma}{R_v T \rho_i r}\right)$$

**Figure-2.7:** Snow grain bonding through dry snow equilibrium metamorphism.

Equilibrium is reached when the dihedral angle between the grains (Figure-2.7) reaches  $150^\circ$  (Colbeck, 1981:1997). This phenomenon has been widely studied and is known to increase the density with a decrease in specific surface area (e.g., Yosida, 1955; Barber *et al.*, 1995) leading to a decrease in specific surface area and a decrease in joint density (Figure-2.8). The joint density

corresponds to the relative number ( $N$ ) of connections from one grain to others per area ( $N \cdot \text{mm}^{-2}$ ). This quantity gives relative accurate information on the density and the metamorphic processes in place (i.e. dry snow vs wet snow metamorphism) (e.g., Yosida, 1955; Buser *et al.*, 1987). This is of great importance in determining the thermal 'state' of the snowpack by distinguishing new snow, snow under low temperature gradient and snow under high temperature gradient (De Quervain, 1958).

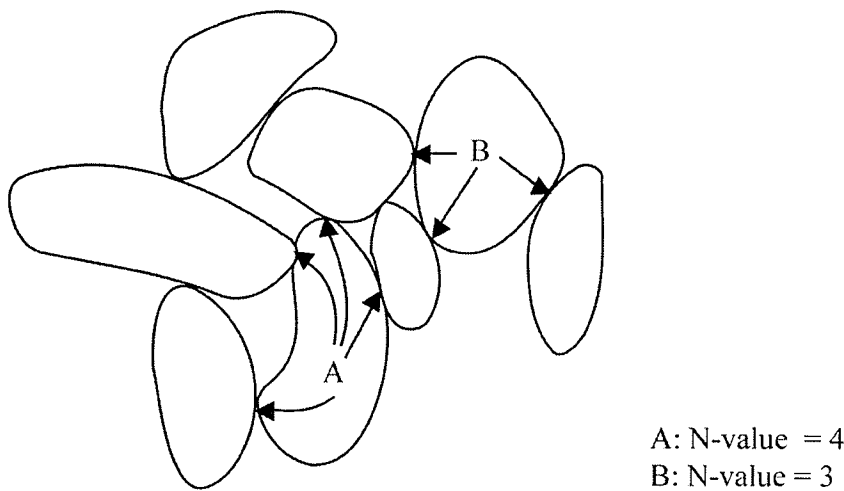


**Figure-2.8:** The joint density of snow grains where A and B have a N-values of 4 and 3 respectively (adapted from Arons and Colbeck, 1995).

### 2.5.2.3. Wet Snow

In presence of high liquid content (saturated conditions), snow metamorphism will be different than in dry snow (Colbeck, 1981). In such conditions, the snow grains are separated from each other. Heat flow propagating through saturated snow will then cause the melting of the smaller particles due to their lower (colder) temperature of melting,  $T_{M-sat}$  (e.g., Wakahama, 1965;

Colbeck, 1983). Therefore, in saturated conditions, small particles (small radius of curvature,  $r$ ) will decrease in size while larger snow grains are expected to grow due to the adhesion of water to the cold ice crystals and a lower melting temperature:

$$T_{M-sat} = -\frac{2T_0}{L\rho_s} \cdot \frac{\sigma_{sl}}{r} \quad [\text{eq. 2.28}]$$

where  $T_0$  is the melting of a flat surface,  $L$  the latent heat associated with phase change,  $\rho_s$  the density of the solid and  $\sigma_{sl}/r$  the difference of pressure between the solid and liquid phase with regards of the surface curvature (Colbeck, 1989).

The metamorphism mechanisms under unsaturated conditions are quite different. While high liquid content tend to leave the snow grains separated from each other, unsaturated conditions lead to grain clusters (Denoth, 1980). Such clusters occur after certain drainage from the funicular regime, but the growth rate of the cluster is slower due to the absence of liquid path for heat flow and a lower melting temperature (Colbeck, 1989) given by:

$$T_{M-unsat} = -\frac{T_0}{\rho_l L} p_c - \frac{2T_0}{\rho_s L} \cdot \frac{\sigma_{sg}}{r} \quad [\text{eq. 2.29}]$$

where  $\rho_l$  is the density of the liquid,  $p_c$  the capillary pressure and  $\sigma_{sg}/r$  the difference of pressure between the solid and gas phase with regards of the surface curvature (Colbeck, 1989). Mass transfer exists between the grains of a given cluster and the concordant growth is faster than the case of equilibrium metamorphism in dry snow.

### 2.5.3. Snow Aeolian Processes

The action of wind redistributes snow (blowing snow) over the Arctic's surface depending mostly on surface roughness, snow density and wind velocity. The kinetic energy ( $e_k$ ) of snow particles being redistributed on the surface is given by [eq. 2.30]:

$$e_k = 0.5mv^2, \quad \text{[eq. 2.30]}$$

where  $m$  is the mass of the particle and  $v$  its velocity. From [eq. 2.30], it is fair to say that the kinetic energy of a wind-driven snow particle increase at the square of wind speed (Kotlyakov, 1961) creating highly dense snow layers. The drifting snow process is similar to drifting sand (Kosugi *et al.*, 1992), however one of the main differences reside in the fact that snow particles can be bonded together by cohesive forces and sublimation is possible during transport (Schmidt 1986; Pomeroy and Gray 1990; Gordon *et al.*, 2006).

The initial movement of fresh snow can be induced by wind speed of approximately  $4.5 \text{ m}\cdot\text{s}^{-1}$  (e.g., Budd *et al.*, 1966; Schmidt, 1982) and is the result of combination of aerodynamic lift and wind pumping (Colbeck, 1989; Waddington *et al.*, 1996). The resulting air convection depends on the air density stratification above the snow surface. Such air movements can have significant impacts on heat, moisture and mass transfer within the snow (i.e. metamorphism), however very little moisture is usually available during the winter period (e.g., Colbeck, 1982; Sturm, 1991; Sturm *et al.*, 2002; Langlois *et al.*, 2007a). Three main factors influence blowing snow namely wind speed, type of transport and transport rates (Kikuchi *et al.*, 2005; O'Rourke *et al.*, 2005):

**Wind Speed:** Movement of snow begins when a surface force (air movement) is applied on the snow particles. Therefore, it corresponds to the velocity at which snow transport begins. It obviously depends mostly on snow characteristics such as density (old snow vs. new snow).

**Type of Transport:** Three major natural mechanisms of snow transport are commonly referred as creeping, saltation and turbulent diffusion (or suspension). Each of these transport mechanisms occurs at different wind speed and carries different proportion of drifting snow. Creeping is characterized by the weakest winds ( $< 5 \text{ m}\cdot\text{s}^{-1}$ ) where the snow particles are rolling on the surface and account for approximately 10 % of the total drifting snow. Saltation is the most common transport method with wind velocities ranging between 5 and  $10 \text{ m}\cdot\text{s}^{-1}$  and represents 80 % of the drifting volume as turbulent diffusion occurs under high wind conditions ( $> 15 \text{ m}\cdot\text{s}^{-1}$ ) and accounts for the remaining 10 % of the total drifting snow. This is of primary importance for SWE studies for both land and ice surfaces since such transport mechanisms have significant impacts on spatial snow thickness distribution. **Transport Rates:** The transport rates depend mostly on surface conditions such as snow availability. The transport rate has been fairly well understood for some time (Komarov, 1954; Kobayashi, 1972) and the spatial distribution and magnitude of the ridges is of primary importance in understanding snow drifting (Tucker *et al.*, 1979).

Drifting snow undergoes significant morphological modifications from well-defined dendrite or plate shape snowflakes to a much smaller and round snow grains (Figure-2.9a and b), which increases density by reducing the fractional volume of air within the snowpack. Early work on the relationships between wind speed and snow density showed that dunes density can increase up to  $450 \text{ kg}\cdot\text{m}^{-3}$  (Kotlyakov, 1961; Budd *et al.*, 1966) and are migrating on the smooth sea ice

surface (Figure-2.10a) and eventually caught up into ridges (Figure-2.10b). However unpublished results from recent work done in the Beaufort Sea and Hudson Bay showed density values up to  $700 \text{ kg}\cdot\text{m}^{-3}$ . Furthermore, blowing snow can redistribute saltier layers on top of practically non-salty snow (e.g., Barber *et al.*, 1995; Langlois *et al.*, 2007a), which can have significant impact the dielectric properties (i.e. microwave signatures).

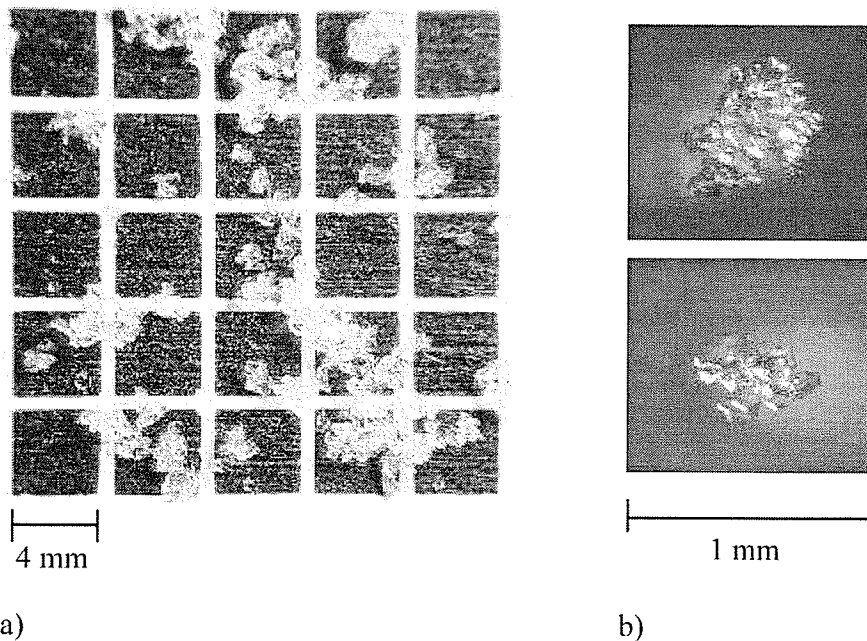
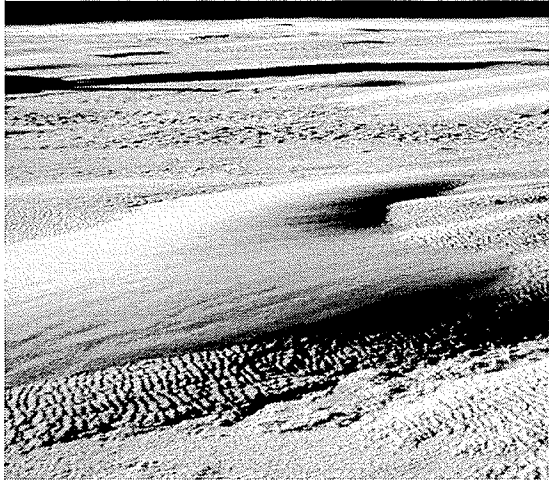
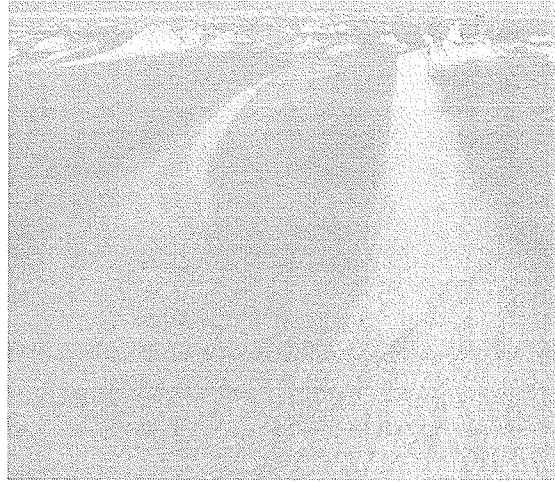


**Figure-2.9:** Scaled snow grain micro-photographs for a) size and b) structure calculations.



a)



b)

Photo: A. Langlois

**Figure-2.10:** Snow drifts over a) smooth and b) rough first-year sea ice.

## 2.6. Microwave Emission and Scattering Processes

As mentioned in the introduction, satellite microwave remote sensing provides a good tool to infer geophysical properties from space due to its capacity to penetrate through clouds and their independence of the sun as a source of illumination (Ulaby *et al.*, 1981). Thus, it is essential to understand how the electromagnetic waves propagate through a layered snowpack and how geophysical properties affect microwave signatures through their control on electrical properties (e.g., Markus *et al.*, 2006a). Among the geophysical properties, we denote salinity, density, grain size and brine volume (wetness) as the ones controlling microwave emission and scattering (e.g., Carsey, 1992; Cordisco *et al.*, 2006).

All physical materials above absolute zero radiate energy according to Planck's law. The emission of radiation is caused by the collision of particles which rate depends on kinetic energy and temperature (which are directly proportional). The specific intensity ( $J$ ) of the radiation per

unit area is given by the Rayleigh-Jean's approximation, and can be used in the microwave region ( $I = KT / \lambda^2$ ) where  $K$  is the Stephan-Boltzmann's constant and  $T$  the temperature in Kelvin. All bodies emit less than a blackbody ( $e = 1$  from Kirchoff) and their specific intensity depends on direction ( $\theta, \phi$ ) of the emission (where  $\theta$  is the elevation angle and  $\phi$  the azimuthal angle). Therefore, the concept of brightness temperature for a given polarization,  $T_{bp}(\theta, \phi)$  is given by:

$$T_{bp}(\theta, \phi) = I_p(\theta, \phi) \frac{\lambda^2}{K}, \quad [\text{eq. 2.31}]$$

With the body having a uniform physical temperature, the emissivity  $e_p(\theta, \phi)$  can be derived such that:

$$e_p(\theta, \phi) = \frac{T_{bp}(\theta, \phi)}{T}, \quad [\text{eq. 2.32}]$$

The brightness temperature of snow is not constant with depth (nonuniform dielectric profile) where each layer ( $L$ ) has specific values of  $T_L$  and  $e_L$ . In such case,  $e_p$  can be calculated with the fluctuation-dissipation theory (Stogryn, 1970; Tsang *et al.*, 1985) where  $T_L$  and  $e_L$  can assume to be constant within  $L$  (Zurk *et al.*, 1997; Matzler and Wiesmann, 1999). The propagation of energy through a layered smooth media (from media 1 to media 2) depends upon the reflectivity ( $R_{1,2}$ ), transmissivity ( $T_{1,2}$ ) and the incidence angle ( $\theta_i$ ) (Tsang *et al.*, 2000). The refraction angle (transmitted) in the new media ( $\theta_t$ ) is a function of the permeability and dielectric constant of the two medias. For a wave propagating from media 1 to media 2, an increase in the dielectric

constant in media 2 would increase  $\theta_i$  (Figure-2.11). Hence, each media has its own dielectric constant, which will affect the refraction angle of the transmitted energy from media 1 to media 2 (Tsang and Kong, 1992). That energy translates into  $e_p$  and  $T$  (i.e.  $T_{bp}$  from eq. 2.32) leaving the surface as shown on Figure-2.11. The propagation of the energy as described above propagates such that energy through a boundary between two different media is described by the initial energy density ( $P_i$ ) and a propagation factor ( $\gamma$ ):

$$P_{(z)} = P_i \exp(-\gamma z) \quad [\text{eq. 2.33}]$$

The propagation factor depends on the absorption by the snow particles and the phase of  $P_i$  from which we can calculate the absorption coefficient ( $K_a$ , where  $K_a^{-1}$  is the penetration depth  $\delta_p$ ). Obviously, the higher the absorption coefficient, the lower the penetration depth. Along with the absorption, the propagating wave will be scattered by scattering mechanisms that differ from a layer to another defined by the scattering coefficient ( $K_s$ ). The deeper the snow, the more scattering will occur ( $\downarrow T_{bp}$ ) which is the underlying principal in depth/SWE retrievals (e.g., Derksen *et al.*, 2005; Powell *et al.*, 2006; Pulliainen, 2006). Snow grains are the most dominant ‘scatterers’ in snow and relatively limited information is available on the role of its shape and size in the radiative transfer process (Foster *et al.*, 1999). At the basal layer of the snow cover, kinetic growth grains dominate scattering and their emission contribution will vary depending on the brine volume (e.g., Barber *et al.*, 1998). The frequencies used in SWE studies have wavelengths larger than the snow grains. In this case, the Mie scattering calculations can be reduce to the Rayleigh region where the radius of the snow grain (assumed spherical) is smaller than  $\lambda$ .

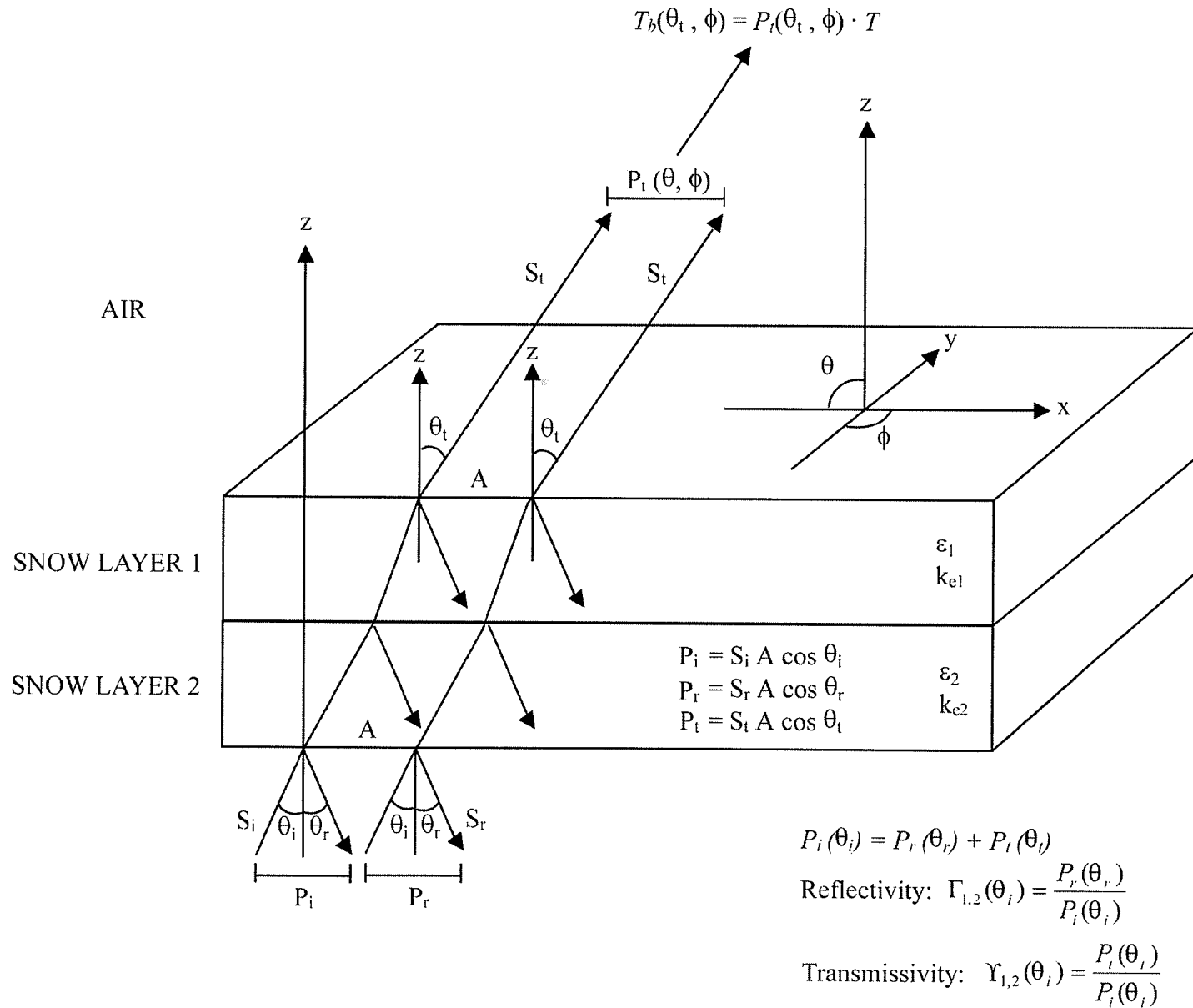


**Figure-2.11:** Geometry of microwave propagation through a layered snowpack.

Both scattering and absorption can be defined as cross section coefficients ( $\zeta_s$  and  $\zeta_a$ ) respectively. In the Rayleigh region, these parameters can be calculated as:

$$\zeta_s = \frac{2\lambda^2}{3\pi} \chi^6 |K|^2, \quad [\text{eq. 2.34}]$$

$$\zeta_a = \frac{\lambda^2}{\pi} \chi^3 \text{Im}\{-K\}, \quad [\text{eq. 2.35}]$$

where  $\chi$  defines the Rayleigh region ( $\chi = 2\pi r / \lambda < 1$ ) with snow grain of radius  $r$  and  $K$  the complex quantity defined from the index of refraction of the snow grain (van de Hulst, 1957; Skolnik, 1980). With both  $\zeta_s$  and  $\zeta_a$  we can derive the total snow extinction coefficient ( $K_e = K_a + K_s$ ) affecting  $P_i$  for a layer at depth  $z$ . The modeling of  $T_{bp}$  requires a full understanding on all parameters affecting  $k_{es}$  namely snow density, grain size, wetness, temperature and frequency (Chen *et al.*, 2003).

Furthermore, microwave emission is strongly influenced by the fractional volume of water in liquid phase within the snow cover (e.g., Grenfell and Lohanick, 1985; Walker and Goodison, 1993) that can easily overshadow the scattering effect of the grains and density. The type of sea ice is also important as their emission contribution varies greatly given their thermodynamic state (Markus *et al.*, 2006b). Radiation emitted from the sea ice is then scattered by the overlying snow cover. Brine wetted snow grains will have different emission values given their size whereas bigger grains contribute to higher emission in the microwave portion of the spectrum (Tedesco *et al.*, 2004). Density will also control  $e$  through an increase in permittivity due to the higher fractional volume of ice within the snow (e.g., Tiuri *et al.*, 1984). The position of the

water in liquid phase will also affect microwave emission and scattering. If the grains are surrounded by water then this will increase the effective scattering of these particles (given that the grains are large enough). If the water is held within the interstices of the snow grains then the scattering will be relatively lower since the grains will be in solid phase and the water particles quite small.

From an active microwave perspective, we refer as the return echo power, given by the backscattering coefficient ( $\sigma_{\gamma\theta}^{\circ}$ ). The initial wave hits the surface/volume and fractions of the initial polarized (V or H) power is reflected, absorbed and scattered. The scattered portion that comes back in the initial direction (polarized as well) is called backscattering (e.g., Nghiem *et al.*, 1995; Yackel *et al.*, 2001). The backscattering efficiency (normalized radar cross section, NRCS) takes into account the factor  $\chi = 2\pi r / \lambda < 1$  for the Rayleigh region (Deirmendjian, 1969). The measured  $\sigma_{\gamma\theta}^{\circ}$  of a snowpack is function of  $K_e$ , which in turn is also related to the dielectric constant of the snow (calculated from thermophysical properties). The penetration depth of the initial power will depend on  $K_e$  so is  $\sigma_{\gamma\theta}^{\circ}$ . The complete set of backscattering coefficients for the scatter fields constitute a covariance matrix (Mueller matrix) characterizing the layered media:

$$\sigma_{\mu\tau\nu k} = \lim_{\substack{r \rightarrow \infty \\ A \rightarrow \infty}} \frac{4\pi r^2}{A} \frac{\langle E_{\mu s} E_{\nu s}^* \rangle}{E_{\tau i} E_{ki}^*}, \text{ where } \lim_{r \rightarrow \infty} \text{ and } A \rightarrow \infty \quad [\text{eq. 2.36}]$$

and the subscripts  $\mu$ ,  $\tau$ ,  $\nu$ , and  $k$  represents polarization (V or H),  $i$  and  $s$  the initial and scattered fields,  $r$  the distance between the radar and the surface and  $A$  the illuminated area.

## 2.7. Snow Processes and Microwave Signatures

The preceding review shows how the thermal and geophysical properties change as a function of season and depth. The thermophysical properties evolve as a direct result of the ocean and atmosphere surface energy balance operating on both sides of the ocean-sea ice-atmosphere interface. It is this change in the thermophysical properties, which drives the complex dielectric constant of the snow/sea ice system. Since microwaves are sensitive to both the dielectric constant and snow geophysics, it follows that microwave emission and scattering should be able to ‘invert’ information out of the time series scattering/emission over snow covered sea ice. In what follows I summarize this relationship throughout the annual sea ice cycle.

### 2.7.1. Fall

The fall period is characterized by the formation of sea ice with limited accumulation of precipitation (both solid and liquid). Fall extends until the air reaches subzero temperatures throughout the diurnal cycle with sea ice covering most of the open water. The transition between open water and snow covered first-year sea ice can occur very rapidly and the impact on passive microwave brightness temperatures is significant (e.g., Hwang *et al.*, 2007). In what follows, I describe the relationship between snow thermophysical/electrical properties, surface energy balance and passive microwaves from the formation of sea ice until the beginning of winter.

Sea ice forms with the freezing of seawater through a convective process. The cold air temperature cools the surface water close to the freezing point. This cold and dense water sinks

down and is replaced by warmer water from below, which is in turn cooled down at the surface (thermohaline convection). The alternating warm and cold surface water masses coupled with surface disturbance and cold air temperatures (thermohaline mixing) create ice crystals that aggregate together forming a 'slush' layer. This layer called 'frazil ice' is formed of needles, spicules and platelets and is the first step in sea ice formation. The further accretion of frazil ice creates grease ice or young first year sea ice under quiescent conditions. If the surface is roughened by wind or currents then 'pancake ice' will form. Pancake ice consists of small 'pans' of ice that eventually cover most of the open water when reaching a thickness of approximately 10 cm (e.g., Lange *et al.*, 1989; Eicken, 2003). This frazil ice layer is characterized by a granular texture grown under turbulent mixing (Weeks, 1998). In regards of SEB, the bulk albedo of the volume will increase as ice thickens (e.g., Maykut, 1986; Perovich, 1996; Steele and Flato, 2000). It has been shown that the bulk albedo can increase from 0.08 to 0.4, which can accelerate ice growth in absence of snow (Perovich, 1996). Furthermore, previous research has shown that the sensible and conductive heat flux (Figure-2.12, #1) are very effective in removing heat from the growing ice (Steffen and DeMaria, 1996), depending on snow accumulation at the surface.

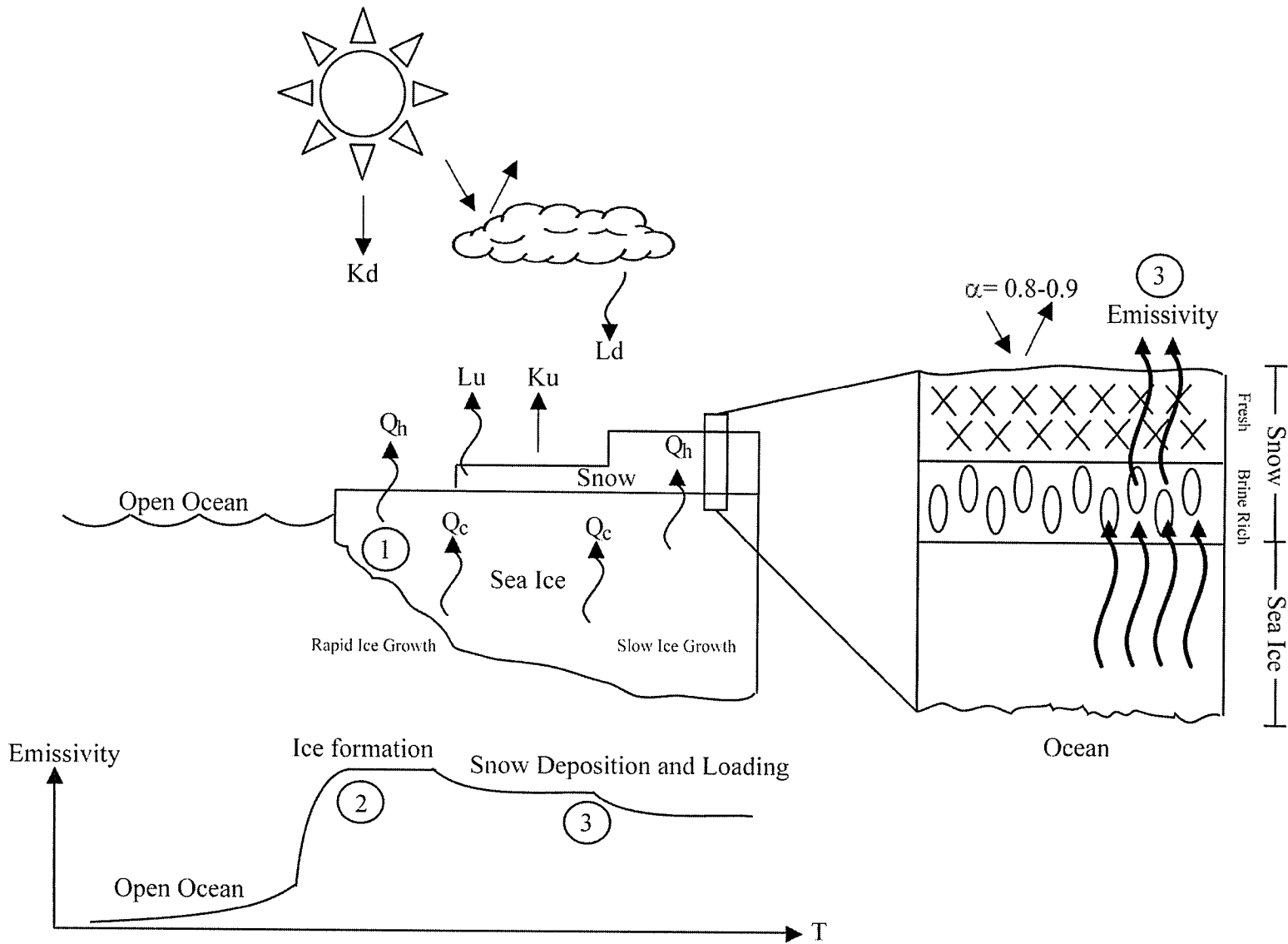


Figure-2.12: Schematic fall snow physical processes.

That smooth thin ice layer causes an increase in brightness temperatures at all frequencies (19, 37, 85/89 GHz) due to the decrease in open water fractional area (Figure-2.12, #2). The  $e_{seawater}$  is much lower than  $e_{new\ ice}$ , which translates into a higher  $T_{bp}$  (Eppler *et al.*, 1992; Onstott *et al.*, 1998). For instance, the emissivity of open water is approximately 0.3, 0.35 and 0.5 for 19, 37 and 89 GHz (H-pol) whereas values of 0.85, 0.87 and 0.85 are usually measured over first-year sea ice (Stogryn and Desargent, 1985). During this period, most of the emission comes from the ice and snow acts as an attenuator through  $k_{es}$  (Eppler *et al.*, 1992).

Once the ice pack is in place, congelation ice will form and ice will grow from the bottom downwards (fall-winter transition), which rate is dictated by snow accumulation at the surface. The conductive flux ( $Q_c$ ) is relatively high over snow-free growing ice and decreases rapidly with the accumulation of snow (decrease of heat transfer up to 50%) due to low snow thermal conductivity. The combination of liquid precipitation, high values of salinity and brine volume allow wet snow metamorphism to occur and can have a significant impact on heat flow. Furthermore, the input of liquid at the surface of the ice will change the temperature profile of the sea ice volume (warmer at top), which can lead to significant melting (e.g., Philip and de Vries, 1957; Sturm, 1991). That water will then refreeze (release of latent heat through phase change) as temperatures cool down at night, creating a layer of 'superimposed' ice. It is also possible that ice crusts form within the snow cover vertical profile. Ice crusts act as a cap for heat and mass transfer from below (Albert, 1996:2002) and contribute to significant microwave scattering, especially in the horizontal polarization (e.g., Ulaby, 1986).

The magnitude and timing of snowfall can also have dramatic effects on  $T_{bp}$ . For instance, a fresh snowfall will decrease the  $T_{bp}$  of the snowpack (increasing volume scattering, Figure-2.12, #3), at both H and V polarizations (Grenfell and Comiso, 1986). Fresh fallen snow would also have a lower thermal conductivity ( $k_s$ ) due to its greater  $V_{air}$ , which also contributes in reducing heat transfer from the sea ice to the atmosphere. Therefore, the magnitude of the snowfall early in the season significantly affects ice growth, heat and radiative transfers (e.g., Maykut, 1978).

From an active microwave perspective, the backscattering coefficient ( $\sigma^{\circ}$ ) is strongly affected by surface roughness and therefore reduced by growing ice (reducing  $\epsilon$ ) and the deposition of snow. As mention above, the ice formation contributes to smoothing the surface towards a specular shape, which acts like a mirror in to radar scattering, but the presence of frost flowers (Dominé *et al.*, 2005) may increase  $\sigma^{\circ}$  values (Yackel *et al.*, 2001). In the fall period, leads can form very rapidly, snow is wet and rain can occur having an effect on both  $T_{bp}$  and  $\sigma^{\circ}$ . However, we should not confuse open water with wet snow (e.g., Grenfell *et al.*, 1998) whereas wet snow acts like a blackbody in the microwave region. Concordantly, the  $e$  increases quite rapidly as ice grows, the fastest rate being observed between 0 and 10 mm over the typical microwave snow range (19 to 89 GHz).

## 2.7.2. Winter

### 2.7.2.1. Cooling Period

The winter period occurs once the sea ice is in place (fast ice) and covers most of the open water. The snow accumulation begins and the first layering is visible. The winter period is separated in

two distinct average thermal regimes namely the ‘cooling period’ and the ‘warming period’. The cooling period occurs until the minimum air temperatures are reached (Figure-2.13) whereas the warming period follows until the first signs of spring early melt occur. Significant internal variability occurs within these average trends but this climatology provides a useful summary of the winter season. In what follows, I describe the relationships between snow thermophysical/electrical properties, surface energy balance and microwave emission and scattering mechanisms throughout those two periods.

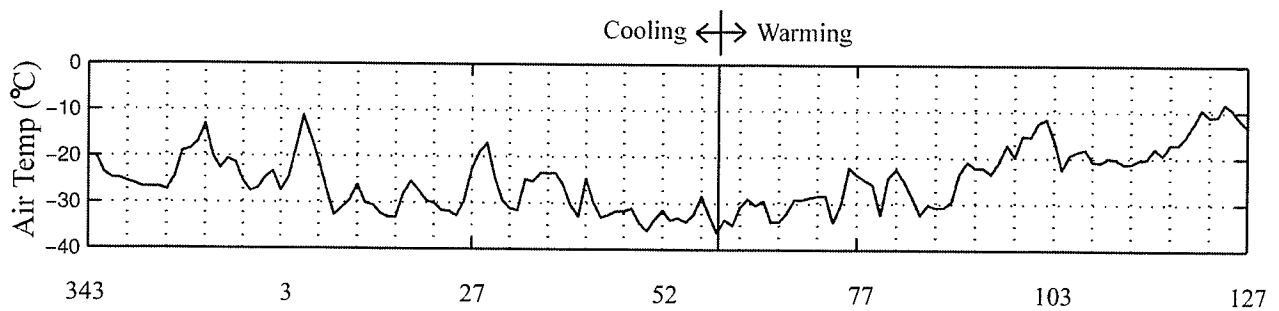


**Figure-2.13:** Temporal evolution of daily averaged air temperatures during the CASES study. The cooling and warming periods are separated by the coldest day

The winter cooling period has not been thoroughly investigated despite its primary importance in snow studies. The winter period in the Arctic includes a wide range of layered snow thickness that differs from each other thermodynamically (Langlois *et al.*, 2007a) affecting the dielectric response and the emission and scattering mechanisms in snow. The combination of cold temperatures and low available wetness leads to equilibrium snow metamorphism and snow drifting is one of the most dominant dynamic process. Hence, an important densification of the snowpack occurs from these processes, which enhances heat transfer due to the decreasing fractional volume of air.

Such increase in density also increases the permittivity of the snowpack, which in turn decreases the ability of the medium to permit the incident microwave radiation from the underlying ice (Figure-2.14, #1) (e.g., Matzler, 1987; Hallikainen, 1989; Comiso *et al.*, 1989; Lohanick, 1993; Barber *et al.*, 1994; Pulliainen and Hallikainen, 2001). Hence, snowdrifts migrating on the ice surface create variation in  $T_{bp}$  where the snowdrift brightness temperatures would be lower than of bare ice (Garrity, 1992). Furthermore, the strong desalination of the snowpack during the cooling period can cause  $T_{bp}$  to increase given constant snow thickness (due to decreasing  $\epsilon^*$ ). Further snow loading increases sea ice/snow interface temperature, creating a brine-wetted layer that may cause an increase in overall  $T_{bp}$ .

Dense and dry snow also affects the  $SEB_{snow}$  by modifying heat transfer and surface albedo, but values of  $K\downarrow$  and  $K\uparrow$  are obviously very low with very few hours of daylight. The range in albedo has been reported to be 0.5 to 0.6 over 1-2 m thick first-year sea ice (Maykut, 1978; 1986), and that value jumps to 0.8-0.85 when including snow (e.g., Grenfell and Perovich, 2004). Values of  $Q^*_{snow}$  are thus mainly driven by  $L^*$ , which relates to atmospheric conditions such as cloud cover (Figure-2.14, #2), opacity and height (e.g., Curry *et al.*, 1996; Barber and Thomas, 1998; Dong and Mace, 2003).

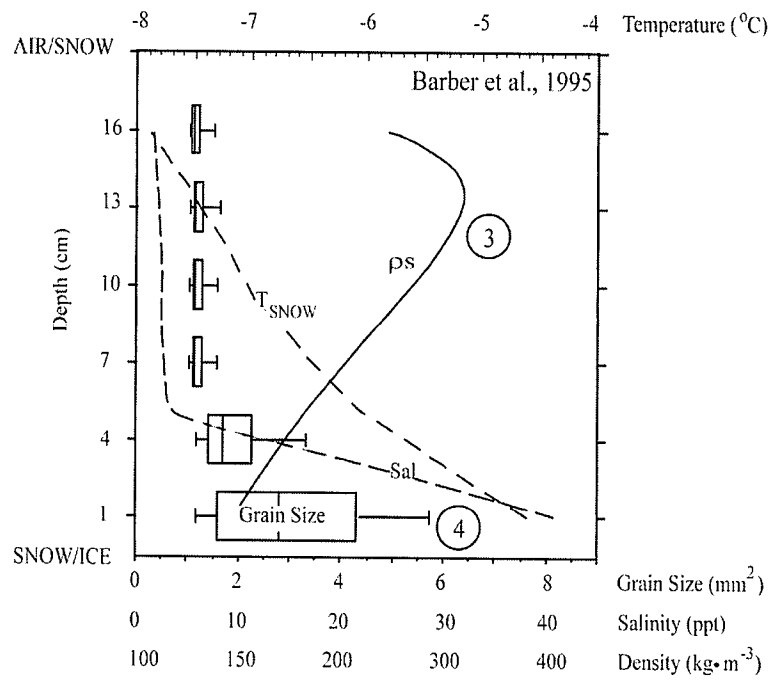
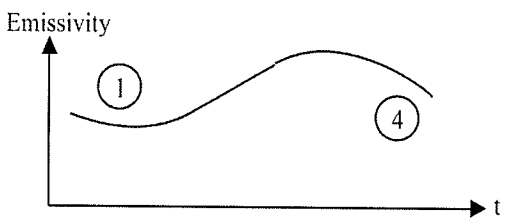
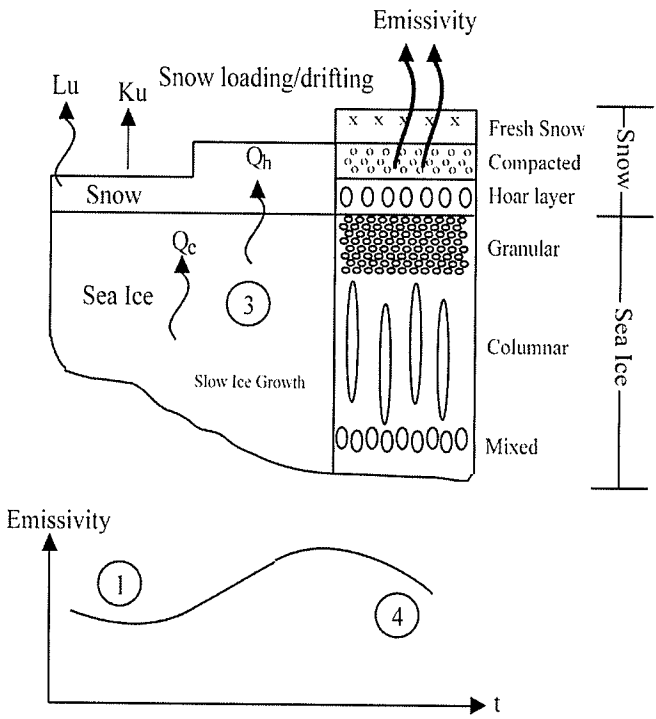
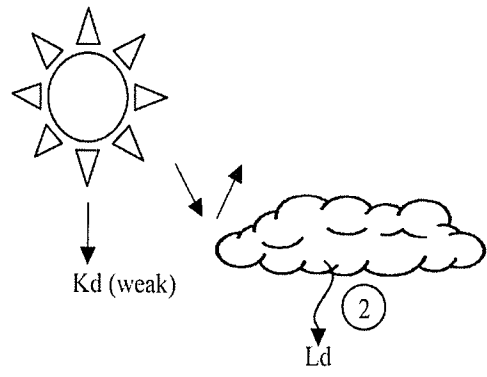


Figure-2.14: Schematic winter snow physical processes.

As the snow and ice thickens, the  $SEB_{snow}$  contribution of latent and conductive fluxes as well as the net radiative budget ( $Q^*_{snow}$ ) will change. For instance, overcast sky conditions lead to an increase in  $L\downarrow$  (i.e. increase in  $Q^*_{snow}$ ), which in turn will increase the snow/air interface temperature (increasing  $L\uparrow$ ). That radiative forcing on the surface decreases the conductive flux ( $Q_c$ ) keeping the volume from cooling. On the other hand, clear sky conditions will decrease  $L^*$  and  $Q^*_{snow}$  since incoming solar radiation is weak during the winter period. This decrease is accompanied by an increase in  $Q_c$  (e.g., Ruffieux *et al.*, 1995) towards the atmosphere allowing the cooling of the surface (radiative cooling). Furthermore, most of the energy at the snow surface comes from latent heat release by growing ice. This energy is then dissipated at the snow/air interface through  $Q_h$  and  $Q^*_{snow}$ . As mentioned for the fall period, the sensible heat and conductive fluxes ( $Q_h$  and  $Q_c$ ) decreases with the snow accumulation. It was shown that the decrease in  $Q_h$  could reach a factor of 4 (Steffen and DeMaria, 1996) as  $Q_e$  plays a very insignificant role during the whole winter with values close to 0.

#### 2.7.2.2. Warming Period

During the warming period, values of  $Q^*_{snow}$  increase steadily due to the increasing solar radiation. The first positive values of  $Q^*_{snow}$  (absorption of energy) are usually measured during the warming period and field values from different projects suggest that this occurs when  $K\downarrow$  reaches an average of  $200 \text{ W}\cdot\text{m}^{-2}$ . First obvious signs of kinetic growth grains are measured (Langlois *et al.*, 2007a), which impact on heat flow is significant as thermal conductivity is influenced by the texture of the snow grains. Sturm and Johnson (1992) did correlate the variations in  $k_s$  with textural parameters of the snow grains as the season evolved. They found

that  $k_s$  increased rapidly under temperature gradient metamorphism (Sturm *et al.*, 2002) and then leveled off when the rate of growth decreased. This was due to an increased flow path length (i.e. bigger grains reduce vapor flow) and increasing fractional volume of air. Kinetic growth grains will also affect microwave scattering especially at high frequencies (e.g., Tiuri *et al.*, 1984; Drinkwater and Crocker, 1988; Hallikanen, 1989; Tsang *et al.*, 2000; Kelly *et al.*, 2003) where significant volume scattering and depolarization are expected to occur.

Even though  $Q_{snow}^*$  is affected by  $K^*$ , the energy budget still depends largely on  $L^*$  and radiative forcing still controls the  $Q_c$  flux. Furthermore, increasing  $K_{\downarrow}$  might counteract in part the radiative cooling in clear sky conditions at solar noon, contrary to the cooling period where the radiative cooling could occur throughout the diurnal cycle. Concomitant to the increase in temperatures and  $Q_{snow}^*$ , increasing brine volume and wetness will control the dielectric constant and passive microwave emission. The presence of liquid water within the snowpack increases the internal absorption along with decreasing volume scattering and increasing depolarization (Foster *et al.*, 1984; Matzler and Huppi, 1989). As snow and ice thickens, both  $Q_c$  and  $Q_h$  are expected to decrease significantly (Figure-2.14, #3). However, this can vary depending on atmospheric stability where an unstable boundary layer (i.e. convective mixing) can give rise to variations in both the direction and magnitude of the turbulent fluxes (Steffen and DeMaria, 1996).

In summary, the cooling period  $T_{bp}$  depends largely on air temperatures, which control thermophysical properties variations (e.g., Lohanick, 1993; Grody and Basist, 1996; Sokol *et al.*, 1999; Rosenfeld and Grody, 2000; Langlois *et al.*, 2007b). Throughout the winter, the variations in  $T_{bp}$  are greater at high incidence angles in the horizontal polarizations due to the lower

penetration depth and stronger snow layering effect (e.g., Hallikainen, 1989; Barber and LeDrew, 1994; Derksen *et al.*, 2005). Snow temperature gradient metamorphism (grain growth) is significant during the warming period increasing volume scattering and depolarization (Figure-2.14, #4). Furthermore, the increase in wetness and brine volume affect both  $T_{bP}$  and  $\Delta P$  at all frequencies and incidence angles.

### 2.7.3. Spring

The spring period begins with increasing surface temperatures due the warm air advection from low-level clouds enhancing radiative warming (e.g., Serreze *et al.*, 1993). This radiative forcing on the surface causes snow grain metamorphism, which in turn decreases the  $\alpha$  (0.77 for melting snow, after Perovich, 1996) allowing significant absorption of solar radiation. In what follows, I describe the three spring regimes namely ‘early melt’, ‘melt onset’ and ‘advanced melt’ (e.g., Yackel *et al.*, 2001) until snow and ice are melted completely.

The early melt period is characterized by a steady increase in solar radiation increasing  $K\downarrow$ . However, this increase can be countered by the increase emitted longwave radiation that responds to the increase in surface temperatures. For that matter, negative values of  $Q^*_{snow}$  can still be found during the night in the early melt period (Papakyriakou, 1999). The decrease in surface albedo due to increasing grain size is the first step to snow melt, which increases the amount of liquid water within the snow (i.e. increase thermal conductivity). This leads to an increase in solar radiation absorption that decreases the temperature gradient. Snow eventually reaches the pendular regime, where isolated bodies are found throughout the vertical profile (Brzoska *et al.*,

1998; Denoth, 2003). Small amounts of water percolate to the bottom of the snowpack and freezes to the contact of the cold ice (Figure-2.15a and b) creating ice-crusts and/or superimposed ice layers (Gogineni *et al.*, 1992; Barber and Thomas, 1998; Hwang *et al.*, 2006). Throughout the pendular regime, snow grains are well rounded but do not tend to sinter (Colbeck, 1982; Sturm *et al.*, 2002). During this period,  $T_{bp}$  are dominated by the diurnal fluctuations in snow/ice interface temperatures (Hwang *et al.*, 2006b). However, the contribution of increasing wetness within the snowpack cannot be ignored as the amplitude of warming air temperature is expected to be lower than the warming  $T_{bp}$  amplitude due to the contribution of wetness to  $e$ .

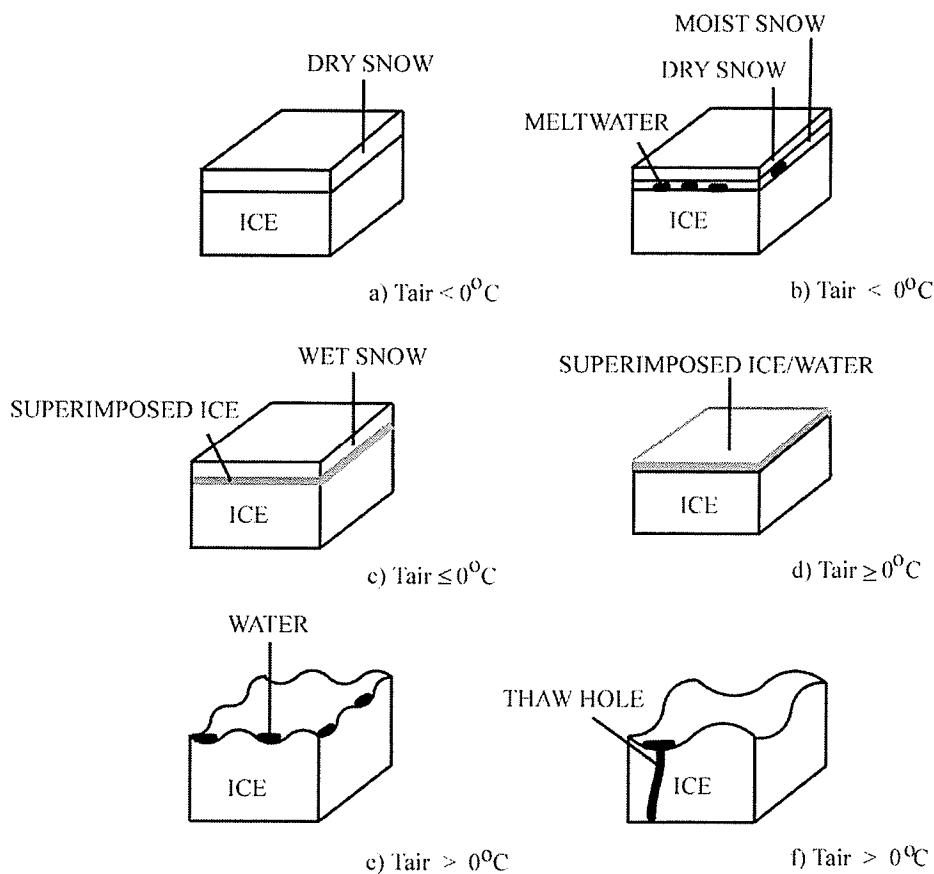


**Figure-2.15:** Spring melt over first-year sea ice (adapted from Gogineni, 1992).

During the melt onset period, the net radiation increases and the transmission of solar radiation within the snow/sea ice can increase by a factor of 10 (Papakyriakou, 1999). Melt onset in the Arctic is defined by the continuous presence of liquid water within the snow cover throughout the diurnal cycle (e.g., Livingstone, 1994; Yackel *et al.*, 2001) and is the longest of the three melt stages (Harouche and Barber, 2001). As the temperature and solar zenith angle increase, the snow will slowly switch from pendular to funicular regime where wetness values approach saturation (Colbeck, 1982). The wetness of the basal layer increases significantly due to the constant percolation of water from surface melting (Figure-2.15c). Snow thickness starts to decrease and density values increase with increasing water content (Goginneni *et al.*, 1992). When the snowpack reaches the funicular regime, drainage occurs and  $\alpha$  is expected to increase again afterwards. Microwave volume scattering is expected to increase with the large brine wetted grains at the basal layers of the snowpack increasing the dielectric constant throughout the vertical profile. The ice crusts also form during this period creating strong polarization effects (Garrity, 1992) and the highest daily variations in  $T_{bp}$  are measured (Harouche and Barber, 2001). The high dielectric loss of wet snow dominates volume scattering and the surface scattering becomes more important (Matzler, 1987).

The advanced melt begins when saturation is reached within the snow cover. Also, rain events can significantly accelerate the melt process (Tucker *et al.*, 1987; Hwang *et al.*, 2006b). In saturated conditions, the percolation occurs in a significant manner causing a steep increase in wetness with respect to depth. The snow/ice surface forms a slush layer and the coincident warming sea ice allows some level of brine drainage (e.g., Jacobs *et al.*, 1975; Eicken, 2003). This period is also characterized by dramatic changes in  $SEB_{snow}$  where albedo values can

decrease from 0.7-0.8 to 0.3-0.5 (Maykut, 1978; Perovich, 1996), with the presence of melt ponds. The surface ponds eventually drain leaving exposed bare ice which albedo oscillates around 0.5. Melt ponds remain in place until the ice is warm enough to allow complete drainage of the surface water (flushing) leaving a layer of superimposed ice on top of sea ice (Figure-2.15d). With constant increase in temperatures and solar radiation, that layer will eventually melt (Figure-2.15e) and drain through thaw holes within the sea ice (Figure-2.15f). This process decreases the  $e$  of the surface; decreasing  $T_{bP}$  at all frequencies and strong ponded areas can have relatively cooler  $T_{bP}$  due to this process (Harouche and Barber, 2001). At this point, brine volume at the basal layer of the snowpack decreases with constant increasing snow wetness at the bottom (from the drainage of the upper snow layers).

## 2.8. Summary

The intention of this chapter was to compartmentalize some of the salient theory as a means of defining how microwave remote sensing may be used to estimate snow thermophysical properties. The effect of a changing climate can affect many aspects of the snow sea ice system. I find that three particular feedback mechanisms (outlined below) are particularly relevant to snow on sea ice. We also summarize the application of passive microwaves to characterize the snowpack, which will be useful in the study of these feedback mechanisms in later chapters.

**Temperature-albedo feedback:** Rising temperatures increase snow wetness, which in turn decreases snow albedo. As a result, the snowpack is expected to decline in both spatial and temporal scales, permitting an increase in the absorption of solar radiation by the surface. In

addition, the timing and magnitude of snowfall in the Arctic exhibits a further control on the growth and decay of sea ice. An early snowfall reduces ice growth (lowers heat conduction), while late snowfalls protect the ice from melting (high albedo).

As mentioned in Section 2.6, passive microwave brightness temperatures are very sensitive to snow wetness through changes in the dielectric constant, thus permitting remote monitoring of the onset and advancement of the melt stage. Previous studies have shown that the transition between pendular and funicular regime can be detected using passive microwave data, taking advantage of melt indicators such as brightness temperature differences and gradient ratio (Hwang *et al.*, 2007). As a result, monitoring of the passive microwave signal becomes a valuable tool in characterizing the present state of this particular feedback and thus the warming of the Arctic.

**Temperature-cloud cover-radiation feedback:** With a warming atmosphere and ocean, evaporation is expected to increase, bringing a concurrent increase in cloud amount and thickness. This has both positive and negative feedbacks, as the high albedo of the cloud reduces the amount of shortwave radiation reaching the surface, while at the same time increasing the absorption and re-radiation of longwave emissions from the ground. At high latitudes, an increase in winter cloudiness will tend to increase mean surface temperatures, while in summer months the opposite will apply.

During springtime, this feedback triggers grain growth at the surface, allowing for more solar radiation to be absorbed, increasing the overall amount of water in liquid phase that can be

detected with passive microwave. Furthermore, strong kinetic growth can occur during this transition resulting in large volume scattering and strong depolarization that can all be detected with passive microwaves (e.g., Eppler, 1992). During the winter period, migrating low-pressure systems bring increased cloudiness with warmer temperatures and increased wind speeds. Passive microwave can be used to detect significant vertical brine volume migration that occurs specifically under such conditions (Langlois *et al.*, 2007c).

**Conductive feedback:** Feedbacks associated with a global increase in temperatures are expected to result in a thinner ice pack and greater heat conduction from the ocean. This feedback will further advance the springtime melt, and in turn allow more heat to penetrate into the ocean (another positive feedback).

Passive microwaves are not sensitive to ice thickness but instead to the feedbacks that may cause the ice thickness to decline as described above. Thinner ice, with its greater heat conduction from the ocean, can lead to a warmer snowpack with associated variations in thermophysical properties that, at least theoretically, can be detected by passive microwaves. However, no work has been conducted specifically on the subject yet.

Hence, this chapter sets the stage for the dissertation providing the necessary background material to understand the results presented from Chapters 4 to 7. All the snow thermophysical processes and passive microwave emission and scattering mechanisms linkages discussed in this chapter will be analyzed using field data. The next chapter (Chapter 3) describes the site location and associated field sampling and modeling techniques pertaining to the research.

## CHAPTER 3: DATA AND METHODS

In this chapter, I first describe the study site location where all the meteorological, micrometeorological and snow measurements occurred. I provide a general description of the different instruments that were setup on the ice to collect the basic weather and micrometeorology information. I then describe the details of snow thermophysical properties sampling, dataset structure and snow dielectric modeling used throughout the dissertation. Finally, I explain how passive microwave signatures were obtained from both the Surface Based Radiometers (SBR, *in-situ*) used for Chapters 4-5-6 and the Advanced Microwave Scanning Radiometer for EOS (AMSR-E, spaceborne) used in Chapter 7.

### 3.1. Study Site

Snow data were collected during the Canadian Arctic Shelf Exchange Study (CASES) overwintering mission from November 26<sup>th</sup> 2003 (day 329), continuously until May 12<sup>th</sup> 2004 (day 132). During the study period, the Canadian Coast Guard research icebreaker, *C.C.G.S. Amundsen*, (a class 1200 Icebreaker) was frozen into a landfast smooth first-year sea ice about 20 km off shore in Franklin Bay, Northwest Territories, Canada (Figure-3.1).

The sea ice surrounding the ship was 80 cm thick on December 5<sup>th</sup> 2003 and had grown to 210 cm by May 31<sup>st</sup> 2004. Maykut and Church (1973) reported that the minimum monthly air temperature for this region was  $-28$  °C for February and the maximum  $+3.9$  °C for July, averaged between 1931 and 1966. Monthly mean vertically integrated precipitable water ranges from 2.9 mm in February and March to 16.2 mm in July (Serreze *et al.*, 1995; Curry *et al.*, 1996).

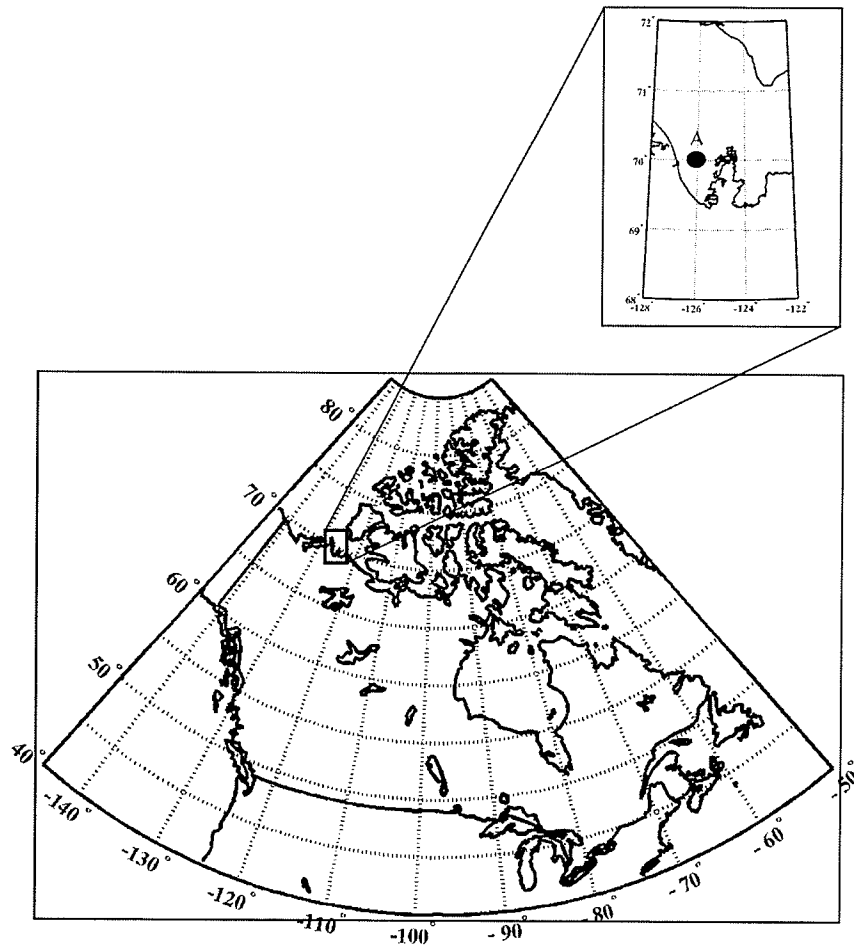


**Figure-3.1:** Canadian Arctic Shelf Exchange Study (CASES) overwintering mission location.

Many sampling sites were erected within 2-km from the ship (Figure-3.2). The ship's orientation was  $105^\circ$  (E-E-SE) and all sites were located on the East side. An undisturbed area (Area A) was dedicated to surface based radiometer measurements along with concomitant snow physical sampling (snowpits). Gas sampling occurred daily at Area B whereas Areas C and D were dedicated to biological and water sampling respectively. Snow fences of different heights were erected approximately 1.6 km east of the ship in order to create multiple snow thickness (Area E) with a dedicated area for ice coring. Basic meteorological and micrometeorological towers were erected south of that area (see Section 3.3).

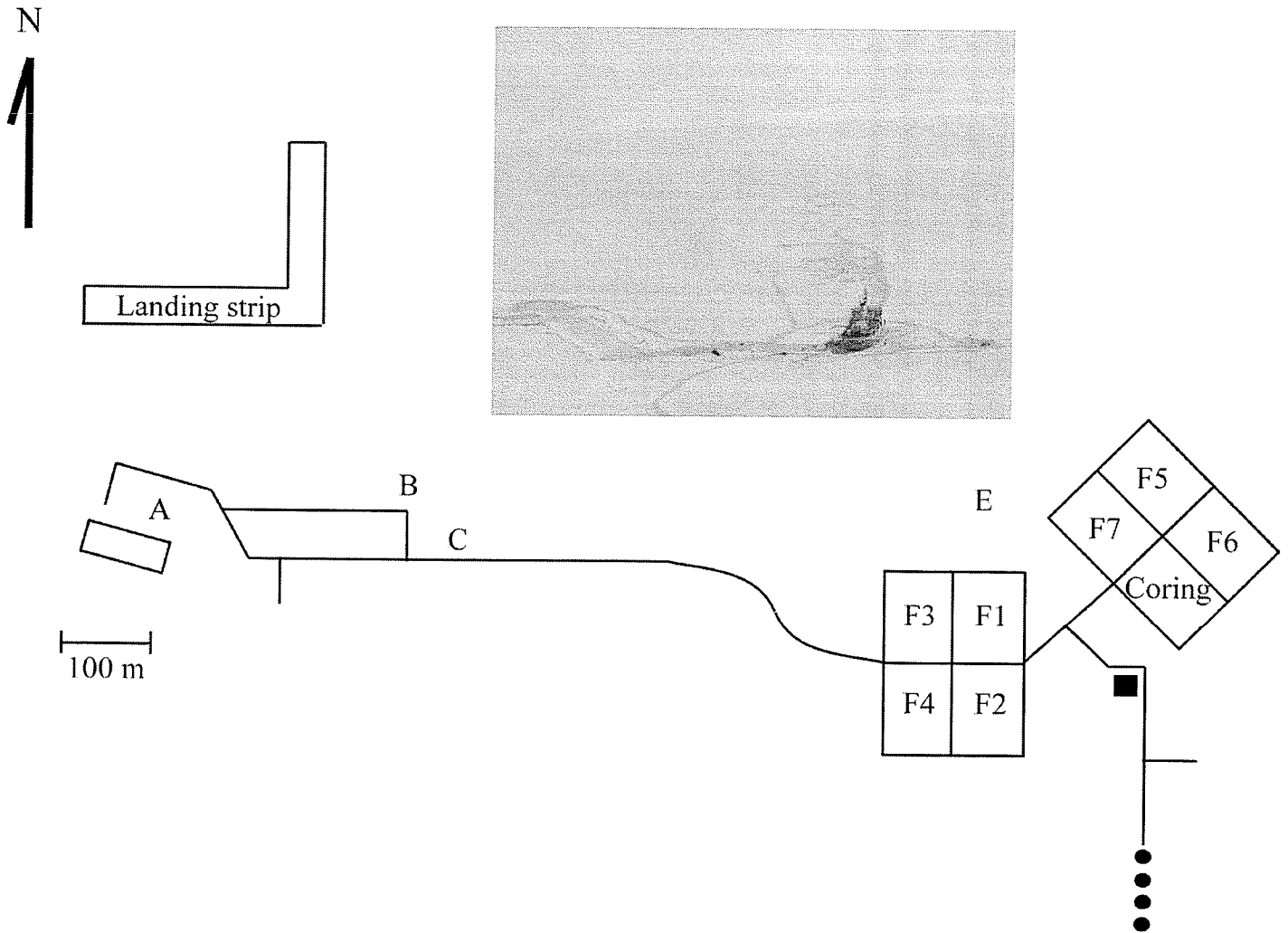


**Figure-3.2:** Sampling sites locations around the ship (ship located beside area A).

### **3.2. Meteorological Observations**

Daily average atmospheric pressure, air temperature, sea surface temperature, wind speed/direction and GPS location were calculated hourly from the AXYS Automated Voluntary Observation Ship (AVOS) system on the roof of the ship's wheelhouse (approximately 20 m above the sea ice). The AVOS is an interactive environmental reporting system that allows ships to transmit current meteorological observations to a central station every hour. Measurements are updated every 10 minutes and displayed on a computer monitor located in the wheelhouse (Fisico, 2005). Cloud amount was monitored hourly in octas (0 is a clear sky and 8 is overcast) and 24-hour observations were carried out throughout the study.

### **3.3. Micrometeorological Data**

Net all-wave radiation  $Q^*$  and its longwave ( $L^*$ ) and shortwave ( $K^*$ ) components were measured at the meteorological station located 1.6 km east of the ship (Area E at  $70^\circ 2.516'N$ ,  $126^\circ 15.894'W$  on Figure-3.2). Net shortwave ( $K^*$ ) and longwave ( $L^*$ ) radiation were determined from the difference between observed downwelling and upwelling radiation using Eppley pyranometers (shortwave) and pyrgeometers (longwave). Sensor output was scanned at 3-second intervals and stored as 10-minute averages by a Campbell Scientific (model 21X) data logger. Data collection occurred between January 23<sup>rd</sup> (day 23) through to May 7<sup>th</sup> (day 127), 2004.

### 3.4. Snow Physical Properties

#### 3.4.1. Snow Sampling

Snow physical properties used throughout my dissertation were collected at a sampling site located adjacent to the ship on the North side. This site consisted of a 80 m by 80 m zone of undisturbed snow (Area A on Figure-3.2). Snow pits were excavated diurnally (morning, noon and afternoon) every second day at areas of thin (4-10 cm) and thick (10-80 cm) snow covers between December 6<sup>th</sup>, 2003 and May 7<sup>th</sup>, 2004. I arranged the sampling so that thin and thick snowpacks would be sampled throughout the study period. These thickness categories were selected to investigate the relationship between the evolution of snow overburden and the rates of grain metamorphism, and thermally dependent physical properties evolution of the snowpack.

Temperature profiles were first measured in the excavated snow pits using a Hart Scientific temperature probe with a published accuracy of +/- 0.025 °C over a temperature range of -200 °C to +100 °C. I used a dielectric method to compute snow wetness ( $W_v$  in %) from permittivity  $\epsilon$ . This technique uses a capacitance plate, which measures the increased conductivity due to small amounts of water in liquid phase (Denoth, 1989). The effective measuring area of the capacitance plate is 12.5 x 13 cm at an operating frequency of 20 MHz. The permittivity  $\epsilon$  is given by:

$$\epsilon = 1 + k \cdot \log_{10}\left(\frac{U}{U_{ref}}\right), \quad [\text{eq. 3.1}]$$

where  $k$  is the sensor specific calibration constant,  $U$  and  $U_{ref}$  are the readings within the snow and in air respectively. The readings display numbers related to the actual capacity of the

dielectric sensor. With density measurements and permittivity values from [eq. 3.1], liquid water content can be derived as shown on [eq. 3.2]:

$$\varepsilon = 1 + 1.92\rho + 0.44\rho^2 + 0.187W_v + 0.0046W_v^2, \quad [\text{eq. 3.2}]$$

This technique has an estimated precision of 0.5 of one percent water by volume when there is no brine in the snow layer. The technique is unable to measure  $W_v$  in the highly brine saturated basal layer of snow on first-year sea ice forms due to the elevated dielectric constant of this volume and the lack of suitable calibration. Further details are available elsewhere (Barber *et al.* 1995).

Snow samples were extracted at 2 cm intervals from the surface to the snow/ice interface with a 66.36 cm<sup>3</sup> density cutter. Each sample was sealed in WhirlPack bags in the field and taken quickly in the ship's cold laboratory (-15 to -20 °C). Each sample was weighed using a Denver Instrument digital scale accurate to obtain density, and melted for salinity measurements using a WTW conductivity meter. Prior to melting, sub-samples were photographed to measure snow grain size and structure. Sub-samples were first placed on a 2 mm gridded plate and photographed to measure the average snow grain size of the sample. Individual grains were then randomly extracted from the grid plate and placed in chemically inactive and optically transparent silicone oil for microstructural photographs (to avoid sublimation loss). All pictures were taken with a Canon PowerShot 4.2 Mega Pixels camera mounted on a Leica MZ 7.5 stereomicroscope (Figure-3.3).

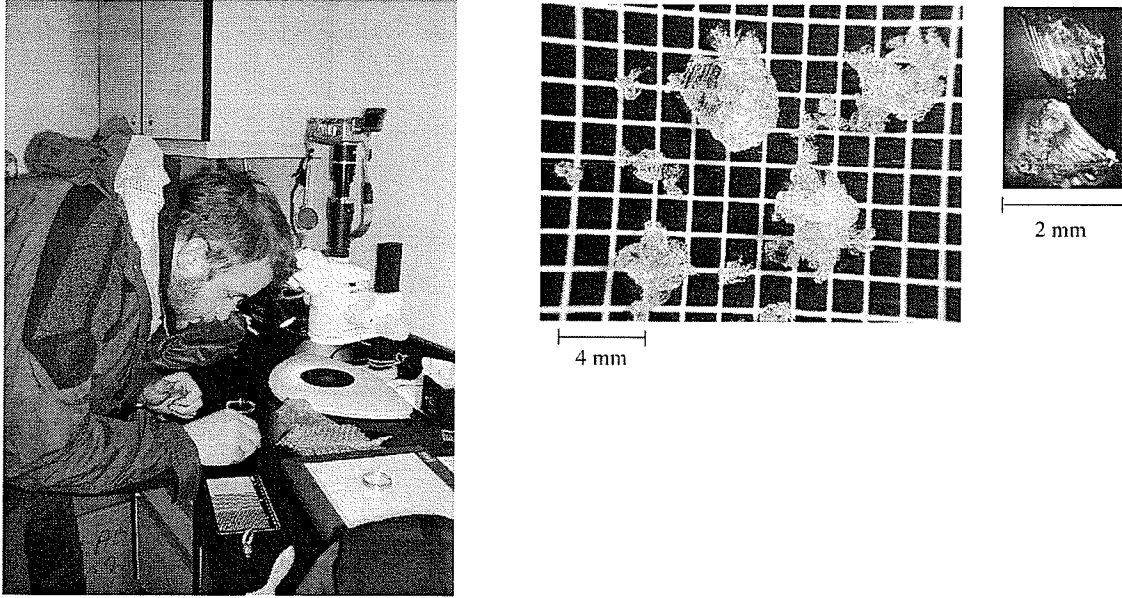


**Figure-3.3:** Snow grain photography in the ship's cold laboratory.

Snow grain photos were analyzed in MatLab using a specially designed polygon analysis code, which extracted snow grain size and structure (e.g., major and minor axes and area). Brine volume was also computed from salinity and temperature for each layer of the snowpack, following a method by Cox and Weeks (1982) after Frankenstein and Garner (1967):

$$v_b = 10^{-3} S_s \left\{ -\frac{52.56}{T_s} - 2.28 \right\}, -0.5^\circ\text{C} \geq T_s \geq -2.06^\circ\text{C} \quad [\text{eq. 3.3}]$$

$$v_b = 10^{-3} S_s \left\{ -\frac{45.917}{T_s} + 0.930 \right\}, -2.06^\circ\text{C} \geq T_s \geq -8.2^\circ\text{C} \quad [\text{eq. 3.4}]$$

$$v_b = 10^{-3} S_s \left\{ -\frac{43.795}{T_s} + 1.189 \right\}, -8.2^\circ\text{C} \geq T_s \geq -22.9^\circ\text{C} \quad [\text{eq. 3.5}]$$

$$v_b = 10^{-3} S_s \left\{ \frac{3079.84}{T_s} + \frac{1.58402 \cdot 10^5}{T_s^2} + \frac{3.61615 \cdot 10^6}{T_s^3} + \frac{3.12862 \cdot 10^7}{T_s^4} + 22.8478 \right\}$$

,  $-22.9^\circ\text{C} \geq T_s \geq -37.8^\circ\text{C}$  [eq. 3.6]

$$v_b = 10^{-3} S_s \left\{ \frac{1642.6}{T_s} + \frac{6.4947 \cdot 10^4}{T_s^2} + \frac{8.3945 \cdot 10^5}{T_s^3} + 14.145 \right\}$$

,  $-37.8^\circ\text{C} \geq T_s \geq -43.2^\circ\text{C}$  [eq. 3.7]

where  $T_s$  is the snow volume temperature in  $^\circ\text{C}$  and  $S_s$  the salinity in ppt. Since all our measurements occurred during the winter, I did not need to use  $v_b$  calculations below  $-0.5^\circ\text{C}$ .

Snow water equivalent (SWE), was calculated as a function of density and thickness. It is a measure of the equivalent amount of water resulting from snowmelt. SWE is a product of density and thickness and can be expressed in  $\text{kg}\cdot\text{m}^{-2}$  or mm (most common):

$$SWE = depth \cdot \rho_s = m \cdot \frac{\text{kg}}{\text{m}^3} = \frac{\text{kg}}{\text{m}^2}$$
 [eq. 3.8]

$$SWE = \frac{(depth \cdot \rho_s)}{\rho_w} = \frac{m \cdot \frac{\text{kg}}{\text{m}^3}}{\frac{\text{kg}}{\text{m}^3}} = m$$
 [eq. 3.9]

where  $\rho_s$  and  $\rho_w$  are the density of snow and water respectively. Since the density of water is approximately  $1 \text{ g}\cdot\text{cm}^{-3}$ , a widely used approximation  $SWE = depth \cdot \rho_s$  is appropriate. The interest in SWE over land resides in its hydrologic applications as it is an important asset of the water budget (e.g., hydroelectric management, agriculture, irrigation etc.), but the interest for SWE over sea ice remains mainly the impact of snow thickness on the timing of sea ice freeze up

and decay and radiative transfer to the base of the sea ice for algae growth. To understand the impact of climate change in the Arctic environment, both magnitude and temporal data on SWE is required and remote sensing provides a useful tool in budgeting snow over sea ice.

Snow water equivalent was also measured in other areas surrounding the ship over smooth, and rough ice using. A series of SWE transects were conducted in the region in different ice roughness conditions, which will be discussed later in Chapter 7 to validate SWE predictions from AMSR-E. Thickness lines were sampled at  $0^\circ$  (E-W direction),  $45^\circ$ ,  $90^\circ$  (N-S direction) and  $135^\circ$  (Figure-3.4). I calculated SWE from the thickness measurements using the density profiles measured at the ship's sampling site (Langlois et al., 2007a) during the same period under the same thickness range.

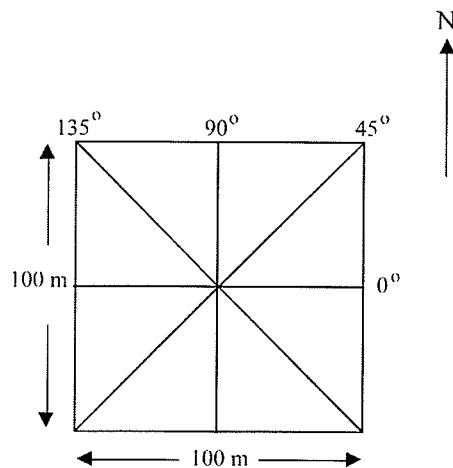


**Figure-3.4:** Schematic of conducted SWE transects over smooth first-year sea ice.

### 3.4.2. Vertical Profile Characterization

Snow thickness at the thin snow site remained stable throughout the study period whereas it increased at the thick snow site (see Chapter 4, Section 4.1). Hence, thin snow pits were treated as one group and were limited to 3 layers (Top, Middle and Bottom) throughout the study period, as most of the snow pits were 6 - 7 cm thick. The thicker snowpacks were separated into three different groups (from 3 major snow depositional events) where the thickness increased throughout the study period (Figure-3.6). I first separated the layers (*L*) with visual interpretation. A 'Tukey' post-hoc ANOVA statistical analysis (Moore and McCabe, 1993) was then conducted to test if these layers were statistically different from one another for both thin and thick snowpacks. Results showed that all layers were statistically different for at least 2 physical properties with 95% confidence. Therefore, snow pits at the thick site were standardized to a scale from 0 to 1 to permit comparison of the same layers throughout the season.

#### *Thin Snow Cover Site:*

One Group (6-7 cm): 3 layers → Top, Middle, and Bottom, days 344 to 127

#### *Thick Snow Cover Site:*

Group 1 (10-17cm): 4 layers → L1, L2, L3, and L4, days 5 to 42<sup>1</sup>

Group 2 (26-34cm): 6 layers → L1, L2, L3, L4, L5 and L6, days 42 and 91<sup>2</sup>

Group 3 (45-80cm): 8 layers → L1, L2, L3, L4, L5, L6, L7 and L8, days 91 to 127<sup>3</sup>

---

<sup>1</sup> L1 is the bottom layer and L4 is the layer in contact with the air

<sup>2</sup> L5 and L6 are deposited on top of L4; L6 is now the layer in contact with the air

<sup>3</sup> L7 and L8 are deposited on top of L6; L8 is now the layer in contact with the air

### 3.5. Snow Electrical Properties

As mentioned in Chapter 2, in pure water, the dielectric constant obeys the Debye equations and depends on frequency and temperature through the relaxation time of water (Ulaby *et al.*, 1986):

$$\varepsilon_w = \varepsilon_w' + j\varepsilon_w'' \quad [\text{eq. 3.10}]$$

where  $\varepsilon_w'$  and  $\varepsilon_w''$  respectively are:

$$\varepsilon_w' = \varepsilon_{w\infty} + \frac{\varepsilon_{w0} - \varepsilon_{w\infty}}{1 + (2\pi f \tau_w)^2} \quad [\text{eq. 3.11}]$$

$$\varepsilon_w'' = \frac{2\pi f \tau_w (\varepsilon_{w0} - \varepsilon_{w\infty})}{1 + (2\pi f \tau_w)^2} \quad [\text{eq. 3.12}]$$

In [eq. 3.11 and 3.12],  $\varepsilon_{w0}$  is the static dielectric constant of pure water at the initial frequency,  $\varepsilon_{w\infty}$  the high-frequency limit dielectric constant,  $\tau_w$  the relaxation time of pure water of and  $f$  the frequency. The relaxation time of pure water  $\tau_w$  and the frequency of relaxation  $f_{w0}$  can be calculated as:

$$2\pi\tau_w = 1.1109 \cdot 10^{-10} - 3.824 \cdot 10^{-12} T + 6.938 \cdot 10^{-14} T^2 - 5.096 \cdot 10^{-16} T^3 \quad [\text{eq. 3.13}]$$

$$f_{w0} = (2\pi\tau_w)^{-1} \quad [\text{eq. 3.14}]$$

The effect of  $\tau_w$  on the dielectric constant where the frequency of relaxation ( $f_{w0}$ ) is referred as the frequency where  $\varepsilon_w''$  is maximum ( $f_{w0} = 9\text{GHz}$  at  $0^\circ\text{C}$ ). At this frequency,  $\varepsilon_w' = (\varepsilon_{w0}' + \varepsilon_{w\infty}')/2$

and  $\varepsilon''_w = (\varepsilon''_{w0} - \varepsilon''_{w\infty})/2$ . The temperature also has a significant effect on  $\tau_w$ , whereas warmer temperatures decrease the relaxation time. However, the effect of temperature on  $\varepsilon_w$  changes considerably (larger decrease at low frequency). Therefore, both  $\varepsilon'_w$  and  $\varepsilon''_w$  are dependent not only on frequency but also on temperature with a relaxation time located in the microwave region.

Brine is the same as saline water, but with much higher values of salinity ( $S_b \gg S_w$ ). The salinity of the brine is temperature dependent where one could refer the work by Frankenstein and Garner (1967), and later modified (extended temperature range) by Cox and Weeks (1982) and Lepparenta and Manninen (1988). Their research led to calculations of brine volume given a temperature and salinity. Therefore, the dielectric constant of brine is given by the modification of [eq. 3.15 and 3.16] such that:

$$\varepsilon'_b = \varepsilon_{w\infty} + \frac{\varepsilon_{b0} - \varepsilon_{w\infty}}{1 + (2\pi f \tau_b)^2}, \quad [\text{eq. 3.15}]$$

$$\varepsilon''_b = (2\pi f \tau_b) \cdot \left\{ \frac{\varepsilon_{b0} - \varepsilon_{w\infty}}{1 + (2\pi f \tau_b)^2} \right\} + \frac{\sigma_b}{2\pi f \varepsilon_0}, \quad [\text{eq. 3.16}]$$

where  $\varepsilon_{w\infty}$ ,  $\varepsilon_{b0}$ ,  $f$ ,  $\tau_b$ ,  $\sigma_b$  and  $\varepsilon_0$  are respectively: the high frequency limit of the dielectric constant of brine, the static dielectric of brine, the frequency, the relaxation time of brine, the ionic conductivity of the brine solution and the permittivity of free space (Stogryn, 1971; Stogryn and Desargeant, 1985). In general, both  $\varepsilon'_b$  and  $\varepsilon''_b$  magnitude of change is governed by  $\sigma_b$  (Hallikainen and Winebrenner, 1992).

Snow is a layered media composed of a mixture of ice, brine and air; therefore it is now appropriate to introduce the concept of mixing formulas for snow over first-year sea ice dielectric calculations. For a medium consisting of a host material with inclusions, the dielectric constant of the mixture consists of:

$$\varepsilon_{mix}^*(x, y, z, \hat{P}) = \varepsilon_m(\hat{P}) + \varepsilon_f(x, y, z, \hat{P}) \quad [\text{eq. 3.17}]$$

where  $\varepsilon_m(\hat{P})$  is the average value of the permittivity of the medium (independent of position but function of polarization vector  $\hat{P}$ ) and  $\varepsilon_f(x, y, z, \hat{P})$  the fluctuation component (dependent on position and  $\hat{P}$ ). Both permittivity and dielectric loss of snow over first-year sea ice can be calculated from a dielectric mixture model (Barber and Thomas, 1998; Barber *et al.*, 2003) of the form proposed by Polder-Van Santen and later modified by de Loor (Ulaby *et al.*, 1986) using snow wetness, density, temperatures and salinity measurements. Wetness below 1% is considered ‘dry’ and treats brine as “inclusion dielectric” within a dry snow “host dielectric” (Barber *et al.*, 1995, after Matzler, 1987 and Drinkwater and Crocker, 1988). From that concept, the dielectric constant of a dry saline snow mixture over first-year sea ice is expressed by:

$$\Delta\varepsilon_{mix}^* = \chi \cdot V_b \cdot \left\{ \frac{\varepsilon_b^* - \varepsilon_{ds}^*}{1 + \left[ \frac{\varepsilon_b^* - 1}{\varepsilon_{ds}^*} \right] \cdot A_0} \right\}, \quad [\text{eq. 3.18}]$$

where  $\epsilon_{ds}^*$  and  $\epsilon_b^*$  are expressed in complex terms and represent the dielectric constant of dry snow (wetness inferior to 1 %) and brine,  $\chi$  the fraction of brine accounted for a depolarization factor  $A_0$  and  $V_b$  is the volume of brine within the snow layer. The dielectric constant of dry snow ( $\epsilon_{ds}^*$ ) is calculated using an empirical model from Hallikanen and Winebrener, 1992. According to Ulaby *et al.* (1986), the permittivity ( $\epsilon'_{ds}$ ) and dielectric loss ( $\epsilon''_{ds}$ ) are calculated using a Debye form:

$$\epsilon'_{ds} = (1 + 0.51 \cdot \rho_s)^3 \quad [\text{eq. 3.19}]$$

$$\epsilon''_{ds} = \frac{0.34 \cdot \frac{\rho_s}{0.916} \cdot 0.001}{(1 - (0.417 \cdot \frac{\rho_s}{0.916}))^2} \quad [\text{eq. 3.20}]$$

Snow wetness over 1% is considered ‘wet’ snow, and the permittivity ( $\epsilon'_{wet}$ ) and dielectric loss ( $\epsilon''_{wet}$ ) are independent of volume temperature and salinity. The dielectric constant of wet snow  $\epsilon_{wet}^*$  is then calculated using the permittivity and dielectric loss of both dry snow and pure water (Tiuri *et al.*, 1984). Water has high dielectric constant; therefore a small amount within the snowpack can greatly influence the dielectric properties of the volume (Ulaby, 1986; Walker and Goodison, 1993). The snowpack is then considered as a mixture between dry snow and pure water. The Polder-Van Santen approach is again used to treat the dry snow as the ‘host dielectric’ and the pure water as the ‘inclusion dielectric’ such that:

$$\epsilon'_{ws} = \epsilon'_{ds} + \epsilon'_w \cdot (0.1 \cdot W_V + 0.8 \cdot W_V^2), \quad [\text{eq. 3.21}]$$

$$\epsilon''_{ws} = \epsilon''_w \cdot (0.1 \cdot W_V + 0.8 \cdot W_V^2), \quad [\text{eq. 3.22}]$$

where  $W_v$  is the snow wetness (%). Both wet and dry snow dielectric constant calculations are dependent upon snow density and the frequency used.

### **3.6. Passive Microwave Data**

#### *3.6.1. Surface Based Radiometer (SBR)*

The surface based radiometer (SBR) receives vertically and horizontally polarized microwave emission at 19, 37 and 85 GHz with 15 degrees beamwidth antennas (Asmus and Grant, 1999). Brightness temperatures for all three frequencies at both vertical and horizontal polarization were measured at a fixed incidence angle of  $53^\circ$  (approximately the same incidence angle used for spaceborne sensors: SMMR, SSM/I and AMSR-E), and also from multi-angular measurements between the incidence angles of  $30^\circ$  and  $70^\circ$  with a  $5^\circ$  increment (used in Chapters 4, 5 and 6). Calibrations for the measured brightness temperatures were done following Grenfell and Lohanick (1985) and Asmus and Grant (1999). The calibration process establishes a linear relationship between the radiometer's voltage and brightness temperatures. The two-point calibration uses a hot load and cold source to establish the linear relationship. I used the sky as the cold source by pointing the radiometers from  $120^\circ$  to  $180^\circ$  of incidence angle and I used blackbody-type foam for hot source. An example of calibration results is depicted on Figure-3.5. This procedure was repeated as often as possible, weather permitting. Only clear sky measurements were conducted otherwise sky reference temperature would be biased by cloud contributions to brightness temperature (Matzler, 1992).

May 6th 2004, SBR Calibration

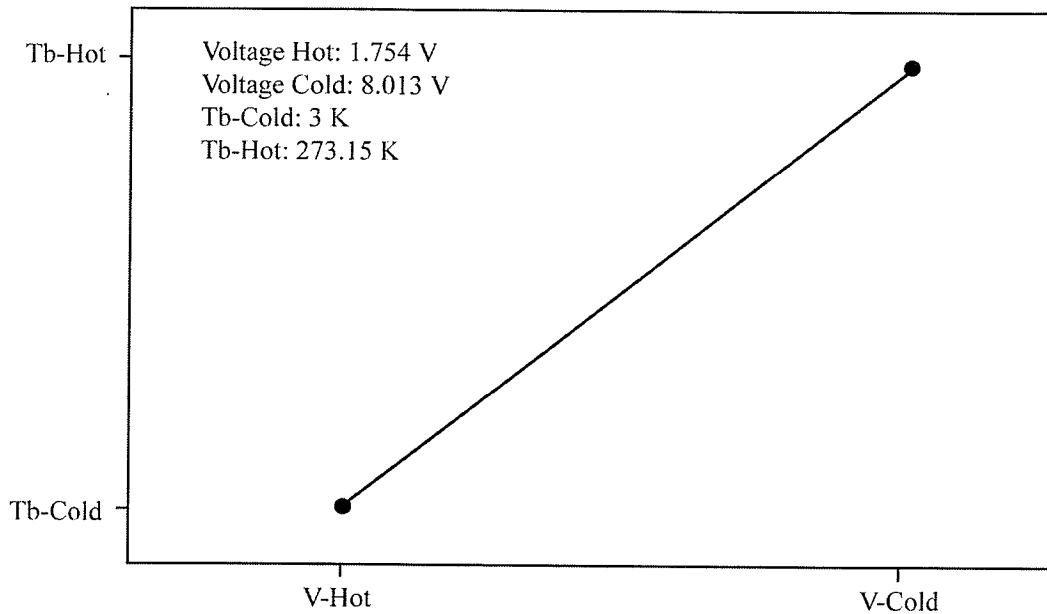


**Figure-3.5:** Surface Based Radiometer calibration results for May 6<sup>th</sup> 2004.

The SBR was mounted in a protected shed on the port side of the ship at a height of 12 to 13 m (Figure-3.6). Due to the fixed location of the ship and various snow events (heavy snowfalls, wind redistribution etc.), thin snow was located near the ship in the incidence angle range of 30° to 40° (footprint of 4 x 4 m at 30°), whereas thicker snowpacks were in the range of 50° to 70° (footprint of 30 x 30 m at 70°) as depicted in Figure-3.7. Diurnal effects were minimal since all measurements were taken during the winter period where the diurnal influence on the brightness temperatures is minimal (Drobot and Barber, 1998).

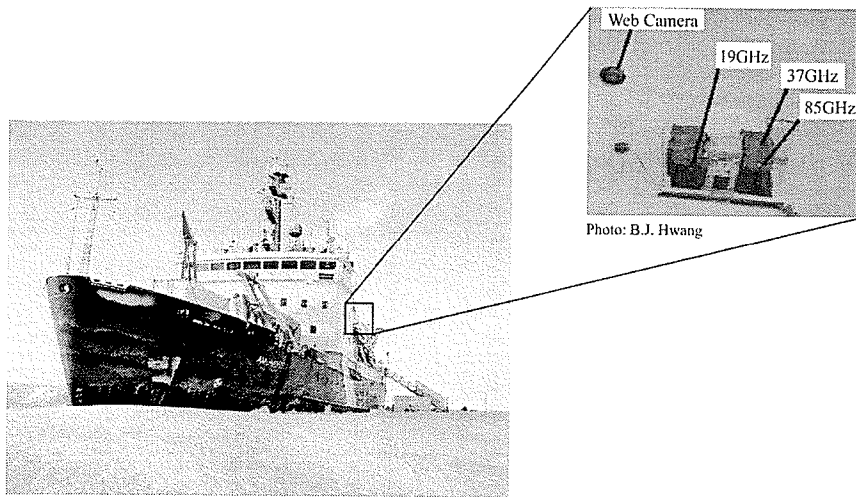


**Figure-3.6:** Surface based radiometer (SBR) mounted on the C.C.G.S. Amundsen.

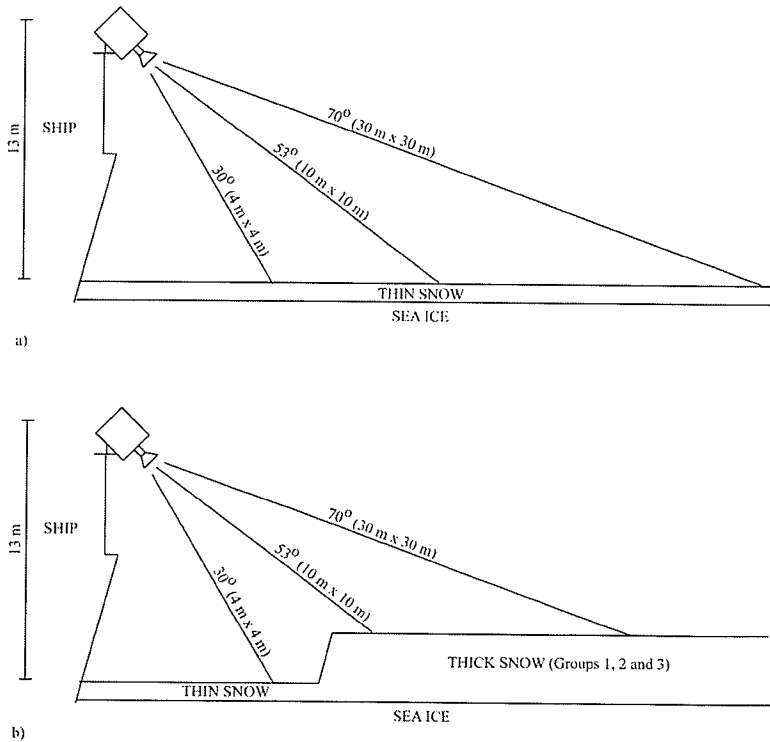


**Figure-3.7:** Surface based Radiometer (SBR) measurements geometry before a) and after b) day 6.

Since the SBR was in a fixed location, the field of view was restricted to certain snow thickness depending on incidence angle. Table-3.1 provides the snow thickness evolution at each incidence angle.

**Table-3.1:** Snow thickness temporal evolution for SBR incidence angles between 30 and 70°.

Incidence angle	Day of Year Periods			
	344-5	5-42	42-91	91-127
30	< 10 cm	< 10 cm	< 10 cm	< 10 cm
35	< 10 cm	< 10 cm	< 10 cm	< 10 cm
40	< 10 cm	< 10 cm	< 10 cm	< 10 cm
45	< 10 cm	Between Thin and Thick, not constant within SBR pixel		
50	< 10 cm	10 - 17 cm	26 - 34 cm	45 - 80 cm
53	< 10 cm	10 - 17 cm	26 - 34 cm	45 - 80 cm
55	< 10 cm	10 - 17 cm	26 - 34 cm	45 - 80 cm
60	< 10 cm	10 - 17 cm	26 - 34 cm	45 - 80 cm
65	< 10 cm	10 - 17 cm	26 - 34 cm	45 - 80 cm
70	< 10 cm	10 - 17 cm	26 - 34 cm	45 - 80 cm

### 3.6.2. Satellite Based Data

Brightness temperatures,  $T_b$ , were extracted from the Advanced Microwave Scanning Radiometer for Earth Observing System (AMSR-E) at 18 and 36 GHz (used in Chapter 7). The sensor was launched on the National Aeronautics and Space Administration (NASA) Aqua satellite (polar/sun-synchronous orbit) in May of 2002. The sensor has six frequencies (6.9, 10.7, 18.7, 36.5, and 89 GHz in both horizontal and vertical polarizations) and spatial resolution varies between 5.4 km to 56 km for 89 and 6.9 GHz respectively. The total precision ranges between 0.66 to 0.68 K at 100 and 250 K respectively.

I extracted passive microwave brightness temperatures from 6 pixels (12.5 km resolution) adjacent to each other within the bay (Figure-3.8).

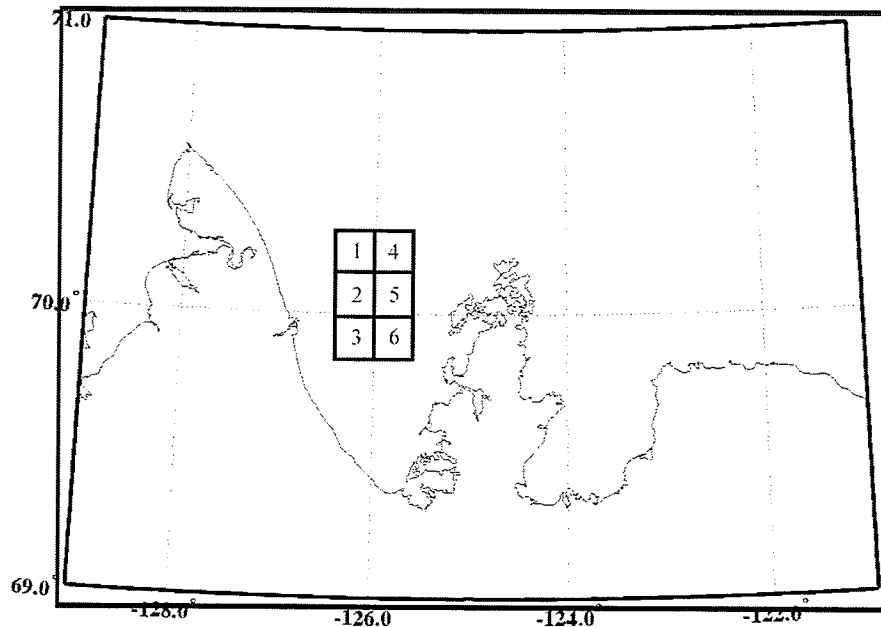


**Figure-3.8:** AMSR-E pixel location within Franklin Bay, N.W.T.

The central coordinates of these pixels are:

Pixel 1:	70.0403 N	-125.9421 W
Pixel 2:	69.9296 N	-125.9934 W
Pixel 3:	69.8190 N	-126.0442 W
Pixel 4:	70.0223 N	-125.6185 W
Pixel 5:	69.9118 N	-125.7241 W
Pixel 6:	69.8013 N	-125.7241 W

I used the daily  $T_b$  average over the ascending and descending passes since there were low diurnal variations throughout the study period. Since the SWE algorithms developed in Chapter 6 were based on SBR measurements (excluding atmospheric influences), I corrected the AMSR-E brightness temperatures with regards to atmospheric transmissivity.

### 3.6.2.1. Atmospheric Corrections

Atmospheric corrections were conducted following Matzler (1992). Optical thickness values were obtained from Matzler (1992) for Arctic regions and fall within what was measured by Hwang *et al.*, (2007) over the same region. To estimate the contribution of atmospheric temperature to the satellite, the transmissivity ( $\Upsilon_{atm}$ ) of the atmosphere needs to be calculated. The transmissivity can be derived from:

$$\Upsilon_{atm} = e^{-\tau_0 \sec \theta}, \quad [\text{eq. 3.23}]$$

where  $\tau_0$  is the optical thickness and  $\theta$  the incidence angle (e.g., Matzler, 1987; Grenfell *et al.*, 1998). Therefore, considering *in-situ* brightness temperatures ( $T_b$ ) measurements, the corresponding satellite brightness temperature ( $T_{b-SAT}$ ) corresponds to:

$$T_{b-SAT} = (T_b \cdot \Upsilon_{atm}) + (1-e) \cdot (\Upsilon_{atm} \cdot T_{atm\downarrow}) + (1-\Upsilon_{atm}) \cdot T_{atm\uparrow}, \quad [\text{eq. 3.24}]$$

where  $(1-\Upsilon_{atm}) \cdot T_{atm\uparrow}$  is the sky brightness temperature. Since the emissivity of the snow ( $e$ ) is very high, I neglected the downward  $T_{atm}$  portion that is being reflected to the satellite and through the atmosphere. Thus, the corrected brightness temperature from satellite measurements can be derived from [eq. 3.25] such that:

$$T_b = \frac{T_{b-SAT} - (1-\Upsilon_{atm})T_{atm\uparrow}}{\Upsilon_{atm}}, \quad [\text{eq. 3.25}]$$

Again, this correction needs to be applied to the satellite  $T_b$  since the SWE algorithms were developed using surface based radiometer measurements. However, the  $T_b$  contributions from clouds during the winter period are rather small and will be discussed later in Chapter 7.

### 3.6.2.2. Sea ice Roughness

Also in Chapter 7, I qualitatively investigated sea ice roughness using both passive and active microwave data. First, the polarization and gradient ratios from passive microwave measurements were analyzed in order to explore the possibility of qualifying the ‘state’ of ice roughness from AMSR-E. Active microwave data (see Section 2.4.2 below) were also used in combination with passive microwave data for investigating the potential impacts of roughness on the SWE predictions.

#### 3.6.2.2.1. Polarization Ratio (PR) and Gradient Ratio (GR)

In passive microwaves, sea ice roughness can be qualified using the polarization and gradient ratios. The brightness temperatures polarization ratio (PR) is given such that:

$$PR = \frac{T_bV - T_bH}{T_bV + T_bH}, \text{ for 18 GHz} \quad [\text{eq. 3.26}]$$

where  $T_bV$  and  $T_bH$  are the brightness temperatures in the vertical (v-pol) and horizontal (h-pol) polarizations respectively. The brightness temperature gradient ratio (GR) uses two different frequencies such that:

$$GR = \frac{T_bV_{f1} - T_bV_{f2}}{T_bV_{f1} + T_bV_{f2}}, \text{ where } f1 > f2 \quad [\text{eq. 3.27}]$$

One of the main advantages in using brightness temperature ratios is that they are independent from ice temperature (Cavalieri *et al.*, 1984; Mäkyinen and Hallikainen, 2005). Previous work by Mäkyinen and Hallikainen, (2005) had success distinguishing rough ice from new ice using both ratios. For the purpose of this study, I used 18 and 36 GHz for the GR in the vertical polarization since the largest impact of ice roughness on brightness temperatures have been measured at these frequencies over dry snow.

#### 3.6.2.2.2. Active Microwave Backscattering Coefficient

A total of 36 ScanSAR Wide-B low-resolution images over the study site were analyzed between December 24<sup>th</sup> 2003 and April 30<sup>th</sup> 2004. No earlier dates were chosen because it was obvious in the imagery that the ice had not yet consolidated and ice dynamics and open water were influencing backscatter more than surface roughness. Furthermore, images taken on day 358 and 3 showed areas of open water that influenced relative backscatter measurements (open water in Figures-3.9a and smooth ice on Figure-3.9b). Areas of high backscattering are represented in yellow, whereas low backscattering values are in blue.

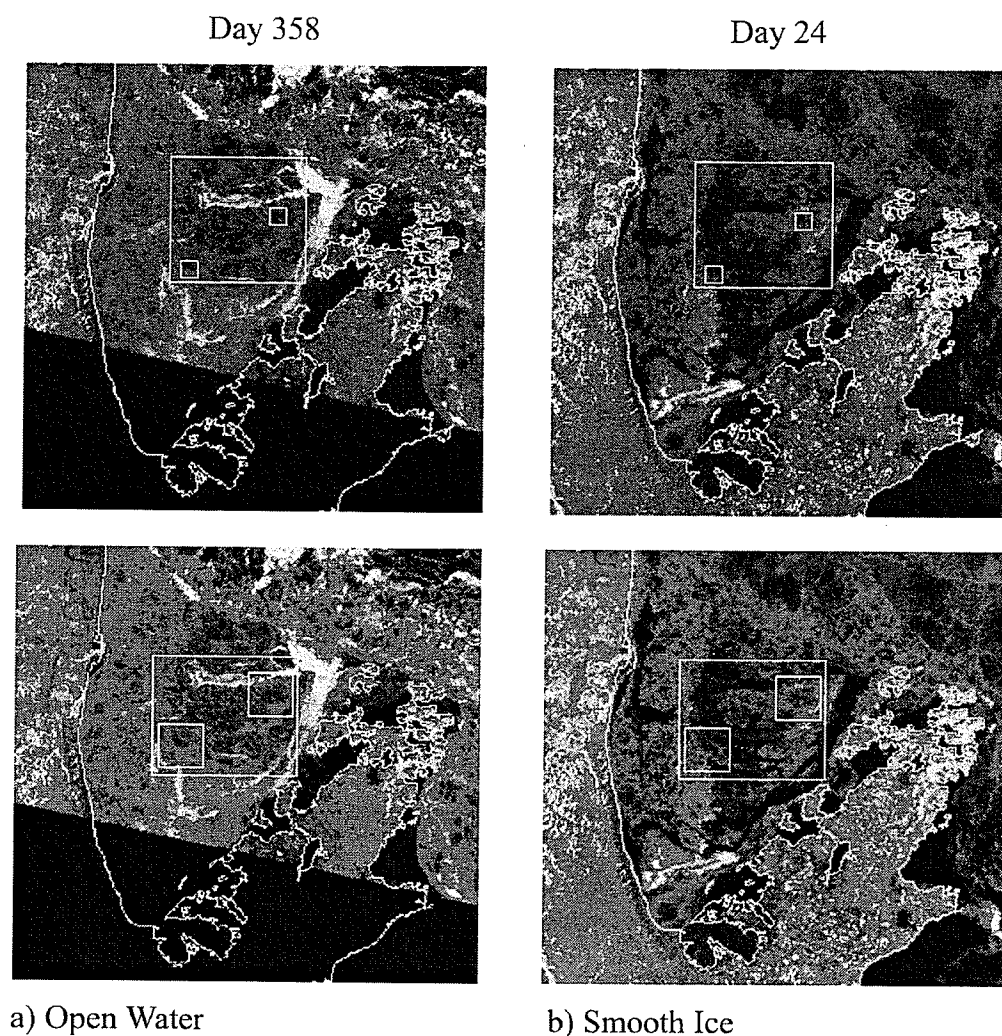


**Figure-3.9:** ScanSAR images taken on a) day 358 and b) day 24. The top two images are at 6 km resolution, and the bottom two at 11.6 km resolution.

Only ascending RADARSAT-1 passes (approximately 2:00 UTC) were used for between-scene consistency. The local incidence angle varied during the time series between approximately 25 and 45°. A 15-by-15 and 29-by-29 pixel windows (i.e., small white box in Figure-3.9) were centered over each of  $p_{Min}$  (pixel with minimum averaged  $T_b$ ) and  $p_{Max}$  (pixel with maximum averaged  $T_b$ ) and mean, calibrated microwave backscatter coefficient ( $\sigma^0$ ) values were

extracted at each date. A measure of within-scene relative  $\sigma^\circ$  for both pixels was acquired at each date by standardizing  $\sigma^\circ$  relative to the mean and standard deviation of  $\sigma^\circ$  (i.e., z-scores) from a larger, 90 by 80 pixels, window centered over landfast-FYI in the region (i.e., see large white box in Figure-3.9). Relative  $\sigma^\circ$  measures provided an indication of roughness-induced scattering from the ice surface (i.e., at C-band SAR frequency) for p\_Min and p\_Max without between-scene ambiguities associated with incidence angle variation. Images taken on day 358 and 3 showed areas indicative of wind-roughened open water that influenced relative backscatter measurements (open water in Figures-3.9a and smooth ice on Figure-3.9b).

### **3.7. Summary**

In this chapter, I described methods pertaining to snow sampling techniques, dielectric modeling and instrumentation. The snow dataset represents the core of my dissertation's work and the detailed temporal evolution analysis of the thermophysical and electrical properties follows in Chapter 4. Chapter 3 also described the passive microwave brightness temperatures data collection from the SBR so as to understand the seasonal and diurnal linkages between snow properties and passive microwaves (Chapter 4 and 5 respectively). I use these data to develop the SWE algorithms in Chapter 6 and satellite applications explored in Chapter 7.

## CHAPTER 4: SEASONAL TIME SCALES

In Chapter 2, I identified the theoretical linkages between snow properties and passive microwave brightness temperatures throughout the fall, winter and spring seasons. I noted that different processes occur throughout the season, with a focus on the winter period that was previously thought to be relatively stable thermodynamically. Hence, in this chapter, I provide field results (see Chapter 3 for details on sampling and study site) on the seasonal variations in winter snow thermophysical/electrical properties and passive microwave brightness temperatures for thin and thick snow covers. I first estate the evolution of snow thickness throughout the study period in Section 4.1 from the sampling scheme described previously in Chapter 3. I then assess in detail the temporal evolution of these properties during the winter cooling and warming periods (Sections 4.2 and 4.3 respectively), whereas discussion and conclusions follow in Section 4.4 and 4.5 respectively. The results presented in this Chapter have been published in the peer review literature in Langlois *et al.*, (2007a and b) and Langlois and Barber, 2007a.

### 4.1. Snow Thickness and Air Temperatures Evolution

Snow depth at the thin snow sampling site varied only a small amount over the course of the study period (6-7 cm between days 343 and 127, Figure-4.1 a). The thick snow site however showed a stepwise increase due to depositional events. Three major snow events, due to snowfall and/or redistribution, occurred during the overwintering period (days 5, 42 and 91), and are circled in Figure-4.1 b. These snow events lead to the delineation of 3 different thickness groups (16-17 cm, 26-34 cm and 64-77 cm) used in the analysis for thick snowpacks (see Chapter 3). The first group included 4 layers (L1 to L4) until the first snow accumulation that added two

layers (L5 and L6) on day 42. Finally, one last depositional event added two more layers (L7 and L8) on day 91 (Figure-4.1 b). Air temperature from the meteorological station aboard the ship was our marker for the temporal analysis. I separated the overwinter mission into two thermal regimes: the cooling period (Section 4.2) and the warming period (Section 4.3) separated by the coldest day (minimum air temperature was recorded at the Automated Voluntary Observation Ship (AVOS) station).

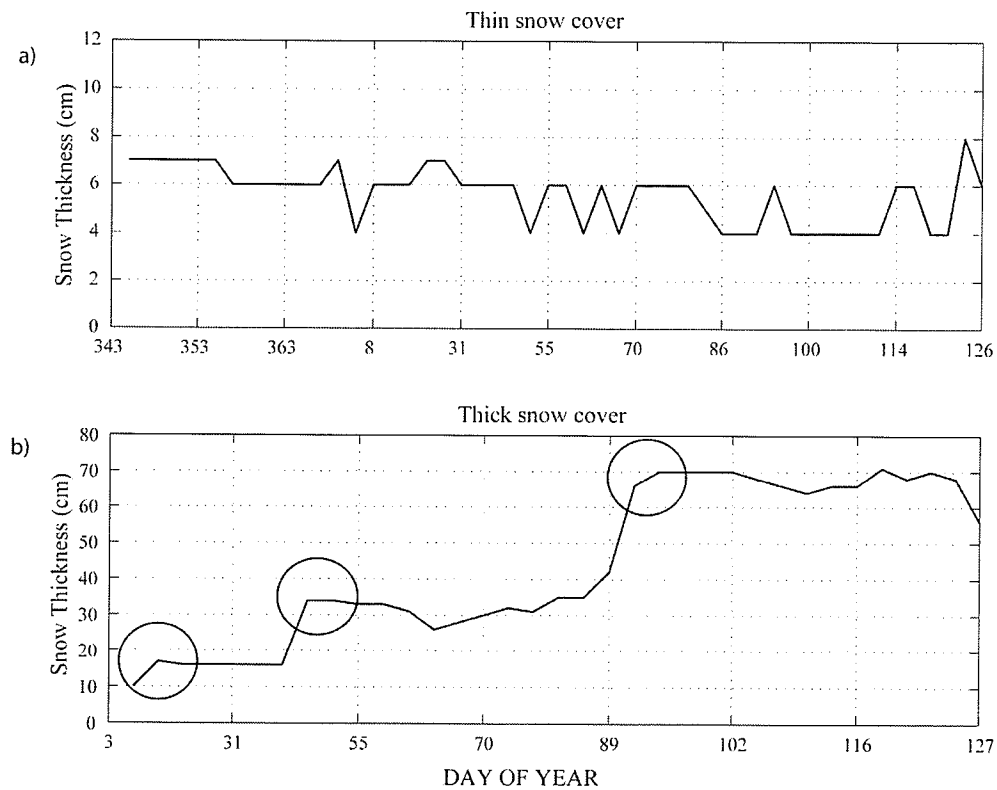


**Figure-4.1:** Temporal evolution of snow thickness at a) thin snow and b) thick snow sites.

## 4.2. Cooling Period

### 4.2.1. Meteorological Observations, Vapor Pressure and Energy Fluxes

The cooling period from day 343 to day 59 was variable with a maximum temperature of  $-11.2$  °C measured on day 5 (Figure-4.2 a). A marked decrease was observed between day 5 and 9 where the temperature dropped to  $-32.6$  °C and stayed relatively cold until the minimum measured on day 59. Wind speeds had a significant impact on snow thickness throughout the period (Figure-4.2 b). The second snow accumulation at the thick snow site event occurred on day 42 where winds reached a daily average of  $10 \text{ m}\cdot\text{s}^{-1}$  (sufficient for saltation, see Chapter 2, Section 2.5.3) between day 38 and 42 (Figure-4.2 b). Cloud amount was highly variable during the cooling period with values oscillating daily between 0 and 8 (Figure-4.2 c).

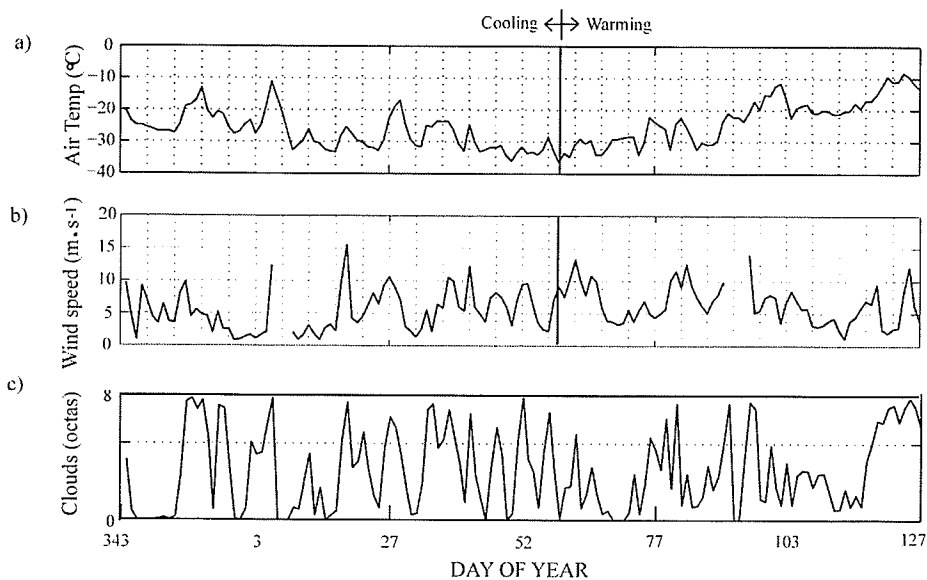


**Figure-4.2:** Temporal evolution of daily averaged a) air temperature, b) wind speed and c) cloud amount.

The vapor pressure of thin snowpacks was relatively high at the beginning of the cooling period where the temperatures were warmer (Figure-4.3 a). Values were higher at the bottom of the snowpack with a maximum of 0.3 kPa. Two marked increases occurred between days 350 to 360 and 5 to 10 (Figure-4.3 a). Due to the later start date of the thick snowpack time series; the vapor pressure was relatively stable during the cooling period where values varied between 0.150 kPa for L1 to 0.1 kPa for L2 to L4 (Figure-4.3 b).

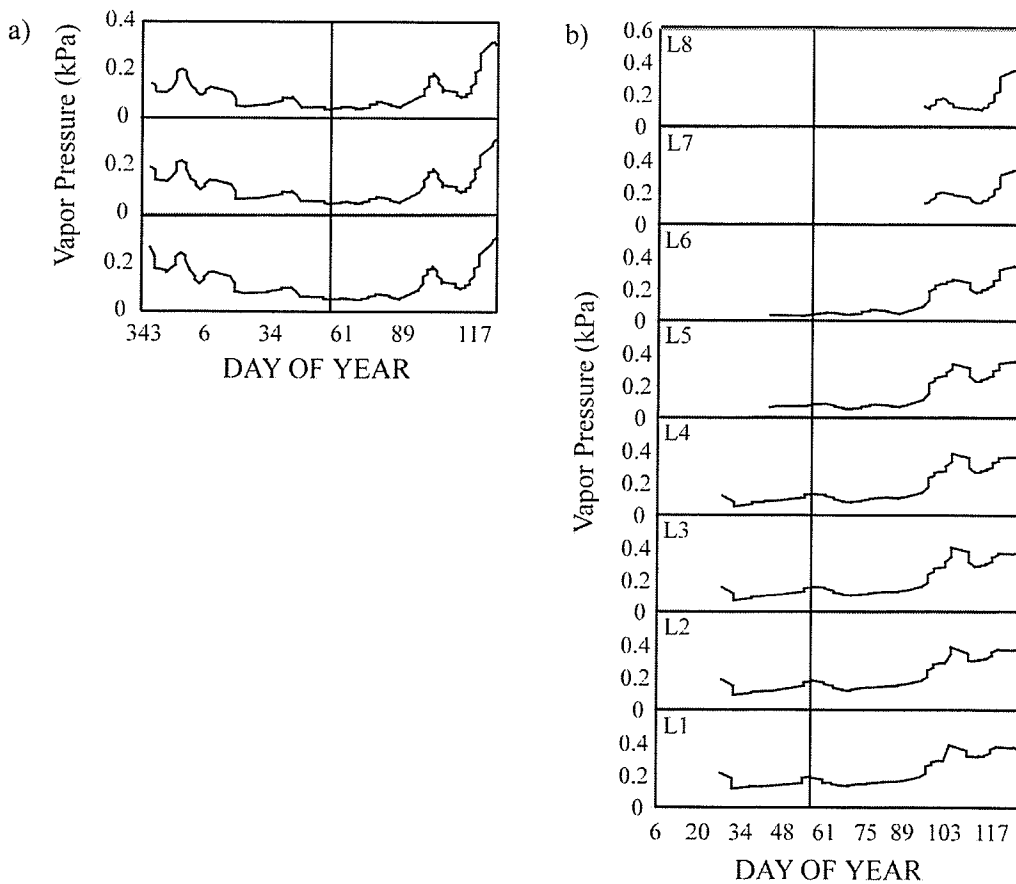


**Figure-4.3:** Temporal evolution of vapor pressure for a) thin and b) thick snow covers.

The daily averaged net radiation ( $Q^*$ ) was highly variable with values varying between 0 and  $-50 \text{ W}\cdot\text{m}^{-2}$ , hence no significant trend was observed (Figure-4.4 a). Daily averaged downwelling (Figure-4.4 b) and upwelling (Figure-4.4 c) shortwave radiation measurements ( $K\downarrow$  and  $K\uparrow$ ) were very low during the cooling period. However, values increased with a maximum of  $100 \text{ W}\cdot\text{m}^{-2}$  on day 58. Downwelling longwave radiation (Figure-4.4 d) measurements ( $L\downarrow$ ) were highly variable during the cooling period reaching a minimum daily average of approximately  $130 \text{ W}\cdot\text{m}^{-2}$  on day 31. Upwelling longwave radiation ( $L\uparrow$ ) demonstrated less daily variation throughout this period averaging approximately  $200 \text{ W}\cdot\text{m}^{-2}$  (Figure-4.4 e).

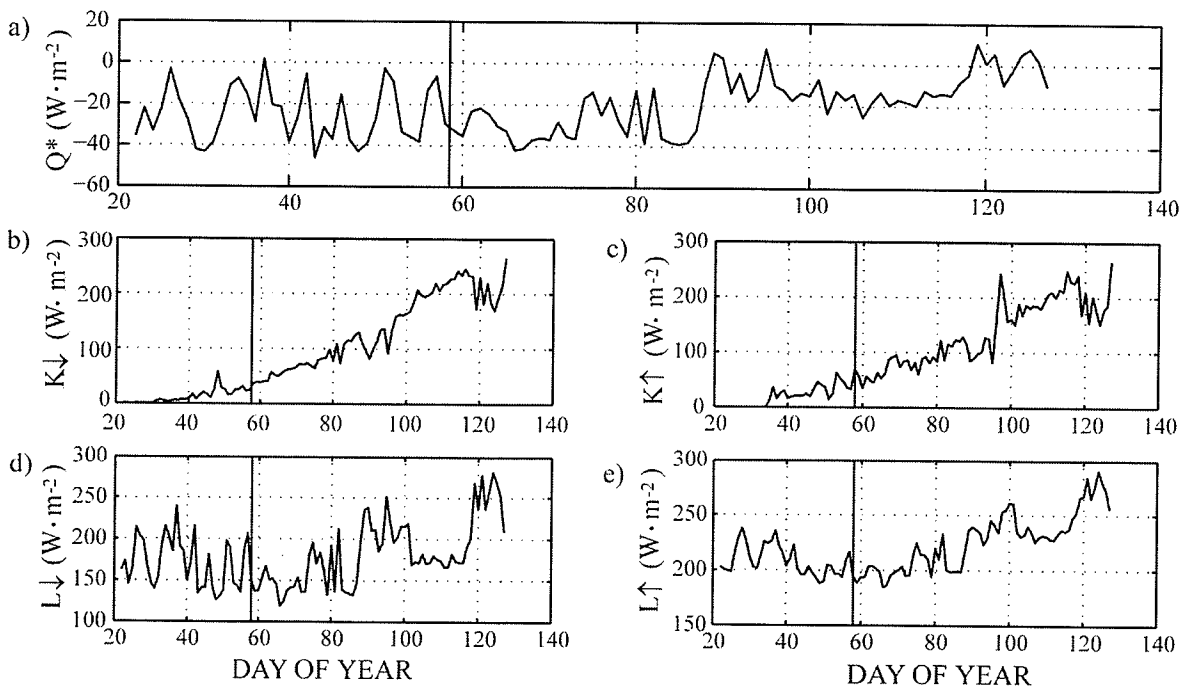


**Figure-4.4:** Temporal evolution of daily averaged a) net, b) downwelling shortwave, c) upwelling shortwave, d) downwelling longwave and e) upwelling longwave radiation.

## 4.2.2. *Snow*

### 4.2.2.1. Thin Snow

#### 4.2.2.1.1. Physical Properties

Snow grain size remained practically unchanged between days 348 and 34 (Figure-4.5 a). A small decrease was noticed between days 34 and 59 where the size reached a minimum for top, middle and bottom layers. Higher values were measured at the bottom layer with grain size varying between 2 and 4 mm<sup>2</sup>. Grain size in the middle and top layers varied between 1 and 2.5 mm<sup>2</sup>. Snow grains ratio (major/minor axis ratio) did not noticeably change for the top layer (Figure-4.5 b). Values in the bottom layer increased during the start of the cooling period, then leveled off following day 25 (Figure-4.5 b). Grain shape in the middle layer was stable throughout the cooling period, whereas in the top layer, the ratio tended to increase, although not significantly.

Snow density values increased between day 343 and 20 where the maximum was reached for the cooling period in the middle and top layers at approximately 350 kg·m<sup>-3</sup> (Figure-4.5 c). A decrease was then measured until day 34 to approximately 250 kg·m<sup>-3</sup> for both layers. The bottom layer density values did not follow any significant trend during the cooling period oscillating around 250 kg·m<sup>-3</sup>. Maximum temperatures were measured on day 357 at -10 °C, -10.1 °C and -9.2 °C for the top, middle and bottom layers, respectively (Figure-4.5 d). Minimum temperatures were recorded on day 59 with values of -30.2 °C, -28.6 °C and -26.1 °C, marking the delineation between the cooling and warming period.

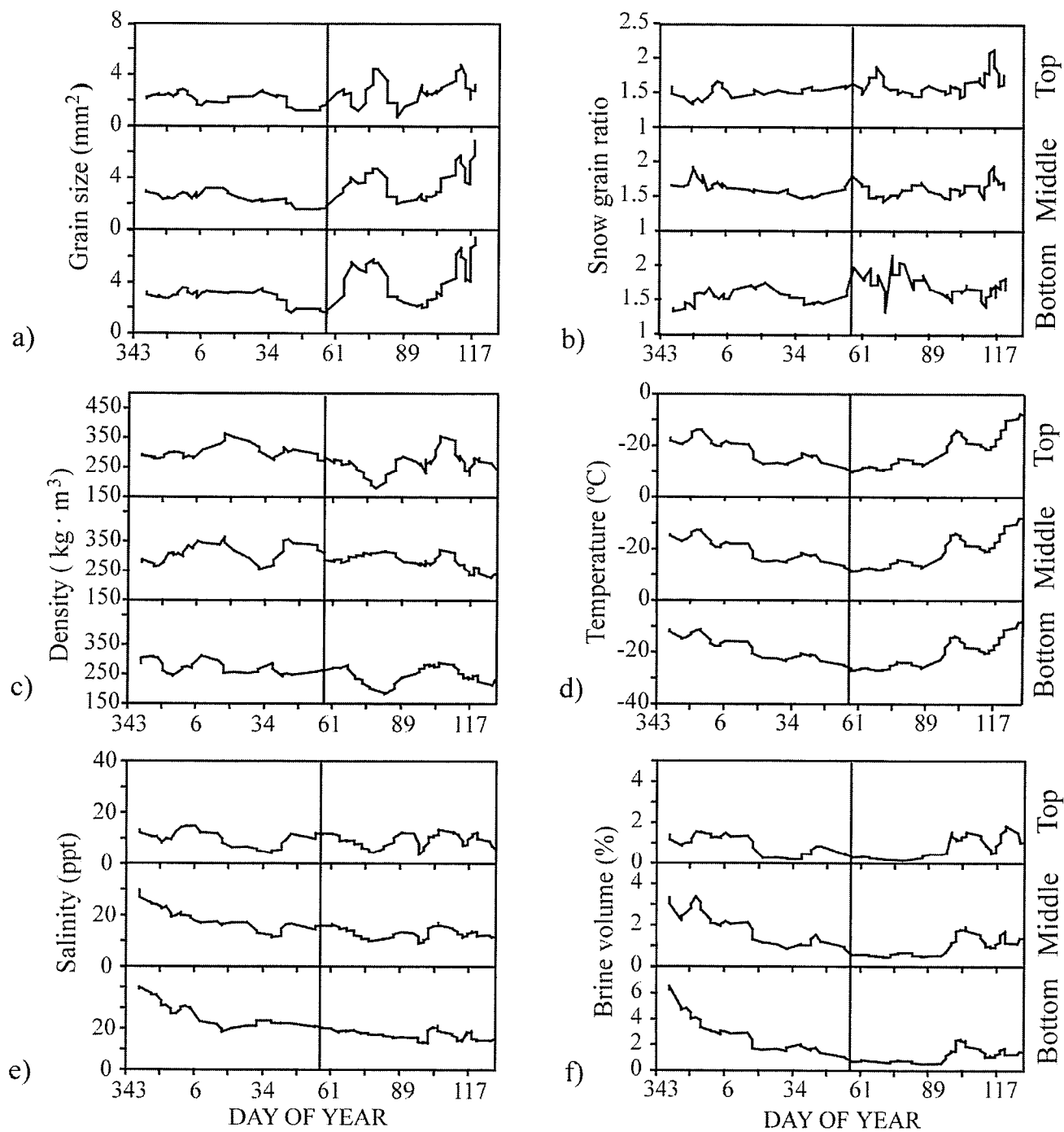


**Figure-4.5:** Temporal evolution of snow a) grain size, b) grain ratio, c) density, d) temperature, e) salinity and f) brine volume for thin snow covers.

A decrease in salinity was observed throughout the cooling period for the middle and bottom layers (Figure-4.5 e). Minimum values were measured between days 31 and 37 for the middle layer, while they were observed between days 17 and 20 for the bottom layer. Brine volume (%) also decreased until day 59 (Figure-4.5 f). However, brine volume reached a peak on around day 360 at the top and middle layers.

#### 4.2.2.1.2. Electrical Properties

The cooling period was characterized by high permittivity values at the middle layer, however these values decreased towards day 59 (Figure-4.6 a). The highest values were calculated around day 31 (near 1.8 for 19 GHz) and the lowest values modeled around day 15 (below 1.4 at all frequencies). However, the differences between 19, 37 and 85 GHz were rather small. Data were not available to determine any significant trend with regards to thin snow. Modeled dielectric loss showed the highest values in the bottom layer just below 0.24 (Figure-4.6 b). The middle layer values stayed below 0.08 so did the top layer with the exception of day 37. Overall, dielectric loss values were higher at 19 GHz when compared to 37 and 85 GHz.

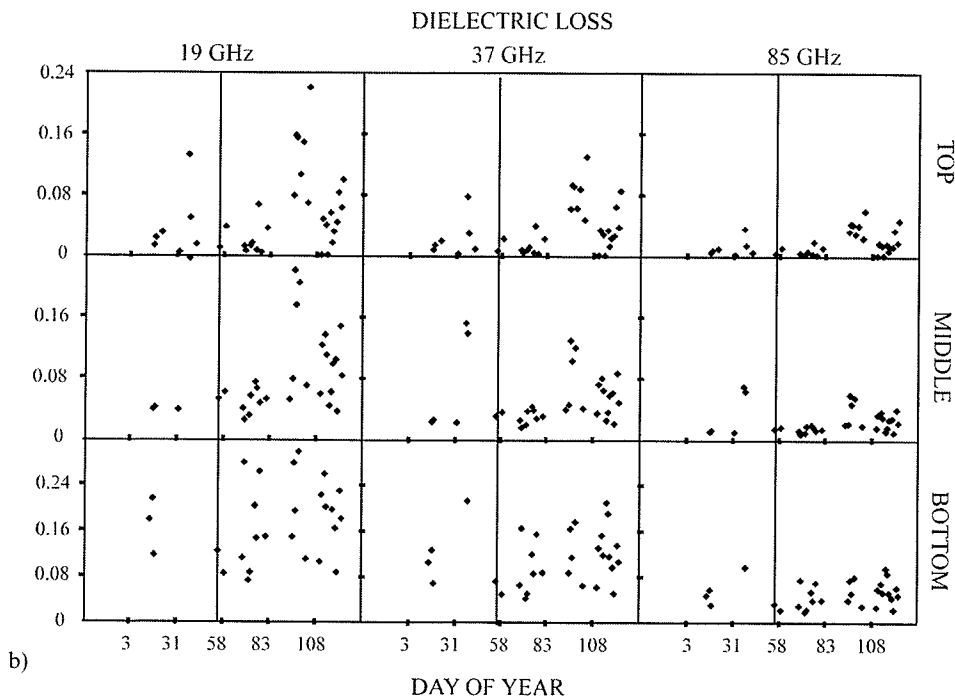
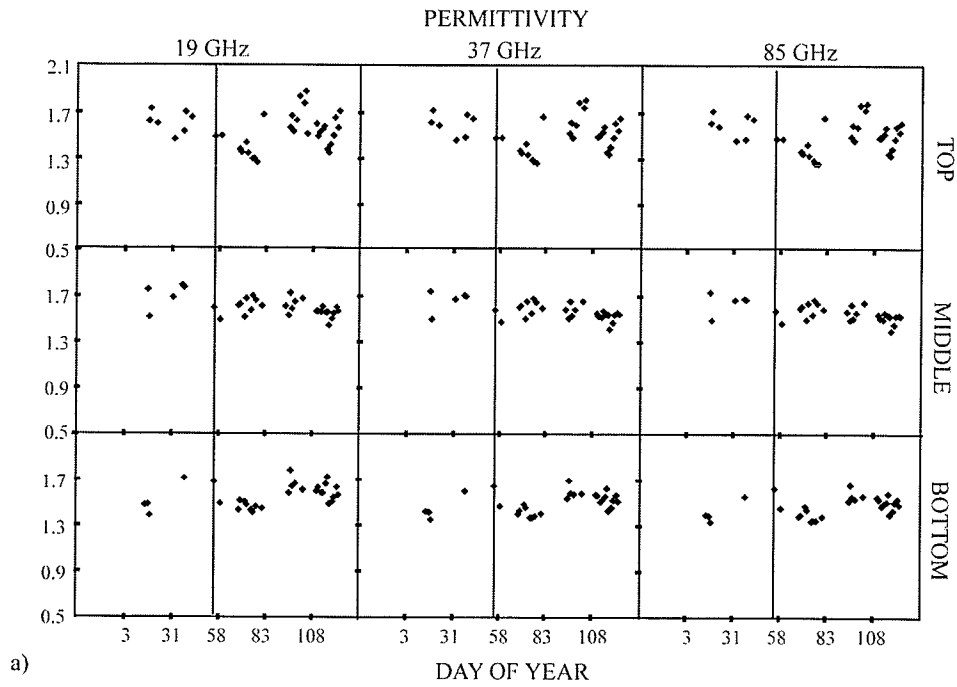


**Figure-4.6:** Temporal evolution of a) permittivity and b) dielectric loss for 19, 37 and 85 GHz for thin snow covers.

#### 4.2.2.2. Thick Snow

##### 4.2.2.2.1. Physical Properties

Snow grain size was unchanged for layer L1 to L4 throughout the cooling period (Figure-4.7 a). When layers L5 and L6 were deposited on day 42, the grain size remained stable at all layers until day 59 with grain size values of 2 mm<sup>2</sup> for L1 and 0.5 mm<sup>2</sup> for L6 on average. The snow grain ratio did not change during the cooling period for layers L1 to L4 (Figure-4.7 b).

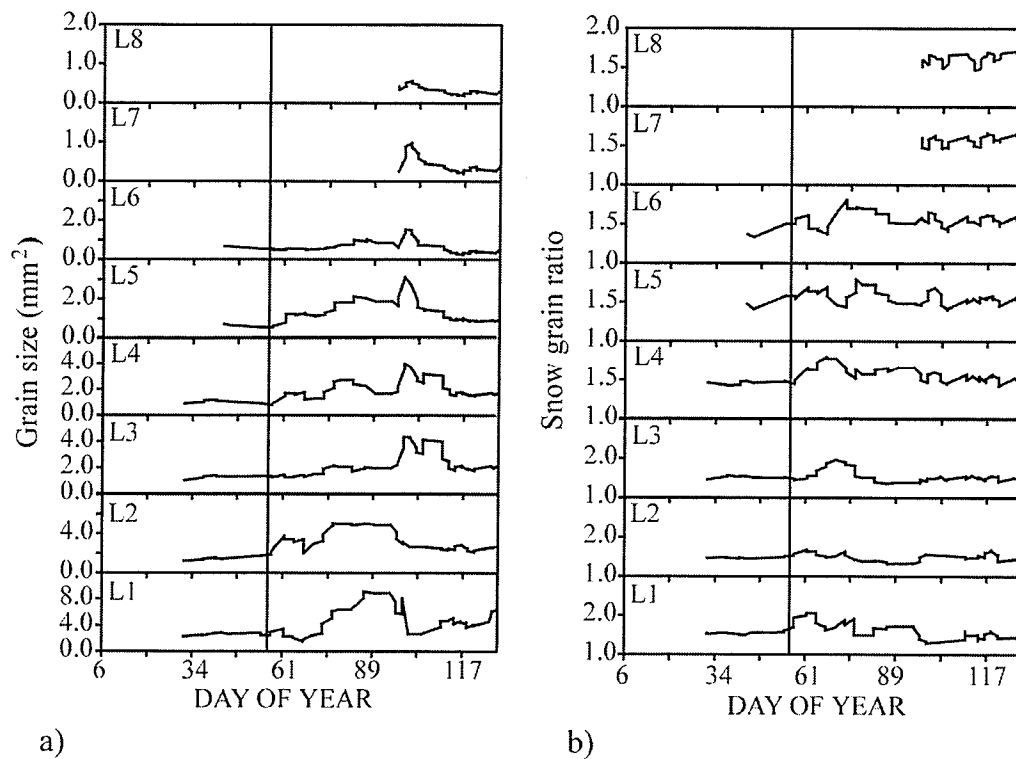


**Figure-4.7:** Temporal evolution of snow grain a) size and b) ratio (major axis/minor axis) for thick snow covers.

Snow density was also unchanged for layers L1 to L4 during the cooling period (Figure-4.8 a). Values varied between  $300 \text{ kg}\cdot\text{m}^{-3}$ ,  $350 \text{ kg}\cdot\text{m}^{-3}$  and  $225 \text{ kg}\cdot\text{m}^{-3}$  for L1, L4 and L6, respectively. The temperature remained stable throughout the vertical profile with values varying between  $-18^\circ\text{C}$  and  $-25^\circ\text{C}$  for L1 and L6 (Figure-4.8 b).

Salinity, on average, increased between day 42 and 59 for L1, L2 and L3 when L5 and L6 were deposited (Figure-4.9 a). Brine volume decreased for the first half of the cooling period at L1 with a minimum value approaching 1 %. Values increased afterwards until day 59. Brine volume increased slightly at L2 and L3, but was relatively stable at L4 to L6 with values below 0.25 % (Figure-4.9 b).

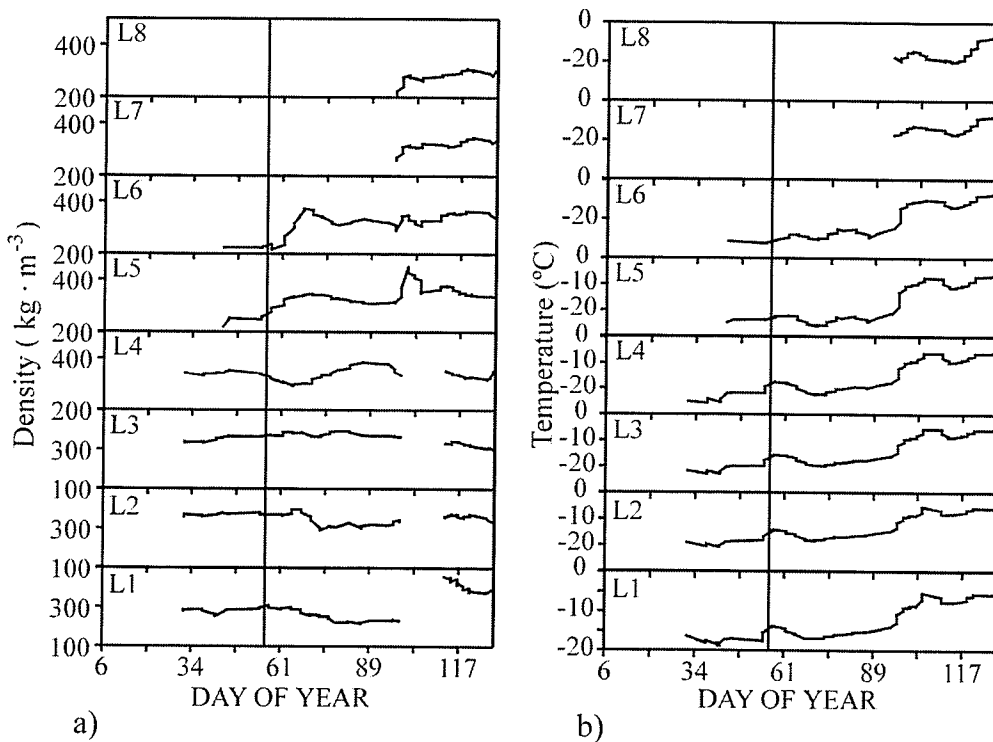


**Figure-4.8:** Temporal evolution of snow a) density and b) temperature for thick snow covers.

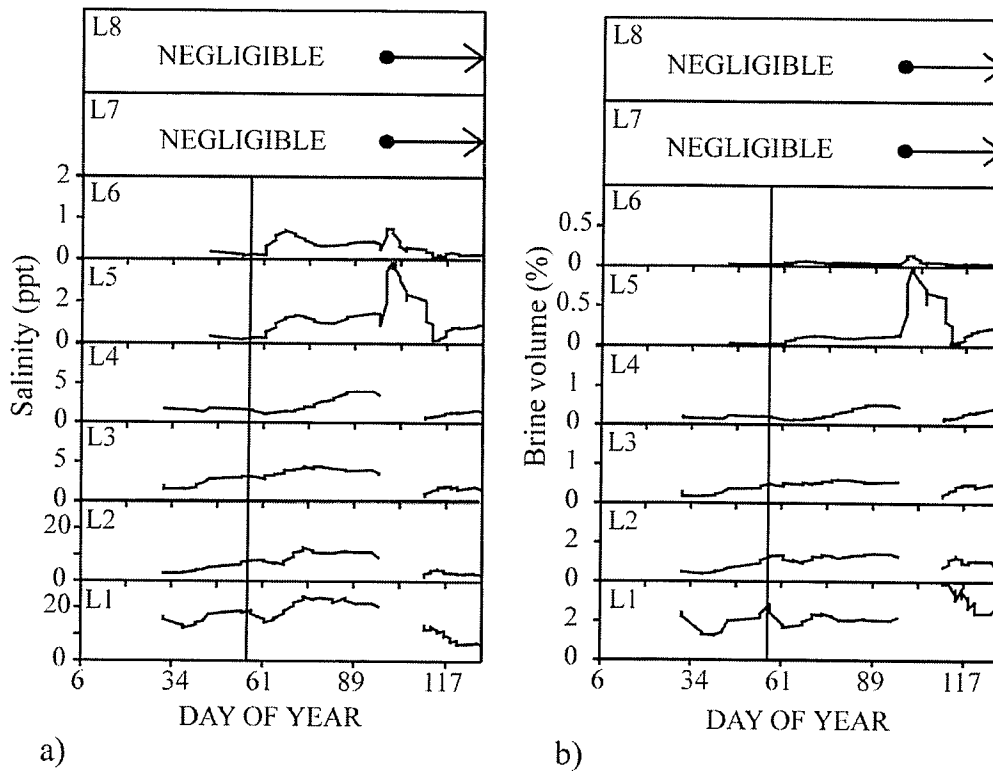


**Figure-4.9:** Temporal evolution of snow a) salinity and b) brine volume for thick snow covers.

#### 4.2.2.2.2. Electrical Properties

Very limited permittivity and dielectric loss data were available through the cooling period for thick snow covers (Figure-4.10 a). However, the highest permittivity values were modeled at L3 (varying around 1.7) and the lowest values at L5 (varying around 1.4) for all three frequencies. Three individual samples were modeled after day 110 for L1 and their permittivity values were highest (between 1.7 and 1.9). Dielectric loss was higher towards the bottom of the snowpack throughout the cooling period (Figure-4.10 b).

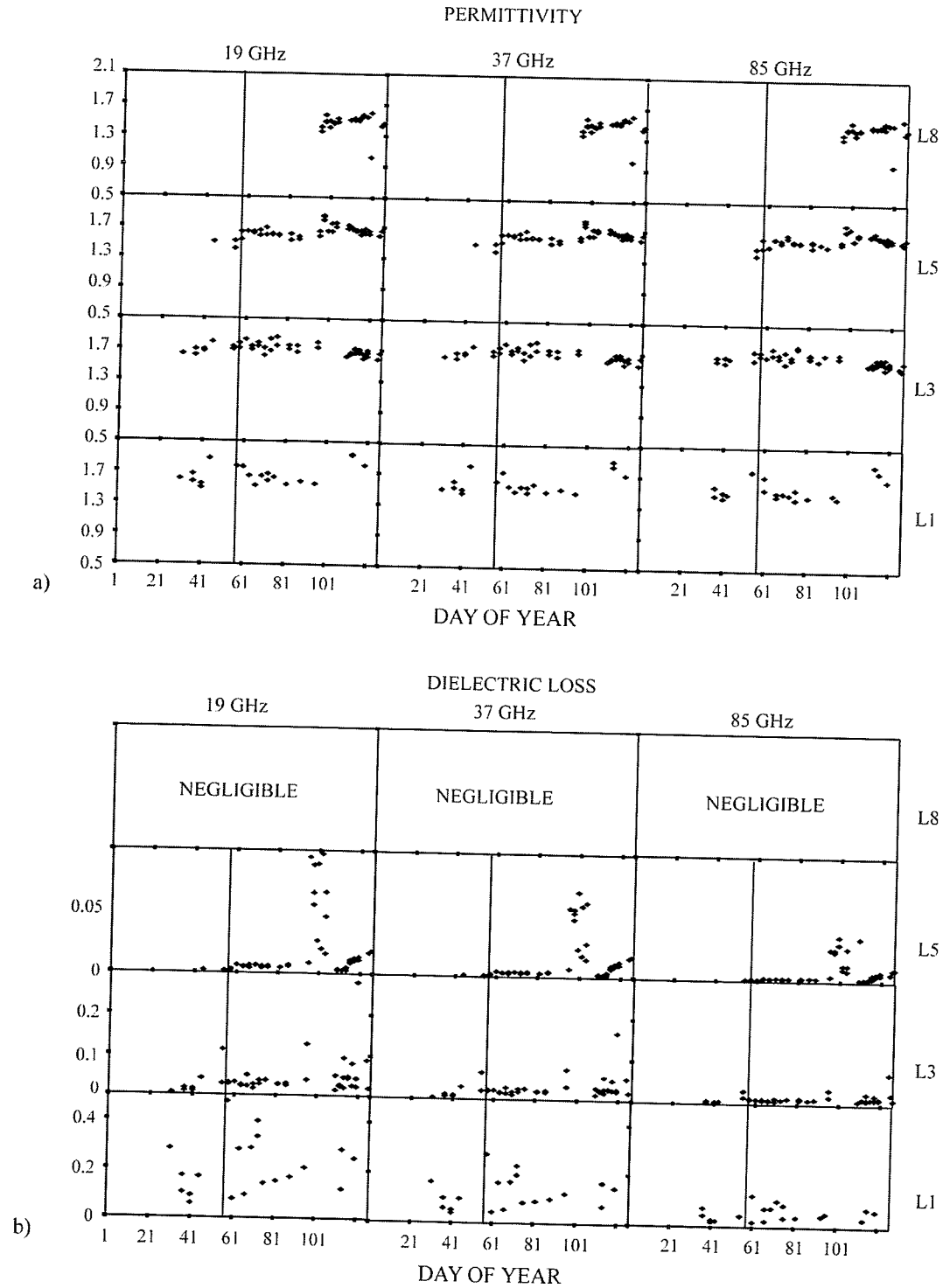


**Figure-4.10:** Temporal evolution of a) permittivity and b) dielectric loss for 19, 37 and 85 GHz for thick snow covers.

### 4.2.3. In-Situ Passive Microwaves

#### 4.2.3.1. Thin (30° - 40°)

As mentioned in Chapter 3, thin snow was measured at low incidence angles (30 to 40°). Brightness temperatures ( $T_b$ ) decreased slightly during the cooling period (day 344 – 57) for all frequencies between 30° and 40° where values ranged between 240 K and 260 K (Figure-4.11 a and b).

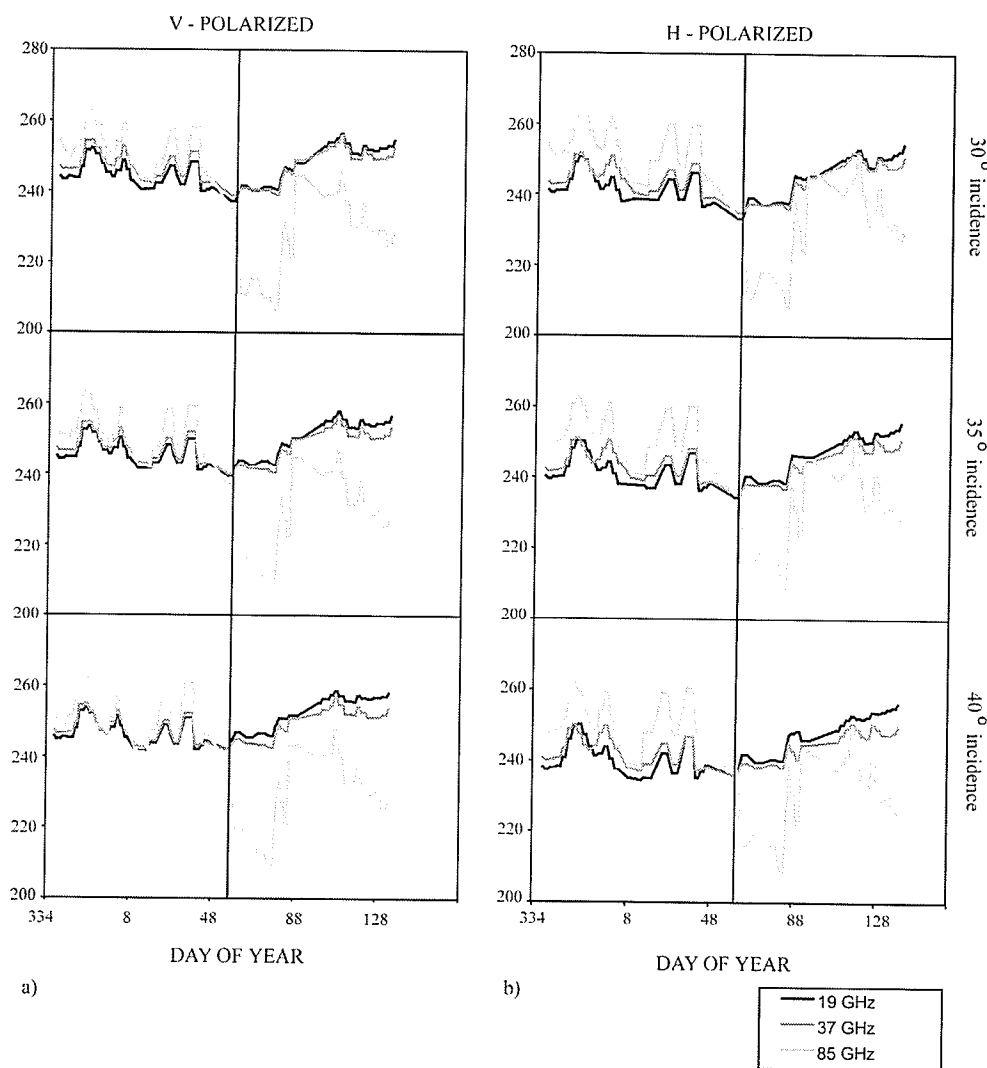


**Figure-4.11:** Temporal evolution of brightness temperatures the a) vertical and b) horizontal polarizations at 19, 37 and 85 GHz over thin snow covers.

From the figure above, I noticed that 85 GHz  $T_b$  were sometimes higher than 19 and 37 GHz. In the first part of the winter we had problems with 85 GHz. It appears that the SBR IF amplifier was unstable at times, in the fact where it was over- or under-amplifying. However, the amplitude of the variations (for example a decrease due to grain growth) remained unchanged since the amplification signal is linear with the resulting  $T_b$ . Maximum brightness temperatures during the cooling period were measured on day 357 for all three frequencies. Furthermore, variations in  $T_b$  were greater at 85 GHz with values oscillating between 265 K and 240 K throughout the cooling period. The difference in polarization ( $\Delta P = V - H$ ) was generally higher at low frequencies ( $\Delta P(f) \rightarrow 19 > 37 > 85$  GHz) with relatively high variability in  $\Delta P$  for 85 GHz. The lowest variations in  $\Delta P$  were measured at 37 GHz. This difference increased with increasing incidence angle ( $\Delta P(\theta) \rightarrow 40^\circ > 35^\circ > 30^\circ$ ). The minimum values in  $\Delta P$  were measured between days 1 and 15, depending on the frequency. Maximum values occurred between days 340 and 344 at 19 and 37 GHz, as well as significant increase on days 6 and 21 for 19 GHz. Both air and brightness temperatures decreased thereafter until the minimum value was achieved on day 57.

#### 4.2.3.2. Thick Snow ( $55^\circ - 70^\circ$ )

No significant trends in thick snow  $T_b$ 's were observed during the cooling period at all frequencies and incidence angles (Figure-4.12 a and b). The maximum  $T_b$ 's were measured at 85 GHz in the vertical polarization (values varying around 265 K at an incidence angle of  $50^\circ$ , Figure-4.12 a). Minimum values were recorded at 19 GHz in the horizontal polarization (values varying around 190 K at  $70^\circ$  on Figure-4.12 b). The depolarization ( $\Delta P(f)$  and  $\Delta P(\theta)$ ) were minimal for 85 GHz when compared to lower frequencies (19 and 37 GHz). The depolarization

derived from Figure-4.12 a and b was higher at wide incidence angles and increases with decreasing frequency (i.e. maximum measured  $\Delta P$  values of 31 K at 19GHz and an incidence angle of  $70^\circ$ ). Throughout the cooling period, values of  $\Delta P(f)$  and  $\Delta P(\theta)$  in thick snow covers were significantly higher than in the thin snow covers.

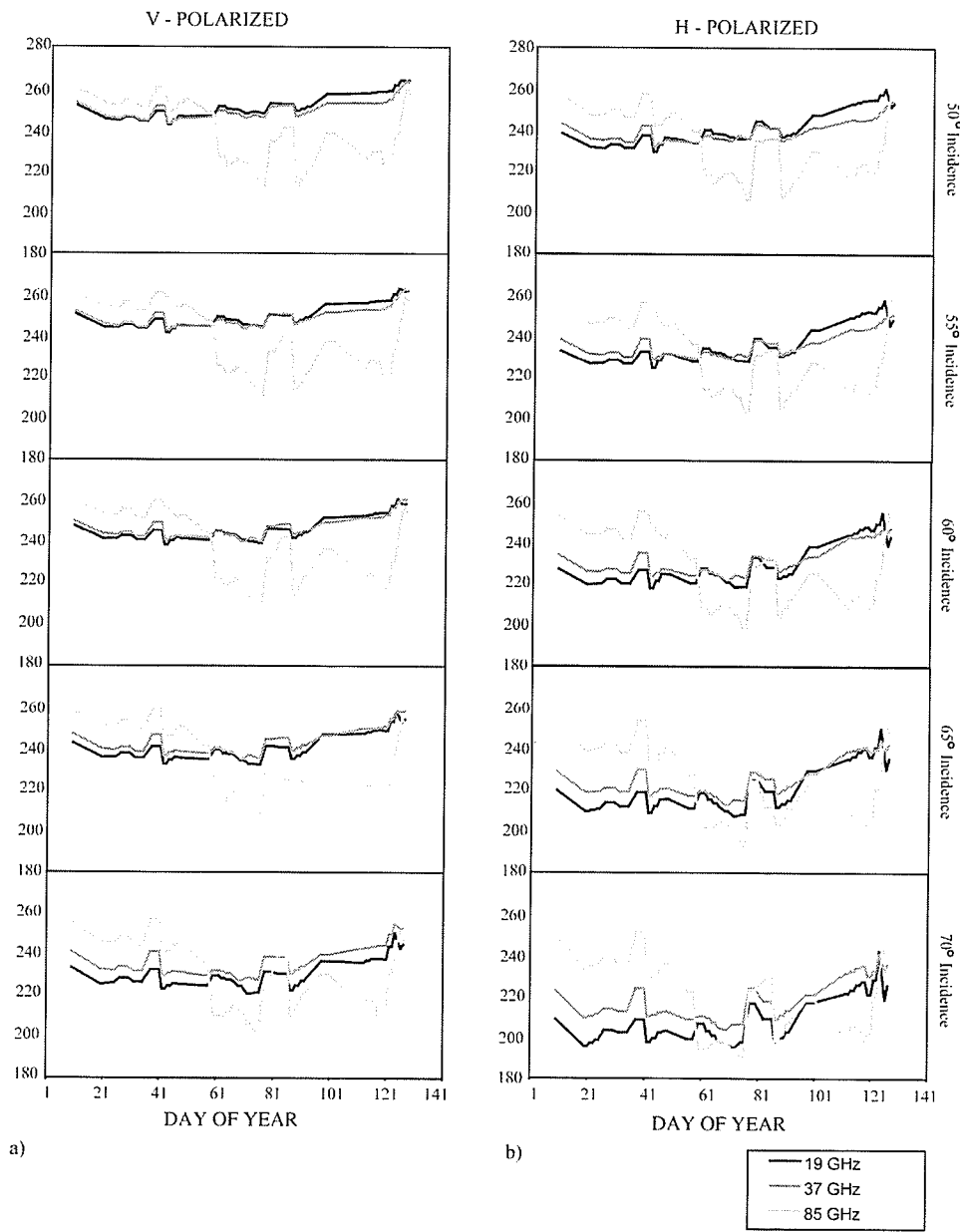


**Figure-4.12:** Temporal evolution of brightness temperatures the a) vertical and b) horizontal polarizations at 19, 37 and 85 GHz over thick snow covers.

### 4.3. Warming Period

#### 4.3.1. Meteorological Observations, Vapor Pressure and Energy Fluxes

Throughout the warming period (between day 60 and 127), the averaged daily temperature increase was  $+0.35 \text{ }^\circ\text{C}\cdot\text{day}^{-1}$  with marked increases following days 88 and 101 (Figure-4.2 a). Strong winds were recorded on days 62, 82, 84, 95 and 126 where recorded speeds were over  $10 \text{ m}\cdot\text{s}^{-1}$ . The last snow redistribution event on day 91 (Figure-4.1 b) was coincident with the strong winds measured between day 90 and 95 (Figure-4.2 b). Low cloud amounts were observed at the beginning of the warming period. However, dense overcast periods were observed between days 76-81, 91, 95 and 118-127 (Figure-4.2 c).

Vapor pressure remained stable during the warming period for thin snow until day 89 where a strong increase was observed (Figure-4.3 a). This increase continued until day 103 where values decreased until day 117 at all layers. The maximum values were measured at 0.334, 0.291 and 0.334 kPa for top, middle and bottom layers respectively. Thick snow covers values were also quite stable until day 95 until the same increase as thin snow was measured (Figure-4.3 b). The maximum values for thick snow ranged between 0.349 and 0.411 kPa from L1 to L8 respectively.

The net radiation ( $Q^*$ ) values at the beginning of the warming period were quite low averaging  $-32.8 \text{ W}\cdot\text{m}^{-2}$  between day 59 and 72 (Figure-4.4 a). A significant increase was measured between day 85 and 90 where values reached  $0 \text{ W}\cdot\text{m}^{-2}$ . The warming period was also characterized by a steady increase in shortwave radiation ( $K\downarrow$  and  $K\uparrow$ ) with maximum values over  $250 \text{ W}\cdot\text{m}^{-2}$  on day 116 and 127 (Figure-4.4 b and c). Both  $L\downarrow$  and  $L\uparrow$  increased during the warming period where maximum values near  $300 \text{ W}\cdot\text{m}^{-2}$  were reached on day 124 (Figure-4.4 d and e).

## 4.3.2. *Snow*

### 4.3.2.1. Thin Snow

#### 4.3.2.1.1. Physical Properties

Snow grain size was characterized by a marked increase at the beginning of the warming period at all three layers between day 59 and 91 (Figure-4.5 a). The rate of growth for this period was steady and highest in the bottom layer. A growth rate of  $0.03 \text{ mm}\cdot\text{day}^{-1}$  was measured in the top layer and  $0.25 \text{ mm}\cdot\text{day}^{-1}$  for the bottom layer. Therefore, the bottom layer snow grains grew about 8 times faster than near the surface where the temperature and wetness values are much lower. Inversely, the period between days 75 and 89 was marked by a significant decrease of  $-0.07 \text{ mm}^2\cdot\text{day}^{-1}$  for the top layer and  $-0.24 \text{ mm}^2\cdot\text{day}^{-1}$  and the middle layer. Snow grain ratios were more variable during the warming period (Figure-4.5 b). Values increased with increasing grain size between day 59 and 70 only for top and middle layers, and then decreased to values around 1.5 until day 103. For the bottom layer, the increase was measured between day 59 and 75 where values jumped from 1.5 to 2.0 in average, coincidentally with increasing grain size.

For the top layer, a decrease in density was measured for the first part of the warming period where values reached a minimum just over  $150 \text{ kg}\cdot\text{m}^{-3}$  around day 80 (Figure-4.5 c). Density then increased between days 78 and 103 where maximum values were just over  $350 \text{ kg}\cdot\text{m}^{-3}$ . The minimum in density occurred on day 76 as  $0.7 \text{ mm}$  of snowfall was recorded between day 59 and 76 affecting surface densities. The highest density values for all layers were observed just after day 103, which was associated with strong increases in temperature (Figure-4.2 a) and wetness (Figure-4.6 c). Volume temperatures increased significantly throughout the warming period, with

a peak on day 103 for all three layers (Figure-4.5 d). Maximum values were measured on day 125 where temperatures reached  $-10^{\circ}\text{C}$  and above at all layers.

Salinity was highly variable for the top layer with fairly low values averaging 10 ppt (Figure-4.5 e). Values decreased until day 75 for both top and middle layers as the bottom layers decreased until day 100. An increase at all layers was measured on day 103 where averaged maximum salinity values of 13 ppt, 17 ppt and 21 ppt were reached for top, middle and bottom layers, respectively. Brine volume was stable and low between day 59 and 95 (Figure-4.5 f). An increase was measured at all three layers between day 95 and day 103 where the maximum varied between 1.2 % to just over 2 %.

#### 4.3.2.1.2. Electrical Properties

During the warming period, maximum modeled values occurred in the top layer between day 100 and 103 where the permittivity reached 1.88, 1.81 and 1.79 for 19, 37 and 85 GHz respectively (Figure-4.6 a). The minimum values were recorded on day 78 for top whereas middle and bottom layers minimum permittivity occurred on days 76 and 116 respectively for all frequencies. On average, values oscillated between 1.3 and 1.9 throughout the study period for all layers and frequencies. No significant trends in dielectric loss were measured for the cooling period (Figure-4.6 b). The warming period was characterized by an increase in the middle and top layers for 19, 37 and 85 GHz respectively. A significant increase was measured on day 103 for 19 and 37 GHz where values tripled from an average of 0.04 to 0.12 (Figure-4.6 b).

#### 4.3.2.2. Thick Snow

##### 4.3.2.2.1. Physical Properties

There was a marked increase in grain size between days 59 and day 85 from layers L1 to L6 (Figure-4.7 a). Snow grain growth rate for this period was larger in the bottom layer ( $0.48 \text{ mm}\cdot\text{day}^{-1}$ ) than the top layer ( $0.02 \text{ mm}\cdot\text{day}^{-1}$ ). Snow grains tended to decrease in size in L1 and L2 after day 85, to reach a minimum on day 103. Interestingly, grain size in L3 through L6 increased after day 103. The snow grain ratio was variable at L1, but decreased towards day 127 (Figure-4.7 b). A slight increase was observed in L3 and L4 between days 59 and 70, but then values decreased until day 127 along with L5 and L6.

Snow density from L1 to L3 was stable until day 97, whereas a marked increase occurred in L5 between days 97 and 111 coincidentally with the deposition of layers L7 and L8 (Figure-4.8 a). Values increased from  $275 \text{ kg}\cdot\text{m}^{-3}$  to nearly  $400 \text{ kg}\cdot\text{m}^{-3}$ . Another increase was also observed at L4 between days 70 and 89. The same situation is observed at L5 where the increase in density between day 97 and 105 coincides with the deposition of L7 and L8. Snow temperature decreased between days 59 and 70 for L1 to L5, then increased until day 127 with a maximum value on day 103 for all layers (Figure-4.8 b).

The salinity at layers L1 to L4 increased between days 59 and 89 for L1 to L4 with values of 20 ppt and 5 ppt, respectively (Figure-4.9 a). A peak in salinity at L5 and L6 coincided with the deposition of L7 and L8. Brine volume remained stable at all layers until day 97 where a dramatic increase occurred at L5 (Figure-4.9 b). However, one should note that brine volume

data were not available from L1 through L4. Values at L1 after day 111 suggest that a significant increase occurred at that particular layer as well.

#### 4.3.2.2.2. Electrical

The warming period showed a significant increase around day 95 at L5, where values jumped from nearly 0 to about 0.09, 0.07 and 0.05 for 19, 37 and 85 GHz respectively (Figure-4.10 a). Overall, values oscillated around an average of 1.68, 1.7, and 1.65 for L1, L3 and L5 respectively for all frequencies. Near the surface, permittivity for L7 and L8 were 1.57 and 1.5 respectively. Dielectric loss values increased dramatically between days 96 and 103 (Figure-4.10 b). The increase was measured in layers L5 and L6 at all frequencies being stronger at 19 GHz. Values at 19 GHz peaked from an average of 0.005 and 0.001 to values of 0.08 and 0.007 at L5 and L6 respectively. The increase was not as strong at 37 and 85 GHz but nonetheless significant.

#### 4.3.3. *Passive Microwaves*

##### 4.3.3.1. Thin ( $30^\circ - 40^\circ$ )

During the warming period, a decrease in  $T_b$  was noticeable at 85 GHz (between days 58 and 127) where values decreased from an average of 250 K to approximately 215 K (Figure-4.11 a and b). Between day 80 and day 100,  $T_b$ 's increased from 215 K to 240 K, then decreased to an average of 230 K until the end of the sampling period for both horizontal (Figure-4.11 a) and vertical (Figure-4.11 b) polarizations. The warming period was also characterized by a significant decrease in  $\Delta P$  at 85 GHz where the average value became close to 0 between day 57

and day 127. The minimum values of  $\Delta P(f)$  occurred between days 70-80 and 110-120 and the maximum measured between day 82 and 103. The  $\Delta P$  behaved similarly to the cooling period in terms of frequency and incidence angle ( $\Delta P(f) \rightarrow 19 > 37 > 85$  GHz;  $\Delta P(\theta) \rightarrow 40^\circ > 35^\circ > 30^\circ$ ). However, the  $\Delta P(f)$  term was less obvious as 19 and 37 GHz exchanged the highest values throughout the warming period.

#### 4.3.3.2. Thick Snow ( $55^\circ - 70^\circ$ )

The warming period was characterized by a slow and steady increase in  $T_b$  for the thick snowpack at both vertical and horizontal polarizations (Figure-4.12 a and b). A significant peak was measured between day 72 and day 84 at all frequencies and angles. The depolarization decreased significantly during this period especially for 19 GHz with an incidence angle of  $70^\circ$ . Generally, the depolarization decreased throughout the warming period except for individual cases at 19 GHz between days 117 and 124.

## 4.4. Discussion

### 4.4.1. Physical Properties

#### 4.4.1.1. Thin Snow

During the cooling period, maximum density values at the top layer were reached on day 20 where winds were the strongest at  $15 \text{ m}\cdot\text{s}^{-1}$ . Wind breaks the snow crystals into rounded shaped grains creating high-density surface layers (Figure-4.5 c). This mechanical process decreases the fraction of air in the layer, therefore increasing the density (e.g., Kotlyakov, 1961; Barber *et al.*,

1995; Sturm *et al.*, 2002; Mundy *et al.*, 2005; Langlois *et al.*, 2007a). The decrease in density at top and middle layers between days 20 and 34 is associated with fresh falling snow (7.2 mm total precipitation) and low winds (average of  $2.8 \text{ m}\cdot\text{s}^{-1}$  between days 30 and day 35). The increase between day 35 and 45 is also related to strong winds that increased from an average of  $2.8 \text{ m}\cdot\text{s}^{-1}$  to  $7.8 \text{ m}\cdot\text{s}^{-1}$  between day 36 and 43.

As previously mentioned, salinity values decreased throughout the cooling period. When sea ice forms, salts are rejected from the ice matrix both towards the atmosphere and ocean through the process of segregation (e.g., Weeks and Ackley, 1986; Eicken, 2003). Therefore young snow covers over forming sea ice can have high salinity values that decrease afterwards with gravity drainage. Brine volume will respond proportionally as the cooling period evolves, further decreasing due to decreasing temperatures. However, for top and middle layers, I measured an increase in brine volume between day 348 and day 15, which was coincident with warming temperatures (Figure-4.5 d) over the same period, due to the sensitivity of brine to the colder temperatures of these upper layers (e.g., Frankenstein and Garner, 1967; Cox and Weeks, 1982). Minimum  $\delta T/\delta_L$  observations were coincident with warming temperature periods (i.e., days 357, 10 and 37) and low variation in vapor pressure layer gradient ( $\delta e_{si}/\delta_L$ ) at the bottom snow-sea ice (SI) transition (Figure-4.13 a and b).

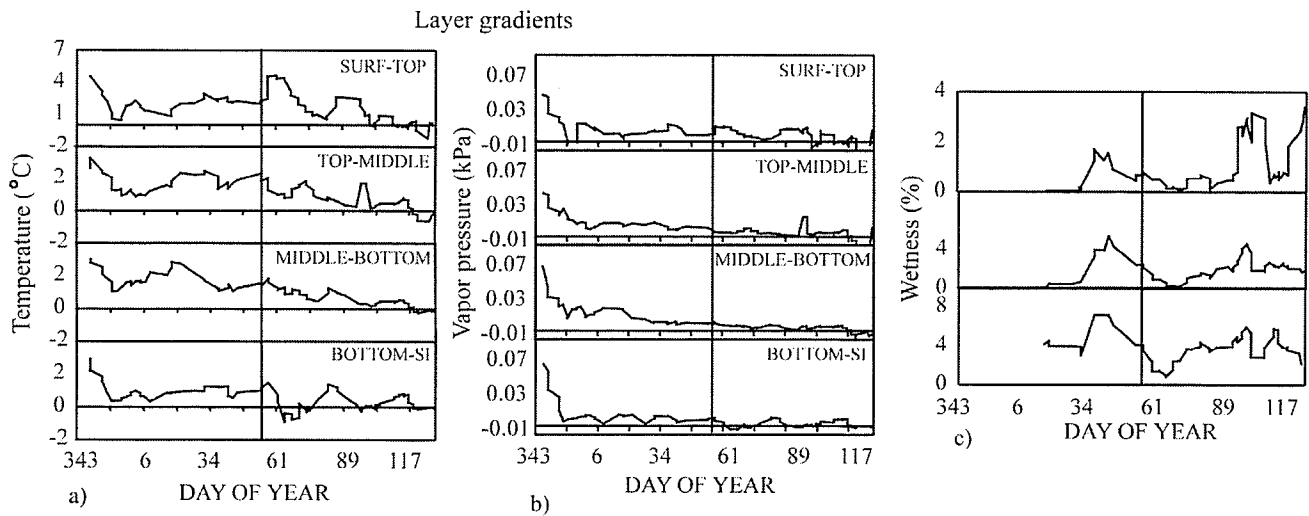


**Figure-4.13:** Temporal evolution of a) temperature gradient ( $^{\circ}\text{C}\cdot\text{cm}^{-1}$ ), b) vapor pressure gradient ( $\text{kPa}\cdot\text{cm}^{-1}$ ) and c) snow wetness for thin snow covers.

With small  $\delta T/\delta_L$  and  $\delta e_s/\delta_L$  at the bottom of the snowpack (i.e. low gradients), no vapor is expected to move upward despite the presence of liquid water (Sturm and Benson, 1997) measured on day between days 34 and 48 (Figure-4.13 c). Therefore, relatively stable grain size and low ratio (Figure-4.5 b) values were observed during this cooling period.

During the warming period, the increase in grain size was due to kinetic growth at the beginning of the warming period resulted from the increase in wetness and  $\delta T/\delta_L$  between days 65 and 85 that initiated the vapor flow (Figure-4.13 a and c). However, the decrease in grain size observed between days 89 and 103 was attributed to destructive metamorphism (Langlois and Barber, 2007b). Destructive metamorphism is the process in which the edge of a snow grain sublimates then recrystallizes towards the center of the snow grain because the vapor pressure on a convex area is much higher than in a concave area (Colbeck, 1997; Granberg, 1998). Such mass

redistribution would decrease snow grain area, but not necessarily its volume. Layers that are characterized with rounder shapes grains result from destructive metamorphism resulting in small fractional air volume when the snowpack resettles. Thus an increase in density would result, which was observed between days 82 and 111 at top and bottom layers. Snow density was variable throughout the warming period (Figure-4.5 c). The decrease in densities at top and bottom layers between days 59 and 75 can be explained by either an increase in grain size, that can affect all layers, or new snow deposition that affects the surface layers. However, the decrease in density in the bottom layer was attributed to the increase in grain size that increases the air volume fraction through the observed kinetic growth and associated vapor mass diffusion. This increase could have been due to an enhanced  $\delta T/\delta_L$  (Figure-4.13 a). The increase of salinity at all layers between days 95 and 103 may have augmented the density and wetness increases as brine-wetted snow has a depressed melting point (Granberg, 1998).

#### 4.4.1.2. Thick Snow

During the cooling period, I measured stable  $\delta T/\delta_L$  at all layers throughout the vertical profile (Figure-4.14 a). Furthermore, there was no substantial increase of  $\delta e_{s/l}/\delta_L$  coincident with negligible wetness for L2 to L6 (Figure-4.14 b). Therefore, liquid water was available in L1 (Figure-4.14 c) but no temperature gradient was available to drag this moisture upward within the snowpack (i.e. no kinetic growth).

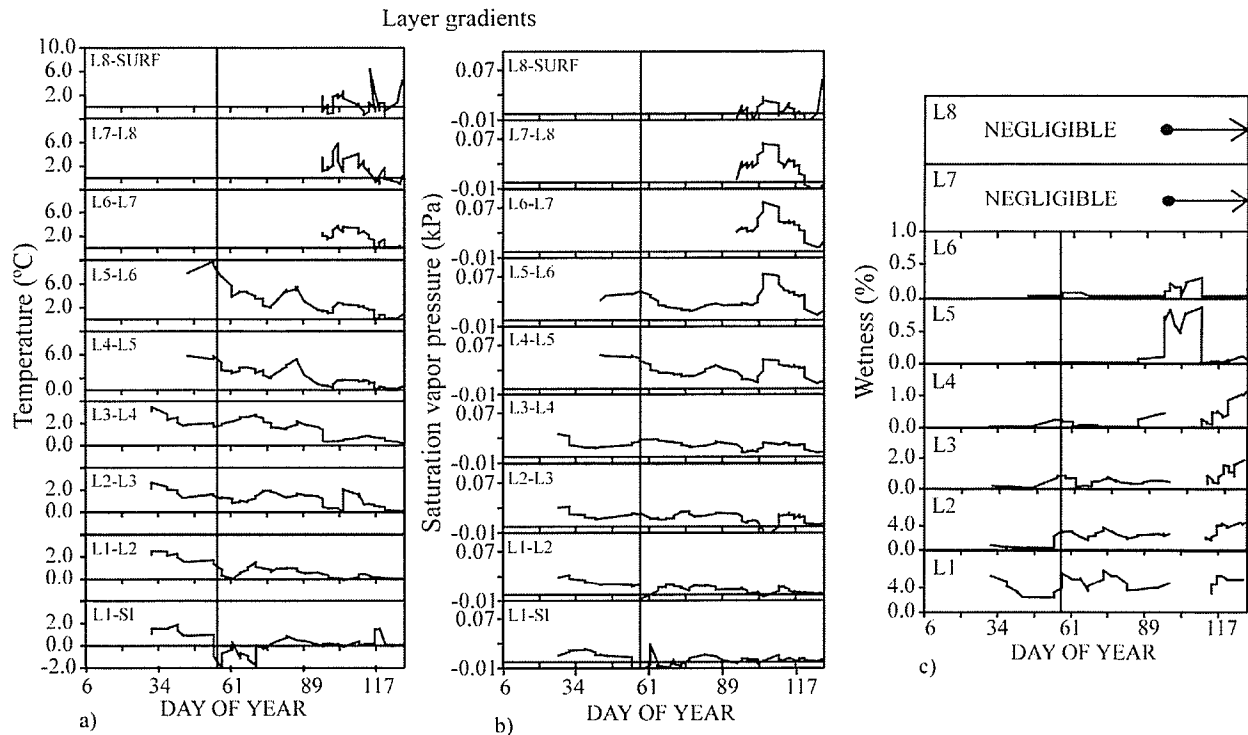


**Figure-4.13:** Temporal evolution of a) temperature gradient ( $^{\circ}\text{C}\cdot\text{cm}^{-1}$ ), b) vapor pressure gradient ( $\text{kPa}\cdot\text{cm}^{-1}$ ) and c) snow wetness for thick snow covers.

During the warming period, the increase in grain size was coincident to increasing values in water volume at L1 and L2 coincidentally with increasing  $\delta T/\delta_L$  and  $\delta \epsilon_{si}/\delta_L$  from L4 to L6 (Figure-4.14 a and b). However, a strong decrease started on day 97 at L1 and L2, as the opposite occurred at L3 to L6, concurrent with the new snow deposition (L7 and L8). The decrease was due to flooding of L1 and L2 that melted the snow grains. This situation occurred with the addition of L7 and L8, which increased the weight of the snowpack. This situation is believed not to be common in the Arctic since the snow thickness is relatively thin in contrast to Antarctica where thick snow covers are more common (e.g., Eicken, 2003; Leppäranta and Hakala, 1992). This type of flooding was also observed at other sampling areas east of the ship

where snow fences intercepted snow covers over 70 cm. The flooding of layers L1 and L2 increased the brine volume (Figure-4.9 b) that moved upward in the snowpack due to an enhanced vapor flow. The vapor pressure gradient increase was very strong between day 100 and day 117 (Figure-4.14 b), which coincided with the increase in salinity, brine and grain size. I would expect this increase to occur throughout the vertical profile, but the extraction of samples for density and salinity measurements was impossible due to the liquid consistency of the layers. However, it was possible to extract snow grains from the flooded surface. The flooding of the basal layers also increased the wetness and  $\delta e_{si}/\delta_L$  increased from L3-L5 to L8-surface transitions (Figure-4.14 b), allowing migration of brine towards the top of the snowpack as observed in Figure-4.9 b.

#### 4.4.2. *Electrical Properties*

##### 4.4.2.1. Thin snow

The observed decrease in permittivity between day 35 and 82 was attributable to coincident decreasing trend in the following snow physical properties: density, temperature, salinity/brine volume and wetness (Langlois *et al.*, 2007b). Permittivity of the snowpack depends upon these physical properties; increased values of these three properties would decrease the ability of the medium to permit the incident microwave radiation (e.g. Ulaby *et al.*, 1986; Hallikainen, 1989; Comiso *et al.*, 1989; Lohanick, 1993; Barber *et al.*, 1994; Pulliainen and Hallikainen, 2001). Concordant to the decrease in snow density and temperature, wetness values also decreased from values varying around 2 % (day 40) to 0 % (day 70) at the top layer and from 7 % to 2 % at the

bottom layer for the same period (Figure-4.13 c). A substantial increase in complex permittivity between day 82 and day 104 were attributable to increasing snow wetness.

#### 4.4.2.2. Thick Snow

Low permittivity and dielectric loss values near the surface were due to the occurrence of dry and fresh snow layer for the most of period (Figure-4.10 a). The significant increase in permittivity in the middle layers after day 91 was attributed to the upward transport of the brine volume forced upward from the underlying layer by capillarity suction following the flooding period (Langlois *et al.*, 2007a). I also observed an increase in permittivity in the bottom layers in three different samples between 110 and 120, concordant with very high brine volume values, again due to the flooding within this particular layer.

#### 4.4.3. *Passive Microwave Linkages*

##### 4.4.3.1. Thin Snow (30° - 40°)

During the cooling period, variations measured were mainly due to variations in air temperatures since low variations were noticed in the snow physical properties. In general, the lower brightness temperatures are a result of very high salinity values throughout the snow cover (Figure-4.5 e). Salinity contributes to high values of permittivity (very little data available for this period), masking the emission from the layers below (Garrity, 1992). Snow cover, though thin, is very dense due to the combined action of wind and equilibrium metamorphism that sinters the snow grains together in the absence of a strong temperature gradient (Colbeck, 1982). Such a

dense layer also decreases the ability of the medium to permit the incident microwave radiation from below (e.g., Matzler, 1987; Hallikainen, 1989; Comiso *et al.*, 1989; Lohanick, 1993; Barber *et al.*, 1994; Pulliainen and Hallikainen, 2001) decreasing the overall  $T_b$ .

During the warming period,  $T_b$ 's decreased at 85 GHz at the beginning of the warming period, coincident to significant increases in grain size (e.g. Matzler, 1987; Foster *et al.*, 2005) as frequencies are more sensitive to scatterers within the snow (e.g. Foster *et al.*, 1999). Maximum grain size values varied from 4 to 6 mm depending on the vertical location and would increase volume scattering at high frequencies (e.g. Tiuri *et al.*, 1984; Drinkwater and Crocker, 1988; Hallikainen, 1989; Tsang *et al.*, 2000; Kelly *et al.*, 2003). Afterwards,  $T_b$  values at 85 GHz coincidentally increased with increasing wetness (i.e. increasing emission at the top layers) until day 82 (Figure-4.13 a). As mentioned in Chapter 2, the presence of liquid water within the snowpack increases the internal absorption along with decreasing volume scattering (Foster *et al.*, 1984). Wet snow brightness temperatures will increase (towards a black body behavior where  $T_b = T_s$ ) at vertical polarization as shown in Figure-4.13 a (e.g., Stiles and Ulaby, 1980; Ulaby *et al.*, 1986; Garrity, 1992; Walker and Goodison, 1993). The significant decrease in  $\Delta P$  measured on day 357 is due to the increase in temperature and consequently increase in liquid, water allowing  $\Delta P$  values to decrease during the warming period at all frequencies and angles.

#### 4.4.3.2. Thick Snow ( $55^\circ - 70^\circ$ )

The steady cooling period  $T_b$ 's were linked to the negligible changes in snow thermophysical properties until day 57. Little variations during this cooling period were coincident with the

increase in  $T_{\text{air}}$  as reported in numerous studies (e.g., Lohanick, 1993; Grody and Basist, 1996; Sokol *et al.*, 1999; Rosenfeld and Grody, 2000). Air temperature increased from  $-23$  to  $-14^{\circ}\text{C}$ ,  $-28$  to  $-21^{\circ}\text{C}$  and from  $-30$  to  $-19^{\circ}\text{C}$  for days 357, 6 and 28 respectively.  $T_b$  values at 85 GHz were higher than 19 and 37 GHz throughout the cooling period. However, it was not possible to relate this behavior with the snow cover properties as the physical/electrical properties dataset only starts on day 6. A possible cause for the  $T_b$ 's at 85 GHz to be so high could be the relatively warm snow/ice interface temperature ( $T_{\text{si}}$ ) measured under thicker snowpacks. Increasing air temperature increases the liquid water volume in the snow cover decreasing the difference between vertical and horizontal polarization as wet snow has a theoretical  $\Delta P$  of 0 (Matzler and Huppi, 1989; Garrity, 1992).

During the warming period, the slight increase in brightness temperatures in both 19 and 37 GHz was due to a combination of many factors. First, this period was marked by an abrupt end to the desalination process that decreased the overall dielectric constant of the snow cover (dielectric data is limited for this period). Previous work by Langlois *et al.*, (2007a) showed a desalination rate of  $-0.12$  ppt day<sup>-1</sup> that ended near the end of the cooling period. Such desalination decreases the permittivity of the medium allowing for more emission from bottom snow layers (Langlois and Barber, 2007b). Furthermore, the thickening snow cover raised the overall volume temperature and wetness of the snowpack thereby increasing the emission of that particular layer (e.g., Foster *et al.*, 1984; Matzler and Huppi, 1989; Walker and Goodison, 1993; Hwang *et al.*, 2007). Variations were greater at horizontal polarization and wide incidence angle, as observed in the cooling period and numerous studies over land and first-year sea ice (e.g., Hallikainen, 1989; Barber and LeDrew, 1994; Derksen *et al.*, 2000; 2005). The increase between day 72 and

day 84 was coincident with a significant increase in air temperature. Another increase was measured on day 91; however this increase is a consequence of flooding that occurred within the basal layers as mentioned previously. Such an intrusion of liquid water significantly increases the microwave emission (e.g., Tiuri *et al.*, 1984; Thomas and Barber, 1998) at L1 (Figure-4.14 a and b). Generally, as the temperatures increased throughout the warming period,  $\Delta P$  values decreased until the end of the sampling period. Again, peaks in air temperatures were coincident with significant decrease in  $\Delta P$  as observed between around day 77 where the temperature warms from  $-34$  to  $-22^{\circ}\text{C}$  (Figure-4.14). Furthermore, the decrease in 85 GHz during the earlier stages of the warming period was attributable to grain growth caused by an increase in available water vapor (warmer temperatures) and a large temperature gradient in the snow pack. The volume scattering triggered by such grain growth changed the temporal evolution of  $T_b$  and was also coincident with the transition between the winter cooling and warming periods (see Langlois *et al.*, 2007a). In addition, the increasing thickness of the snowpack was reflected in rising densities in the top and middle layers, a change that had a direct effect on the permittivity and dielectric loss at L5. Continuing increases in snowpack thickness and grain size (volume scattering) caused 85 GHz brightness temperatures to remain low. Concordant with increasing temperatures, the increased liquid fraction throughout the snow cover vertical profile in turn increased the density and permittivity in L5 (e.g., Lohanick 1993; Grody and Basist, 1996; Sokol *et al.*, 1999; Rosenfeld and Grody, 2000) and decreased the polarization (Tiuri, 1984; Grenfell and Lohanick, 1985), thus decreasing the overall  $T_b$ .

## 4.5. Conclusions

### 4.5.1. Snow Properties

In this chapter I have characterized the fall to winter vertical evolution of thin and thick snowpack physical properties and associated meteorological forcing over landfast first-year sea ice. From these data, I showed that snow physical and thermal properties evolve according to whether the system is categorized into ‘cooling’ or ‘warming’ periods. During the cooling period I observed only very small changes in the geophysical characteristics of the snowpack except for salinity, which decreased throughout the cooling period. This snow desalination was stronger at the bottom of thin snowpacks with a rate of  $-0.12 \text{ ppt}\cdot\text{day}^{-1}$ . I could not compare this rate with thick snow as that sampling started later in the season. Net shortwave and longwave radiation did not appear to have a significant influence on either thin or thick snow covers with high variability in  $L\uparrow$  and  $L\downarrow$  and low values for  $K\uparrow$  and  $K\downarrow$ . The warming period initiated significant changes in the morphology of the snow grains for both thin and thick snowpacks. The rate of growth was stronger under thick snowpacks ( $0.25$  and  $0.48 \text{ mm}\cdot\text{day}^{-1}$  for thin and thick snow respectively) where  $\delta T/\delta t$  and  $\delta e_s/\delta t$  were larger (i.e. stronger vapor flow) and  $Q^*$  values near 0. The concordant change in grain shape impacted on snow density and therefore on the thermal properties (Langlois and Barber, 2007b) of the snow and ice volume.

With thick and heavy snowpacks, flooding can occur and its impact on vertical geophysical properties is substantial. I showed that the input of seawater at the bottom of the snowpack increased the vertical vapor pressure difference, initiating a strong vapor flow that increases the grain size towards the surface. Although this feature is not currently that common in the Arctic it

may be a scenario of increasing interest if ice thickness is reduced, and snow thickness increased in the future.

#### 4.5.2. *Passive Microwaves*

I found that the seasonal pattern in  $T_b$  was quite different given the effect of cold versus warm thermal regimes and the associated presence of kinetic growth grains. During the first half of the winter,  $T_b$  was dictated by the desalination process, as the thickness did not yet play an important role in volume scattering. Overall, the results showed that the variations in  $T_b$ 's for thin snow over the cooling period were mainly attributable to changes in air temperature with fairly constant snow physical properties. The thick snowpack properties also showed little variation during the cooling period and brightness temperatures were again strongly linked to air temperature.

Significant changes occurred in thin snow with increasing wetness and grain growth that increased volume scattering. As temperatures increased, the amount of water in liquid phase in the upper part of the snow cover increased the permittivity, which decreased the emissivity contribution of the bottom part of the snowpack (decrease in  $T_b$ ). Thick snow was characterized by significant changes in high frequency  $T_b$ 's, coincidentally with increasing grain size (i.e. increasing volume scattering), temperatures and liquid water content (increasing absorption). Further changes occurred with flooding of the snow basal layers which significantly increased microwave emission. Therefore,  $T_b$ 's were strongly linked to water content (approaching black

body behavior), which is an important result when investigating the nature of SWE prediction algorithm variations.

In conclusion, this chapter represents one of the most complete snow-on-sea ice winter properties dataset available. I provided an acute understanding on the thermophysical and electrical properties behavior throughout the cold and dry Arctic winter season. I also provided an improved understanding of linkages between snow and passive microwave brightness temperatures on longer term (i.e., seasonal scale), following the theoretical perspective provided in Chapter 2. To strengthen our understanding of the system, the next chapter will look at short-term variations (i.e., diurnal scale) in snow properties associated with daily atmospheric pressure variations and the impact of those changes on brightness temperatures.

## CHAPTER 5: DIURNAL TIME SCALES

Following the seasonal analysis from Chapter 4, this chapter focuses on short-term changes in snow thermophysical properties and the associated brightness temperatures that can affect SWE retrieval algorithms. On a diurnal scale, weather systems such as low-pressure fronts can cause sudden changes in snow temperature, grain size and brine volume, which in turn affect the dielectric properties of the snowpack. A case study was conducted during the CASES project where snow thermophysical/electrical properties were investigated throughout a diurnal cycle. During this experiment, a low-pressure system (hereinafter referred as a low-pressure disturbance, LPD) came through the area providing a unique chance to look at the impact of short-term atmospheric forcing mechanisms on snow properties and microwave signatures. Therefore, in this chapter I first provide background material on low-pressure disturbances in the Arctic and an overview for the CASES period. I then describe the type of LPD that occurred throughout our diurnal study, and the associated changes measured in snow properties and brightness temperatures. Finally, I conclude with a discussion of the implications of this case study on the broader issue of increased Arctic cyclogenesis and the response of the snow/sea ice system. The material in this chapter was published in the peer review literature and can be found in Langlois *et al.*, 2007c.

## 5.1. Low-Pressure Disturbances (LPDs)

### 5.1.1. Background

An increase in occurrence and intensity of low-pressure systems through polar regions is expected (Lambert, 1995; McCabe *et al.*, 2001; Zhang *et al.*, 2004) and their accumulated impact on the ocean-sea ice-snow-atmosphere interface has yet to be investigated thoroughly. Studies have suggested that current temperature trends linked with climate change may allow more low pressure systems with mid-latitude origin to track northward (McCabe *et al.*, 2001; Zhang *et al.*, 2004). As these systems are generally associated with increased advection of warm air and usually strong surface flow, they have the potential to significantly alter SWE predictions through enhanced forced convection (changes in snow properties). Forced convection in snow, also termed ‘wind pumping’ (Chapter 2), occurs when wind disturbances create variations in surface pressure that can affect airflow within the snow (Colbeck, 1989). Diffusion and convection are most likely to be enhanced by these variations, which in turn affect heat transfer and snow metamorphism (Clarke *et al.*, 1987). Therefore, I speculated that the accumulated effects of increased cyclogenesis will have an effect on the geophysics, thermodynamics and associated radiative transfer through the snow sea ice system. These thermophysical modifications can lead to changes in microwave signatures used for snow water equivalent (SWE) estimation.

The atmosphere imparts changes on the geophysics of snow covered sea ice through mass, gas and energy fluxes. Organized circulations of surface air are a result of a vertical cascade of atmospheric motion, driven by the latitudinal gradient of atmospheric density from the equator to the pole and the influence of the rotation of the earth. Extratropical and Arctic low pressure disturbances are of specific concern when studying cumulative effects at the surface as they result

in the movement of temperature and moisture northward over a given area (classically on the eastern side of the disturbance in the Northern Hemisphere). With the advancement of a warm boundary or ‘front’, increased cloudiness, temperatures and wind speeds, as well as a wind shift are observed at the surface. These characteristics have implications on sea ice growth and extent (spatial and temporal), which is controlled by the surface energy balance and snow thermophysical properties (Maykut, 1978; Barber *et al.*, 1994; Perovich and Elder, 2001; Sturm *et al.*, 2002; Langlois *et al.*, 2007a) thereby determining sea ice freeze-up and melt dates (e.g., Flato and Brown, 1996; Hanesiak *et al.*, 1999).

A pattern in regional formation zones for LPDs in the northern latitudes does exist, though frequency of cyclogenesis does vary with season (Serreze *et al.*, 2001, Zhang *et al.*, 2004). In the context of the Canadian Arctic, the Gulf of Alaska and Baffin Bay are identified as prominent formation zones, with a greater number of disturbances originating from Alaska and extending south–eastward, lee of the Rocky Mountains in Western Canada in summer. These findings correspond with the results of Hudak *et al.*, (2002), where it was found that the majority of intense low-pressure system tracks originated from the “Pacific” region between the months of June to November in the Southern Beaufort Sea. In winter, the majority of disturbances are created east of Greenland, over the Barents Sea and Baffin Bay, with a noticeable maximum of LPD generation remaining in lee of the Rocky Mountains (Serreze *et al.*, 2001). While regions of cyclogenesis in northern latitudes vary minimally from winter to summer, their intensities vary greatly (Zhang *et al.*, 2004). Overall, LPDs that are generated in the winter are stronger than those occurring during the summer season, and those that originate from extratropical latitudes and track northward into the Arctic, particularly from oceanic origins, tend to be annually

stronger than those generated locally (Serreze *et al.*, 1988, Zhang *et al.*, 2004). More importantly, interannual variations in frequency and intensity suggest that a larger number of more intense extratropical depressions have been migrating northward into Arctic regions over the last sixty years (e.g., Hanesiak *et al.*, 1997; McCabe *et al.*, 2001; Déry and Yau, 2002) and more of these systems are to be expected in the Arctic in a near future (IPCC, 2001; Serreze *et al.*, 2003; Barber and Hanesiak, 2004).

The resulting surface energy balance variations can affect snow metamorphism, brine volume migration, thereby affecting brightness temperatures through the electrical properties of the snow cover (e.g., Carsey, 1992; Armstrong *et al.*, 1993; Barber *et al.*, 1995). Many studies have examined short-term variations of spring snow covered first-year sea ice (e.g., Yackel *et al.*, 2001; Sturm *et al.*, 2002) but none have assessed the effect of winter low-pressure events on the snow covered sea ice.

### 5.1.2. Overview During CASES

Several LPDs were observed during the CASES overwintering study. We selected one as a case study to examine the coupling between the cyclone and the geophysics/thermodynamics of the snow covered sea ice system. From October 2003 to June 2004, a total of 42 LPDs were documented in the CASES region, with 55% of those originating from the Arctic, 40% originating from the Pacific, and 5% of the total originated from irregular sources where the most synoptically active months were November and March. Early season disturbances developed and terminated west of the ship location providing the Southern Beaufort Sea with warm and moist

air from southern latitudes. This coincides with previous findings in our climatological investigation, where it was found, especially during the months of October and November, that temperature and moisture over the Beaufort Sea were anomalously positive compared to previous years. Conversely, in the late winter/early spring months, very little cyclonic activity was noted, indicating a strong and persistent Arctic High for much of the period, allowing the advection of frigid arctic air into the CASES region for much of this time and causing lower than normal temperatures and moisture content. It is apparent that low-pressure systems affect the southern Beaufort sea throughout the annual cycle.

## **5.2. Results from the Case Study**

In our case study we examine the passage of a warm boundary (small cyclone) from day 33 to 35 (February 2 to February 4, 2004) during the CASES project. These small cyclones forming over open sea during the cold season within polar or arctic air masses are called "polar lows." Typically several hundred kilometers in diameter, and often possessing strong winds, polar lows tend to form beneath cold upper-level troughs or lows when frigid arctic air flows southward over a warm body of water. Polar lows last on average only a day or two. They can develop rapidly, reaching maximum strength within 12 to 24 hours of the time of formation. They often dissipate just as quickly, especially upon making landfall. In some instances several may exist in a region at the same time or develop in rapid succession. In this particular case the driver of the warm boundary was not a closed circulation in itself, but an elongated area of lower pressure extending eastward from the Gulf of Alaska to west of the Smith Arm of Great Bear Lake. However, based on surface observations, this situation can be extrapolated for the purposes of this study to

represent similar influences of warm sectors associated with closed low pressure circulations, and as such, it is necessary to investigate the trends and origins of such disturbances. In the next few sections, I will provide results on meteorological observations, snow properties and microwave signatures (Section 5.2) during our case study. Discussion and conclusions will follow in sections 5.3 and 5.4 respectively.

### *5.2.1. Meteorological Observations*

The atmospheric pressure on day 32 was, on average, 1020 mbar until the low-pressure system decreased the values slowly to an average of 1014 mbar on the morning of day 34 (between 0400 and 1200 on Figure-5.1 a). Air temperatures oscillated around  $-32\text{ }^{\circ}\text{C}$  (Figure-5.1 b). A peak was measured between the two first sets of snowpits (SP1 and SP2) where the values increased from an average of  $-32\text{ }^{\circ}\text{C}$  to  $-30\text{ }^{\circ}\text{C}$  at 13h00 local time. The most significant warming occurred overnight between SP2 and SP6 where the maximum temperature reached  $-23.8\text{ }^{\circ}\text{C}$  shortly before 4h00 on day 34. The increase rate was in the order of  $+0.6\text{ }^{\circ}\text{C}\cdot\text{h}^{-1}$  between 16h00 and 4h00, after which the temperatures remained stable at around  $-25\text{ }^{\circ}\text{C}$  until the end of the sampling period. Relative humidity increased slightly over the diurnal period (Figure-5.1 c) and wind speed (maximum recorded at 4h00 on day 34 on Figure-5.1 d). A shift in wind direction was also measured at the end of the depression where the direction varied from below  $100^{\circ}$  at 19h00 on day 33 to over  $300^{\circ}$  at 22h00 on the next day (Figure-5.1 e). The total cloud cover increased from 0 to 8 octas over day 33 and remained mostly covered until day 35 (Figure-5.1 f).

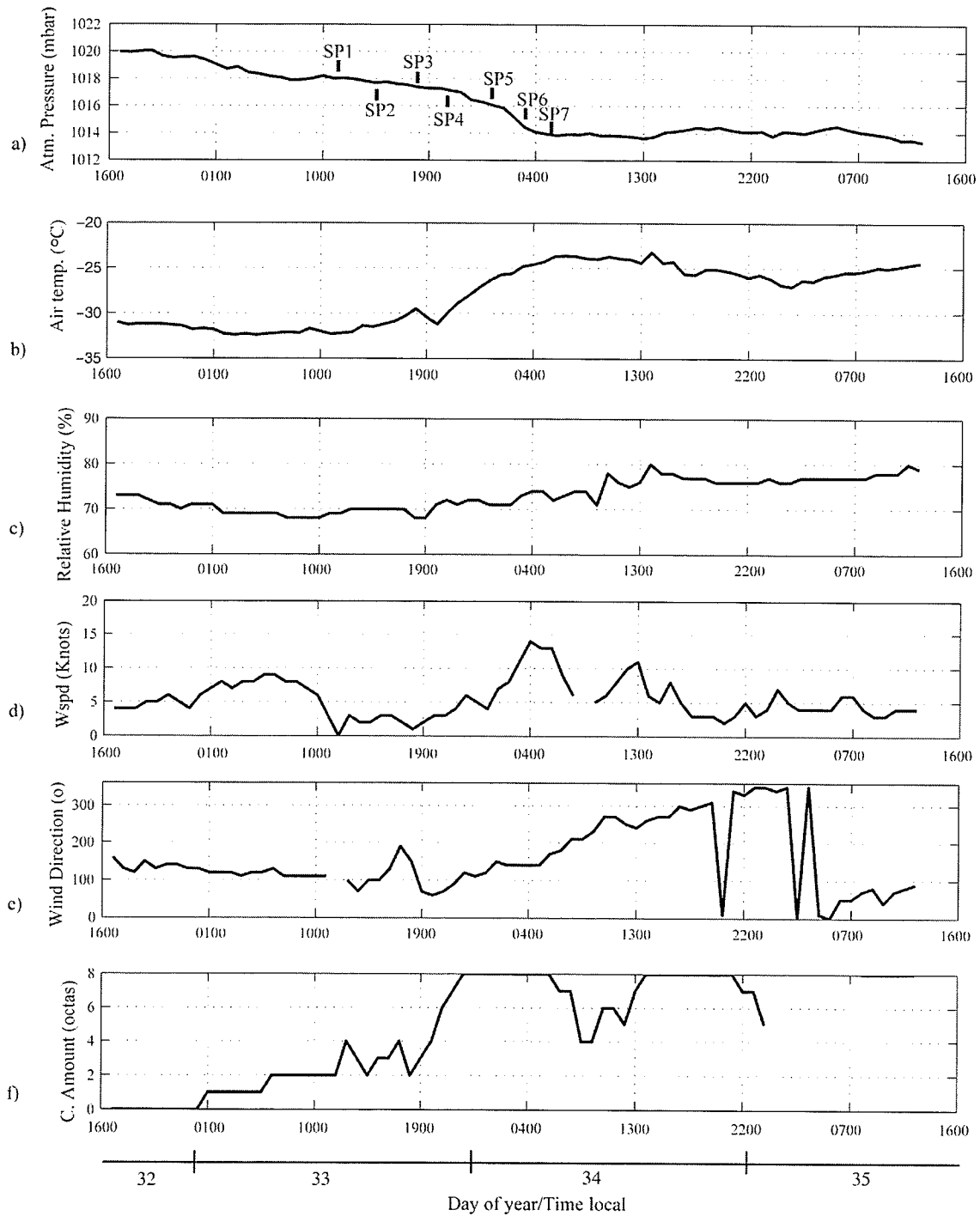


**Figure-5.1:** Temporal evolution of hourly averaged a) atmospheric pressure, b) air temperature, c) relative humidity, d) wind speed, e) wind direction and f) cloud amount.

### 5.2.2. Snow

Thin and thick snow sampling occurred every 3 hours (Table-5.1) at the undisturbed site near the ship (Chapter 3). The first measurements occurred at 12h08 local time on day 33 and were continued until 6h40 on day 34. Concomitant to snow sampling, microwave radiometer measurements were conducted between 30 and 70° of incidence angle (Table-5.1).

**Table-5.1:** Sampling times (local ship time) for thin/thick snow covers and surface based radiometer (SBR) measurements.

Flag	SNOW		SBR
	THICK	THIN	
SP1	1208	1250	1151
SP2	1500	1525	1435
SP3	1800	1830	1735
SP4	2100	2130	2143
SP5	0005	0035	2333
SP6	0300	0330	0243
SP7	0605	0640	0538

#### 5.2.2.1. Thin Snow

##### 5.2.2.1.1. Physical and Electrical Properties

Snow volume temperatures in thin snow increased significantly throughout day 33 (Figure-5.2 a). Values started at a minimum of  $-28^{\circ}\text{C}$  and  $-24.4^{\circ}\text{C}$  for both layer 6-4 (L6\_4) and layer 2-si (L2\_si) respectively at 12h50, and maximum temperatures were reached at 00h35. On average,

the warming rate is in the order of  $+0.47^{\circ}\text{C} \cdot \text{h}^{-1}$  for L6-4 and  $+0.43^{\circ}\text{C} \cdot \text{h}^{-1}$  for L2-si. The temperature difference between the top and the bottom of the snowpack was  $7.1^{\circ}\text{C}$ , which corresponds to a gradient of  $1.2^{\circ}\text{C} \cdot \text{cm}^{-1}$  compared to  $0.65^{\circ}\text{C} \cdot \text{cm}^{-1}$  on the last series of snowpits (SP7 on Figure-5.1 a) on day 34.

Snow density was practically unchanged where small variations are due to the uncertainty with the sampling methodology and natural small-scale variability. On average, density at the top of the snowpack was  $270 \text{ kg} \cdot \text{m}^{-3}$  and  $240 \text{ kg} \cdot \text{m}^{-3}$  at the bottom. Salinity at both L4-2 and L6-4 increased between day 34 and day 35 where values peaked from 8.3 to 18 ppt and 1.8 to 5.6 ppt for L4\_2 and L6-4 respectively. Values at L2-si remained high between 20 and 25 ppt without following any particular trend (Figure-5.3 a). Brine volume increased for both L6-4 and L4-2 and reached a maximum at 3h00 where the values doubled. The most significant increase was measured at L4\_2 with an increase of 153 % between 12h50 on day 33 and 03h30 on day 34. Values at the bottom L2-si varied between 1.2 % and 1.9 % with a minimum measured at 15h25 and a maximum at 18h30 on day 33 (Figure-5.3 b).

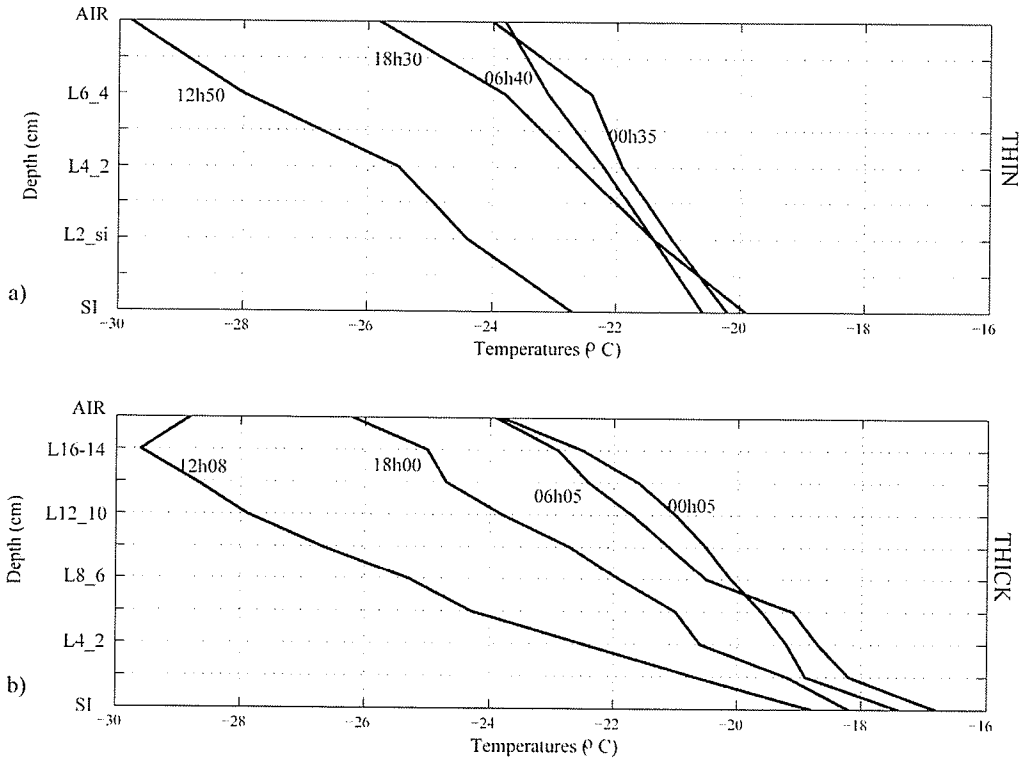


**Figure-5.2:** Temperature profiles measured throughout the diurnal study for a) thin and b) thick snow covers.

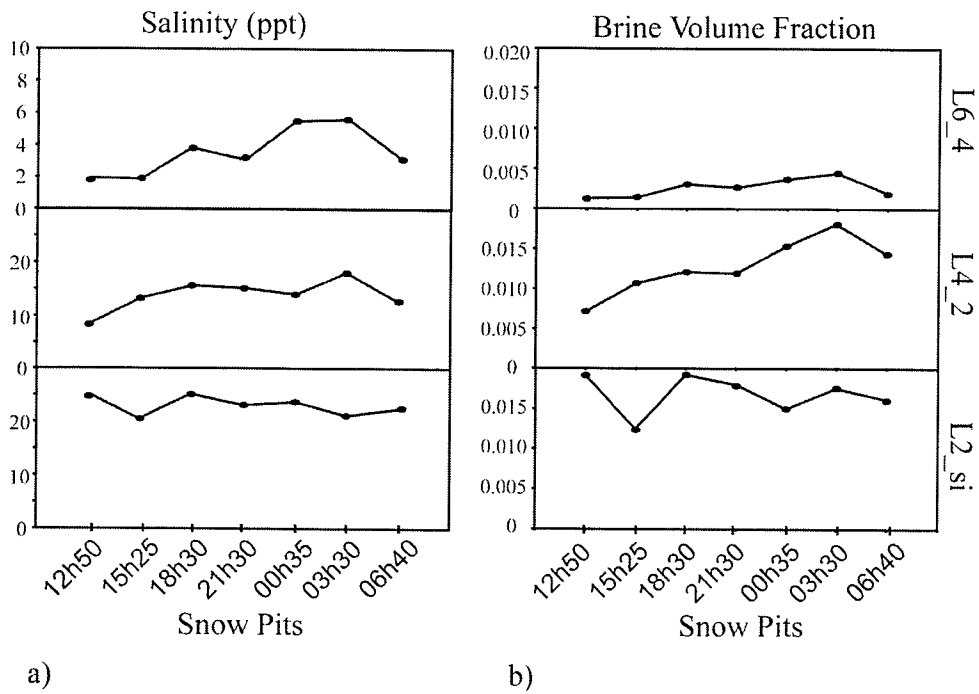


**Figure-5.3:** Vertical profiles of thin snow a) salinity and b) brine volume temporal evolution.

Thin snow permittivity values remained relatively stable for L6\_4 and L4\_2 averaging 1.52 and 1.54 until 21h30 (Figure-5.4 a). The lowest value of 1.41 was recorded at 15h25 at L2\_si, then increased until 21h30 where all layers had similar values at 1.55, 1.51 and 1.50 at L6\_4, L4\_2 and L2\_si respectively. A sharp increase was measured at L4\_2 until the end of the sampling period where values jumped from the average of 1.54 prior to 21h30 up to 1.81 at 06h40 on day 34. Values at L6\_4 and L2\_si were similar to each other within 0.01. The dielectric loss was very low at L6\_4 as it increased by a factor of 10 at L4\_2 from 0.004 at 12h50 on day 33 to a maximum of 0.044 at 3h30 on day 34 (Figure-5.4 b). The values at L2\_si remained relatively stable oscillating slightly around an average of 0.051.

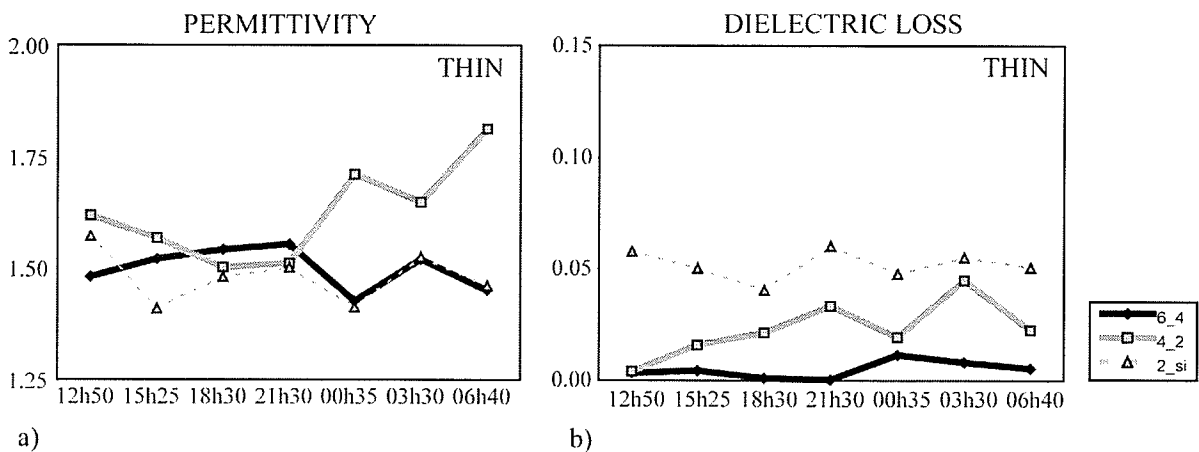


**Figure-5.4:** Thin snow modeled a) permittivity and b) dielectric loss temporal evolution.

#### 5.2.2.1.2. Heat/Mass Transfer and Snow Metamorphism

The thermal conductivity of both bottom and top layers did not vary significantly throughout the sampling period (Figure-5.5 a). Large variations were measured at L4\_2 where  $k_s$  decreased until 21h30 ( $0.095 \text{ W}\cdot\text{m}^{-1}\cdot\text{K}^{-1}$ ) and then increased significantly until the end of the sampling period,

reaching a maximum of  $0.258 \text{ W}\cdot\text{m}^{-1}\cdot\text{K}^{-1}$ . Specific heat values remained unchanged in the top layer (Figure-5.5 b). However, an increase was measured between 18h30 and 00h35 for both L4\_2 and L2\_si where values reached a maximum of 2428 and 2928  $\text{J}\cdot\text{kg}^{-1}\cdot\text{K}^{-1}$ . The values then decreased significantly to 2059 and 2021  $\text{J}\cdot\text{kg}^{-1}\cdot\text{K}^{-1}$ , three hours later. Values of thermal diffusivity were proportional to  $k_s$  for both L6\_4 and L2\_si with minimum values of 1.56 and  $1.12\cdot 10^{-7} \text{ m}^2\cdot\text{s}^{-1}$  respectively at 00h35 (Figure-5.5 c). Thermal diffusivity values at the middle layer increased after 21h30 from 1.5 to  $2.96\cdot 10^{-7} \text{ m}^2\cdot\text{s}^{-1}$  at 6h40 on day 34.

The average vapor flux was  $+1.5\cdot 10^{-7} \text{ kg}\cdot\text{m}^{-2}\cdot\text{s}^{-1}$  ( $\pm 0.78\cdot 10^{-7}$ ) with positive values (gain in mass) throughout the sampling period. Accordingly, snow grain size increased approximately  $1 \text{ mm}^2$  (Figure-5.6) when values were at maximum measured at 6h40 on day 34 ( $5.69 \text{ mm}^2$ ). The growth rate was approximately  $0.053 \text{ mm}^2\cdot\text{h}^{-1}$  over the 18-hour period, suggesting a daily increase of  $1.28 \text{ mm}^2\cdot\text{day}^{-1}$  when applying a least squares linear relationship to the data. The increase in grain size was coincident with increased saturation vapor pressure at the basal layer of 0.023 kPa throughout the sampling period with an  $R^2$  of 0.58.

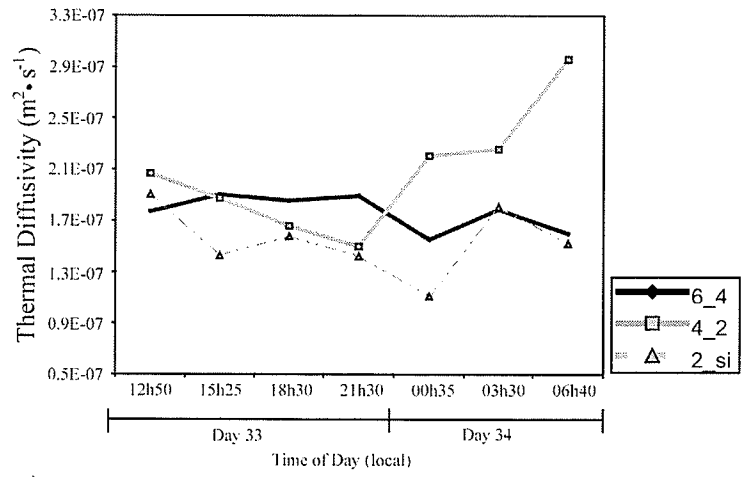
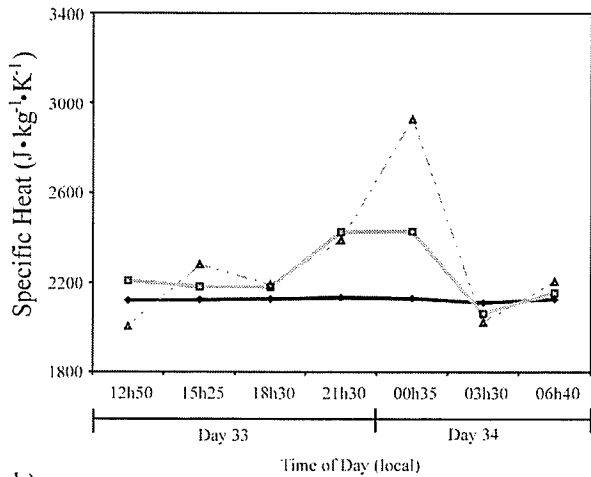
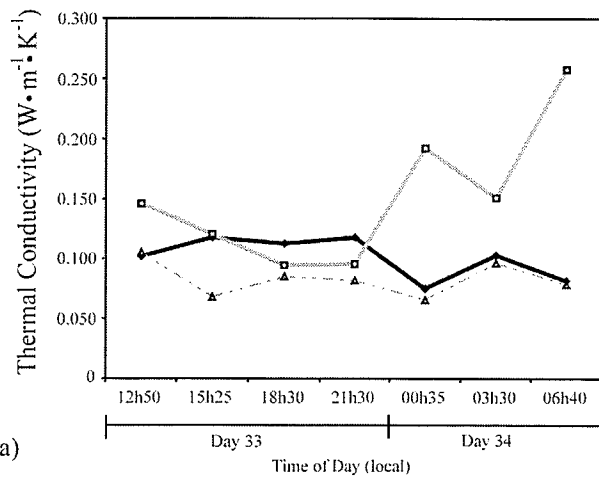


**Figure-5.5:** Thin snow calculated a) thermal conductivity, b) specific heat and c) thermal diffusivity temporal evolution.

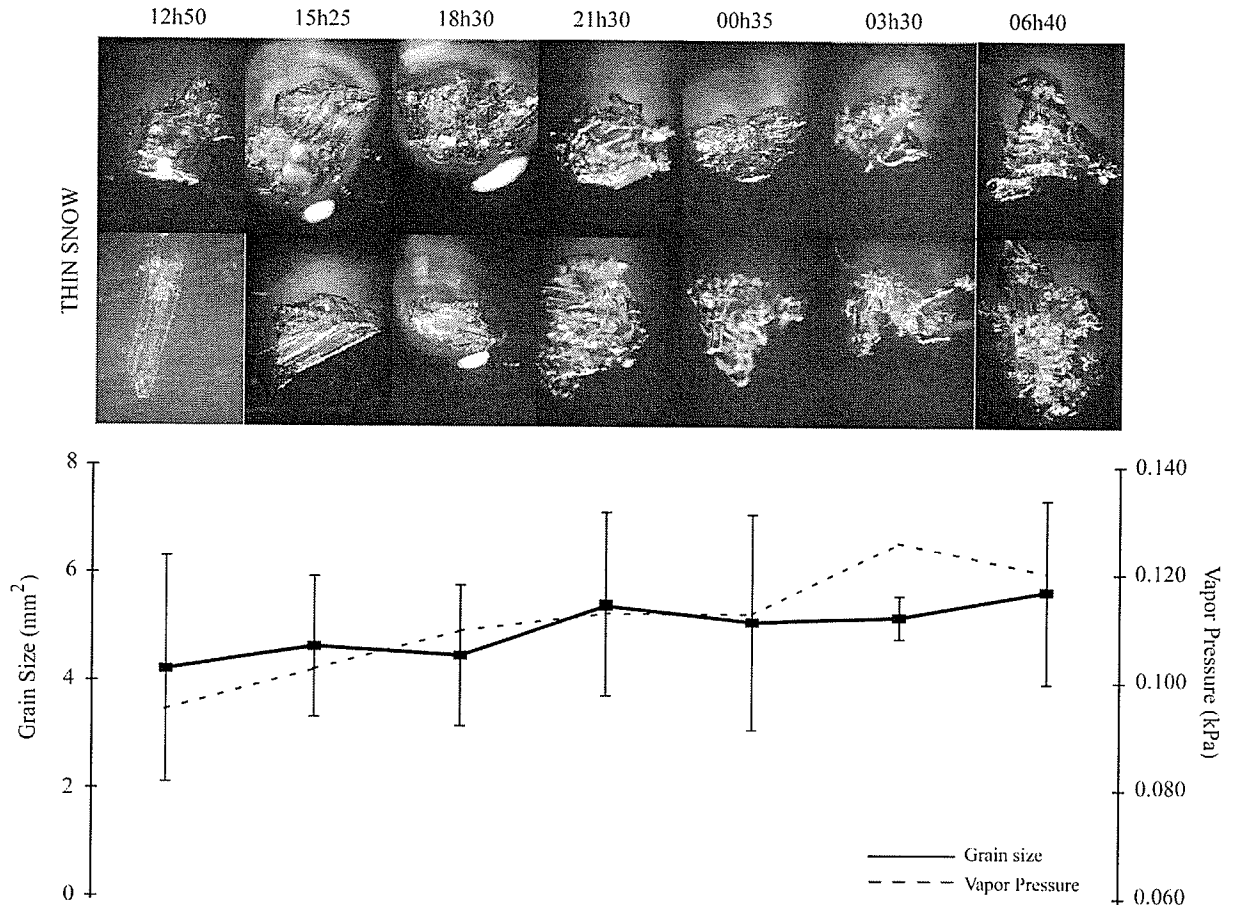


**Figure-5.6:** Thin snow grain size and vapor pressure temporal evolution.

### 5.2.2.2. Thick Snow

#### 5.2.2.2.1. Physical and Electrical Properties

Thick snow volume temperatures increased throughout the vertical profile until 03h00 (not shown here) where the maximum temperatures were reached at all layers (Figure-5.2 b). The warming rate was higher near the snow cover surface where values increase by  $0.5\text{ }^{\circ}\text{C}\cdot\text{h}^{-1}$  at L16-14 compared to  $0.2\text{ }^{\circ}\text{C}\cdot\text{h}^{-1}$  at L2-si. Maximum temperatures were reached at  $-17.7^{\circ}\text{C}$  for L2-si and  $-22.2^{\circ}\text{C}$  for L16-14. The temperature gradient was approximately linear between day 33 and

day 34, however the strongest gradient was measured at 12h08 on day 33 (Figure-5.2 b). The difference between the top and the bottom of the snowpack was then 10 °C, which corresponded to a gradient of 0.63 °C·cm<sup>-1</sup> compared to 0.44 °C·cm<sup>-1</sup> at the end of the sampling period on day 34.

Averaged snow density values remained high throughout the snowpack with the exception of L2\_si. The average value for L2\_si is 233.96 kg·m<sup>-3</sup> as it varied between 302.56 and 393.17 kg·m<sup>-3</sup> for the remainder of the vertical profile. Maximum salinity values were reached at 03h00 for all layers between L6\_4 and L16\_14 (Figure-5.7 a). Values at the bottom layers L4\_2 and L2\_si remained high throughout the diurnal study with averages of 8.7 and 19.8 respectively. Brine volume at L2\_si decreased slightly until 18h00 on day 33 as the decrease was measured until 21h00 at L4\_2 (Figure-5.7 b). Afterwards, values increased until the end of the sampling period for L2\_si (69 % increase) whereas L4\_2 was variable with a maximum value reached at 00h05.

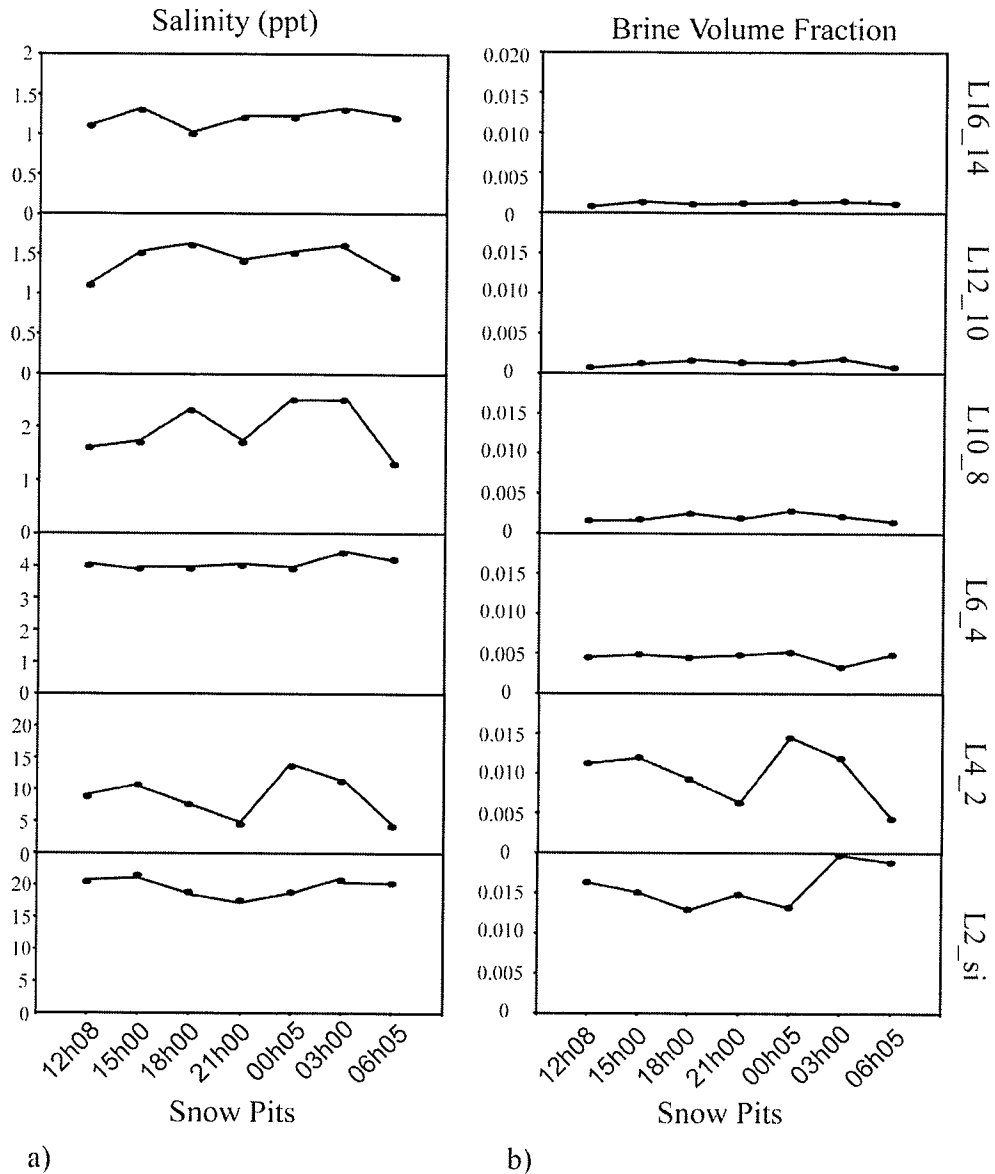


**Figure-5.7:** Vertical profiles of thick snow a) salinity and b) brine volume temporal evolution.

The permittivity values in thick snowpacks did not follow any significant trends throughout the diurnal period (Figure-5.8 a). However, two distinct peaks are measured at 15h00 and 3h00 at the surface layer L16\_14 where the values reached 1.79 and 1.72 respectively. The permittivity at L10\_8 and L2\_si were relatively unchanged between 12h08 on day 33 and 00h05 on day 34 with a very small peak at 21h00 at both layers. A significant decrease was measured at L10\_8

and L6\_4 between 00h05 and 3h00 where the minimum values were reached at 1.51 and 1.52 respectively. The dielectric loss was quite stable for the top two layers at a small average of 0.005 (Figure-5.8 b). Values at L6\_4 peaked at 15h00 on day 33 to a dielectric loss close to 0.02. A visible plateau is observed between 21h00 and 3h00 on day 34 at around 0.02, then decreased back to values close to 0 at the end of the sampling period. The strongest variations were measured at L2\_si with a maximum value of 0.078 at 18h00 and a minimum of 0.037 recorded at 3h00.

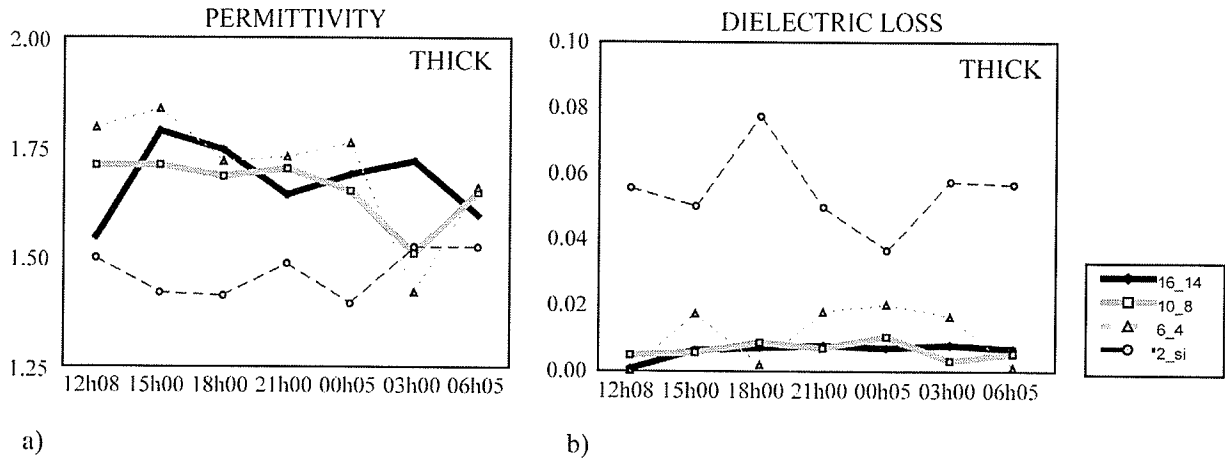


**Figure-5.8:** Thick snow modeled a) permittivity and b) dielectric loss temporal evolution.

#### 5.2.2.2.2. Heat/Mass Transfer and Snow Metamorphism

The thermal conductivity decreased in the layers L10\_8 and L6\_4 until 3h00 on day 34 whereas values remained stable throughout the period for L2\_si (Figure-5.9 a). The decrease was significant between 00h35 and 3h00 where the minimum was reached at 0.1 and 0.07  $\text{W}\cdot\text{m}^{-1}\cdot\text{K}^{-1}$  for both L\_10\_8 and L6\_4 respectively. Surface  $k_s$  values were variable between 0.13 and 0.27  $\text{W}\cdot\text{m}^{-1}\cdot\text{K}^{-1}$  without following any apparent trend. Values of specific heat (Figure-5.9 b) were

stable for the near-surface layers as an increase was measured between 15h00 and 18h00 at L2\_si (from 2150 to 2368 J·kg<sup>-1</sup>·K<sup>-1</sup>). Specific heat at layer L6\_4 remained unchanged until 3h00 where a peak was measured increasing  $c_s$  of over 500 J·kg<sup>-1</sup>·K<sup>-1</sup> to reach a maximum value for the sampling period at 2604 J·kg<sup>-1</sup>·K<sup>-1</sup>. The peak was also measured at L4\_2 and with smaller amplitude at L8\_6 (not shown on Figure-5.9 b). The thermal diffusivity followed the same trends as measured for  $k_s$  with a decrease at the middle layers and stable L2\_si (Figure-5.9 c). I again measured a significant decrease at 3h00 for L10\_8 and L6\_4 where the values reached the minimum for the sampling period at 1.74 and 1.26 m<sup>2</sup>·s<sup>-1</sup> respectively.

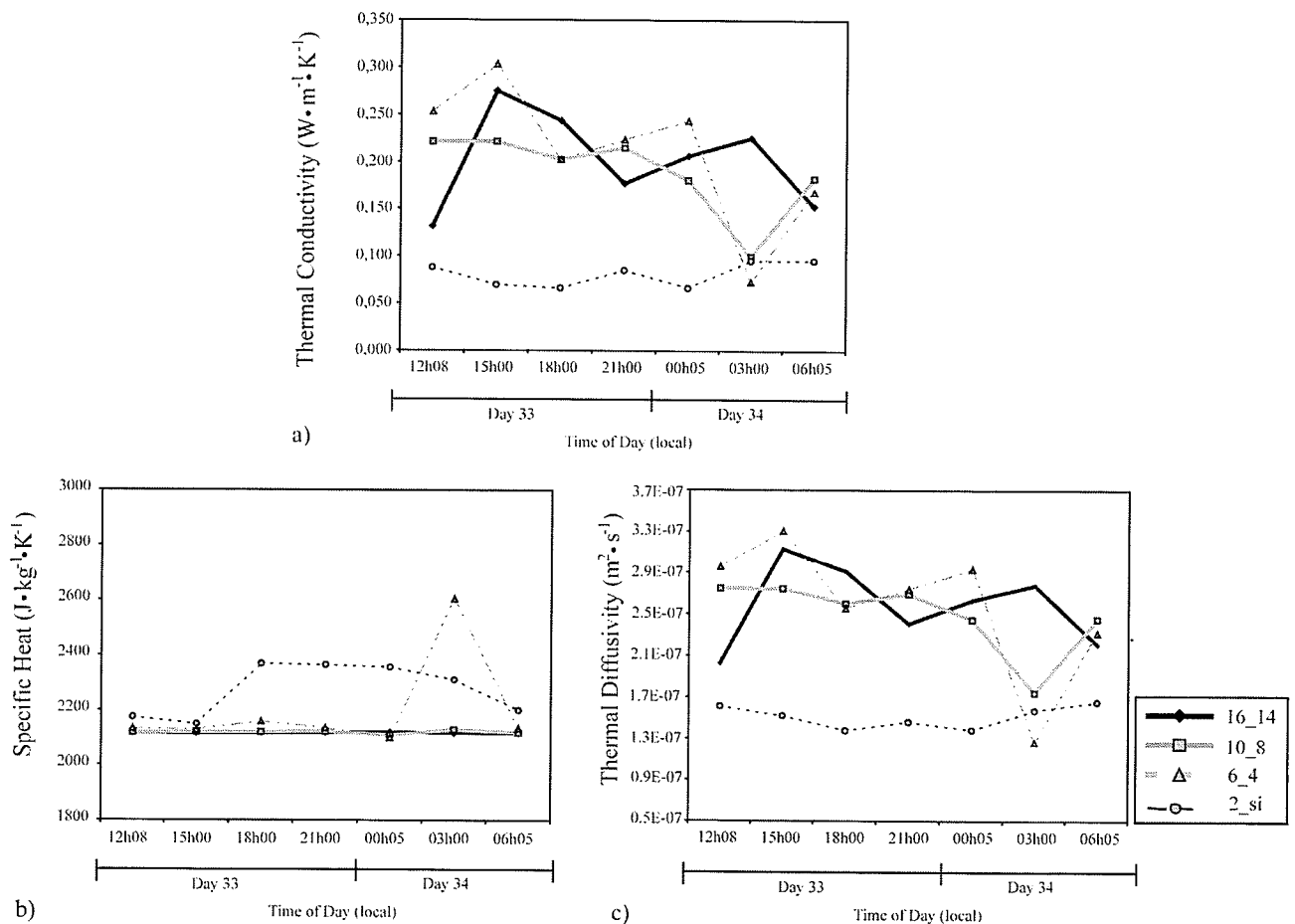


**Figure-5.9:** Thick snow calculated a) thermal conductivity, b) specific heat and c) thermal diffusivity temporal evolution.

The average vapor flux was  $+1.93 \cdot 10^{-7} \text{ kg} \cdot \text{m}^{-2} \cdot \text{s}^{-1}$  ( $\pm 0.71 \cdot 10^{-7}$ ) again with positive values (gain in mass) throughout the sampling period (Figure-5.10). The total snow grain growth was measured at approximately  $1.8 \text{ mm}^2$  and the maximum was reached at 3h00 ( $6.5 \text{ mm}^2$ ). The growth rate was  $0.096 \text{ mm}^2 \cdot \text{h}^{-1}$  corresponding to a daily growth of  $2.3 \text{ mm}^2 \cdot \text{day}^{-1}$ . The saturation vapor pressure also increased accordingly at L2\_si from 0.095 to 0.126 kPa at 3h00 where the maximum grain size was reached. Both grain size and saturation vapor pressure were directly proportional with a  $R^2$  value of 0.72.

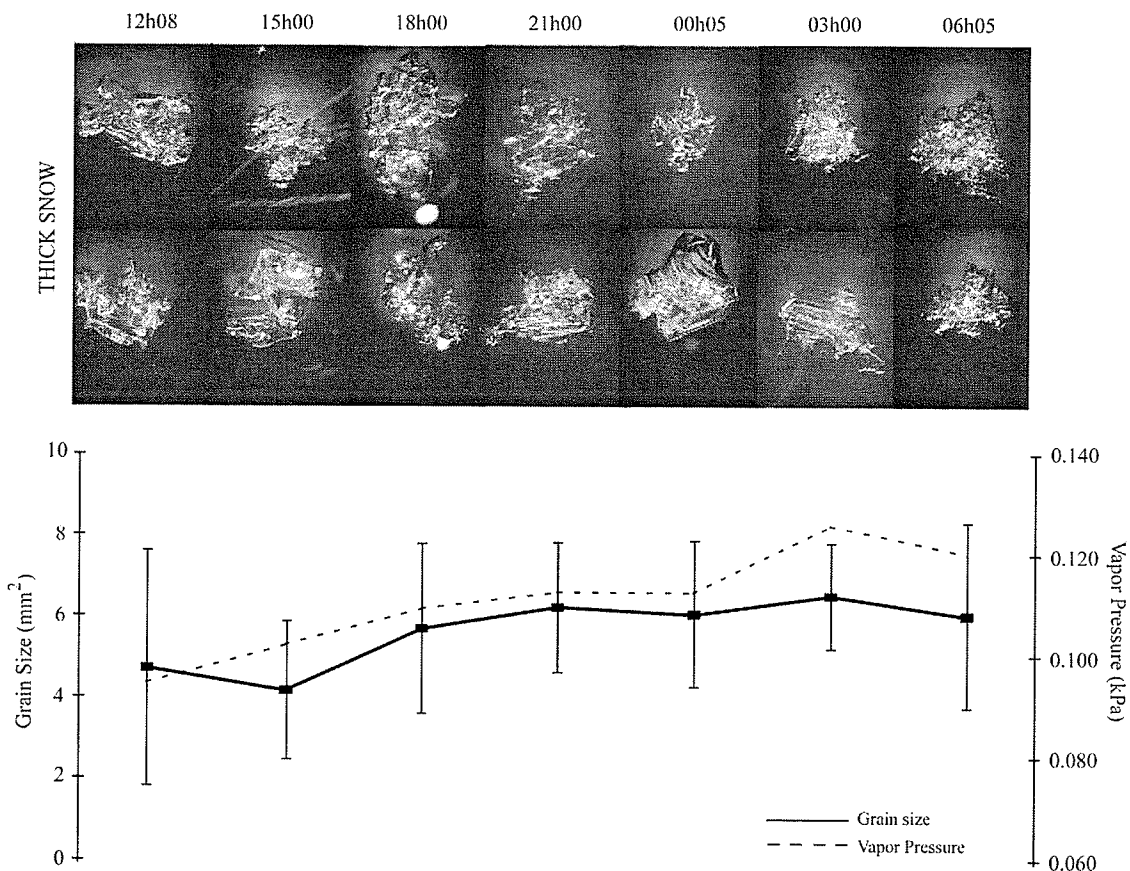


**Figure-5.10:** Thick snow grain size and vapor pressure temporal evolution.

### 5.2.3. *In-Situ Passive Microwaves*

#### 5.2.3.1. Thin Snow

The minimum brightness temperatures values over thin snow were reached at 14h35 after which a significant increase of approximately  $0.3 \text{ K}\cdot\text{h}^{-1}$  was measured until 23h33 for both 19 and 37 GHz (Figure-5.11 a, b, c and d). The vertical polarization (V-pol) values were higher throughout the sampling period (average 4 K higher than H-pol measurements) and the difference between 19 and 37 GHz ( $\Delta T_b$ ) was very small. Brightness temperatures at 85 GHz warmed up quicker than 19 and 37 GHz until the maximum was reached at 23h33 (Figure-5.11 e and f). A significant decrease, in the order of 5 K in V-pol (Figure-5.11 e) and 10 K in H-pol (Figure-5.11 f), was measured at 2h43 for all incidence angles and both polarizations.

#### 5.2.3.2. Thick Snow

Overall, the brightness temperatures at both 19 and 37 GHz increased throughout the diurnal study (Figure-5.11 a, b, c and d) for thick snow incidence angles ( $53^\circ$  and  $70^\circ$ ). The maximum values were reached at 23h33 for all frequency/polarization/incidence angle combinations with a warming rate of  $0.34$  and  $0.4 \text{ K}\cdot\text{h}^{-1}$  for  $53^\circ$  and  $70^\circ$  respectively. In the vertical polarization,  $T_b$ 's were higher at an incidence angle of  $53^\circ$  than they were at  $30^\circ$  in the horizontal polarization. As we observed in thin snow covers, 85 GHz brightness temperatures decreased at 2h43 in both polarizations (Figure-5.11 e and f). The decrease was of the same order of magnitude as measured over thin snow (i.e. 5 K in the V-pol. and 10 K in the H-pol.).

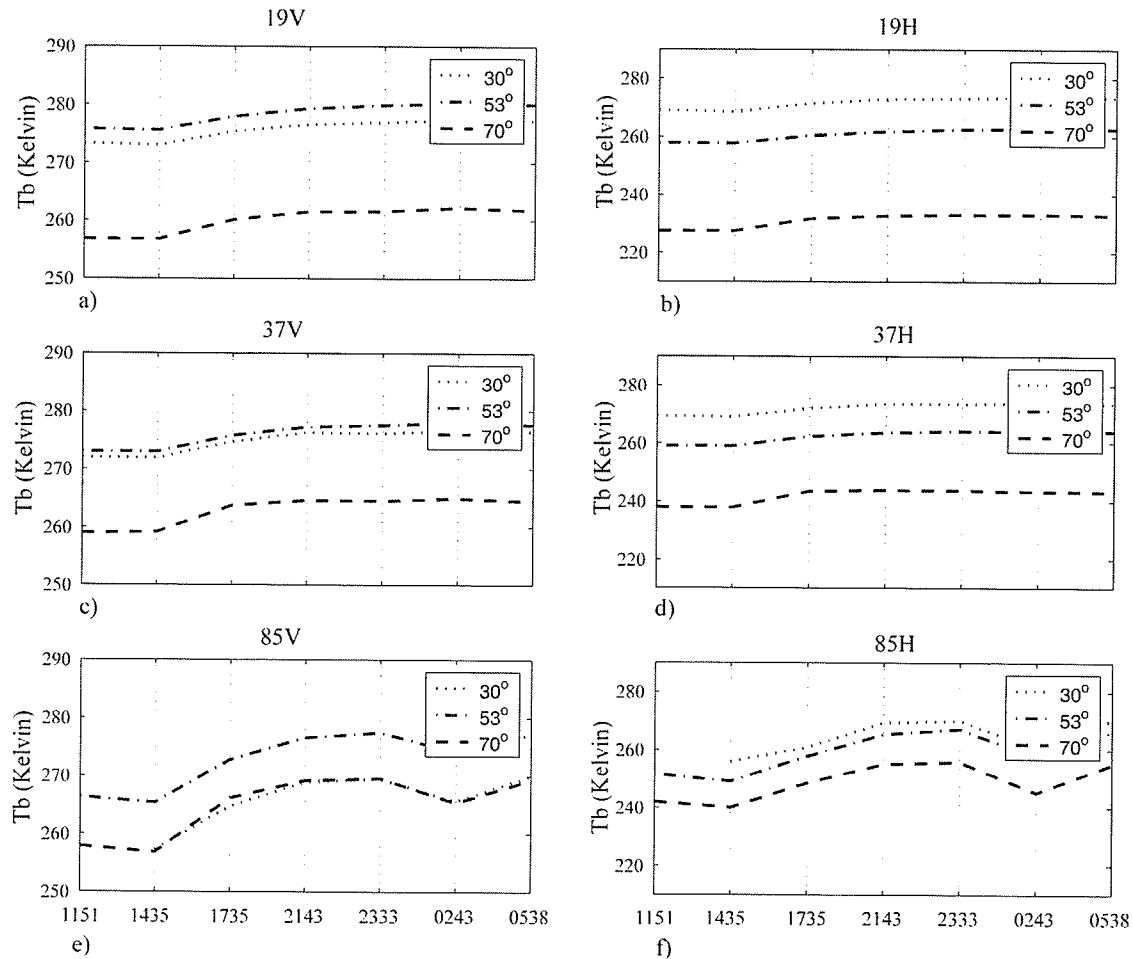


**Figure-5.11:** Temporal evolution of passive microwave brightness temperatures for the vertical and horizontal polarizations at 19 GHz (a and b), 37 GHz (c and d) and 85 GHz (e and f).

### 5.3. Discussion

#### 5.3.1. Thin Snow Processes

The passage of a low-pressure system produced detectable changes in snow geophysical properties including temperature and brine volume. The LPD gave rise to wind pumping, known to change heat and mass transfer. Brine volume migrated upward within the air pores in L4\_2 as depicted in Figure-5.3 b. Concordantly,  $k_s$  increased significantly between 21h30 and 6h40 since brine volume thermal conductivity is close to ice ( $\sim 1.6$  and  $2.2 \text{ W}\cdot\text{m}^{-1}\cdot\text{K}^{-1}$ ), which is much higher

than  $k_{air}$  at  $\sim 0.025 \text{ W}\cdot\text{m}^{-1}\cdot\text{K}^{-1}$  (McKay, 2000; Pollard and Kasting, 2005). Furthermore, the migration of brine within a layer increased the specific heat until 00h35 (Pollack *et al.*, 2003). Such increase is translated by a decrease in thermal diffusivity as more energy is used within one layer (i.e. less available for diffusion). We observed this inversely proportional relationship on Figure-5.5 b and c as the maximum  $c_s$  values at 00h35 correspond to the minimum value of  $v_s$  (Yen, 1981; Sturm *et al.*, 1997). This concept is of primary importance due to its control on the snow/ice interface temperatures (Sturm *et al.*, 1997; Bartlett *et al.*, 2004), which in turn can greatly affect microwave emission and scattering mechanisms (Eppler, 1992; Barber *et al.*, 1998). This concept will be discussed in details in the following section.

We showed over the diurnal period that there was a detectable increase in grain size under a LPD. Langlois *et al.* (2007a) measured growth rate of  $0.25 \text{ mm}^2\cdot\text{day}^{-1}$  in thin snow covers (4-10 cm) during the coldest season, a much lower value than what was measured in this study ( $1.28 \text{ mm}^2\cdot\text{day}^{-1}$ ). The temperature gradients (Figure-5.2 a) we measured in this study (maximum of  $1.2 \text{ }^\circ\text{C}\cdot\text{cm}^{-1}$  at 12h50) are sufficient to induce snow grain metamorphism, which seemed to occur throughout our sampling period (e.g., Bergen, 1968; Colbeck, 1982, 1993). Interestingly, Colbeck (1980) showed that a local temperature gradient as small as  $10^{-2} \text{ }^\circ\text{C}\cdot\text{cm}^{-1}$  could result in a grain growth of 0.1 mm. We speculate from these results that grain growth may be episodically large under the influence of LPD's and that the accumulation of many LPD events may have a cumulative effect on the mid pack snow grains, and through this on the surface albedo.

The vapor flux was on average  $+1.5\cdot 10^{-7} \text{ kg}\cdot\text{m}^{-2}\cdot\text{s}^{-1}$ , which positive value suggests a gain in mass (Sturm and Benson, 1997), but no other data set provides such data over first-year sea ice.

However, work done by Sokratov and Maeno (2000) suggest that our vapor flux values fall within the range of what they measured over land. Since the diurnal period occurred in the cooling period (see Langlois *et al.*, 2007a), we looked at the vapor flux values under high-pressure systems to see if any differences exist between the two cases. Between day 57 and 62, a high-pressure system was located over the region and concordant snowpit analysis showed vapor fluxes of  $-1.22 \cdot 10^{-7} \text{ kg} \cdot \text{m}^{-2} \cdot \text{s}^{-1}$  suggest a loss of mass due to sublimation (Sturm and Benson, 1997; Baunach *et al.*, 2001). We also calculated the vapor flux between days 37 and 41 where another important high-pressure system resulted in vapor flux values oscillating around  $8 \cdot 10^{-7} \text{ kg} \cdot \text{m}^{-2} \cdot \text{s}^{-1}$ . Since both systems resulted in lower vapor pressure values than under a LPD, we can speculate that the vapor flux is accelerated by low-pressure systems. We note that further investigations are required to further refine this speculation. However, the temperature gradient between day 37 and 41 were lower (average of 1.22 and 0.98  $^{\circ}\text{C} \cdot \text{cm}^{-1}$  through L6\_4 and L2\_si respectively) than recorded on the previous snow sampling set on day 31 (average of 2.35 and 2.1  $^{\circ}\text{C} \cdot \text{cm}^{-1}$ ). Assuming an accelerated vapor flux, snow grain kinetic growth is expected to increase (Albert., 2002).

### 5.3.2. *Thick Snow Processes*

The upward brine migration measured in thin snow covers was also measured in thick snow as shown in Figure-5.7 b. There is no evidence of increasing permittivity and dielectric loss (Figure-5.8 a and b) in the middle layers due to discrepancies in the density measurements affecting the dielectric calculations. The variations measured in the density values were too large to be natural thereby significantly affecting the dielectric calculations. The decrease at L10\_8

and L6\_6 is due to abnormal low-density measurements at 3h00. However, values at L16\_14 and L2\_si did increase at the end of the sampling period between 00h05 and 6h05. The increase in brine was measured at L4\_2 and L2\_si, but the impact on thermal conductivity was only noticed at L2\_si with a slight increase between 00h05 and 6h05. The effect of brine migration was mostly noticed through specific heat, which values at L4\_2 peaked at 3h00 (Figure-5.9 b). As observed in thin snow, the thermal diffusivity decreased accordingly and reached its minimal value for the diurnal period.

Thick snow grain growth rate was measured at  $0.5 \text{ mm}^2 \cdot \text{day}^{-1}$  by Langlois *et al.* (2007a) during the same period and location, and again this value is much lower than what we measured under the LPD at  $2.3 \text{ mm}^2 \cdot \text{day}^{-1}$  (Figure-5.10). The average temperature gradient  $0.5 \text{ }^\circ\text{C} \cdot \text{cm}^{-1}$  during the duration of the sampling period, a value well above what is necessary to trigger temperature gradient metamorphism ( $\sim 0.25$  to  $0.3 \text{ }^\circ\text{C} \cdot \text{cm}^{-1}$  in Colbeck, 1983; Sturm *et al.*, 2002). The average vapor flux was  $+1.94 \cdot 10^{-7} \text{ kg} \cdot \text{m}^{-2} \cdot \text{s}^{-1}$ , higher than what was observed in thin snow. However, no physical data were available for thick snow to calculate a comparable vapor flux under a high-pressure system during this period. It is not surprising to have higher vapor flux values in thick snow covers due to the greater amount of liquid water content (e.g., Sturm and Johnson, 1991; Zhekamukhova, 2004). Due to the high rate of grain growth, it can be assumed that the LPD accelerated kinetic growth as observed in thin snow.

### 5.3.3. Snow Properties and $T_b$ Variations

During our sampling period, the temperature gradients remained linear, but more brine was available throughout the night with maximum air temperatures. The brine volume migration increased the permittivity and dielectric loss of the snow. The sensitivity of dielectric properties to increasing brine volume is well understood (e.g., Tiuri *et al.*, 1984; Carsey, 1992; Eppler, 1992), however no dataset has yet shown that this migration could occur over a single diurnal period in the middle of the arctic winter.

The microwave response did not appear to capture the observed increase in grain size, or at least it was masked by a corresponding increase in microwave emission due to increased brine volume. In either case the 19 and 37 GHz frequencies both showed a small increase in brightness temperature over the diurnal period (Figure-5.11 a to d). Interestingly, there was a decrease of 5 K at 85 GHz vertically polarized and 10 K in the horizontal polarization at 2h43 where the basal layer snow grains were at their maximum size. However, it is not likely that grain size explains the variations in 85 GHz  $T_b$ 's since large grains were also present on the previous snowpit sampling (SP4) without measuring any changes in the 85 GHz brightness temperatures. However, coincident to this decrease in 85 GHz  $T_b$ 's, we measured maximum values in salinity and brine volume (i.e. high permittivity and dielectric loss). The increasing permittivity decreased the emission contribution from the brine-rich basal layer that will decrease the overall brightness temperature (e.g., Tiuri *et al.*, 1984; Walker and Goodison, 1993; Barber *et al.*, 2003), confirming the high sensitivity of high frequencies to small increase in liquid water fraction and brine in the snow.

#### 5.4. Conclusion

Our intention in examining this case study was to 1) document the geophysical, and thermodynamic response of snow over landfast first-year sea ice to a low pressure system and 2) determine whether microwave radiometry could detect the changes imparted by this low pressure system on the snow/sea ice geophysics. We showed that grain size changed over the study period at the bottom of both thin and thick snowpacks. We speculate that the LPD imparted a sufficiently strong effect on grain metamorphism that these systems could be considered as forcing episodic increases in grain size due to kinetic grain growth. The accumulation of several episodes of large rates of grain growth, from many LPDs, may be a significant seasonal feature of cyclones over snow covered sea ice due to the control this will have on radiative transfer in the spring. We note however that these grain size changes were not large enough to be detected by microwave radiometry directly. We speculate that this was because the absolute grain size increase had less of an effect than the concomitant increase in permittivity and loss (due to increased brine volume) at 19 and 37 GHz. It is difficult to compare both thin and thick snow from a passive microwave response perspective, as the incidence angles are not the same. However, at both low and high incidence angles ( $30^\circ$  to  $45^\circ$  over thin;  $55^\circ$  to  $70^\circ$  over thick), 85 GHz did respond to increasing salinity and brine volume in the middle layers of the snowpack due to the combined influence of wind pumping (common under low-pressure systems) and low-to-medium temperature gradient. The maximum brine volume was reached between 3h00 and 3h30 on day 34 where the brightness temperature at 85 GHz did decrease significantly at both polarization. It was also shown that the snow grain growth rate is larger under the influence of a LPD. Rates of  $1.28$  and  $2.3 \text{ mm}^2 \cdot \text{day}^{-1}$  for thin and thick snow were measured between day 33 and 34 whereas previous work indicate rates of  $0.25$  and  $0.5 \text{ mm}^2 \cdot \text{day}^{-1}$  respectively.

It is an open question as to the possibility to detect LPD influences on the snow/sea ice geophysics at a satellite remote sensing scale. Our in situ observations suggest that 85 GHz data can detect the increased grain size and or increased brine volume. We can assume that stronger cyclonic events might be needed to detect the changes in snow thermophysical properties from a passive microwave spaceborne instrument such as AMSR-E, which resolution is 12.5 km. Furthermore, the amplitude of the change might allow detection at lower frequencies such as 19 and 37GHz. At this scale, the changes would still occur, but the spatial features (ridges, cracks, leads) might play a more important role in the microwave emission due to sub-pixel scale effects. I see this research as providing a first-step in understanding the role of cyclones in modifying snow and sea ice geophysics and the associated effects on gas, mass and energy transfer across the ocean-sea ice-atmosphere interface. As we move into the decades ahead we can expect cyclones to play an increasingly important role in the climate of fast and marginal sea ice zones.

Over the last two chapters, I have highlighted the linkages between snow thermophysical and electrical properties with passive microwaves. I have shown that seasonal (Chapter 4) and diurnal processes (this chapter) affect to different amplitudes, passive microwave brightness temperatures. The knowledge and data provided in these chapters allows me to now develop a snow water equivalence algorithm using *in-situ* snow and  $T_b$  measurements and discuss the limitations associated with its application. Thus, in the next chapter, I investigate the development of candidate SWE algorithms for different snow thickness, which I then apply to satellite remote sensing in Chapter 7.

## CHAPTER 6: DEVELOPMENT OF A SNOW WATER EQUIVALENT (SWE) ALGORITHM FROM *IN-SITU* DATA

In chapters 4 and 5, I established the linkages between snow thermophysical/electrical properties and *in-situ* passive microwave scattering and emission mechanisms on both short- and long-term scales. The understanding of those linkages is of primary importance in order to develop SWE algorithms and discuss their limitations. Hence, in this chapter, I provide results on the development of snow water equivalent algorithms over seasonally thin and thick snow as well as over a variable snow thickness. I then provide a validation and comparison with existing algorithms that were developed using both *in-situ* and satellite data and discuss the various processes that explain the differences observed. The material in this chapter has been published in the peer reviewed literature in Langlois *et al.* 2007b and Langlois and Barber 2007a.

### 6.1. Algorithm Development

To develop new SWE statistical algorithms, I used a multiple regression analysis with two independent variables (SWE and  $T_{\text{air}}$ ) and one dependent variable (brightness temperatures,  $T_b$ ). I tested the SWE predictions using other temperature combinations such as temperature gradient and snow/ice interface temperature ( $T_{\text{si}}$ ), but air temperature always provided the best predictions. I evaluated the normality of  $T_{\text{air}}$ , SWE and the associated brightness temperatures using a Lilliefors test for goodness of fit. Furthermore, I will explain later why I did not use the normalized brightness temperature difference ( $\Delta T_b$ ) commonly referred to in the literature as a good proxy for snow thickness.

I showed in Chapter 4 that brightness temperatures from thin to thick snow covers are quite different, but no threshold was clearly identified. The analysis from Langlois *et al.*, (2007b) did not provide information of the threshold since it focused on seasonally thin ( $< 40^\circ$  of incidence angle) and thick ( $> 55^\circ$  of incidence angle) snow covers separately as well as looking at the effect of incidence angle and polarization on the development of the algorithms. Between  $40$  and  $50^\circ$ , the snow thickness was not constant within the SBR field of view (Chapter 3), therefore was not used in the analysis. To provide a potential threshold, I needed to combine both thin and thick snow analysis at one incidence angle. At  $53^\circ$  and above, snow started thin, and then evolved in thickness whereas values at incidence angles below  $40^\circ$  remained thin throughout the study period (Figure-3.5). The thin to thick snow transition was then found between  $53$  and  $70^\circ$ , but only the range  $53 - 54^\circ$  is found on the current satellite passive microwave sensors. Nonetheless, the effect of incidence angle on SWE algorithm development is still unknown and needed to be clarified. Thus, this chapter first explores the effect of incidence angle on SWE algorithm development over thin ( $< 40^\circ$ , Section 6.1.1) and thick ( $> 55^\circ$ , Section 6.1.2) snow covers. Then, a SWE algorithm is developed at using the same methodology at incidence angles applicable to satellite remote sensing in terms of a measured thickness threshold between thin and thick snow covers ( $53^\circ$ , Section 6.1.3).

#### 6.1.1. Thin Snow ( $30^\circ - 40^\circ$ )

As mentioned above, low incidence angles sampled thin snow throughout the season ( $< 10$  cm). Thin snow can be found anywhere at anytime in the Arctic, therefore a SWE algorithm needed to be developed. From the normality score results, a candidate algorithm was proposed at

horizontally polarized 19 GHz brightness temperatures with an incidence angle of 40° (19H40). Using multiple regression analysis on the dependent variable ( $T_b$ ) and independent variables ( $T_{air}$  and SWE), the following algorithm provided the best SWE predictions with measured *in-situ* data:

$$SWE_{THIN} = \frac{(T_b 19H_{40^\circ} - 277.01 - 0.57T_{air})}{-1.15} \quad [\text{eq. 6.1}]$$

The comparison between modeled and measured SWE showed a good correlation with an  $R^2$  of 0.7 (RMSE = +/- 4.02 mm) and a slope of 0.76 (Figure-6.1 a). The temporal evolution of the residuals showed less scatter during the cold period than the warm period (lower dielectric constant in the cold period), which was divided on day 57 (Figure-6.1 b). The measured variations in % can be explained by slight spatial variability of snow thickness in the thin snow sampling area (Langlois *et al.*, 2007b). Furthermore, the radiometer's ground field of view was much larger than a snowpit (approximately 0.4 x 0.4 m). For example, over a thin snow cover, a difference between 4 cm and 6 cm in snow thickness can create difference up to 5 to 10 mm in SWE (up to 50 %) depending on the density of the missing thickness. As the sampling was arranged so that only thin snow covers were sampled, small variations in spatial thickness distribution will cause errors in SWE predictions.

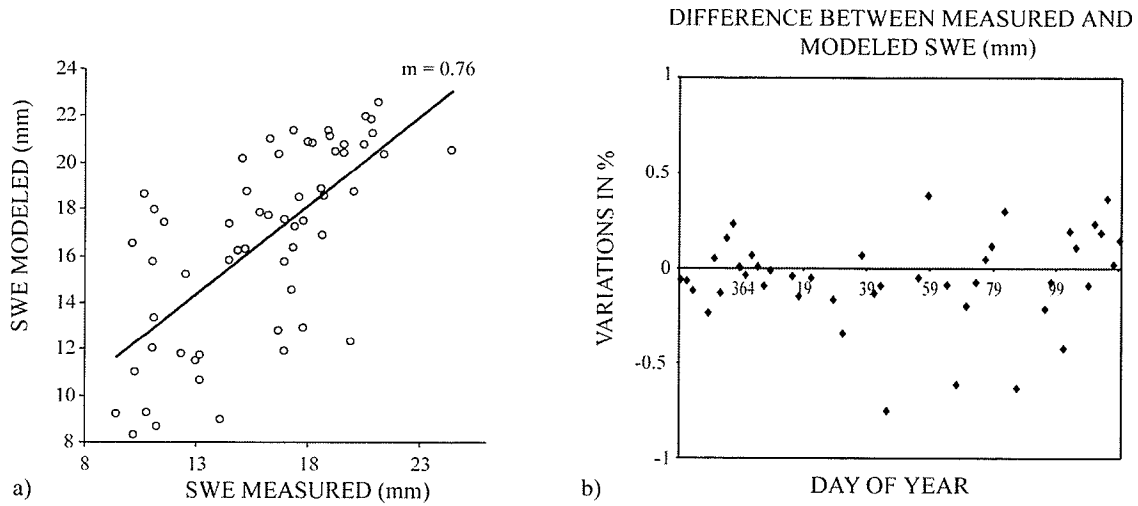


**Figure-6.1:** Comparison between the modeled and measured SWE values (a) and the temporal evolution of the variation (b) for thin snow covers.

### 6.1.2. Thick Snow ( $55^{\circ} - 70^{\circ}$ )

For seasonally thick snow covers, wide incidence angles were used again due to the snow distribution around the SBR location (see Chapter 3). From the normality test in the thick snow covers, the horizontally polarized brightness temperatures at  $55^{\circ}$  of incidence angle (19H55) was used in order to retrieve thick snowpacks SWE values. I use multiple regression with SWE and air temperature to propose the following algorithm to estimate SWE for thick snow covers:

$$SWE_{THICK} = \frac{(T_b 19H_{55^{\circ}} - 235.33 - 0.43T_{air})}{0.1} \quad [\text{eq. 6.2}]$$

Using the above algorithm, very good agreement between the measured and modeled SWE was measured ( $R^2 = 0.94$  and  $RMSE = \pm 29$  mm in Figure-6.2 a). The slope of 1.05 indicated very little bias from our proposed algorithm. The temporal evolution of the residuals between the measured and the modeled SWE showed stronger variations in the warming period between day 58 and 127 (Figure-6.2 b), which were concordant with increasing temperatures as the liquid water from melting affects the  $T_b$  signatures significantly (e.g., Lohanick and Grenfell, 1986; Walker and Goodison, 1993; Markus and Cavalieri, 1998; Singh and Gan, 2000; Pulliainen and Hallikainen, 2001; Barber *et al.*, 2003). The minimum differences between measured and modeled SWE were found during the coldest period of the sampling period between day 57 and day 67.

In both thin and thick snow covers, 19 GHz in the horizontal polarization showed better correlation with SWE when compared to 37 GHz. However, predictions at 37 GHz were statistically significant and one could use the same approach using this frequency with decent predictions. Furthermore, I used the same approach using the normalized brightness temperatures between 37 and 19 GHz ( $\Delta T_b$ ) as the dependent variable instead of  $T_b$ , but the results on the SWE prediction were not as good. This  $\Delta T_b$  is normally used for SWE retrieval over land, but the concept over sea ice more complicated since the relatively thin snow does not provide a good contrast between 19 and 37 GHz.

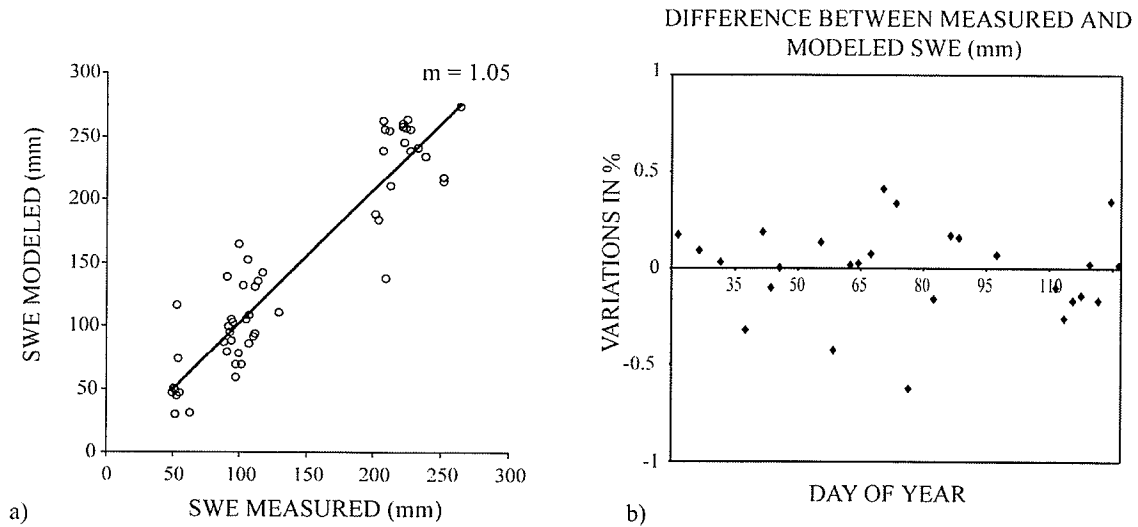
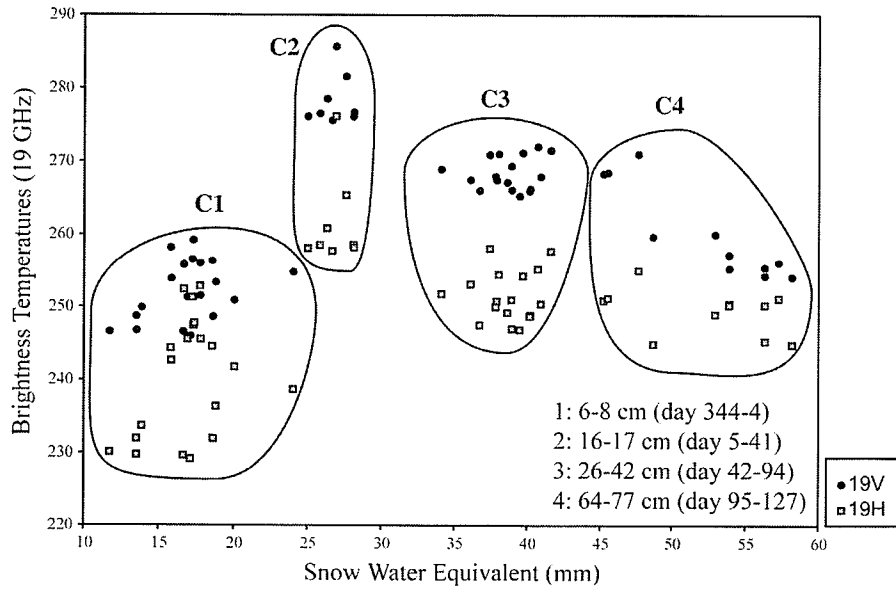


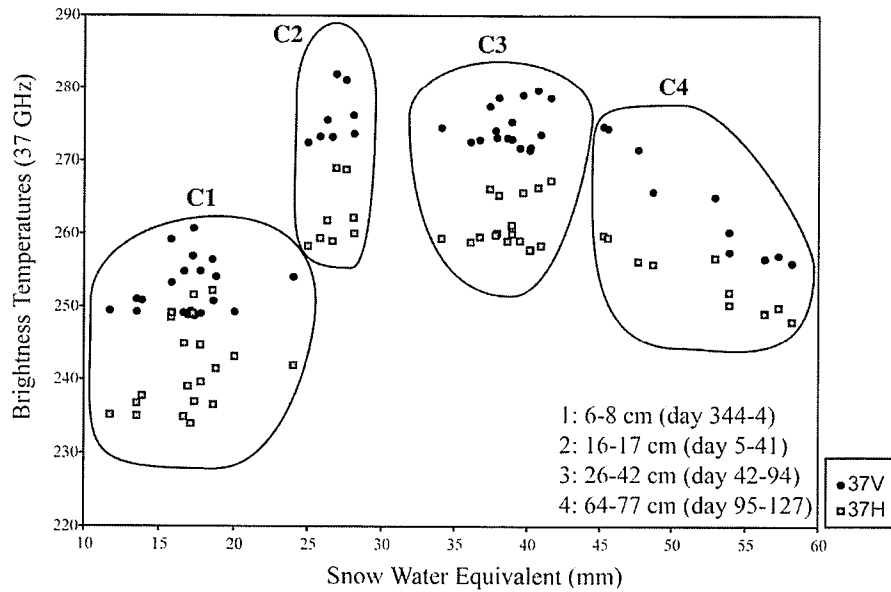
**Figure-6.2:** Comparison between the modeled and measured SWE values (a) and the temporal evolution of the variation (b) for thick snow covers.

### 6.1.3. Seasonally Evolving Snow Thickness (53°)

In Chapter 4, I did not include brightness temperatures at Brewster angle since the analysis was developed in order to apply the SWE algorithm over thin and thick snow cover separately (Sections 6.1.1 and 6.1.2). Though, as mentioned at the beginning of this chapter, I needed an analysis providing an evolving snow thickness (with identified threshold) at 53°. To do so, the snow analysis needed to be different since the coupling of evolving snow thickness with brightness temperatures was required in order to identify a threshold between the two thickness regimes. To develop this algorithm, the snow cooling period was separated in two clustered (C) periods (C1 and C2) and the warming period was also separated in two periods (C3 and C4). The reason for this is depicted in Figure-6.3 a and b where one can clearly distinguish 4 different ‘regimes’ in the SWE/ $T_b$  relationship at 53°.



a)



b)

**Figure-6.3:** Relationship between brightness temperatures ( $53^\circ$ ) and evolving snow water equivalent (SWE) for a) 19 GHz and b) 37 GHz.

Both C1 and C2 brightness temperatures increased with increasing SWE, whereas C3 and C4  $T_b$  decreased with increasing SWE. The ‘switch’ occurred between C2 and C3 at a median thickness value of 24 cm (33 mm of SWE on Figure-6.4).

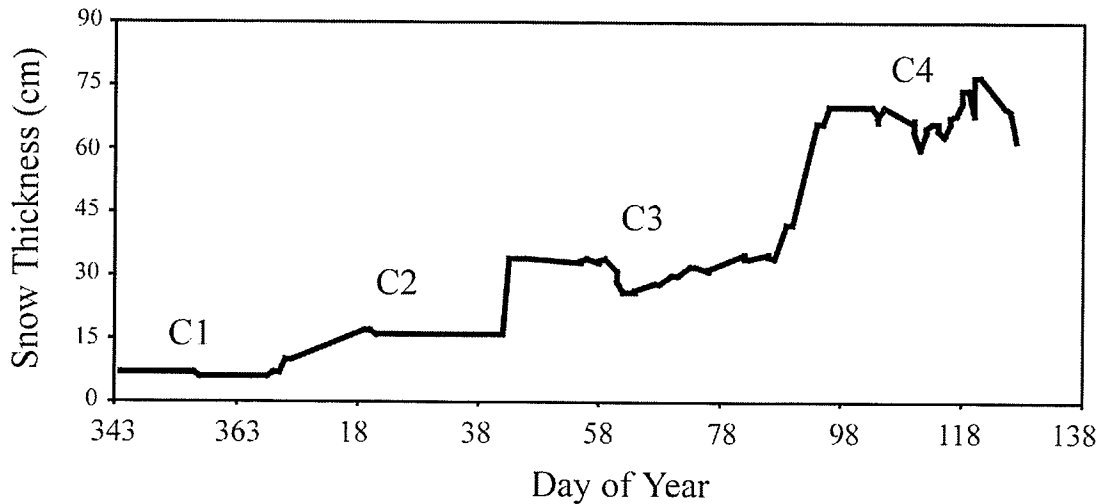


**Figure-6.4:** Temporal evolution of snow thickness (cm) at 53° of incidence angle.

Using a similar methodology as in Section 6.1.1 and Section 6.1.2, I applied a multiple regression analysis on C1 and C2 separately from C3 and C4 using one of air, surface, or snow/ice interface temperatures along with the SWE as independent variables (Table-6.1a and b) and a combination of frequency and polarization as the dependent variable.

In general, better-fit results were found during C1 and C2 using the vertical polarization signal at both 19 and 37 GHz. For C1 and C2 snow, the 19 GHz v-pol signal with  $T_{air}$  gives the best results (Table-6.1 a) whereas results C3 and C4 obtained better results using the 37 GHz v-pol signal with  $T_{air}$  (Table-6.1 b).

**Table-6.1:** Correlation coefficient between air, surface, snow/ice interface temperatures and temperature gradient with 19 and 37 GHz for a) C1 and C2 periods and b) C3 and C4 periods.

Multiple Regression $R^2$ values for C1 and C2				
	Tair	Tsurface	Tsi	Tair-Tsi
19V	0,81	0,80	0,80	0,81
19H	0,61	0,61	0,59	0,65
37V	0,81	0,80	0,79	0,80
37H	0,77	0,76	0,72	0,78

a)

Multiple Regression $R^2$ values for C3 and C4				
	Tair	Tsurface	Tsi	Tair-Tsi
19V	0,75	0,75	0,74	0,75
19H	0,13	0,13	0,13	0,22
37V	0,80	0,80	0,80	0,81
37H	0,67	0,67	0,66	0,68

b)

A significant relationship was also found using the  $T_{air} - T_{si}$ , gradient but  $T_{air}$  is much easier to retrieve from a weather station, regional reanalysis or satellite datasets (see Chapter 7). My best-fit SWE prediction algorithm then becomes:

$$SWE = \frac{T_{h-19V} - 0.24T_{air} - 219.54}{2.29}, \quad [\text{eq. 6.3}]$$

for  $0 < SWE < 33$  mm,  $-30.3 < T^\circ < -5$  ° C and  $246 < T_b < 288$  K and

$$SWE = \frac{T_{b-37V} + 0.01T_{air} - 309.69}{-0.9}, \quad [\text{eq. 6.4}]$$

for  $33 < SWE < 55 \text{ mm}$ ,  $-30.3 < T^\circ < -5^\circ \text{ C}$  and  $256 < T_b < 280 \text{ K}$ .

The pair of algorithms accumulate snow using [eq. 6.3] until SWE reaches 33 mm at which point it switches to [eq. 6.4], valid up to 55 mm. This range of application is typical of snow thickness distributions on first-year sea ice (Iacoza and Barber 2001). Coupling our algorithms to the annual *in-situ* measurements, I obtained a correlation ( $R^2$ ) of 0.95 (RMSE of +/- 3.25 mm,  $m = 1.007$ ) for the period from December to May (Figure-6.5).

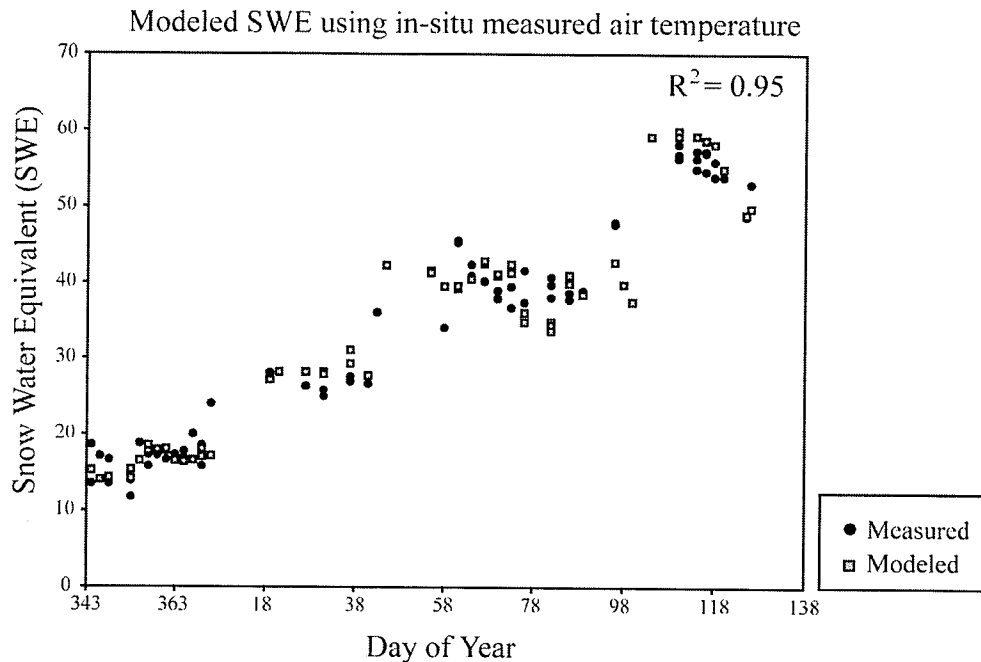


**Figure-6.5:** Correlation between measured and modeled snow water equivalent (SWE) at  $53^\circ$  of incidence angle.

These results provide a significant improvement over previous research in the range for which the algorithms are valid. The predicted values shown in Figure-6.5 are typical for a snow thickness evolution of  $0.50 \text{ cm day}^{-1}$  between day 344 and 127 with air temperatures below  $-5 \text{ }^\circ \text{C}$  throughout the period.

## 6.2. Comparison

I compared our results from Section 6.1.3 with other SWE prediction algorithms published in the literature. I focused on two algorithms that apply to *in-situ* measurements of snow over sea ice (Barber *et al.* 2003 and Section 6.1.2) and two for satellite measurements (Markus *et al.* 2006, Cavalieri and Comiso 2004).

### 6.2.1. In-Situ Algorithms

Research done by Barber *et al.*, (2003) also used a multiple regression solution based on temperatures to produce a prediction of SWE. Interestingly, they too found better results using a single frequency and polarization (37 GHz, h-pol) based on the surface-based radiometer data so that:

$$SWE = \frac{T_b 37H_{55^\circ} - 264.301 - 0.726 \cdot T_{air}}{0.014}, \quad [\text{eq. 6.5}]$$

I obtained poor results after testing this algorithm against our *in-situ* measurements of SWE. The algorithm was most accurate during the C2 and C3 periods only in the range of snow thickness

for which it was developed. Predictions underestimated measured SWE by approximately 50 % throughout C2 and C3.

The shortcomings observed are likely due to the short seasonal development of the algorithm, conducted between April 29th and May 8th when snow thickness varied between 9 and 29 cm. It is for reasons such as this that this work focuses on the whole seasonal evolution of the snowpack, valid over a variety of snow thickness and air temperatures, encompassing the period used in Barber *et al.*, (2003).

From the algorithms in Sections 6.1.1 and 6.1.2 (Langlois *et al.*, 2007b), I obtained the most significant results by distinguishing thin and thick snow cover but no threshold value was identified. I applied the thin snow SWE algorithm to C1 and C2 as:

$$SWE_{THIN} = \frac{(T_b 19H_{40^\circ} - 277.01 - 0.57T_{air})}{-1.15} \quad [\text{eq. 6.6}]$$

When using this algorithm at the Brewster angle, I obtained reasonable results, with an  $R^2$  of 0.68. The algorithm overestimated C1 SWE (by approximately 31 %) and dramatically underestimated those in C2.

$$SWE_{THICK} = \frac{(T_b 19H_{55^\circ} - 235.33 - 0.43T_{air})}{0.1} \quad [\text{eq. 6.7}]$$

When applying the thick snow algorithm (to C3 and C4), I also obtained poor results due to the limited range of thickness upon which the algorithm was based. The predicted values overestimated our measured values by a factor of 10. Furthermore, the incidence angle in their study was different than the one in this work, a complication that can cause significant differences in the brightness temperatures, especially in the warmer period (e.g., Tiuri, 1984; Eppler, 1992; Powell *et al.*, 2006).

### 6.2.2. Satellite Algorithms

Markus *et al.*, (2006) used satellite based AMSR-E brightness temperatures accounting for ice ( $T_{b-ICE}$ ) and open-water ( $T_{b-OW}$ ) brightness temperatures and ice concentration ( $C$ ) (Markus and Cavalieri 2000):

$$T_{b-SAT} = C \cdot T_{b-ICE} + (1 - C) \cdot T_{b-OW} , \quad [\text{eq. 6.8}]$$

In our case, the sampling area was located in a smooth pan of landfast first-year sea ice (Langlois *et al.*, 2007a), which covered 100 % of the Franklin Bay region so that:

$$T_{b-SAT} = T_{b-ICE} , \quad [\text{eq. 6.9}]$$

In Markus *et al.*, (2006), the spectral-ratio difference in brightness temperatures between 19 and 37 GHz (GR) in the vertical polarization was analysed, such that  $GR_{ICE} = GR$  from [eq. 6.10]:

$$GR = \frac{T_b 37V - T_b 19V}{T_b 37V + T_b 19V}, \quad [\text{eq. 6.10}]$$

Snow depth ( $h_s$ ) was then retrieved using:

$$h_s[\text{cm}] = 2.9 - 782 \cdot GR, \quad [\text{eq. 6.11}]$$

The coefficients in [eq. 6.11] are from the AMSR-E sensor (Comiso, 2003). This algorithm was developed in the Antarctic so that it can only be applied over first-year sea ice in the Arctic due to the similar brightness temperatures signatures between multi-year sea ice and deep snow. When I applied this equation to our *in-situ* measurements, I obtained poor thickness predictions, with negative values in 56 % of the cases. Otherwise, the algorithm underestimated thickness in all C1, C2, C3 and C4 periods, confirming the observation that brightness temperature difference might not appropriate over first-year sea ice (Armstrong and Brodzik, 2001; Barber *et al.*, 2003; Foster *et al.*, 2005; Langlois *et al.*, 2007b).

Another satellite-based algorithm, developed by Cavalieri and Comiso (2000), also used [eq. 6.9 and 6.10], but with different coefficients. Snow depth was retrieved using:

$$h_s[\text{cm}] = -2.34 - 771 \cdot GR, \quad [\text{eq. 6.12}]$$

This algorithm did not perform better than that developed by Markus *et al.*, (2006), with negative thickness values in 84 % of our measurements and a greater underestimation in the positive values. Again, these algorithms were developed using AMSR-E brightness temperatures data

that can be significantly different than SBR measurements due to the contribution of various spatial features in a 12.5 km pixel compared to the protected area where our measurements occurred. This issue of mixed-pixel measurements will be addressed later in Chapter 7.

### **6.3. Conclusions**

#### *6.3.1. Seasonally Thin and Thick Snow Algorithms*

In both thin and thick snow covers (Sections 6.1.1 and 6.1.2), 19 GHz in the horizontal polarization showed better correlation with SWE when compared to 37 GHz. I used the same approach using the normalized brightness temperatures between 37 and 19 GHz (37-19), but the results on the SWE predictions were not as good in both cases. During the cooling period, the snowpack was characterized by very little changes in thermophysical properties (Chapter 4). The results showed that the variations in  $T_b$  for thin snow ( $< 40^\circ$ ) over the cooling period were mainly attributable to changes in air temperature with fairly constant snow physical properties. The warming period was characterized by significant changes in high frequency  $T_b$ , coincidentally with increasing grain size (i.e. increasing volume scattering), temperatures and liquid water content (increasing absorption). The thick snowpack ( $> 50^\circ$ ) properties also show little variation during the cooling period and brightness temperatures were again strongly linked to air temperature. Significant changes occurred during the warming period with flooding of the snow basal layers that significantly increased microwave emission. Therefore,  $T_b$  were strongly linked to water content (towards a black body behavior), which furthers our understanding of our SWE prediction variations.

The algorithm over thin snow covers used 19H40 (Section 6.1.1) as the best frequency/polarization/incidence angle combination for multiple regression with  $T_{\text{air}}$  and SWE. Throughout the observational period, good correlation was found for this algorithm when compared with field data. The algorithm performed better during the cold and dry period due to very limited metamorphism during this period. The differences were attributed to the variations in  $T_{\text{air}}$  and snow wetness, which affects the  $T_b$  without affecting significantly the SWE values. Scale difference (spatial heterogeneity) between the radiometer ( $\text{m}^2$ ) and the snow pit ( $\text{cm}^2$ ) had also played a role in the SWE prediction variations.

The same statistical approach was used to retrieve SWE from thicker snowpacks (Section 6.1.2). Results showed that the 19H55 combination gave the best prediction results. Validation of the proposed algorithm also showed significant results between the observed and modeled data. I explain the prediction errors with sudden variations in air temperature and flooding (starting on day 91) that significantly increased the  $T_b$ . Furthermore, spatial heterogeneity in snow thickness also contributed in the SWE prediction variations (Derksen *et al.*, 2005) since the radiometer measured thick snow cover emissivity at wide incidence angles (50 to 70°) when compared to thin snowpacks (30 to 40°).

Generally, my proposed algorithms from Sections 6.1.1 and 6.1.2 performed quite well throughout the study period using all the diurnal data morning, noon and afternoon measurements (algorithm developed using morning data only). The performance of both algorithms was stronger at cold temperatures, where snow metamorphism is not a determining factor in changing SWE values (Langlois *et al.*, 2007a). From the algorithmic perspective, the sensitivity to air

temperature decreased with increasing snow thickness. Variation in air temperature over thin snow covers had a greater impact on the variations when compared with thick snow covers. For example, with a constant measured SWE value, a sudden increase of 10°C in  $T_{\text{air}}$  means an uncertainty of approximately 45 % over thin and 17 % over thick snowpacks. This is why the most important variations occurred in the transition seasons (fall-winter and winter-spring) where the air temperatures vary on a daily basis.

### 6.3.2. *Variable Thickness Snow Algorithm*

In Section 6.1.3, I evaluated the impact of seasonal snow thermophysical properties on the brightness temperatures at an incidence angle of 53° for both 19 and 37 GHz. I found that the seasonal pattern in  $T_b$  was quite different given the seasonally variable thermal regime that affects snow thermodynamic processes such as kinetic growth. During the first half of the winter (C1 and C2),  $T_b$  was dictated by desalination processes, as thickness did not yet play an important role in volume scattering (Figure-6.3). In the latter part of the winter, significant changes occurred in the snow with increasing grain growth and consequent volume scattering. As temperatures rose, the amount of liquid water in the upper part of the snow cover increased the permittivity, which decreased the emissivity contribution of the bottom part of the snowpack (decrease in  $T_b$ ).

I developed a seasonal SWE retrieval algorithm over first-year sea ice valid from 0 to 55 mm for a temperature range between -30.3 and -5 °C. I showed in Chapters 4 and 5 that different snow thickness behaves quite differently thermodynamically on short- and long-terms, thereby

affecting the snow microwave emissivity. For an evolving snow cover, I identified a snow thickness at which a different algorithm is needed to retrieve SWE prediction values (33 mm of SWE). The combination of both algorithms was necessary and provided a seasonal SWE prediction  $R^2$  of 0.95. This is a significant advance over previous results and is currently the only seasonally valid SWE algorithm for application over first-year sea ice.

I compared our algorithm with existing *in-situ* and satellite products and achieved superior results. The main shortcoming of previous work seems to be due to the limited thickness and temperature ranges over which earlier algorithms were developed. Further complications in the use of satellite data arise from the radiometry physics that must account for such factors as the atmospheric upwelling and downwelling contributions on  $T_b$  (e.g., Matzler, 1992; Kerr and Njoku, 1990). Furthermore, the satellite algorithms are constrained by large 12.5 x 12.5 km pixels that, in addition to the spatial variability of snow thickness, encompass a variety of spatial features such as ice ridges and re-frozen leads. Ice roughness affects brightness temperatures, and its potential effect on the application of the algorithm proposed in Section 6.1.3 to satellite remote sensing is addressed in the next chapter.

## **CHAPTER 7: SATELLITE REMOTE SENSING OF SNOW WATER EQUIVALENT (SWE)**

In Chapter 6, I developed snow water equivalence algorithms using *in-situ* surface based radiometers and snow measurements. In the conclusions, I discussed the applicability of the algorithms from Section 6.1.3 to satellite passive microwave data. Thus, as mentioned in Chapters 1 and 2, the difference in scale from *in-situ* measurements to satellite signatures represents one of the main challenges in SWE retrievals due to the atmospheric contributions to  $T_b$  and the spatial heterogeneity of snow thickness and ice roughness (i.e. different processes affecting different scales). These limitations are minimal in surface based radiometer (SBR) measurements since the atmospheric contribution to the antenna is rather low and the footprint (see Chapter 3) very small (low spatial heterogeneity). Therefore, in this chapter I evaluate the performance of the algorithm developed in Chapter 6 when applied to AMSR-E satellite data using measured *in-situ* SWE measurements and discuss the differences observed. Also, I explore the effect of surface roughness on SWE predictions using a combination of satellite passive and active microwave measurements.

### **7.1. SWE Algorithms**

I employed the SWE algorithms developed in Langlois and Barber, (2007a) using *in-situ* SBR passive microwave data coupled with ancillary seasonal snow thermophysical properties (see Chapter 6). This algorithm adjusts for evolving snow thickness using a combination of two

multiple regression-based algorithms valid over the range  $-30 < T^{\circ} < -5$  °C and  $0 < SWE < 55$  mm given as:

$$SWE = \frac{T_{b-19V} - 0.24T_{air} - 219.54}{2.29}, \quad [\text{eq. 7.1}]$$

for  $0 < SWE < 33$  mm,  $-30.3 < T^{\circ} < -5$  °C and  $246 < T_b < 288$  K and

$$SWE = \frac{T_{b-37V} + 0.01T_{air} - 309.69}{-0.9}, \quad [\text{eq. 7.2}]$$

for  $33 < SWE < 55$  mm,  $-30.3 < T^{\circ} < -5$  °C and  $256 < T_b < 280$  K.

From the above equations, air temperatures are required to predict SWE and *in-situ* air temperatures were available through the CASES period (Langlois *et al.*, 2007a and b). For satellite remote sensing applications, I compared *in-situ* meteorological tower measurements with MODIS ice surface temperatures and the modeled North American Regional Reanalysis (NARR) 2-m air temperature data in order to decide which of the two products would be the most appropriate for [eq. 7.1 and 7.2].

### 7.1.1. *In-situ Meteorological Tower*

The *in-situ* values of  $T_{air}$  were taken from a meteorological tower that was maintained on the ship throughout the CASES overwintering mission. The ship was equipped with an AXYS Automated Voluntary Observation Ship (AVOS) system on the roof of the wheelhouse away from all disturbances caused by the proximity of the ship (see Chapter 3). The AVOS system is an interactive environmental reporting system that transmitted hourly weather conditions.

Temperatures (air and sea surface), pressure, wind speed, wind direction, and current GPS location were updated every 10 minutes and averaged daily.

### 7.1.2. MODIS

MODIS/Aqua Daily L3 Global 4km EASE-Grid ice surface 'skin' temperatures (IST) were retrieved for the AMSR-E pixels locations from Chapter 3 and assumed to be equal to air temperatures. I averaged the temperatures values of 3 x 3 pixels encompassed within each AMSR-E pixel. The MODIS data algorithm uses a Normalized Difference Snow Index (NDSI) modified for sea ice to distinguish sea ice from open ocean based on reflective and thermal characteristics (Hall *et al.*, 2007). The ice surface temperature data are expressed in Kelvin using local calibration data. The algorithm assumes that sea ice is snow covered and that snow dominates the reflectance characteristics. Furthermore, a cloud mask algorithm distinguishes clouds from ice in the output product (Hall, 2004). Accuracy of IST is estimated to be 0.3 to 2.1 K over the 245-270 K range for all ice types (Key *et al.*, 1997). MODIS Airborne Simulator (MAS) data and campaign field data are currently used to establish bounds for MODIS IST accuracy. I retrieved the average temperatures over a 3200 km<sup>2</sup> area within Franklin Bay (average over 10 x 20 pixels at 4 km resolution).

### 7.1.3. North American Regional Reanalysis (NARR)

Finally, I also extracted 2-m air temperatures from the North American Regional Reanalysis (NARR) model from the National Centers for Environmental Prediction (NCEP) Environmental Modeling Center (EMC). I used daily average values from 9 pixels (3 x 3 at 32 km resolution) located within Franklin Bay and Amundsen Gulf encompassing AMSR-E and MODIS pixels.

The horizontal resolution is 0.3 degrees on the Eta AWIP grid and the temporal resolution is 8 times daily (every 3 hours) and averaged over a 24-hour period. Further details on the NARR reanalysis can be found at <http://wwwt.emc.ncep.noaa.gov/mmb/rrean/>.

## 7.2. Results and Discussion

### 7.2.1. Air temperatures

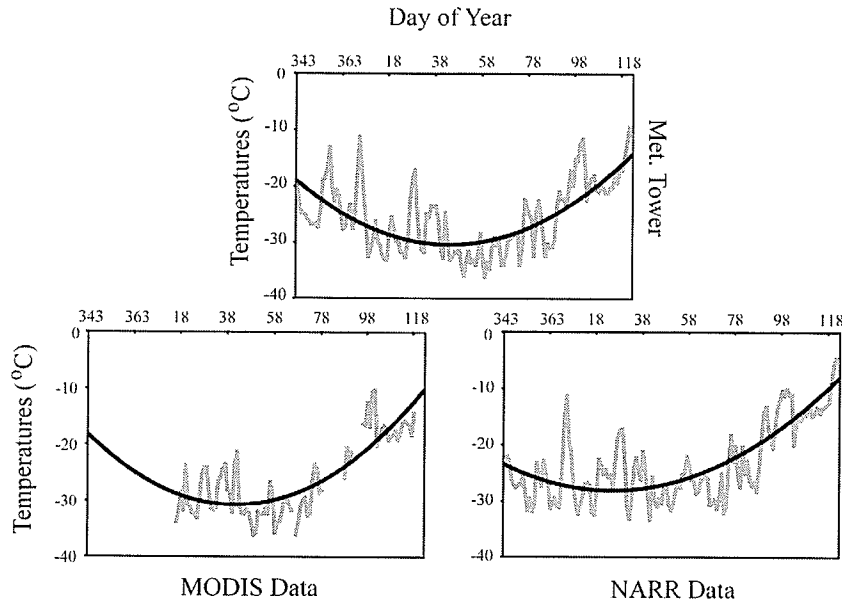
The *in-situ* air temperatures from the meteorological tower followed a typical seasonal evolution pattern with a cooling period (days 343-59) and a warming period (days 60-122). Values between days 343 and 59 decreased at a rate of  $0.2\text{ }^{\circ}\text{C}\cdot\text{day}^{-1}$  then reached a minimum daily average value of  $-36.24\text{ }^{\circ}\text{C}$  (Figure-7.1a). The largest variations were measured on days 357, 5 and 29 where temperatures peaked to  $-13.1$ ,  $-11.23$  and  $-17\text{ }^{\circ}\text{C}$  respectively. Smaller variations were observed during the warming period with the exception of one significant increase between days 85 and 101 in the order of  $1.3\text{ }^{\circ}\text{C}\cdot\text{day}^{-1}$ .

Daily MODIS ice surface temperatures were only available for day 14 onward (Figure-7.1a). The minimum temperatures were reached on day 67 at  $-36.15\text{ }^{\circ}\text{C}$  and increased afterwards until the end of the sampling period on day 122. Maximum temperatures were measured on day 101 at  $-10.28\text{ }^{\circ}\text{C}$ , and the warming rate between day 67 and day 122 was  $0.46\text{ }^{\circ}\text{C}\cdot\text{day}^{-1}$ .

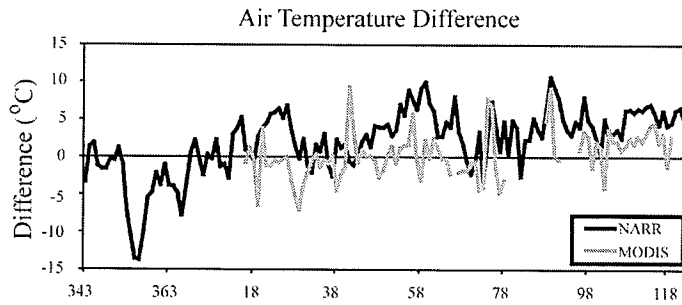
Daily NARR 2-m air temperature data are depicted in Figure-7.1a. These data were available for the entire study period from day 343 and 122. Air temperature values decreased between day 343 and 41 where the seasonal minimum was reached for the region at  $-33.4\text{ }^{\circ}\text{C}$ . The decrease was in

the order of  $0.17 \text{ }^{\circ}\text{C}\cdot\text{day}^{-1}$  followed by a steady warming period until day 122. The warming rate was approximately  $0.35 \text{ }^{\circ}\text{C}\cdot\text{day}^{-1}$  and the values were maximum on day 121.

Overall, the temperatures from the meteorological tower agreed quite well with MODIS ice surface temperatures (assumed to be equal to air temperature) with a  $R^2$  of 0.82 and an average error of  $+0.29 \text{ }^{\circ}\text{C}$  (Figure-7.1b). There are no particular temporal trends in the error where the largest overestimation occurred on day 41 ( $+9.38 \text{ }^{\circ}\text{C}$ ) and the largest underestimation was on day 29 ( $-7.07 \text{ }^{\circ}\text{C}$ ). NARR data also correlated well with the meteorological tower measurements with a  $R^2$  of 0.61. The error from the NARR data underestimated air temperatures until day 18, whereas it overestimated slightly the values for the remaining period. The maximum error measured was  $+10.6 \text{ }^{\circ}\text{C}$  on day 89 and a minimum of  $-13.7 \text{ }^{\circ}\text{C}$  on day 14. However, since MODIS data contains gaps in the time series due to cloud cover, I suggest using NARR air temperature data in [eq. 7.1 and 7.2] since the temporal coverage is better.



a)



b)

**Figure-7.1:** Temporal evolution of a) meteorological tower, MODIS and NARR air temperatures and b) the differences between MODIS and NARR data with respect to the meteorological tower (considered as reference).

### 7.2.2. AMSR-E $T_b$

The atmospherically corrected (see Chapter 3) brightness temperatures difference between the ascending and descending passes was negligible (no diurnal effects). Therefore I used the daily average  $T_b$  measurements for the SWE algorithm application. The brightness temperature values did not vary much throughout the bay from pixel to pixel (spatial variability). As mentioned in Chapter 3, I extracted  $T_b$  values for 6 pixels within Franklin Bay. The atmospherically corrected

brightness temperatures for both 18 and 36 GHz in h-pol and v-pol are depicted on Figure-7.2 for p\_Min (pixel with lowest  $T_b$  throughout the season) and p\_Max (pixel with highest  $T_b$  throughout the season).

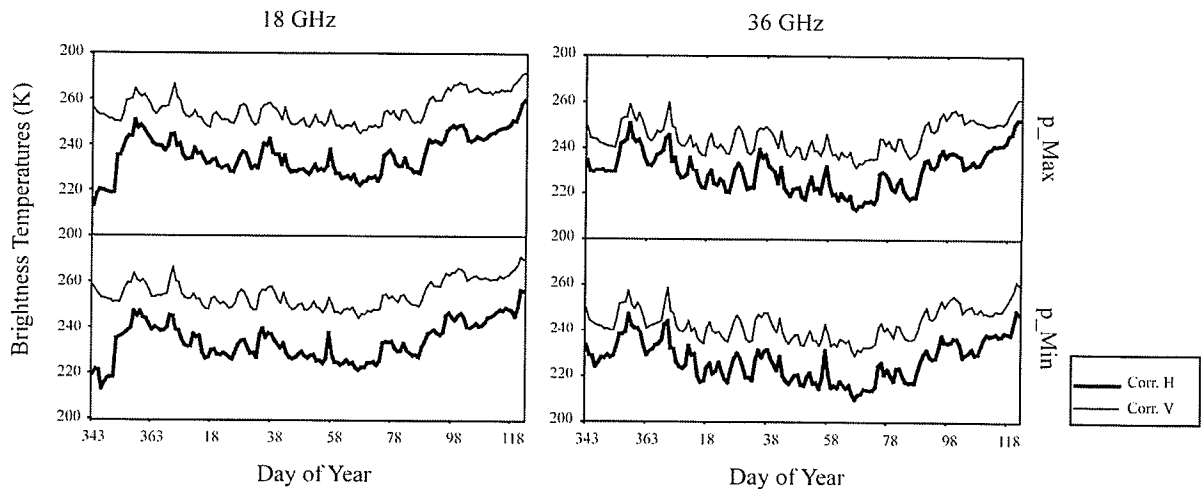


**Figure-7.2:** Temporal evolution of atmospherically corrected AMSR-E brightness temperatures in both vertical and horizontal polarizations.

The brightness temperatures at 36 GHz varied slightly more than 18 GHz with small differences between the pixels (Figure-7.2). Overall, a strong increase was measured early during the sampling period at 18 GHz in the h-pol whereas a general decrease was observed until day 67 where the minimal seasonal values were reached at both 18 and 36 GHz. A constant increase was then measured until the end of the sampling period where values were at a maximum.

### 7.2.3. SWE Predictions

Predicted snow water equivalent data using air temperatures from the NARR re-analysis (Section 7.2.1) and AMSR-E brightness temperatures (Section 7.2.2) are depicted on Figure-7.3. Overall,

the SWE values oscillated between 15 and 25 mm. As mentioned in Chapter 4, three major depositional events occurred around days 5, 42 and 91 (circled in Figure-7.3). It appears that AMSR-E responded to those depositional (precipitations) events and other peaks in predicted SWE values could be due to blowing snow that redistributes snow thickness without necessarily needing precipitations. For instance, the peaks in SWE predicted on days 19, 29, 52 and 82 corresponded to daily averaged wind speed over  $10 \text{ m}\cdot\text{s}^{-1}$ . Even though no statistical analysis was conducted due to a lack of *in-situ* SWE measurements, an extended look at wind data and predicted SWE values showed that the predictions could potentially be affected by blowing snow. Results showed that all wind events where daily average wind speed exceeded  $10 \text{ m}\cdot\text{s}^{-1}$  were associated with an increase in predicted SWE. In a total of 10 events, all showed an increase in SWE, however the amplitude of the increase were quite variable (from approximately 0.5 mm to 4 mm). The amplitude of the daily variations decreased between day 343 and day 70 and predicted values generally increased between days 78 and the end of the sampling period, although no relationships were established between those variations and blowing snow events. Maximum seasonal values were recorded at the end of the sampling period at 23.3 and 23 mm for p\_Min and p\_Max respectively. Again, the overall difference between the two pixels was very small with an average of 0.3 mm and a maximum of 1.2 mm.

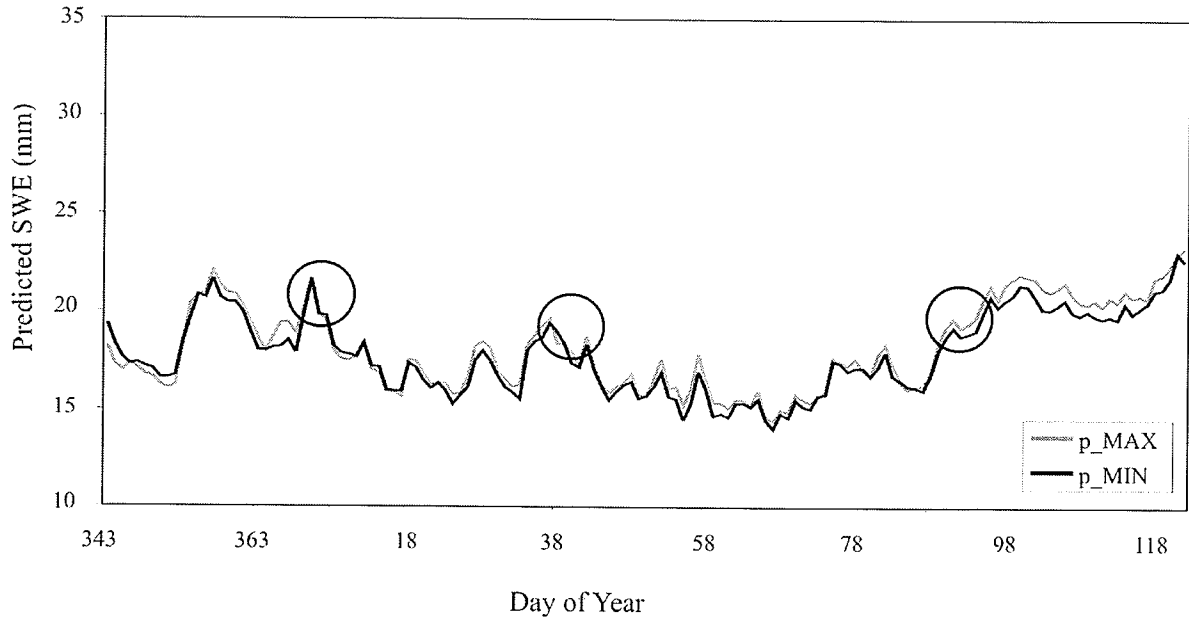


**Figure-7.3:** Temporal evolution of predicted SWE using air temperature data from the NARR re-analysis and AMSR-E brightness temperatures.

The pair of algorithms from [eq. 7.1 and 7.2] is not sensitive to large variations in air temperature since the SWE variations are much smaller than air temperatures variations. Specifically, an increase of 5 °C in [eq. 7.1] corresponds to an offset of 0.52 mm whereas a much smaller value is measured in [eq. 7.2] at 0.08 mm. Therefore, the thicker the snow gets, the less sensitive the algorithm is to air temperature variations. Furthermore, brightness temperatures from AMSR-E remained between 244 and 271 K, within the range of validity for the algorithm. However, the SWE values did not increase over the 33 mm threshold identified in Langlois and Barber, (2007a) since predictions from p\_Min and p\_Max remained between 14 and 23 mm (no switch from [eq. 7.1] to [eq. 7.2]). The details of this result will be discussed later.

Hence, I compared my SWE predictions from [eq. 7.1] for both p\_Min and p\_Max with *in-situ* snow water equivalent (SWE) transects collected over smooth and rough ice (see Chapter 3)

within the AMSR-E pixels (Table-7.1). In what follows, I provide a comparison between measured and predicted SWE values for both smooth and rough ice environments.

### 7.2.3.1. Smooth Ice Snow Water Equivalent Data

Basic statistical data (minimum, maximum, mean and standard deviation) for all smooth SWE transects are depicted in Table-7.1.

**Table-7.1:** Basic SWE statistical data calculated from smooth ice snow thickness data.

ID	Day	Latitude	Longitude	Transects SWE				AMSR-E SWE	
				Min	Max	Mean	StD	p-Min	p-Max
1	21	70.033	126.342	11.3	18.7	12.9	11.0	16.1	16.3
2	24	70.043	126.258	11.5	27.6	15.6	13.5	15.3	15.8
3	28	70.042	126.26	11.7	25.9	14.5	13.0	18.0	18.5
4	32	70.04	126.255	11.8	27.4	15.6	13.8	15.9	16.2
5	40	70.041	126.255	11.7	34.1	16.5	13.6	17.4	17.9
6	48	70.048	126.313	11.2	28.4	14.2	13.0	16.4	16.9
7	57	70.051	126.3	12.6	26.6	15.4	12.8	17.0	17.9
8	65	70.052	126.302	11.0	38.0	14.9	13.5	15.6	16.0
9	71	70.052	126.302	11.7	34.1	15.7	14.0	15.2	15.5
10	76	70.042	126.271	12.6	37.6	16.0	13.9	17.4	17.5
11	80	70.051	126.288	12.1	48.6	18.7	16.8	16.7	16.7
12	83	70.056	126.281	12.3	39.2	16.7	14.9	16.8	17.3
13	96	70.058	126.29	14.4	46.6	23.7	17.7	20.8	21.4
14	99	70.039	126.254	13.0	42.7	20.5	16.4	20.9	21.6
15	101	70.045	126.256	13.8	58.6	23.6	17.4	21.4	21.8
16	119	70.044	126.305	10.8	42.1	21.6	17.2	21.2	21.9

I found that the SWE predictions are statistically significant with the measured smooth ice SWE values within +/- 1 standard deviation of the measured *in-situ* values from Table-7.1 (Figure-7.4). A strong correlation was found between modeled and measured data with  $R^2$  values of 0.75 and 0.73 in p\_Min and p\_Max respectively. The measured SWE standard deviation increased throughout the study as shown in Table-7.1 and Figure-7.4, which can be explained by higher spatial variations in snow thickness as snow thickens (Iacozza and Barber, 2001). Measured SWE over smooth ice increased from an average of 15 mm (prior to day 65) to 19.1 mm (after

day 65) whereas the predicted SWE increased from 16.8 mm to 18.6 mm combining both p\_Min and p\_Max (Table-7.1). The differences between predicted and modeled values were on average 1.5 and 1.7 mm for both p\_Min and p\_Max respectively.

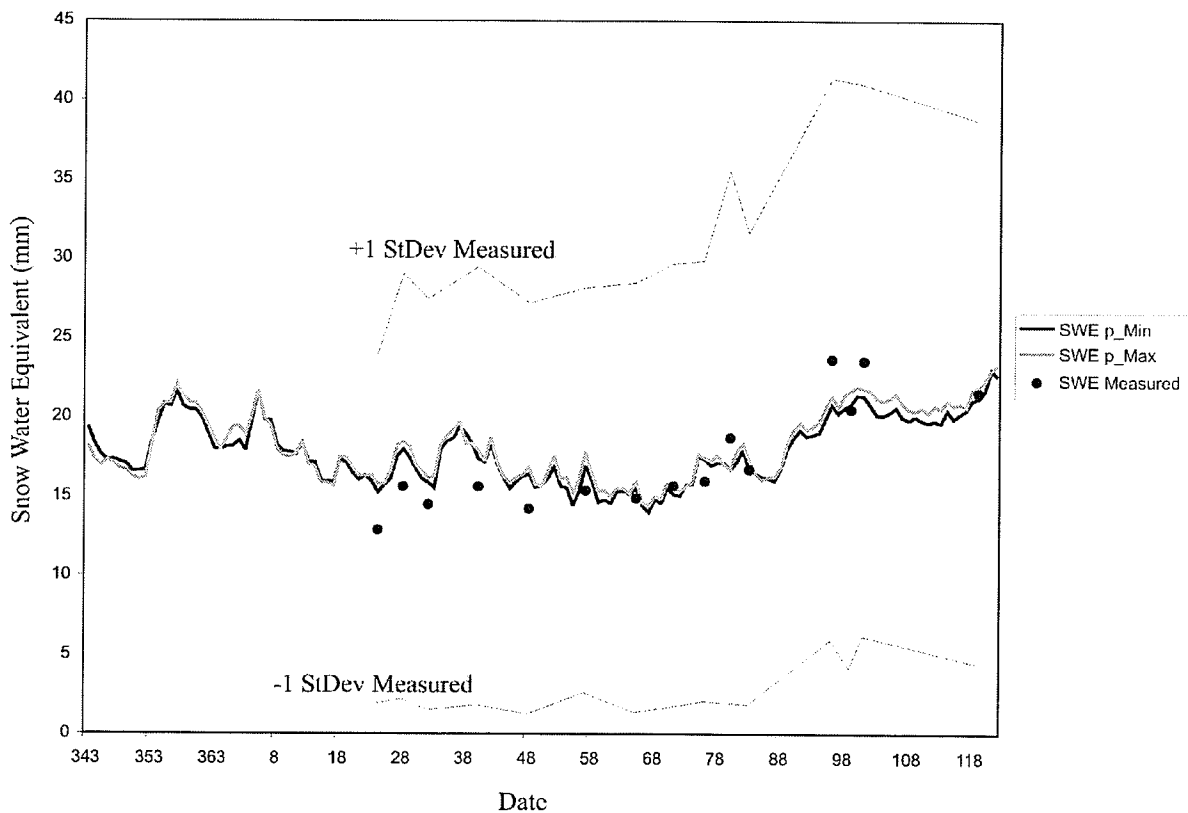


**Figure-7.4:** Temporal evolution of SWE predictions for modeled p\_Min and p\_Max (black and gray lines), and measured at the smooth SWE transects sites (dots).

### 7.2.3.2. Rough Ice Snow Water Equivalent Data

Basic statistical data (minimum, maximum, mean and standard deviation) for all rough ice SWE transects are depicted in Table-7.2. I also found the SWE predictions to be statistically significant within +/- 1 standard deviation of the measured SWE values over rough ice, although predictions are not as strong as measured over smooth ice. The measured roughness elevation

varied between 15 and 140 cm on average including snow thickness, which generally increased as the season progressed.

**Table-7.2:** Basic SWE statistical data calculated from rough ice snow thickness data.

ID	Day	Latitude	Longitude	Transects SWE				AMSR-E SWE	
				Min	Max	Mean	StD	p-Min	p-Max
1	36	70.038	126.29	11.4	54.9	28.1	19.3	18.7	19.3
2	54	70.048	126.255	12.0	39.3	15.3	13.3	15.6	16.2
3	66	70.045	126.235	11.7	59.1	22.2	19.9	14.5	14.6
4	74	70.047	126.232	11.0	71.5	23.1	19.9	15.8	15.9
5	78	70.045	126.251	12.2	80.3	39.0	23.0	17.2	17.6
6	97	70.036	126.31	13.4	79.6	29.9	20.7	20.3	20.6
7	100	NA	NA	10.7	98.1	28.3	22.0	21.4	21.9
8	105	70.05	126.25	11.4	75.7	27.3	20.3	20.3	21.2

The temporal evolution of the measured SWE over rough ice did not follow any particular trend, although higher values were recorded towards the end of the sampling period (Table-7.2 and Figure-7.5). The algorithm generally underestimated SWE by -8.7 and -8.2 mm for p\_Min and p\_Max respectively (Figure-7.5). The largest difference was measured on day 78, where the average measured SWE value was 39 mm (difference of approximately 22 mm with the predicted values), by far the highest value recorded throughout the study period. If we exclude this SWE transect from the average, the underestimation decreased to -6.8 and -6.3 mm for p\_Min and p\_Max respectively.

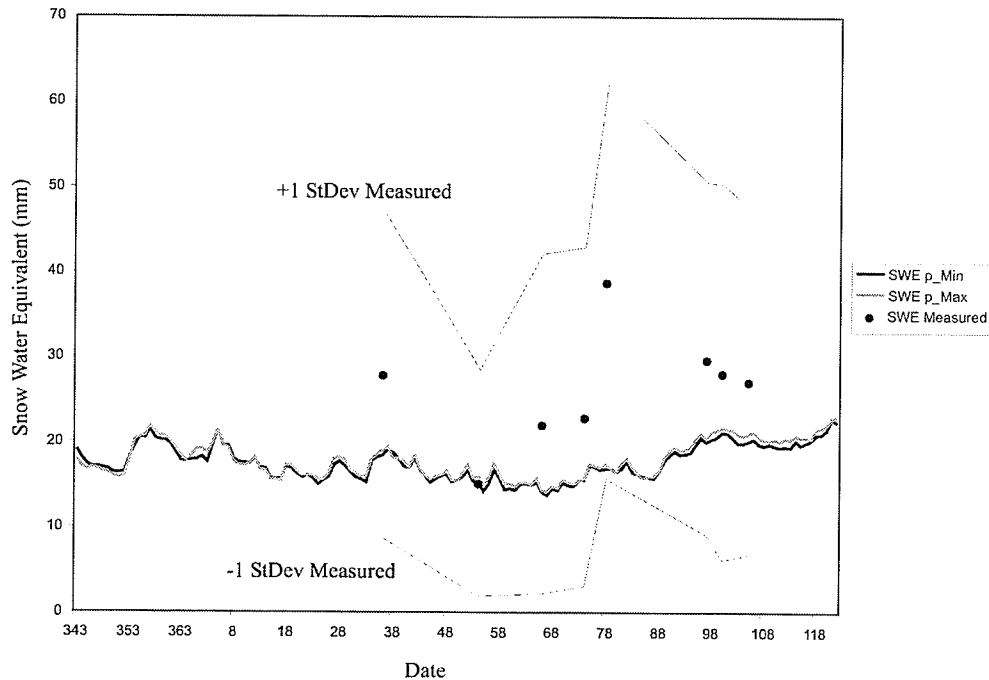


**Figure-7.5:** Temporal evolution of SWE predictions for modeled p\_Min and p\_Max, and measured at the rough snow thickness transects sites.

I mentioned earlier that the algorithm did not switch from thin to thick snow. Hence, one may think that the thick snow algorithm should be applied in rougher ice since thicker snow is found given Table-7.2 due to snow catchments by the ice ridges (e.g. Granberg, 1998). Hence, I applied the thick snow algorithm from [eq. 7.2] to see if better predictions would be found in Figure-7.5 in rougher ice. Results showed that predictions were too high with SWE values of approximately 60 mm for both p\_Min and p\_Max. This can be explained by the differences measured between the SBR brightness temperatures (over which the algorithm was developed) and the brightness temperatures from AMSR-E. The comparison of both  $T_b$  showed that the brightness temperatures measured by the SBR were higher during the periods C3 and C4 (see Chapter 6) resulting in lower SWE predictions using [eq. 7.1]. On average, the SBR  $T_b$  at 36 GHz [eq. 7.2] were 35 K higher than measured with AMSR-E. The difference was smaller at 18

GHz, which is used in the thin snow algorithm [eq. 7.1] explaining the better results found using this algorithm. Furthermore, I demonstrated in Chapter 4 that thick snow thermodynamic processes such as volume scattering and brine volume migration governed microwave emission at the SBR scale over smooth ice during the C2 and C3 periods. Those processes are not dominant in a rough ice environment which might explain the better predictions obtained over smooth ice. Unfortunately, we did not carry an experiment with the SBR over rough ice, and this should be a priority in future work.

Also, it was showed in Mäkynen and Hallikainen (2005) that  $T_b$  decreases with increasing ice deformation at 18 and 36 GHz in the vertical polarization (used in [eq. 7.1 and 7.2]) over a partial (mix of bare ice and snow) dry snow cover typically found in rough ice. This situation was found in the study area (i.e. AMSR-E scale), although not in the SBR field of view. Hence, decrease in  $T_b$  due to ice roughness was not measured by the SBR over smooth ice (totally covered by snow), which was also observed by Mäkynen and Hallikainen (2005). A decrease in  $T_b$  measured by AMSR-E through ice roughness will increase SWE predictions using [eq. 7.2]. More specifically, an increase in the order of 35 K (measured average difference at 36 GHz during C2 and C3), would decrease SWE values of approximately 40 mm. Therefore, a correction should be applied to AMSR-E brightness temperatures if one wants to apply the thick snow algorithm over [eq. 7.2] a rough ice environments.

Limited SWE data were available in rough ice, and limited roughness amplitudes were sampled. However, to test this roughness hypothesis, I simply corrected the AMSR-E brightness temperatures so that they match SBR measurements during the C2 and C3 periods. By doing so,

I found the SWE predictions from [eq. 7.2] to vary between 31 and 42 mm, +/- 2.5 mm for both p\_Min and p\_Max respectively. This represents a much better result given Figure-7.5, when compared to the 60-80 mm predictions without correcting the initial  $T_b$  for [eq. 7.2] However, more data over a wider range of snow thickness and ice roughness would be required to develop statistically viable corrections to [eq. 7.2] for rough ice applications.

This simple analysis however confirms that a certain degree of correction is required using the thick snow algorithm over rough ice. Although atmospheric corrections were conducted, it appears that the scale difference between the SBR and AMSR-E can be a significant factor due to the different dynamic and thermodynamic processes (highlighted in Chapter 4) affecting both scales at different amplitudes. Since no SBR measurements occurred over rough ice, I could not develop nor modify the existing algorithm even though it appears that a certain degree of correction would greatly enhance prediction results. Furthermore, the fraction and amplitude of ice roughness within one AMSR-E pixel should be analyzed, but a lot of uncertainties remain on how to do so from a satellite perspective. In what follows, I provide insight as to where future roughness analysis should go in order to first qualify and quantify ice roughness using a combination of passive and active microwave satellite information for SWE prediction applications. Details on future work addressing those issues will be discussed in greater details in Chapter 8.

### 7.3. Roughness Analysis

As shown in the previous section, ice roughness can alter SWE predictions where the algorithm underestimates SWE values in rough ice, although still significant within +/- 1 standard deviation from the measured data (Figure-7.5). Hence, the state of roughness in both p\_Min and p\_Max needs to be addressed from a satellite perspective. In what follows, I provide insight on qualifying ice roughness using both passive and active satellite microwave information. The effect of roughness on the SWE predictions will be discussed later.

#### *7.3.1. Passive Microwaves*

As previously discussed in Chapter 3, the polarization ratio (PR) was calculated at 18 GHz for both pixels using [eq. 3.26]. A sharp decrease in PR was measured from 0.91 on day 343 to 0.294 on day 352 for p\_Max (Figure-7.6a) whereas it decreased from 0.812 to 0.315 at p\_Min. Values increased slightly afterwards until days 67-68 and decreased again until the end of the sampling period. The gradient ratio (GR) at 18 and 36 GHz values decreased slightly throughout the study period (Figure-7.6b). Values were at maximum early on day 354 for p\_Min (-0.0106) and 357 for p\_Max (-0.0115). The minimum was reached on days 67 and 85 for p\_Min and p\_Max respectively (-0.0325 and -0.0288). A plot of GR against PR is given in Figure-7.6c. Two statistically distinct clusters arise (A and B) where A are PR and GR values from day 351 to 122 and B values prior to day 351 (343-351).

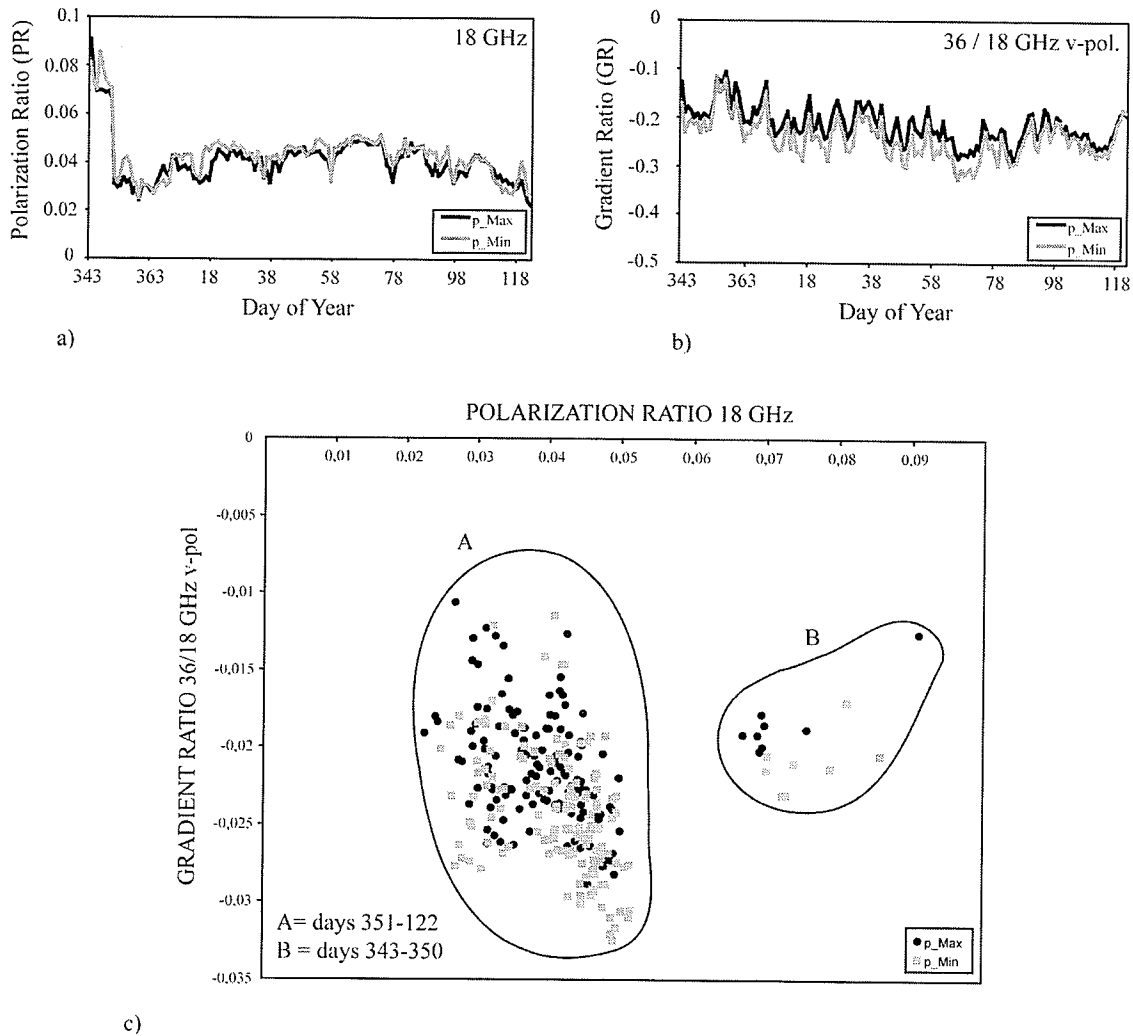


**Figure-7.6:** Temporal evolution of a) polarization ratio at 18 GHz and b) the gradient ratio between 18 and 36 GHz for both p\_Min and p\_Max. In c) a scatter plot of the polarization ratio and gradient ratio.

It was found in Mäkynen and Hallikainen (2005) that as surface roughness increases, dry snow brightness temperatures decreases in the vertical polarization, whereas values in the horizontal polarization did not change as significantly (i.e., decrease in PR with increasing ice roughness). From their conclusions, Figure-7.6 could suggest that a transition from new ice to rough ice was observed within our AMSR-E pixels early in the season, but it could also be due to an open water

to new ice transition which would also decrease the PR values. Open water is reflective in microwave bands and has a very strong polarization effect ( $T_b V \gg T_b H$ ) compared to first-year sea ice (Figure-7.6a). Furthermore, brightness temperatures from Figure-7.2 were rather low (low  $T_b$  for open water) early in the period, supporting the idea that open water was present within the pixels. Unfortunately, no video data were available to support this statement and current work on linking the PR and GR with the fraction of open water is currently being conducted by other researchers in our lab.

In order to find evidence of open water between days 343 and 3 where a large decrease in PR was measured, I looked at ice charts from the Canadian Ice Service (CIS). On January 1<sup>st</sup>, all of Franklin Bay was considered as fast ice, however, no information was available prior to that. Hence, I extracted sea ice concentration (SIC) values from the AMSR-E algorithm (Markus and Cavalieri, 2000) to examine any evidence of open water detected over the same period. Sea ice concentration results extracted from  $p\_Min$  and  $p\_Max$  did not provide any evidence of open water since ice concentration varied from 98 to 100% between days 343 and 3, in agreement with the CIS ice charts. Furthermore, I extracted SIC from 12 pixels within Franklin Bay for the same period, are results were similar throughout the bay suggesting that the ice was consolidated at AMSR-E scales on day 343. However, given the results presented in Figure-7.6, open water was most likely present in the early stages of the sampling period, although its fraction was probably sufficiently small so that both CIS charts and AMSR-E SIC algorithm considered the region as fast ice. For further insight regarding  $p\_Min$  and  $p\_Max$  spatial features temporal evolution (ice roughness, open water etc.), I looked at active microwave satellite data (see Chapter 3) which might help understand the results presented above.

### 7.3.2. Active Microwaves

Mean backscatter values were analyzed at 6 and 11.6 km resolutions, centered on the AMSR-E p\_Min and p\_Max pixels to evaluate the scaling effect on  $\sigma^\circ$  in both p\_Min and p\_Max (Figure-7.7) and provide further information on sea ice roughness.

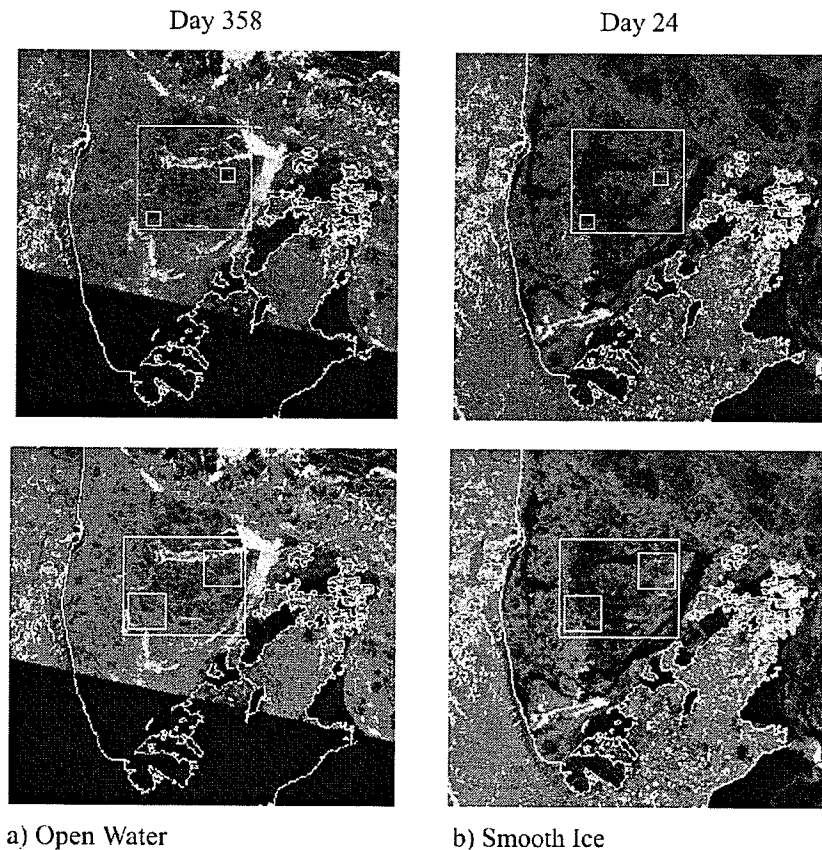


**Figure-7.7:** ScanSAR images taken on a) day 358 and b) day 24. The top two images are at 6 km resolution, and the bottom two at 11.6 km resolution (p\_Min at top right, and p\_Max at bottom left).

Throughout the study period, mean  $\sigma^\circ$  values at 6 km resolution within p\_Min were consistently higher than p\_Max. Backscatter values did not follow any particular trend throughout the study period oscillating between -15 and -20 dB. The maximum was recorded on day 66 for where  $\sigma^\circ$

reached -14.7 and -15.5 dB and minimum on day 106 at -19.9 and -20.3 dB for both p\_Min and p\_Max respectively (Figure-7.8a). This appears to be irrespective of incidence angle, as it is fairly consistent from about day 10 to day 107. Overall,  $\sigma^\circ$  prior to day 48 did not vary greatly whereas the maximum variations were measured between days 66 and 75. Results at 11.6 km showed the same temporal behavior with maximum (-14.5 and -15.1 dB) and minimum (-19.5 and -20.2dB)  $\sigma^\circ$  measured on day 66 and 106 for p\_Min and p\_Max respectively (Figure-7.8b). The differences between both scales are minimal with slightly higher  $\sigma^\circ$  values measured at 11.6 km. On average, values were higher of 0.33 and 0.38 dB in p\_Max and p\_Min respectively. The largest differences between the two scales were measured on day 358 (Figure-7.8).

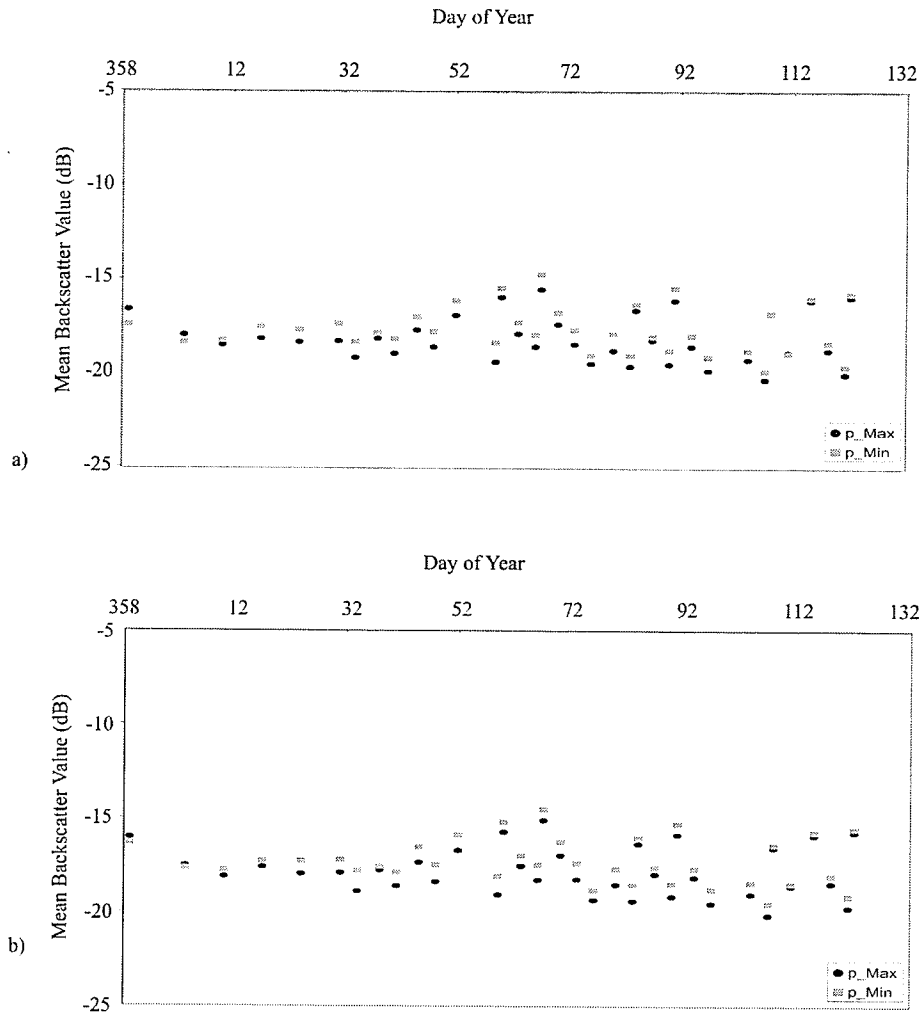


**Figure-7.8:** Mean backscatter values for p\_Min and p\_Max at a) 6 km and b) 11.6 km of resolution.

Furthermore, z-scores from Figure-7.9 shows that both p\_Min and p\_Max were rougher (higher backscatter values) relative to the surrounding areas (i.e., the larger pixel window from Figure-7.7) and that p\_Min is consistently rougher at both 6 km on Figure-7.9a and 11.6 km on Figure-7.9b. From day 10 to day 106, p\_Max backscatter was on average 0.15 standard deviations above the mean of the larger pixel window whereas p\_Min reached 0.43 standard deviations above the mean of the larger pixel window (Figure-7.9). That value increased to 0.2 and 0.49 at

11.6 km for both p\_Max and p\_Min respectively. While p\_Min and p\_Max both represent smooth first-year sea ice (FYI), in a relative sense they both exhibit above average roughness for the FYI in this region.

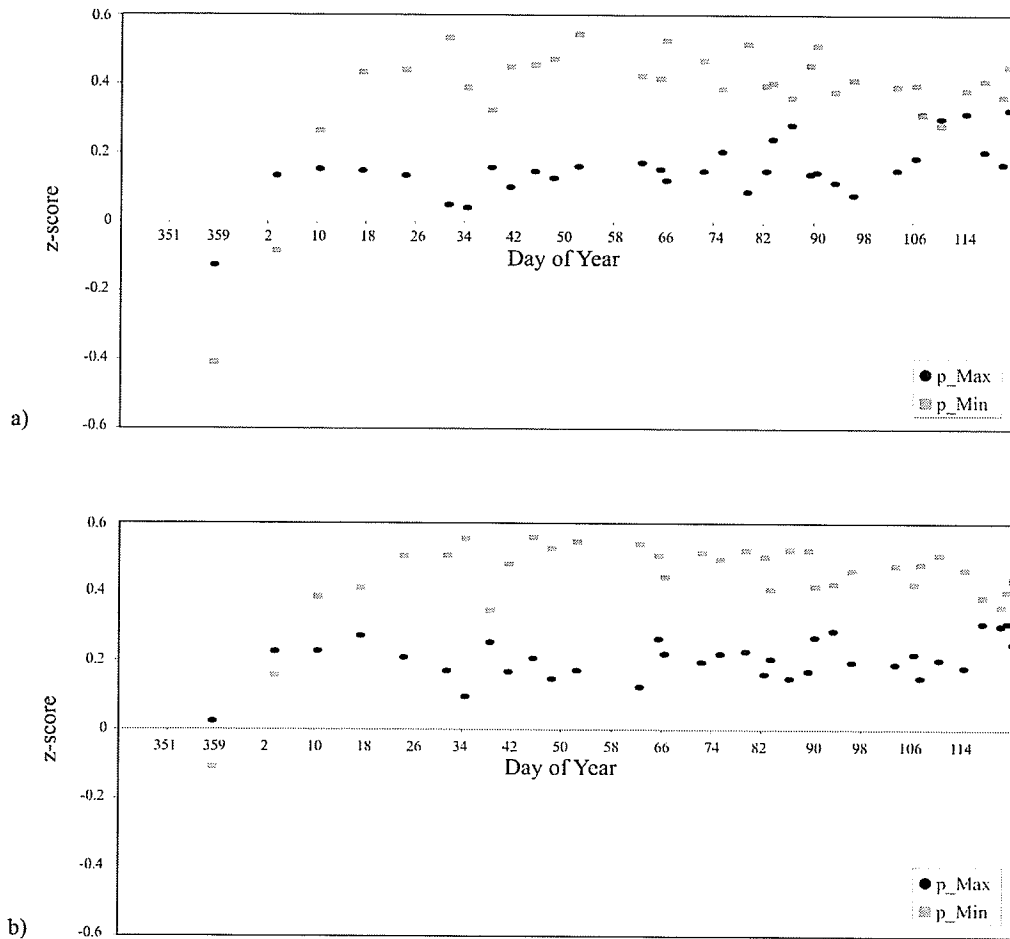


**Figure-7.9:** Standardized backscatter values for both p\_Min and p\_Max relative to the surrounding area (see Figure-3.9) at a) 6 km and b) 11.6 km resolutions.

Mäkynen and Hallikainen (2004) reported an increase in  $\sigma^\circ$  with increasing ice roughness. The increase was in the order of 10 dB in both co- and cross polarizations at  $23^\circ$  and  $45^\circ$  of incidence angle from new ice to highly deformed ice. Once the ice was in place, we did measure an

increase in  $\sigma^\circ$  between day 12 and 65, however the increase was in the order of approximately +5 dB. It is well known that SAR  $\sigma^\circ$  measurements are very sensitive to small scale roughness (i.e., on the order of 1/10 the incident radar wavelength,  $\lambda$ ), but it is also sensitive to changes in the orientation of small-scale scatterers induced by larger scale roughness features. Using  $\sigma^\circ$  to strictly quantify 'roughness' becomes a problem given that roughness can be thought of as a relative term that is associated with the distribution of scatterers at multiple scales (e.g., mm-scale ice roughness superimposed upon larger cm-scale ice blocks). Surface roughness would change very little with time in a consolidated, landfast FYI zone such as our sampling area. As such, multiple measurements of the same site during winter should acquire approximately the same look at surface roughness each time, with only incidence angle related sensitivity to surface roughness varying between scenes. Additional fluctuations in  $\sigma^\circ$  during winter were most likely caused by changes in snow and ice thermodynamic processes and related thermophysical properties such as increased brine volume of the ice and brine-wetting of snow grains at the snow/ice interface (Barber and Thomas, 1998; Barber and Nghiem, 1999; Nghiem and Bertoina, 2001).

From the SAR analysis, I was unable to quantify roughness in terms of amplitude. I found that the two pixels analyzed are likely rougher than what is found elsewhere in the bay. Since the brightness temperatures were very stable throughout Franklin Bay, it is not likely that the amplitude of roughness variations from one pixel to another significantly affected the brightness temperature (i.e. SWE predictions). However, I found that the algorithm underestimated SWE in areas of rough ice (Figure-7.5), but no quantification of the fraction of roughness within one AMSR-E pixel could be determined.

Results also showed that absolute and relative  $\sigma^\circ$  were consistently different between p\_Min and p\_Max. Backscatter results between day 358 and 3 do not show evidence of open to new ice transition, although open water was present elsewhere in the area (bright yellow in Figure-7.7a). At 11.6 km, I noticed that the analyzed window is fairly close to this zone of open water (North East of p\_Min and South West of p\_Max) which might explain its effect on AMSR-E 12.5 km pixel (Figure-7.6). Hence, open water was most likely present within the AMSR-E pixels, although its fraction was not large enough to have a significant impact on the SIC algorithm and the CIS ice charts.

## 7.4. Conclusions

### 7.4.1. Ice Roughness vs Passive and Active Microwaves

Both p\_Min and p\_Max had similar  $T_b$  and  $\sigma^\circ$  values once the ice was consolidated (according to ScanSAR imagery from Figure-7.7). As mentioned above, it appeared that the difference in roughness between p\_Min and p\_Max was not large enough to create a significant difference in the observed brightness temperatures. Unfortunately, no *in-situ* SBR brightness temperatures were available over rough ice throughout the study period. Such measurements might provide further insight on the exact effect of ice roughness on passive microwave signatures, and SWE algorithms should be adapted for such environment.

I showed that higher  $\sigma^\circ$  values corresponded to lower brightness temperatures but also to higher polarization ratio values (although not significantly). Furthermore, during a winter time series of FYI  $\sigma^\circ$  over one site, I can only say with confidence whether or not the dielectric behaviour, i.e.

as a result of thermodynamic changes of the ice, has changed for a given site since surface roughness does not change significantly after winter consolidation. It thus becomes difficult to correlate time series changes in  $\sigma^\circ$  to passive microwave polarization behaviour in the context of surface roughness.

Hence, from the passive and active microwave data analysis, it is hard to conclude on which of the two pixels is the roughest. Within a satellite footprint, spatial heterogeneity is quite important as it is not likely to contain 100% snow cover throughout the pixel, but rather a mix a snow, bare ice, ice ridges and open water. In such case, previous research showed that rough pixels will exhibit 1) decrease the brightness temperatures in the vertical polarization, 2) decrease the polarization ratio and 3) increase  $\sigma^\circ$  values. From the results presented in this chapter, it appears that p\_Min would be the roughest pixel since the brightness temperatures are lower and backscattering measurements higher once the ice was consolidated.

#### *7.4.2. Scaling Effects on SWE Predictions*

Looking at our SWE predictions temporal evolution, I examined how sensitive the SWE predictions were to variations in PR during the open water to new ice transition around day 350. No apparent relationship between the PR decrease and SWE prediction was found, and more work is required due to the limited data available. It is well known that open water strongly influences  $T_b$  values and existing spaceborne SWE algorithms already consider the fraction of open water within one pixel (Markus *et al.*, 2006a). Furthermore, the scaling effect was obvious when comparing the SBR  $T_b$  values from Chapter 4 and the  $T_b$  measured from AMSR-E in this

chapter. Both brightness temperatures agreed relatively well at the beginning and towards the end of the sampling period, however, SBR values were higher throughout the periods C2 and C3 at both  $p_{\text{Min}}$  and  $p_{\text{Max}}$ . Using [eq. 7.1], a lower brightness temperature means a lower predicted SWE value, which could explain the difficulty of the algorithm to increase SWE in a rough ice environment. I showed that the use of the thick snow algorithm provides much better results, although a level of correction was required. This suggests that a ‘corrected’ thick snow algorithm should be applied even though calculated SWE values did not reach the threshold identified in Langlois and Barber, 2007a at 33 mm. However, the data presented in this chapter are not sufficient to provide an exact correction to be applied on the AMSR-E  $T_b$ . It might be advisable to explore the possibility of using 18 GHz as well for thick SWE retrievals (in eq. 7.2) since I showed that the difference between SBR and AMSR-E  $T_b$  are smaller at this frequency. However, more field data are required to develop, compare and test such an algorithm. As discussed in Chapter 4, different processes govern  $T_b$  temporal evolution at a small scale, and it is apparent that those processes are not affecting AMSR-E  $T_b$ ’s to the same degree.

Further work is required to increase the range of SWE values measured in different ice roughness environments and the quantification of roughness, although difficult, is essential. I showed that the predictions over smooth ice were very good, and results over rough ice (using a certain level of correction) are promising. However, the fractions of smooth vs rough ice within  $p_{\text{Min}}$  and  $p_{\text{Max}}$  are still unknown and will need to be addressed in future field work using a combination of both passive and active microwave information as shown in this chapter. A target for a level of tolerance as to what fraction and amplitude of roughness is appropriate for the SWE from [eq. 7.1 and eq. 7.2] should also be identified and extended large-scale *in-situ* validation is required.

Hence, it appears that the SWE predictions will not be significantly affected by a certain level of ice roughness (up to 140 cm as measured in the SWE transects) given that the pixels were 'rougher' than average (Figure-7.9a and b), but the spatial fraction of roughness within the AMSR-E pixel still needs to be addressed. Also, it was showed that a degree of sensitivity to blowing snow exists (with wind  $> 10 \text{ m}\cdot\text{s}^{-1}$ ) due to changes in the spatial distribution of snow thickness. However, more work is required to increase the amount of *in-situ* data after blowing snow events in order to understand the role of roughness in such conditions with regards to spatial redistribution of snow thickness. SWE transects should be conducted in various wind conditions over smooth and rough ice to quantify the impact on the predictions for different rates of wind speed associated with the transport mechanisms highlighted in Chapter 2 (i.e. creeping  $< 5 \text{ m}\cdot\text{s}^{-1}$ , saltation  $5\text{-}10 \text{ m}\cdot\text{s}^{-1}$ , and suspension  $> 15 \text{ m}\cdot\text{s}^{-1}$ ).

## CHAPTER 8: SUMMARY AND CONCLUSIONS

### 8.1. Thesis summary

The geophysical, thermodynamic and dielectric properties of snow are important state variables, which are known to be sensitive to Arctic climate variability and change. Given recent observations of changes in the Arctic physical system (ACIA, 2004) it is important to focus on the processes which give rise to variability in the horizontal, vertical and temporal dimensions of the life-history of snow on sea ice. The objectives of my dissertation were to present these 'state' variables and to investigate the processes, which govern variability in the vertical, horizontal and temporal dimensions. This acute understanding of the system allowed for the development of a snow water equivalent algorithm valid over landfast first-year sea ice. This knowledge is also required in other global-scale Arctic studies using models and satellite remote sensing products due to the importance of snow microscale thermodynamic and dynamic processes highlighted in Chapters 1 and 2.

In Chapter 4, I addressed objective 1, providing a detailed understanding of the seasonal temporal evolution of snow thermodynamic and dynamic processes. More specifically, I:

- evaluated the winter seasonal evolution of snow electrical and thermophysical properties,
- provided an understanding of the seasonal thermodynamic processes within the snow cover,

- identified the forcing agents and understood their impact on the surface energy balance.

I presented the results from two sampling areas (thin and thick snowpacks) and showed that differences in snow thickness substantially changed the vertical and temporal evolution of snow properties. During the late fall and early winter (cooling period) no significant changes in the physical properties were measured except for thin snow cover salinity which decreased throughout the period. Fall snow desalination was stronger at the bottom of thin snowpacks with a rate of  $-0.12 \text{ ppt}\cdot\text{day}^{-1}$ . In the late winter and early spring (warming period) significant changes occurred especially for snow grain size. Snow grain kinetic growth of  $0.25\text{-}0.48 \text{ mm}\cdot\text{day}^{-1}$  was measured coincidentally with increasing salinity and wetness for both thin and thick snowpacks respectively.

Also in Chapter 4, I investigated the effect of the snow processes, highlighted above, on microwave signatures addressing objective 2. Specifically, I:

- provided an understanding of snow seasonal evolution on passive microwave emission and scattering mechanisms,
- evaluated the impact of polarization and incidence angles at a seasonal scale.

Results showed that the behavior of brightness temperatures in thin snow covers differed significantly from thicker snow. Furthermore, snow thermophysical/electrical properties and brightness temperatures behaved quite differently from the winter cooling period to warming

period, where temperature gradient metamorphism began at a SWE threshold value of 33 mm (see Chapter 6). Brightness temperatures increased with increasing thickness during the cooling period until the threshold was reached whereas it decreased with further snow thickness increase during the warming period.

While I concentrated the analysis on seasonal changes in Chapter 4, Chapter 5 addressed objectives 1 and 2 from a short-term evolution perspective. More specifically, I:

- evaluated the winter short-term snow properties variations associated with atmospheric pressure variations (low-pressure disturbance),
- provided an understanding of the short-term thermodynamic processes within the snow cover,
- identified the forcing agents and understood their impacts on the surface energy balance,
- provided an understanding of snow short-term change impacts on passive microwave signatures,
- evaluated the impact of polarization and incidence angles on the measured brightness temperature variations.

This work is of primary importance as a result of recent studies that have shown that increased *in-situ* cyclogenesis and advection into the arctic regions can be expected, which significantly affect snow properties on a daily scale (i.e. SWE predictions). Furthermore, since these cyclones are associated with warm air advection, increased wind speed, relative humidity and cloud cover, and

their impact on snow surface energy balance may also be significant. The thermophysical response of snow covered first-year sea ice to a low-pressure disturbance was investigated along with corresponding surface based radiometer brightness temperature measurements. The data were collected between year days 33 and 34 of 2004 where a warm front moved through the study area. Snow grain size increased throughout the sampling period with growth rates of 1.28 and 2.3 mm<sup>2</sup>·day<sup>-1</sup> for thin and thick snow covers respectively. This rate was much faster than expected based on results from Chapter 4. Furthermore, brine volume migrated upward in both thin and thick snow cover environments due to the probable action of wind pumping, affecting the dielectric constant of the snow middle layers. The concordant increase in permittivity caused a decrease in brightness temperatures at 85 GHz of approximately 5 K and 10 K in the vertical and horizontal polarizations respectively.

In Chapter 6, I used the understanding of snow evolution provided in Chapters 4 and 5 (long and short terms) to develop a snow water equivalent algorithm using *in-situ* passive microwave data (objective 3). Specifically, I:

- provided an understanding of the effect of frequency, polarization and incidence angle in SWE predictions,
- developed different algorithms for both thin and thick snow covers at different incidence angles,
- compared these algorithms with existing *in-situ* and satellite products,
- developed a SWE algorithm applicable to satellite remote sensing that adjust from thin to thick snow given a measured thickness threshold.

SWE predictions using the thick algorithm were quite precise, and showed very good agreement with the physical data ( $R^2 = 0.94$ ) especially during the cooling period (i.e. from freeze up to the minimum air temperature recorded) where the snow is dry and cold. Thin snow SWE predictions also showed fairly good agreement with field data ( $R^2 = 0.70$ ) during the cold season. The differences between modeled and *in-situ* SWE for both thin and thick snow cover were mainly attributable to variations in air temperature, snow wetness and snow thickness spatial heterogeneity.

Once the threshold was identified between thin and thick snow, I adjusted the algorithms and results were valid for air temperatures between  $-5$  and  $-30$  °C and SWE in the range of 0-55 mm. The algorithm successfully predicted SWE when compared with *in-situ* measured values with a high degree of correlation ( $R^2 = 0.95$ ) including the thin to thick snow transition. The comparison with other *in-situ* and satellite algorithms did not provide significant correlations due to the limited range of thickness and temperatures over which these algorithms were developed and other limitations discussed below in Section 8.2.

Finally, in Chapter 7, I applied the evolving snow water equivalent algorithm from Chapter 6 to satellite passive microwave data from the Advanced Microwave Scanning Radiometer for Earth Observation System (AMSR-E) addressing objective 4. Specifically, I:

- applied the SWE algorithm developed *in-situ* from Chapter 7 to AMSR-E satellite data,
- validated the predictions with *in-situ* snow thickness transect data,

- evaluated the potential of qualifying ice roughness using passive and active microwave sensors,
- evaluated the effect of surface roughness on SWE predictions using passive and active microwave data.

The SWE algorithm developed in Chapter 6 was applied to atmospherically corrected AMSR-E brightness temperatures throughout one full winter season. Results showed that both MODIS and the North American Regional Reanalysis (NARR) air temperatures products provided good agreement with the *in-situ* meteorological tower and could both be used in the SWE algorithm. SWE predictions were validated with local snow thickness data assumed to be representative of the region for both smooth and rough ice environments. Results showed that the predictions were statistically significant within +/- 1 standard deviation of the measured data for both smooth and rough ice, but results over smooth ice were much better.

Furthermore, the effect of sea ice roughness on the SWE predictions was investigated using passive microwave brightness temperatures (AMSR-E) and active microwave backscattering measurements (ScanSAR). I showed that the use of the polarization ratio along with a regional analysis of the radar backscattering could qualitatively distinguish rougher pixels, and open water to new ice transitions. This technique however did not provide quantitative information related to the amplitude of the surface roughness. In my results I showed that the SWE predictions were not significantly affected by the levels of roughness found in the AMSR-E pixels since no relationship was established between  $\sigma^{\circ}$  and/or PR and the difference between measured and predicted data. Further, I showed that the algorithm underestimated SWE in rough ice and

suggested that a correction should be applied to thick snow SWE algorithm due to the strong scale effect in rough ice.

## **8.2. Limitations**

Even though the dissertation provided unique results using one of the few complete seasonal snow dataset over first-year sea ice, limitations exist and need to be discussed. Throughout my research, those limitations can be regrouped in two main areas namely field sampling and the surface based radiometer. In what follows, I will discuss the uncertainties associated with field sampling and the instrumentation used throughout the study period. I will then discuss the limitations of the SBR using some of the findings from my dissertation.

### *8.2.1. Field Sampling*

As mentioned above, uncertainties arise from the field sampling and methods highlighted in Chapter 3. With regards to the instruments used in physical snow sampling, the capacitance plate created minor problems. Hence, many missing snow wetness values were in fact due to limitations from the conductivity range of our capacitance plate in a brine-wetted environment. Snow wetness is essential information since it is required in dielectric calculations (see 3.5), and improved/modified instruments would be required for future sea ice studies. Furthermore, we had some hardware problems early in the season so that limited wetness (i.e. dielectric) measurements were available during the cooling period. The missing data would increase our understanding of the processes associated with the cooling-warming period transition as well as with the strong desalination measured during the cooling period. However, wetness values can

be assumed to be below 1% throughout this period and the dielectric model could be used with this assumption if absolutely needed.

Uncertainties also arose from the snow grain photographs made in the ship's cold laboratory due to the limited time available from snow sampling. Even though extra care was taken in the transportation of snow samples, mass loss through sublimation or break (snow grain breaking during transport) can occur. I did not find any obvious evidence of mass loss in the snow pictures, but limited transportation time confined the analysis to the surroundings of the ship. Therefore no extended studies on spatial variability of snow grain size were conducted within the region. Thus, an adapted field method should be developed to retrieve grain size information quickly and accurately on site, but so far, the method described in Chapter 3 provides the best compromise for data quantity and quality given the reality of Arctic research. Previous studies tried to solve this issue using infrared cameras (Matzl, 2006) or laser diodes mounted on an integrating sphere (Dominé *et al.*, 2006). Although those methods have proven to be quite precise, they are very time consuming and therefore not the ideal approach for ship-based research.

Finally, uncertainties are also associated the physical sampling of snow density under similar snow thickness. The density cutter provides a relatively good vertical resolution, but the exact location of the cutter itself may vary slightly from one snowpit to another. Hence, as mentioned in Chapter 6, little variations in density can affect SWE calculations under thin snow and care should be taken when strong variations are suddenly measured. I would also recommend the

development of a non-invasive technique for the measurement of snow density (e.g., dielectric or sonar technique).

### 8.2.2. *Surface Based Radiometer (SBR)*

The main limitation related to the surface based radiometer measurements was its 'fixed' location during the study. Due to logistical constraints, there was no opportunity to move the SBR on the ice; therefore different snow thickness measurements were limited at specific incidence angles as described in Chapter 3. Despite this, the site was well protected and evolved 'naturally' with limited influence from the ship. I compared the ship's snow thermophysical data with other sites within Franklin Bay and did not find any significant variations that could be associated with the proximity of the ship. As mentioned Chapter 6, a snow thickness evolution was measured at incidence angle above  $50^\circ$  allowing the development of a SWE algorithm applicable to satellite remote sensing (Chapter 7), but it would be interesting to measure the evolution of snow at all incidence angles.

Another caveat for *in-situ* SBR measurements was related to calibration. As mentioned in Chapter 3, clear sky conditions are required and calibrations should be done as often as possible. During February, we had several problems with the positioner and limited calibrations were conducted. We then relied on our best results from January and March calibrations under similar weather conditions and temperatures to correct the raw brightness temperatures for February. However, we did not find any significant changes in the  $T_b$  associated with the calibration during this period assuming January and March calibrations to be representative of February.

### **8.3. Future Work**

#### *8.3.1. Data Collection and Modeling*

The results provided in my dissertation will assist in further development of snow geophysical and thermodynamic models for Arctic first-year sea ice. However, greater efforts are required in field data collection and limitations still exist with regards to snow sampling. Unfortunately, strong assumptions do exist in current GCMs, and improved data quality and quantity will help address this issue. As discussed throughout my thesis, snow represents a key parameter within the Arctic system but is still poorly studied. My dissertation provides a first glance at a seasonal evolution of an Arctic snowpack, but yearly data would allow greater improvement of current climate models given the understanding of microscale processes effects on the broader Arctic system. Given the recent dramatic ice depletion, snow properties will more than ever control the surface energy balance and potentially the fate of Arctic sea ice.

Future work on developing empirical relationships between geophysical/electrical properties coupled with passive microwave scattering and emission mechanisms should be conducted in order to model these properties over an annual cycle. With improved data collection and computer technology, those relationships can be modeled spatially and temporally. Hence, I see the coupling of global climate, snow thermodynamic and microwave emission models as one of the most important elements of future work. That said, more fieldwork is necessary to address specific issues related to microscale process effects on macroscale satellite measurements.

### 8.3.2. Remote Sensing

Some of the limitations discussed above should be addressed in future research. For instance, a main limitation of Chapter 7 was the absence of video data to support the roughness analysis. Therefore, a coupling between *in-situ*/airborne/satellite passive microwave measurements along with digital video recording is required to understand the true effect of different spatial features on brightness temperatures. The next intuitive step is then to relate different winter scenes from passive and active microwaves through a spatial analysis of roughness using different scales as suggested above. Obviously, *in-situ* measurements of snow and sea ice thermophysical properties should be conducted coincidentally given the usual financial and logistical constraints of Arctic research.

### 8.4. Closing Comments

As mentioned throughout the dissertation, variations in surface energy balance can affect snow thermophysical and electrical properties under the influence of the three relevant feedbacks noted in Chapter 2. These in turn can affect microwave brightness temperatures scattering and emission mechanisms (i.e., SWE predictions) over a range of temporal and spatial scales. The Arctic environment is a complex system with many competing forcings and feedbacks that require a multi-disciplinary approach to their disentanglement. Microwave remote sensing from satellite is a valuable tool in this challenge, helping to understand the climate response that occur over short, mid, and long terms as I showed its utility in the study of snow and sea ice geophysical and thermodynamic processes.

To date, there have been very few studies of the thermophysical properties of snow-covered sea ice. This is particularly true for annual studies that measure geophysical and thermodynamic processes throughout an annual cycle. A better understanding of the interconnections between snow geophysics, thermodynamics, and microwave emission and scattering is critical for the assessment of future impacts on the Arctic, especially as early responses to climate change have already been detected. Even though recent SWE studies are promising, lingering uncertainties remained with regards to spatial variability. Given the importance of snow in the Arctic's system, those issues should be prioritized in future research.

## LITERATURE CITED

- ABEL, G. 1893. Daily Variation of Temperature in Snow and the Relation between the Thermal Conductivity of Snow and Its Density. *Meteorologicheskii Vestnik*, 3.
- AKITAYA, E., 1974. *Studies on depth hoar*, Contributions from the Institute of Low Temperature Science, 26 (Series A), 1-67.
- ALBERT, M.R. AND MCGILVARY, W.R. 1992. Thermal Effects Due to Air Flow and Vapor Transport in Dry Snow. *Journal of Glaciology*, 38, 273-281.
- ALBERT, M.R. 1996. Modeling Heat, Mass, and Species Transport in Polar Firn. *Annals of Glaciology*, 23, 138-143.
- ALBERT, M.R. 2002. Effects of Snow and Firn Ventilation on Sublimation Rates. *Annals of Glaciology*, 35, 510-514.
- ALBERT, M.R. AND SHULTZ, E. 2002. Snow and Firn Properties and Air-Snow Transport Processes at Summit, Greenland. *Atmospheric Environment*, 36, 2789-2797.
- Arctic Climate Impact Assessment (ACIA). *Impacts of a Warming Arctic*. Cambridge University Press, 2004.
- ARMSTRONG, R.L., CHANG, A.T.C., RANGO, A. AND JOSBERGER, E. 1993. Snow depths and grain size relationships with relevance for passive microwave studies. *Annals of Glaciology*, 17, 171-176.
- ARMSTRONG, R.L. AND BRODZIK, M.J. 2001. Recent northern hemisphere snow extent: A comparison of data derived from visible and microwave satellite sensors. *Geophysical Research Letters*, 28, 3673-3676.
- ARONS, E.M. AND COLBECK, S.C. 1995. Geometry of heat and mass transfer in dry snow: A review of theory and experiment. *Reviews of Geophysics*, 33, 463-493.

- ARYA, S.P. 1988. *Introduction to Micrometeorology*, Academic Press, Toronto.
- ASMUS, K. AND GRANT, C. 1999. Surface Based Radiometer (SBR) Data Acquisition System. *International Journal of Remote Sensing*, 20, 3125-3129.
- BADER, H.P., HAEFELI, R., BUCHER, E., NEHER, J., ECKEL, O., THARMS, C. AND NIGGLE, P. 1939. *Snow and its metamorphism*. U.S. Army Corps of Engineers Snow, Ice, and Permafrost Research Establishment Translation, 14, 313 pages.
- BADER, H. AND KUROIWA, D. 1962. *Cold regions science and engineering*. Part II. Physical Science. Section B: The physics and mechanics of snow as a material, CRREL Report, AD0287052, 99 pages.
- BAILEY, M. AND HALLETT, J. 2002. Nucleation, Growth and Habit Distribution of Cirrus Type Crystals Under Controlled Laboratory Conditions. *Q.J.R. Meteorol. Soc.*, 128, 1461-1484.
- BAKER-JARVIS, J. 2000. A generalized dielectric polarization evolution equation. *IEEE Transactions on Dielectrics and Electrical Insulation*, 7, 374-386.
- BARBER, D.G., FLETT, D.G., DE ABREU, R.A. AND LEDREW, E.F. 1992a. Spatial and Temporal Variation of Sea Ice Geophysical Properties and Microwave Remote Sensing Observations: The SIMMS'90 Experiment. *Arctic*, 45, 233-251.
- BARBER, D.G., LEDREW, E.F., FLETT, D.G., SHOKR, M. AND FALKINGHAM, J. 1992b. Seasonal and Diurnal Variations in SAR Signatures of Landfast Sea Ice. *IEEE Transactions on Geoscience and Remote Sensing*, 30, 5 pages.
- BARBER, D.G. AND LEDREW, E.F. 1994. On the links between microwave and solar wavelengths interactions with snow covered first year sea ice. *Arctic*, 47, 298-309.
- BARBER D.G, PAPAKYRIAKOU T.N. AND LEDREW E.F. 1994. On the Relationship between Energy Fluxes, Dielectric Properties, and Microwave Scattering over Snow Covered First-Year Sea Ice During the Spring Transition Period. *Journal of Geophysical Research*. 99, 22,401-22,411.

- BARBER, D.G., PAPAKYRIAKOU, T.N., LEDREW, E.F. AND SHOKR, M.E. 1995. An examination of the relation between the spring period evolution of the scattering coefficient and radiative fluxes over landfast sea-ice. *International Journal of Remote Sensing*, 16, 3343-3363.
- BARBER, D.G., REDDAN, S.P. AND LEDREW, E.F. 1995. Statistical characterization of the geophysical and electrical properties of snow on landfast first-year sea ice. *Journal of Geophysical Research*, 100, 2673-2686.
- BARBER, D.G., FUNG, A.K. GRENFELL, T.C. NGHIEM, S.V., ONSTOTT, R.G. LYTLE, V.I., PEROVICH, D.K. AND GOW, A.J. 1998. The role of snow on microwave emission and scattering over first-year sea ice. *IEEE Transactions on Geoscience and Remote Sensing*, 36, 13 pages.
- BARBER, D.G. AND THOMAS, A. 1998. The influence of cloud cover on the radiation budget, physical properties and microwave scattering coefficient of first-year and multi-year sea ice. *IEEE Transactions on Geoscience and Remote Sensing*, 36, 13 pages.
- BARBER, D.G. AND NGHIEM, S.V. 1999. The role of snow on the thermal dependence of microwave backscatter over sea ice. *Journal of Geophysical Research*, 104, 25,789-25,803.
- BARBER, D., IACOZZA, J. AND WALKER, A. 2003. Estimation of snow water equivalent using microwave radiometry over Arctic first-year sea ice. *Hydrological Processes*, 17, 3503-3517.
- BARBER D.G. AND HANESIAK J.M. 2004. Meteorological forcing of sea ice concentrations in the southern Beaufort Sea over the period 1979 to 2000. *Journal of Geophysical Research*, 109, 16 pages.
- BARTLETT, M.G., CHAPMAN, D.S. AND HARRIS, R.N. 2004. Snow and the ground temperature record of climate change. *Journal of Geophysical Research*, 109, doi:10.1029/2004JF000224.
- BAUNACH, T., FIERZ, C., SATYAWALI, P.K. AND SCHNEEBELI, M. 2001. A model for kinetic grain growth. *Annals of Glaciology*, 32, 1-6.

- BERGEN, J.D. 1968. Vapor transport as estimated from heat flow in a rocky mountain snowpack. *I.A.S.H.*, 61, 62-74.
- BOER G.J, FLATO G, RAMSDEN D. 2000. A transient climate change simulation with greenhouse gas and aerosol forcing: projected climate to the twenty-first century. *Climate Dynamics*, 16: 427-450.
- BRUN, E., TOUVIER, F. AND BRUGNOT, G. 1987. *Experimental study on thermal convection and grains picture analysis*, In Seasonal Snow covers: Physics, Chemistry, Hydrology, H. Jones G. and Orville-Thomas, W.J. (eds.), NATO ASI Series C: Mathematical and Physical Sciences, 211. D. Reidel Publishing Co., Dordrecht, p. 75-94.
- BRZOSKA, J.-B., COLEOU, C. AND LESAFFRE, B. 1998. Thin-sectioning of wet snow after flash-freezing. *Journal of Glaciology*, 44, 54-62.
- BUDD, W.F., DINGLE, R.J. AND RADOK, U. 1966. *The Byrd Snow Drift Project: outline and basic results*, In Rubin, M. J., ed. Studies in Antarctic meteorology. Washington, DC, American Geophysical Union, 71-134. (Ant. Research Series 9.)
- BUSER, O., BÜTTLER, M. AND GOOD, W. 1987. Avalanche forecast by the nearest neighbor method, Proceedings of the Davos Symposium. *I.A.H.S.*, Publ.no.162.
- CARSEY, F. 1992. Remote sensing of ice and snow: review and status. *International Journal of Remote Sensing*, 13, 5-11.
- CAVALIERI, D.J., GLOERSEN, P. AND CAMPBELL, W.J. 1984. Determination of sea ice parameters with the NIMBUS-7 SMMR. *Journal of Geophysical Research*, 89, 5355-5369.
- CAVALIERI, D. AND COMISO, J. 2000. *Algorithm Theoretical Basis Document for the AMSR-E Sea Ice Algorithm*, Revised December 1. Landover, MD, USA: Goddard Space Flight Center.

- CAVALIERI, D. AND COMISO, J. 2004. updated daily. *AMSR-E/Aqua Daily L3 12.5 km Tb, Sea Ice Conc., & Snow Depth Polar Grids V001*, March to June 2004. Boulder, CO, USA: National Snow and Ice Data Center. Digital media.
- CHANG, A.T.C., FOSTER, J.L., HALL, D.K., RANGO, A. AND HARTLINE, B.K. 1982. Snow water equivalent estimation by microwave radiometry. *Cold Regions Science and Technology*, 5, 259-267.
- CHANG, A.T.C, FOSTER, J.L. AND HALL, D.K. 1987. Nimbus-7 derived global snow cover parameters. *Annals of Glaciology*, 9, 39-44.
- CHEN, F.W., LECKMAN, A.M. AND STAELIN, D.H. 2003. Satellite Observations of Polar Precipitation Using Aqua, *7th Conference on Polar Meteorology and Oceanography and Joint Symposium on High-Latitude Climate Variations*, Hyannis, MA, American Meteorological Society.
- CLARKE, G.K.C., FISHER, D.A. AND WADDINGTON, E.D. 1987. Wind pumping : a potentially significant heat source in ice sheets. *International Association of Hydrological Sciences Publication 170*, (Symposium at Vancouver, Canada-The Physical Basis of Ice Sheet Modeling), 169-180.
- CLARKE, G.K.C. AND WADDINGTON, E.D. 1991. A three-dimensional theory of wind pumping. *Journal of Glaciology*, 37,89-96.
- COLBECK, S.C. 1980. Thermodynamics of snow metamorphism due to variations in curvature. *Journal of Glaciology*, 26, 291-301.
- COLBECK, S.C. 1982. An Overview of Seasonal Snow Metamorphism. *Reviews of Geophysics and Space Physics*, 20, 45-61.
- COLBECK, S.C. 1983. Theory of metamorphism of dry snow. *Journal of Geophysical Research*, 88, 5475-5482.

- COLBECK, S.C. 1989. On the micrometeorology of surface hoar growth on snow in mountainous area. *BOUNDARY-LAYER METEOROLOGY*, 44, 1-12.
- COLBECK, S.C., 1993. The Vapor Diffusion Coefficient for Snow. *Water Resources Research*, 29, 109-115.
- COLBECK, S.C. 1997. *A Review of Sintering in Seasonal Snow*. CRREL Report, 97-10: 1-11.
- COMISO, J.C., GRENFELL, T.C., BELL, D.L., LANGE, M.A. AND ACKLEY, S.F. 1989. Passive microwave in-situ observations of winter Wedell sea ice. *Journal of Geophysical Research*, 95, 10,891-10,905.
- COMISO J.C. 2002. A rapidly declining perennial sea ice cover in the Arctic. *Geophysical Research Letters*, 29, doi: 1029/2002GL015650.
- COMISO, J.C. 2003. Warming trends in the Arctic from clear sky satellite observations. *Journal of Climate*, 16, 3498-3510.
- COMISO, J.C. 2003. *Large-scale characteristics and variability of the global sea ice cover. In Sea Ice: An Introduction to its Physics, Chemistry, Biology and Geology*, In D.N. Thomas and G.S. Dieckmann (eds), pp. 112-142 (Blackwell Science Ltd., Oxford, UK.)
- CORDISCO, E., PRIGENT, C. AND AIRES, F. 2006. Snow characterization at a global scale with passive microwave satellite observations. *Journal of Geophysical Research*, 111, doi:10.1029/2005JD006773, 15 pages.
- COX G.F.N, WEEKS W.F. 1982. *Equations for determining the gas and brine volume in sea ice samples*. CRREL Report, 1-20.
- CURRY, J.A., ROSSOW, W.B., RANDALL, D. AND SCHRAMM, J.L. 1996. Overview of Arctic cloud and radiation characteristics. *Journal of Climate*, 9, 1731– 1764.
- DEIRMENDJIAN, D. 1969. Electromagnetic scattering on spherical polydispersions. *American Elsevier Publishing Co.* (New York, 1969).

- DE QUERVAIN, M.B. 1958. On the metamorphism and hardening of snow under constant temperature gradient. *I.A.S.H.*, 46, 225-239.
- DE QUERVAIN, M.B. 1972. Snow structure, heat and mass flux through snow. *International Symposium on the role of snow and ice hydrology*, UNESCO-WMO, Banff, Canada.
- DENOTH, A. 1980. The pendular-funicular liquid transition in snow. *Journal of Glaciology*, 25, 93-97.
- DENOTH, A., 1989. Snow dielectric measurements. *Advances in Space Research*, 9, 233-243.
- DENOTH, A. 2003. Structural phase changes of the liquid water component in Alpine snow. *Cold Regions Science and Technology*, 37, 227-232.
- DERKSEN, C., LEDREW, E., AND GOODISON, B. 2000. Temporal and spatial variability of North American prairie snow cover (1988-1995) inferred from passive microwave-derived snow water equivalent imagery. *Water Resource Research*, 36, 255-266.
- DERKSEN, C., WALKER, A. AND GOODISON, B. 2005. Evaluation of passive microwave snow water equivalent retrievals across the boreal forest/tundra transition of western Canada. *Remote Sensing of Environment*, 96, 315-327.
- DÉRY, S.J. AND YAU, M.K. 2002. Large-scale mass balance effects of blowing snow and surface sublimation, *Geophysical research Letters*, 107, 8-17.
- DESER, C., WALSH, J.E. AND TIMLIN, M.S. 2000. Arctic sea ice variability in the context of recent wintertime atmospheric circulation trends. *Journal of Climate*, 13, 617-633.
- DETHLOFF, K., RINKE, A., BENKEL, A., KØLTZOW, M., SOKOLOVA, E., KUMAR SAHA, S., HANDORF, D., DORN, W., ROCKEL, B., VON STORCH, H., HAUGEN, J. E., RØED, L. P., ROECKNER, E., CHRISTENSEN AND STENDEL, M. 2006. A dynamic link between the arctic and the global climate system. *Geophysical Research Letters*, 33, doi: 10.1029/2005GL025245, 4pp.

- DOMINÉ, F., TAILLANDIER, A.S., SIMPSON, W.R. AND SEVERIN, K. 2005. Specific surface area, density and microstructure of frost flowers. *Geophysical Research Letters*, 32, doi.10.1029/2005GL023245, 4 pages.
- DOMINÉ, F., SALVATORI, R., LEGAGNEUX, L., SALZANO, R., FILY, M. AND CASACCHIA, R. 2006. Correlation between the specific surface area and the short wave infrared (SWIR) reflectance of snow. *COLD REGIONS SCIENCE AND TECHNOLOGY*, 46, 60-68.
- DONG, X. AND MACE, G.G. 2003. Arctic stratus cloud properties and radiative forcing derived from ground-based data collected at Barrow, Alaska. *Journal of Climate*, 16, 445-461.
- DORONIN, Y.P. AND KHEISIN, D.E. 1977. *Sea Ice*. Amerind Publishing, New Delhi, 323 pp.
- DRINKWATER, M.R. AND CROCKER, G.B. 1988. Modeling changes in the dielectric and scattering properties of young snow-covered sea ice at GHz frequencies. *Journal of Glaciology*, 34, 274-282.
- DROBOT, S.D. AND BARBER, D.G. 1998. Towards Development of a Snow Water Equivalence (SWE) Algorithm Using Microwave Radiometry over Snow Covered First-Year Sea Ice. *Photogrammetric Engineering & Remote Sensing*, 64, 414-423.
- EBERT, E.E. AND CURRY, J.A. 1993. An intermediate one-dimensional thermodynamic sea ice model for investigating ice-atmosphere interactions. *Journal of Geophysical Research*, 98, 10085-10109.
- EICKEN H, FISCHER H, LEMKE P. 1995. Effects of the snow cover on Antarctic sea ice and potential modulation of its response to climate change. *Annals of Glaciology*, 21, 369-376.
- EIKEN H. 2003. *From the microscopic, to the macroscopic, to the regional scale: growth, microstructure and properties of sea ice*. IN *Sea Ice: An Introduction to its Physics, Chemistry, biology and Geology*, D.N. Thomas and G.S. Dieckmann (Eds). Blackwell Science Ltd., Oxford, UK. 22-81.

- EPPLER, D. T. 1992. *Passive microwave signatures of sea ice*. In F. Carsey, Editor, Microwave remote sensing of sea ice, American Geophysical Union, Washington, D.C., 47-71.
- FEDOSEEVA, V.I. AND FEDOSEEV, N.F. 1988. Evaluation of the coefficient of diffusion of water vapor in snow cover. *Meteorologîa i gidrologîa*, 2, 132–135.
- FISICO T. 2005. *Section 3.3. Meteorological Observations*. In Langlois A., Fisico T., Galley R. and Barber D.G. (Eds.), CASES 2003-2004 Field Summary, CEOS-TEC-2004-09-01. 70-110.
- FLANNER, M.G. AND ZENDER, C.S. 2006. Linking snowpack microphysics and albedo evolution. *Journal of Geophysical Research*, 111, doi:10.1029/2005JD006834, 12 pages.
- FLATO, G.M. AND BROWN, R.D. 1996. Variability and climate sensitivity of landfast Arctic sea ice. *Journal of Geophysical Research*, 101, 25,767-25,777.
- FLATO G.M. AND BOER G.J. 2001. Warming asymmetry in climate change simulations. *Geophysical Research Letters*, 28, 195-198.
- FOSTER, J.L., HALL, D.K., CHANG, A.T.C. AND RANGO, A. 1984. An overview of passive microwave snow research and results. *Reviews of Geophysics*, 22, 195-208.
- FOSTER, J.L., HALL, D.K., CHANG, A.T.C., RANGO, A., WERGIN, W. AND ERBE, E. 1999. Effects of snow crystal shape on the scattering of passive microwave radiation. *IEEE Transactions on Remote Sensing*, 37, 1165-1168.
- FOSTER, J.L., SUN, C., WALKER, J.P., KELLY, R., CHANG, A., DONG, J. AND POWELL, H. 2005. Quantifying the uncertainty in passive microwave snow water equivalent observations. *Remote Sensing of Environment*, 94, 187-203.
- FRANCIS, J.A., HUNTER, E., KEY, J.R. AND WANG, X. 2005. Clues to variability in Arctic minimum sea ice extent. *Geophysical Research Letters*, 32, 4 pages.

- FRANKENSTEIN, G. AND GARNER, R. 1967. Equations for determining the brine volume of sea ice from  $-0.5$  to  $-22.9$  degrees C. *Journal of Glaciology*, 6, 943-944.
- FUKUSAKO, S. 1990. Thermophysical properties of ice, snow and sea ice. *International Journal of Thermophysics*, 11, 19 pp.
- GARRITY, C. 1992. *Characterization of snow on floating ice and case studies of brightness temperature changes during the onset of melt*. In Microwave remote sensing of sea ice, F. Carsey, (ed), American Geophysical Union, Washington, D.C., 313-328.
- GERDES, R. 2006. Atmospheric response to changes in Arctic thickness. *Geophysical Research Letters*, 33, 4 pages.
- GIDDINGS, J. C. AND LACHAPELLE, E. 1962. The formation rate of depth hoar. *Journal of Geophysical Research*, 67, 2377.
- GJESSING, Y.T. 1977. The filtering effect of snow, In Isotopes and impurities in snow and ice, *IAHS-AISH Publication*, 118, 199-203.
- GOGINENI, S.P., MOORE, R.K., GRENFELL, T.C., BARBER, D.G., DIGBY, S. AND DRINKWATER, M.D. 1992. *The Effects of Freeze-up and Melt Processes on Microwave Signatures*. In F. Carsey, editor, Microwave remote sensing of sea ice, American Geophysical Union, Washington, D.C., 327-341.
- GOLDEN, K.M., ACKLEY, S.F. AND LYTLE, V.I. 1998. The percolation phase transition in sea ice. *Science*, 282, 2238-2241.
- GRANBERG, H. 1998. *Physics of ice-covered seas, vol. 2*. Lecture notes from a summer school in Savonlinna, Leppäranta M. (Ed.)605-649.
- GRANGER, R. J. AND ESSERY, R. 2004. . *Observation and Modeling of the Thermal Boundary Layer over Snow and soil Patches* Geophysical Union, Fall Meeting 2004.

- GRENFELL, T.C. AND MAYKUT, G.A. 1977. The optical properties of ice and snow in the Arctic Basin. *Journal of Glaciology*, 18, 445-463.
- GRENFELL, T.C. AND LOHANICK, A.W. 1985. Temporal variations of the microwave signatures of sea ice during late spring and early summer near Mould Bay NWT. *Journal of Geophysical Research*, 90, 5063-5074.
- GRENFELL, T.C. AND COMISO, J.C. 1986. Multifrequency passive-microwave observations of first-year sea ice grown in a tank. *IEEE Transactions on Geoscience and Remote Sensing*, GE-24, 862-831.
- GRENFELL, T.C., BARBER, D.G., FUNG, A.K., GOW, A.J., JEZEK, K.C., KNAPP, E.J., NGHIEM, S.V., ONSTOTT, R.G., PEROVICH, D.K., ROESLER, C.S., SWIFT, C.T. AND TANIS, F. 1998. Evolution of electromagnetic signatures of sea ice from initial formation to the establishment of thick first-year ice. *IEEE Transactions on Geoscience and Remote Sensing*, 39, 13 pages.
- GRENFELL, T.C. AND PEROVICH, D.K. 2004. The seasonal and spatial evolution of albedo in a snow-ice-land-ocean environment. *Journal of Geophysical Research*, 109, doi:10.1029/2003JC001866.
- GRODY, N. AND BASIST, A. 1996. Global identification of snow cover using SSM/I measurements. *IEEE Transaction on Geoscience and Remote Sensing*, 34, 12 pages.
- GUBLER, H. 1985. Model for dry snow metamorphism by interparticle vapor flux. *Journal of Geophysical Research*, 90, 8081-8092.
- HALL, D.K., FOSTER, J.L., VERBYLA, D.L., KLEIN, A.G. AND BENSON, C.S. 1998. Assessment of snow cover mapping accuracy in a variety of vegetation cover densities in central Alaska. *Remote Sensing of the Environment*, 66, 129-137.
- HALL, D.K., SOLBERG, R. AND RIGGS, G.A. 2004. Sea ice surface temperature product from MODIS. *IEEE Transactions on Geoscience and Remote Sensing*, 42, 1076-1087.

- HALL, D. K., RIGGS, G.A. AND SALOMONSON, V.V. 2007. *Updated daily. MODIS/Aqua snow cover daily L3 global 0.05deg CMG V005*, [December 2003 – May 2004]. Boulder, Colorado USA: National Snow and Ice Data Center. Digital media.
- HALLIKAINEN, M. T. 1989. Microwave radiometry of snow. *Advances in Space Research*, 9, 267-275.
- HALLIKAINEN, M. AND WINEBRENNER, D.P. 1992. The physical basis for sea ice remote sensing. *Microwave Remote Sensing of Sea Ice, Geophys. Monogr. Ser.*, 68, 29-44.
- HALLIWELL, D.H. AND ROUSE, W.R. 1989. A comparison of sensible and latent heat flux calculations using the Bowen ratio and aerodynamic methods. *J. Atm. Tech.*, 6, 563-574.
- HANESIAK, J., BARBER, D.G. AND FLATO, G.M. 1999. Role of diurnal processes in the seasonal evolution of sea ice and its snow cover. *Journal of Geophysical Research*, 104, 13,593-13,603.
- HANESIAK, J.M. 2001. *Development of a one-dimensional Electro-Thermophysical model of the snow-sea ice system: Arctic Climate Processes and Microwave remote sensing Applications*. PhD. Thesis, University of Manitoba, 293 pages.
- HAROUCHE, I. AND BARBER, D.G. 2001. Seasonal characterization of microwave emission from snow covered first-year sea ice. *Hydrological Processes*, 15, 3571-3583.
- HILMER, M. AND LEMKE, P. 2000. On the decrease of arctic sea ice volume. *Geophysical Research Letters*, 27, 3751.
- HOLLMAN, J.P. 1997: *Heat Transfer*. 8th Edition. McGraw-Hill.
- HOLTSLAG, A.A.M. AND DE BRUIN, H.A.R. 1988. Applied modeling of the nighttime surface energy balance over land. *J. Appl. Meteorol.*, 37, 689-704.

- HORNBERGER, G.H., BENCALA, K.E. AND MCKNIGHT, D.M. 1994. Hydrological controls on dissolved organic carbon during snowmelt in the Snake River near Montezuma, Colorado. *Biogeochemistry*, 25, 147–165.
- HUDAK, D.R., AND YOUNG, J.M.C. 2002. Storm climatology of the southern Beaufort Sea. *Atmosphere-Ocean*, 40, 145-158.
- HWANG, B.J., EHN, J.K. AND BARBER, D.G. 2006. Relationships Between Sea Ice Albedo and Microwave Emissions During Fall Freeze-up: An in-situ study. *Geophysical Research Letters*, 33, doi:10.1029/2006GL027300.
- HWANG, B.J., LANGLOIS, A., BARBER, D.G. AND PAPAKYRIAKOU, T.N. 2007. Detection of the thermophysical state of landfast first-year sea ice using in-situ microwave emission during spring melt. *Remote Sensing of Environment*, In Press, RSE-D-06-00435R2.
- IACOZZA, J. AND BARBER, D.G. 2001. Ablation patterns of snow cover over smooth first-year sea ice in the Canadian Arctic. *Hydrological Processes*, 15, 3559-3569.
- Intergovernmental Panel on Climate Change (IPCC), Climate change 2001: The Scientific Basis, Contribution of Working Group I to the Third Assessment Report of the Intergovernmental Panel on Climate Change. Cambridge University Press, New York, 2001.
- IZUMI, K. AND HUZIOKA, T. 1975. Studies of metamorphism and thermal conductivity of snow. *Low Temperature Science Series*, A, 33, 91-102.
- JENSEN, E., AND PFISTER, L. 2005. Implications of persistent ice supersaturation in cold cirrus for stratospheric water vapor. *Geophysical Research Letters*, 32, L01808.
- JONSCHER, A.K. 1996: Universal relaxation law. Chelsea Dielectrics Press, London.
- JORDAN, R.E. AND ANDREAS, E.L. 1999. Heat budget of snow-covered sea ice at North Pole 4. *Journal of Geophysical Research*, 104, 7785-7806.

- KEELER, C.M. 1969. The growth of bonds and the increase of mechanical strength in a dry seasonal snow-pack. *Journal of Glaciology*, 8, 441-450.
- KELLER, V. AND HALLETT, J. 1982. Influence of air velocity on the habit of ice crystal growth from the vapour. *Journal of Crystal Growth*., 60, 91-106.
- KELLY, R., CHANG, A.T.C., TSANG, L. AND FOSTER, J. 2003. A prototype AMSR-E global snow area and snow depth algorithm. *IEEE Transactions on Geoscience and Remote Sensing*, 41, 230-242.
- KERR, Y.H. AND NJOKU, E.G. 1990. A semi empirical model for interpreting microwave emission from semiarid land surfaces as seen from space. *IEEE Transactions on Geoscience and Remote Sensing*, 28, 384-393.
- KEY, J.R., COLLINS, J.B., FOWLER, C. AND STONE, R.S. 1997. High latitude surface temperature estimates from thermal satellite data. *Remote Sensing of the Environment*, 61, 302-309.
- KOOP, T., LUO, B., TSIAS, A. AND PETER, T. 2000. Water activity as the determinant for homogeneous ice nucleation in aqueous solutions. *Nature*, 406, 611-614, 2000.
- KOTLYAKOV, V.M. 1961. The snow cover of the Antarctic and its role in the present-day glaciation of the continent. *Israel Program for Scientific Translation*.
- KUNZI, K.F., PATIL, S. AND ROTT, H. 1982. Snow cover parameters retrieved from Nimbus-7 Scanning Multichannel Microwave Radiometer (SMMR) data. *IEEE Transactions on Geoscience and Remote Sensing*, 20, 452-467.
- KURVONEN, L. AND HALLIKAINEN, M. 1997. Influence of land-cover category on brightness temperature of snow. *IEEE Transactions on Geoscience and Remote Sensing*, 35, 367-377.
- LANGE, M.A. AND FORKER, G.M. 1952. *Handbook of Chemistry*. Ohio, Handbook Publishers, 8th Edition.

- LANGE, M.A., ACKLEY, S.F., WADHAMS, P., DIECKMANN, G.S. AND EICKEN, H. 1989. Development of sea ice in the Wedell Sea. *Annals of Glaciology*, 12, 92-96.
- LANGLOIS, A, MUNDY, C.J. AND BARBER, D.G. 2007a. On the winter evolution of snow thermophysical properties over landfast first-year sea ice. *Hydrological Processes*, 21, 705-716.
- LANGLOIS, A., BARBER, D.G. AND HWANG, B.J. 2007b. Development of a winter snow water equivalent algorithm using in-situ passive microwave radiometry over snow covered first-year sea ice. *Remote Sensing of Environment*, 106, 75-88, doi: 10.1016/j.rse.2006.07.018.
- LANGLOIS, A., FISICO, T., BARBER, D.G. AND PAPAKYRIAKOU, T.N. 2007c. The response of snow thermophysical processes to the passage of a polar low-pressure system and its impact on in-situ passive microwave data: A case study. *Journal of Geophysical Research*, Submitted, February 2007, 2007JC004197.
- LANGLOIS, A. AND BARBER, D.G. 2007a. Advances in seasonal snow water equivalent (SWE) retrieval using in-situ passive microwave measurements over first-year sea ice. *International Journal of Remote Sensing*, Accepted July 2007, TRES-PAP-2007-0210.
- LANGLOIS, A. AND BARBER, D.G. 2007b. Passive Microwave Remote Sensing of Seasonal Snow Covered Sea Ice, *Progress in Physical Geography*, Accepted July 2007.
- LANGLOIS, A., SCHARIEN, R., GELSETZER, T., IACOZZA, J., BARBER, D.G. AND YACKEL, J. 2007d. Estimating Snow Water Equivalent over First-Year Sea Ice using Satellite Microwave Remote Sensing. *Remote Sensing of Environment*, Submitted 2007.
- LAUNIAINEN J., VIHMA T. 1990. Derivation of turbulent surface fluxes - an iterative flux - profile method allowing arbitrary observing heights. *Environmental Software*, 5, 3, 113 – 124.
- LEDLEY, T.S. 1991. Snow on sea ice: Competing effects in shaping climate. *Journal of Geophysical Research*, 96, 197-17,208.

- LEPPÄRANTA, M. AND MANNINEN, T. 1988. *The brine and gas content of sea ice with attention to low salinities and high temperatures*, Finnish Institute of Marine Research, Internal Report 2.
- LEPPÄRANTA, M. AND HAKALA, R. 1992. The structure and strength of first-year ice ridges in the Baltic Sea. *Cold Region Science and Technology*, 20: 295-311.
- LI, W., STAMNES, K., CHEN, B. AND XIONG, X. 2001. Snow grain size retrieved from near-infrared radiances at multiple wavelengths. *Geophysical Research Letters*, 28, 1699-1702.
- LIVINGSTONE, C.E. 1994. *Synthetic aperture radar images of sea ice*, In *Remote sensing of sea ice and icebergs*. Edited by S. Haykin, E.O. Lewis, R.K. Raney and J.R. Rossiter. John Wiley & Sons, Inc., New York, Chapter 11, 540-569.
- LOGSDON, S.D. AND LAIRD, D.A. 2004. Cation and Water Content Effects on Dipole Rotation Activation Energy of Smectites. *Soil Science Society of America Journal*, 68, 1586-1591.
- LOHANICK, A.W. AND GRENFELL, T.C. 1986. Variations in brightness temperature over cold first-year sea ice near Tuktoyaktuk, NT. *Journal of Geophysical Research*, 91, 5133-5144.
- LOHANICK, A.W. 1993. Microwave brightness temperatures of laboratory-grown undeformed first-year ice with an evolving snow cover. *Journal of Geophysical Research*, 98, 4667-4674.
- MÄKYNEN, M. AND HALLIKAINEN M. 2004. Investigation of C- and X-band backscattering signatures of Baltic Sea ice. *International Journal of Remote Sensing*, 25, 2061-2086.
- MÄKYNEN, M. AND HALLIKAINEN, M. 2005. Passive microwave signature observations of the Baltic Sea ice. *International Journal of Remote Sensing*, 26, 2081-2106.
- MARKUS, T. AND CAVALIERI, D.J. 1998. *Snow depth distribution over sea ice in the southern ocean from satellite passive microwave data*. Antarctic Sea Ice Physical Processes, Interactions and Variability. Antarctic Research Series, 74, American Geophysical Union: Washington, DC; 19-39.

MARKUS, T. AND CAVALIERI, D.J., 2000. An enhancement of the NASA Team sea ice algorithm. *IEEE Transactions on Geoscience and Remote Sensing*, 38, 1387-1398.

MARKUS, T., POWELL, D.C. AND WANG, J.R. 2006a. Sensitivity of passive microwave snow depth retrievals to weather effects and snow evolution. *IEEE Transactions on Geoscience and Remote Sensing*, 44, 68-77.

MARKUS, T., CAVALIERI, D.J., GASIEWSKI, A.J., KLEIN, M., MASLANIK, J.A., POWELL, D.C., STANKOV, B.B., STROEVE, J.C. AND STURM, M. 2006b. Microwave signatures of snow on sea ice: Observations. *IEEE Transactions on Geoscience and Remote Sensing*, 44, 3081-3090.

MARSH, P. 1999. Snow cover formation and melt: recent advances and future prospects. *Hydrological Processes*, 13, 2117-2134.

MASSOM, R.A., EICKEN, H., HAAS, C., JEFFRIES, M.O., DRINKWATER, M.R., STURM, M., WORBY, A.P., WU, X., LYTLE, V.I., USHIO, S., MORRIS, K., REID, P.A., WARREN, S.G. AND ALLISON, I. 2001. Snow on Antarctic sea ice. *Review of Geophysics*, 39, 413-445.

MATZL, M. 2006. *Quantifying the stratigraphy of snow profiles*. PhD Dissertation, Swiss Federal Institute of Technology, Zurich, Switzerland, 2006, no. 16570.

MÄTZLER, C. 1987. Applications of the interaction of microwaves with natural snow cover. *Remote Sensing Reviews*, 2, 259-387.

MÄTZLER, C. AND HUPPI, R. 1989. Review of Signatures studies for Microwave Remote Sensing of Snow Packs. *Advanced Space Research*, 9, 253-265.

MÄTZLER, C. 1992. *Passive Microwave Signature Catalogue 1989-1992*. Report, Vol. 1, Institute of Applied Physics, University of Berne.

MÄTZLER, C. AND WIESMANN, A. 1999. Extension of the microwave emission model of layered snowpacks to coarse-grained snow, *Remote Sensing of Environment*, 70, 317-325.

- MAYKUT, G.A. AND CHURCH, P.E. 1973. Radiation climate of Barrow, Alaska, 1962-66. *Journal of Applied Meteorology*, 12, 620– 628.
- MAYKUT, G.A. 1978. Energy exchange over young sea ice in the central Arctic. *Journal of Geophysical Research*, 83, 3646-3658.
- MAYKUT, G.A. 1986. *The surface heat and mass balance*. In N. Untersteiner, editor, *The geophysics of sea ice*, New York: Plenum.
- MCCONNELL, J.R., BALES, R.C., STEWART, R.W., THOMPSON, A.M., ALBERT, M.R. AND RAMOS, R. 1998. Physically based modeling of atmosphere-to-snow-to-firn transfer of H<sub>2</sub>O<sub>2</sub> at the South Pole. *Journal of Geophysical Research*, 103, 10561–10570.
- MCKAY, C.P. 2000. Thickness of tropical ice and photosynthesis on a snowball Earth. *Geophysical Research Letters*, 27, 2153-6.
- MELLOR, M. 1977. Engineering properties of snow. *Journal of Glaciology*, 19, 15-66.
- MOORE D.S. AND MCCABE G.P. 1993. *Introduction to the practice of statistics*. 2nd Edition. Purdue University, W.H. Freeman and Company, 854 pages.
- MORITZ, R.E. AND PEROVICH, D.K. 1996. *Surface Heat budget of the Arctic Science Plan*. ARCSS/OAII report number 5, University of Washington, Seattle, 64 pages.
- MUNDY, C.J., BARBER, D.G. AND MICHEL, C. 2005. Variability of snow and ice thermal, physical and optical properties pertinent to sea ice algae biomass during spring. *Journal of Marine Systems*, 58, 107-120.
- NGHIEM, S.V., KWOK, R., YUEH, S.H. AND DRINKWATER, M.R. 1995. Polarimetric signatures of sea ice. 1. Theoretical model. *Journal of Geophysical Research*, 100, 13,665-13,679.
- NGHIEM, S.V. AND BERTOIA C. 2001. Multi-polarization C-Band SAR signatures of arctic sea ice. *IEEE International Geoscience and Remote Sensing Symposium*, IGARSS 2001, 9-13, July 2001. Sydney, Australia. IEEE Inc. Piscataway N.J. pp. 1792-1794.

- NIKOLENKO, A.V. 1988. Laboratory-determined characteristics of water vapor diffusion in snow cover. *Mater. Gliatsiologicheskikh Issled.*, 62, 90-96.
- OKE, T.R. 1987. *Boundary layer climates*. Methuen, New York, 435 p.
- ONO, N. 1966. Thermal properties of sea ice. III. On the specific heat of sea ice. *Low Temperature Science*, 249-258.
- ONSTOTT, R.G., GOGINENI, P., GOW, A.J., GRENFELL, T.C., JEZEK, K., PEROVICH, D.K. AND SWIFT, C.T. 1998. Electromagnetic and Physical Properties of Sea Ice Formed in the Presence of Wave Action. *IEEE Transactions on Geoscience and Remote Sensing*, 36, 1764-1783.
- PALM, E. AND TVEITERED, M. 1979. On heat and mass flow through dry snow. *Journal of Geophysical Research*, 84, 745-749.
- PAPAKYRIAKOU, T. 1999. *An Examination of Relationships among the Energy Balance, Surface Properties and Climate over Snow Covered Sea Ice during the Spring Season*. PhD Thesis University of Waterloo, 364.
- PEROVICH, D.K. 1996. *The Optical Properties of Sea Ice*. CRREL Monograph, 96-1, US Army Corps of Eng. Cold Regions Research and Engineering Lab., Hanover, NH.
- PEROVICH, D.K., AND ELDER, B. 2001. Temporal evolution and spatial variability of the temperature of Arctic sea ice. *Annals of Glaciology*, 33, 207-212.
- PHILIP, J.R. AND DE VRIES, D.A. 1957. Moisture movement in porous materials under temperature gradients. *Transactions of the American Geophysical Union*, 38, 222-232.
- POLLACK, H.N., DEMEZHKO, D.Y., DUCHKOV, A.D. GOLOVANOVA, I.V. HUANG, S., SHCHAPOV, V.A. AND SMERDON, J.E. 2003. Surface temperature trends in Russia over the past five centuries reconstructed from borehole temperatures, *Journal of Geophysical Research*, 108, doi:10.1029/2002JB002154.

- POLLARD, D. AND KASTING, J.F. 2005. Snowball Earth: A thin-ice solution with flowing sea glaciers. *Journal of Geophysical Research*, 110, doi: 10.1029/2004JC002525, 16 pp.
- POLYAKOV, I.V., ALEKSEEV, G.V., BEKRYAEV, R.V., BHATT, U.S., COLONY, R., JOHNSON, M.A., KARKLIN, V.P. WALSH, D. AND YULIN, A.V. 2003. Long-Term Ice Variability in Arctic Marginal Seas. *Journal of Climate*, 16, 2078-2085.
- POWELL, D.C., MARKUS, T. AND STOSSEL, A. 2005. Effects of snow depth forcing on Southern Ocean sea ice simulations. *Journal of Geophysical Research*, 110, 10 pages.
- POWELL, D.C., MARKUS, T., CAVALIERI, D.J., GASIEWSKI, A.J., KLEIN, M., MASLANIK, J.A., STROEVE, J.C. AND STURM, M. 2006. Microwave signatures of snow on sea ice: modeling. *IEEE Transactions on Geoscience and Remote Sensing*, 44, 3091-3101.
- PULLIAINEN, J. AND HALLIKAINEN, M. 2001. Retrieval of regional snow water equivalent from space-borne passive microwave observations. *Remote Sensing of Environment*, 75, 76-85.
- PULLIAINEN, J. 2006. Mapping of snow water equivalent and snow depth in boreal and sub-arctic zones by assimilating space-borne microwave radiometer data and ground-based observations. *Remote Sensing of Environment*, 101, 257-269.
- REES, D.A.S. AND RILEY, D.S. 1989. The effects of boundary imperfections on convection in a saturated porous layer: near-resonant wavelength excitation. *Journal of Fluid Mechanics Digital Archive*, 199, doi: 10.1017/S0022112089000327, 133-154.
- RIND, D., HEALY, R., PARKINSON, C. AND MARTINSON, D. 1995. The role of sea ice in 2 x CO<sub>2</sub> climate model sensitivity. Part 1: The total influence of sea ice thickness and extent. *Journal of Climate*, 8, 449-463.
- ROGERS R.R. AND YAU M.K. 1989. *A Short Course in Cloud Physics*. 3d ed. Butterworth-Heinemann, 290 pp.

- ROSENFELD, S. AND GRODY, N. 2000. Anomalous microwave spectra of snow cover observed from Special Sensor Microwave Imager measurements. *Journal of Geophysical Research*, 105, 913-14,925.
- ROTHROCK, D.A. AND ZHANG, J. 2005. Arctic Ocean sea ice volume: What explains its recent depletion? *Journal of Geophysical Research*, 110, 10 pp.
- RUFFIEUX, D. R., OLA, P., PERSSON, G., FAIRALL, C.W. AND WOLFE, D.E. 1995. Ice pack and lead surface energy budgets during LEADDEX 92. *Journal of Geophysical Research*, 100, 4593-4612.
- SERREZE, M., MASLANIK, J., SCHARFEN, G., BARRY, R. AND ROBINSON, D. 1993. Interannual variations in snow melt over Arctic Ocean and relationships to atmospheric forcings. *Annals of Glaciology*, 17, 327-331.
- SERREZE, M.C, BARRY, R.G. AND WALSH, J.E. 1995. Atmospheric water vapor characteristics at 70oN. *Journal of Climate*, 8, 719-731.
- SERREZE, M.C., MASLANIK, J.A., SCAMBOS, T.A., FETTERER, F., STROEVE, J., KNOWLES, K., FOWLER, C., DROBOT, S., BARRY, R.G. AND HARAN, T.M. 2003. A record minimum arctic sea ice extent and area in 2002. *Geophysical Research Letters*, 30, 4 pages.
- SINGH, P.R. AND GAN, T.Y. 2000. Retrieval of snow water equivalent using passive microwave brightness temperature data. *Remote Sensing of Environment*, 74, 275-286.
- SKOLNIK, M. I. 1980. *Introduction to Radar Systems*. 2nd Ed., McGraw-Hill, 1980.
- SOKOL, J., PULTZ, T.J. AND WALKER, A.E. 1999. Passive and Active Airborne Microwave Remote Sensing of Snow Cover. *4th International Airborne Remote Sensing Conference/21st Canadian Symposium on Remote Sensing*, 1999.
- SOKRATOV, S.A. AND MAENO, N. 2000. Effective water vapor diffusion coefficient of snow under a temperature gradient. *Water Resources Research*, 36, 1269-1276.

- STEELE, M. AND FLATO, G.M. 2000. *Growth, Melt, and Modeling: A Survey*. In E.L. Lewis et al., editors, *The Freshwater Budget of the Arctic Ocean*, Kluwer, 549-587.
- STEFFEN, K. AND DEMARIA, T. 1996. Surface energy fluxes over Arctic winter sea ice in Barrow Strait. *Journal of Applied Meteorology*, 35, 2067-2079.
- STILES, W.H. AND ULABY, F.T. 1980. The active and passive microwave response to snow parameters, Part I: Wetness. *Journal of Geophysical Research*, 83, 1037-1044.
- STOGRYN, A. 1970. The brightness temperature of a vertically structured medium. *Radio Science*, 5, 1397-1406.
- STOGRYN, A. 1971. Equations for calculating the dielectric constant of saline water. *IEEE Transactions on Microwave Theory and Technology*, MTT-19, 733-736.
- STOGRYN, A. AND DESARGANT, G.J. 1985. The dielectric properties of brine in sea ice at microwave frequencies. *IEEE Trans. Ant. Prop.*, AP-33, 523-532.
- STROEVE, J.C., SERREZE, M.C., FETTERER, F., ARBETTER, T., MEIER, W., MASLANIK, J. AND KNOWLES, K. 2005. Tracking the Arctic's shrinking ice cover: Another extreme minimum in 2004. *Geophysical Research Letters*, 32, 4 pages.
- STURM, M. 1991. *The role of thermal convection in heat and mass transport in the subarctic snow cover*, CRREL Report, 91-19, 84 p.
- STURM, M. AND JOHNSON, J.B. 1991. Natural Convection in the subarctic snow cover. *Journal of Geophysical Research*, 96, 11,657-11,671.
- STURM, M., HOLMGREN, J., KÖNIG, M. AND MORRIS, K. 1997. The Thermal Conductivity of Seasonal Snow Cover. *Journal of Glaciology*, 43, 26-41.
- STURM M. AND BENSON C.S. 1997. Vapour transport, grain growth and depth-hoar development in the subarctic snow. *Journal of Glaciology*, 43(143): 42-59.

STURM M, HOLMGREN J, PEROVICH D.K. 2002. Winter snow cover on the sea ice of the Arctic Ocean at the Surface Heat Budget of the Arctic Ocean (SHEBA): Temporal evolution and spatial variability. *Journal of Geophysical Research*, 107(C10): 23,1-23,16. DOI: 10.1029/2000JC000400.

STURM, M., MASLANIK, J.A., PEROVICH, D.K., STROEVE, J.C., RICHTER-MENGE, J., MARKUS, T., HOLMGREN, J., HEINRICHS, J.F. AND TAPE, K. 2006. Snow Depth and Ice Thickness Measurements From the Beaufort and Chukchi Seas Collected During the AMSR-Ice03 Campaign. *IEEE Transactions on Geoscience and Remote Sensing*, 44, 3009-3020.

TAIT, A.B. 1998. Estimation of snow water equivalent using passive microwave radiation data. *Remote Sensing of Environment*, 64, p. 286-291.

TEDESCO, M., PULLIAINEN, J., TAKALA, M., HALLIKAINEN, M. AND PAMPALONI, P. 2004. Artificial neural network-based techniques for the retrieval of SWE and snow depth from SSM/I data. *Remote Sensing of Environment*, 90, doi: 10.1016/j.rse.2003.12.002, 76-85.

THOMAS, A. AND BARBER, D.G. 1998. On the use of multi-year ice ERS-1 scattering coefficient as a proxy indicator of melt period sea ice albedo. *International Journal of Remote Sensing*, 19, 2807-2821.

THORNDIKE, A.S., PARKINSON, C. AND ROTHROCK, D.A. (Eds.). 1992. *Report of the Sea Ice Thickness Workshop, 19–21 November 1991*, New Carrollton, edited by A. S. Thorndike, C. Parkinson, and D. A. Rothrock, 162 pp., Appl. Phys. Lab., Univ. of Wash., Seattle, 1992.

TIURI, M.E., SIHVOLA, A.H., NYFORS, E.G. AND HALLIKAINEN, M.T. 1984. The complex dielectric constant of snow at microwave frequencies. *IEEE Journal of Oceanic Engineering*, OE-9, 377-382.

TRABANT, D. AND BENSON, C.S. 1972. Field experiments on the development of depth hoar. *Geol. Soc. Amer. Memoir*, 135, 309– 322.

TREIDL, R.A. 1970. A case study of warm air advection over a melting snow surface. *Bound.-Layer Meteor.*, 1, 155–168.

TSANG, L., KONG, J.A. AND SHIN, R.T. 1985. *Theory of Microwave Remote Sensing*. New York, Wiley.

TSANG, L. AND KONG, J.A. 1992. Scattering of electromagnetic waves from a dense medium consisting of correlated Mie scatterers with size distributions and applications to dry snow. *Journal of Electromagnetic Waves and Applications*, 6, 265-286.

TSANG, L., CHEN, C.T., CHANG, A.T.C., GUO, J. AND DING, K.H. 2000. Dense Media Radiative Transfer Theory Based on Quasicrystalline Approximation with Application to Passive Microwave Remote Sensing of Snow. *Radio Science*, 35, 731-749.

TUCKER, W.B.III., GOW, A.J. AND WEEKS, W.F. 1987. Physical properties of summer sea ice in Fram Strait. *Journal of Geophysical Research*, 92, 6787-6803.

TURCOTTE, D.L. AND SCHUBERT, G. 1982. *Geodynamics — application of continuum physics to geological problems*. John Wiley and Sons, New York, 1982, 450 pages.

ULABY, F.T., MOORE, R.K. AND FUNG, A.K. 1981. *Microwave Remote Sensing*. 1, Artech house, Norwood, MA.

ULABY, F.T., MOORE, R.K. AND FUNG, A.K. 1986. *Microwave Remote Sensing*. 3, Artech house, Norwood, MA.

VAN DE HULST, H.C. 1957. *Light Scattering by Small Particles*. Wiley, New York, NY.

VOWINKEL E. AND ORVIG S. 1970. *The climates of the North Polar Basin, in Climates of the Polar Region*. edited by S. Orvig, 129–226, Elsevier Sci.

WADDINGTON, E.D., CUNNINGHAM, J. AND HARDER, S.L. 1996. *The effects of snow ventilation on chemical concentrations*. In E.W. Wolff and R.C. Bales, editors, Processes of chemical exchange between the atmosphere and polar snow, (NATO ASI Series I). Berlin: Springer-Verlag.

- WADHAMS, P. AND DAVIS, N.R. 2000. Further evidence of ice Arctic Ocean, *Geophysical Research Letters*, 27, 3973-3975.
- WAKAHAMA, G. 1965. The metamorphism of wet snow. *Low temperature Science Series*, A(23), 51-66.
- WALKER, A. AND GOODISON, B. 1993. Discrimination of a wet snow cover using passive microwave satellite data. *Annals of glaciology*, 17, 6 pages.
- WALKER, A. AND SILIS, A. 2002. Snow-cover variations over the Mackenzie River Basin, Canada, derived from SSM/I passive microwave satellite data. *Annals of Glaciology*, 34, 8-14.
- WARREN, S.G. 1982. Optical Properties of Snow. *Reviews of Geophysics and Space Physics*, 23 pages.
- WARREN S.G, RIGOR I.G, UNTERSTEINER N, RADIONOV V.F, BRYAZGIN N.N, ALEKSANDROV Y.I, AND COLONY R. 1999. Snow depth on Arctic sea ice. *Journal of Climate*, 12, 1814-1829.
- WEEKS W.F. AND ACKLEY S.F. 1986. *The growth, structure and properties of sea ice*. In The Geophysics of Sea Ice, N. Untersteiner (Ed). NATO ASI Series B: Physics vol. 146, Plenum Press, New York. 9-164.
- WEEKS, W.F. 1998. *Growth conditions and the structure and properties of sea ice*. In M. Leppäranta, editor, Physics of Ice-Covered Seas, 1, 25-104, Helsinki Univ. Press, Helsinki.
- WELCH, H.E. AND BERGMANN, M.A. 1989. Seasonal development of ice algae and its prediction from environmental factors near Resolute, N.W.T., Canada. *Journal of Fisheries and Aquatic Sciences*, 46, 1793-1804.
- WU, X., BUDD W.F, LYTLE V.I. AND MASSOM R.A. 1999. The effect of snow on Antarctic sea ice simulations in a coupled atmosphere-sea ice model. *Climate Dynamics*, 15, p. 127-143.

- XIN J. AND BARBER D.G. 2005. An assessment of the sensitivity of cloud radiative forcing on the initiation and rate of melt over snow covered landfast first year sea ice with Terra/MODIS data. *Hydrological Processes*, In Press.
- YACKEL, J., BARBER, D.G. AND PAPAKYRIAKOU, T.N. 2001. On the estimation of spring melt in the North Polynya using RADARSAT-1. *Atmosphere-Ocean*, 39, 195-208.
- YANG, Z.-L, DICKINSON R.E, HAHMANN A.N, NIU G.-Y, SHAIKH M, GAO X, BALES R.C, SOROOSHIAN S. AND JIN J.M. 1999. Simulation of snow mass and extent in global climate models. *Hydrological Processes*, 13, 2097-2113.
- YEN, Y.-C. 1981. *Review of Thermal Properties of Snow, Ice and Sea Ice*. CRREL Report, 81-10.
- YOSIDA, Z. 1955. Physical studies on deposited snow. I. Thermal properties. *Inst. Low Temp. Sci. Ser. A*, 7, 19-74.
- YU, Y., MAYKUT, G.A. AND ROTHROCK, D.A. 2004. Changes in the thickness distribution of Arctic sea ice between 1958–1970 and 1993–1997. *Journal of Geophysical Research*, 109, 13 pages.
- ZHANG, J., ROTHROCK, D. AND STEELE, M. 2000. Recent changes in Arctic sea ice: the interplay between ice dynamics and thermodynamics. *Journal of Climate*, 13, 3099-3114.
- ZHANG, W. AND SCHNEIBEL, J.H. 1995. The sintering of two particles by surface and grain boundary diffusion: a two-dimensional numerical study. *Acta metallurgica et materialia*, 43, 4377-4386.
- ZHANG, X., WALSH, J.E., ZHANG, J., BHATT, U.S. AND IKEDA, M. 2004. Climatology and interannual variability of Arctic cyclone activity, 1948–2002. *Journal of Climate*, 17, 2300–2317.
- ZHEKAMUKHOV, M.K. AND SHUKHOVA, L.Z. 1999. Convective instability of air in snow. *Journal of Applied Mechanics and Technical Physics*, 40, 1042-1047.

ZHEKAMUKHOV, M.K. AND ZHEKAMUKHOVA, I.M. 2002. On Convective Instability of Air in the Snow Cover. *Journal of Engineering Physics and Thermophysics*, 75, 849-858.

ZHEKAMUKHOVA, I.M. 2004. Heat Conduction and Diffusion Equation of Steam in Snow Cover. *Journal of Engineering Physics and Thermophysics*, 77, 816-820.

ZHOU, X. AND LI S. 2002. Phase functions of large snow meltclusters calculated using the geometrical optics method. *IEEE 2002 International Geoscience and Remote Sensing Symposium (IGARSS'02)*. VI, 3576-3578.

ZURK, L., TSANG, L., SHI, J. AND DAVIS, R.E. 1997. Electromagnetic scattering calculated from pair distribution functions retrieved from planar snow sections. *IEEE Transactions on Geoscience and Remote Sensing*, 35, 1419-1429.

## APPENDIX A

### *List of abbreviations:*

ACIA: Arctic Climate Impact Assessment  
AMSR-E: Advanced Microwave Scanning Radiometer for Earth Observing System  
AVOS: AXYS Automated Voluntary Observation Ship  
C.C.G.S.: Canadian Coast Guard Ship  
CASES: Canadian Arctic Shelf Exchange Study  
GPS: Global Positioning System  
GR: Brightness temperatures Gradient Ratio  
IPCC: Intergovernmental Panel on Climate Change  
NASA: National Aeronautics and Space Administration  
OSA: Ocean-Sea Ice-Atmosphere interface  
PR: Brightness temperatures Polarization Ratio  
SAR: Synthetic Aperture Radar  
SBR: Surface Based Radiometer  
SEB: Surface Energy Balance  
SMMR: Scanning Multi-channel Microwave Radiometer  
SSM/I: Special Sensor Microwave/Imager  
SWE: Snow Water Equivalent

### *List of acronyms:*

A : Illuminated area by incident energy  
 $A_\theta$  : Depolarization factor  
 $\alpha$ : Surface albedo  
 $\beta$ : Phase constant  
B : Isobaric coefficient for thermal expansion  
 $C_s$ : Snow heat capacity  
 $c_s$ : Specific heat of snow  
 $c_{pureice}$ : Specific heat of freshwater ice  
 $c_{brine}$ : Specific heat of brine  
 $\zeta_s$ : Scattering cross section coefficient  
 $\zeta_a$ : Absorption cross section coefficient  
 $C_{Hz}$ : Transfer coefficient for sensible heat flux  
 $C_{Ez}$ : Transfer coefficient for latent heat flux  
D: Diffusivity of water vapor  
 $D_S$ : Coefficient of surface diffusion  
 $e_P$ : Snow emissivity  
E: Electrical field  
 $E_z$ : Intensity of the electrical field in terms of snow depth  
 $E_\theta$ : Initial intensity of electrical field  
 $\epsilon$ : Dielectric constant  
 $\epsilon'$ : Permittivity  
 $\epsilon''$ : Dielectric loss  
 $\epsilon'_w$ : Permittivity of freshwater  
 $\epsilon''_w$ : Dielectric loss of freshwater  
 $\epsilon_{w0}$ : Static dielectric constant for freshwater

$\epsilon_{w\infty}$ : High-frequency limit dielectric constant for water  
 $\epsilon_0$ : permittivity of free space  
 $\epsilon_{mix}^*$ : Complex dielectric constant of a snow mixture  
 $\epsilon_{w\infty}$ : High frequency limit dielectric constant  
 $\epsilon_{b0}^*$ : Complex dielectric constant of brine  
 $\epsilon_{b0}$ : Static dielectric constant of brine  
 $\epsilon'_{ds}$ : Permittivity of dry snow  
 $\epsilon''_{ds}$ : Dielectric loss of dry snow  
 $\epsilon'_{wet}$ : Permittivity of wet snow  
 $\epsilon''_{wet}$ : Dielectric loss of wet snow  
 $\epsilon_{wet}^*$ : Complex dielectric constant of wet snow  
 $\epsilon_{ds}^*$ : Complex dielectric constant of dry snow  
 $e_k$ : Kinetic energy of snow particles  
 $f$ : Frequency used in GHz  
 $f_{w0}$ : frequency of relaxation of pure water  
 $F_a$ : Absorbed shortwave radiation  
 $g$ : Acceleration due to gravity  
 $h_{c-snow}$ : Thermal contact conductance coefficient  
 $I$ : Intensity of incident energy  
 $J$ : Vapor flux  
 $J_S$ : Vapor flux going away from the convex surface of snow grains  
 $J_B$ : Vapor influx at the boundary concave surface of snow grains  
 $k_s$ : Snow thermal conductivity  
 $k_{air}$ : Air thermal conductivity  
 $k_b$ : Brine thermal conductivity  
 $k_{ice}$ : Freshwater ice thermal conductivity  
 $K_{is}\downarrow$ : Downwelling shortwave radiation at the snow-ice interface  
 $K_{is}\uparrow$ : Reflected shortwave radiation at the snow-ice interface  
 $K^*$ : Net shortwave radiation  
 $K\downarrow$ : Downwelling shortwave radiation at the snow surface  
 $K\hat{\uparrow}$ : Reflected shortwave radiation from the snow surface  
 $\kappa_i$ : Coefficient of air permeability  
 $k_0$ : Wave number in free space  
 $K_e$ : Extinction coefficient  
 $K_a$ : Absorption coefficient  
 $K_s$ : Scattering coefficient  
 $K$ : Stephan-Boltzmann's constant  
 $L^*$ : Net longwave radiation at the snow surface  
 $L\downarrow$ : Downwelling longwave radiation at the snow surface  
 $L\hat{\uparrow}$ : Upwelling longwave radiation from the snow surface  
 $L_w$ : Latent heat of fusion  
 $\lambda$ : Wavelength  
 $L$ : Latent heat of evaporation  
 $\ell$ : Latent heat of vaporization  
 $\gamma$ : Propagation factor  
 $m$ : Mass of a snow particle  
 $M$ : Total mass of the snow volume  
 $M_{brine}$ : Mass of brine within the snow volume

$\rho_s$ : Snow density  
 $\rho_i$ : Freshwater ice density  
 $\rho_w$ : Freshwater density  
 $\rho_{air}$ : Density of air  
 $\rho_l$ : Density of a liquid  
 $p_c$ : Capillary pressure  
 $p_{eq}$ : Saturation vapor pressure over planar surface  
 $P_i$ : Incident energy  
 $P_t$ : Transmitted energy  
 $P_r$ : Reflected energy  
 $\psi$ : Surface tension of ice  
 $Q_{snow}^*$ : Net radiation budget over snow  
 $Q_{is}^*$ : Net radiation budget at the snow and ice interface  
 $Q_i$ : Conductive heat flux at the snow-ice interface  
 $Q_s$ : Conductive heat flux at the snow-air interface  
 $Q_{ms}$ : Heat flux associated with phase change  
 $Q_w$ : Heat flux associated with water percolation  
 $Q_c$ : Conductive flux  
 $Q_h$ : Sensible heat flux  
 $Q_e$ : Latent heat flux  
 $Q_p$ : Heat conducted by precipitation  
 $q$ : Heat flux within the snow  
 $R_v$ : Specific gas constant for vapor  
 $r$ : Snow grain radius  
 $F$ : Snow reflectivity  
 $Ra$ : Rayleigh number  
 $Ra_c$ : Critical Rayleigh number  
 $s$ : Length of snow grain curvature  
 $\sigma^\alpha$ : Backscattering coefficient  
 $\sigma_b$ : Ionic conductivity of brine  
 $S_s$ : Salinity of snow  
 $S_b$ : Salinity of brine  
 $S_w$ : Salinity of water  
 $\delta_s$ : Snow grain surface diffusivity  
 $\delta_p$ : Penetration depth  
 $\sigma_{sl}$ : Difference of pressure between the solid and liquid phase  
 $\sigma_{sg}$ : Difference of pressure between the solid and gas phase  
 $\tau_w$ : Relaxation time of pure water  
 $\tau_b$ : Relaxation time of brine  
 $\tau_0$ : Atmosphere transmissivity  
 $T_s$ : Snow surface temperature  
 $T_{air}$ : Air temperature  
 $T_{si}$ : Snow-ice interface temperature  
 $T_b$ : Brightness temperatures  
 $\Delta T_b$ : Brightness temperature difference between 19 and 37 GHz  
 $\mathcal{T}$ : Snow transmissivity  
 $v$ : Velocity of moving snow particle  
 $\omega$ : Viscosity of snow  
 $\nu_s$ : Snow thermal diffusivity

$V_{ice}$ : Fractional volume of ice within the snow  
 $V_{air}$ : Fractional volume of air within the snow  
 $V_{brine}$ : Fractional volume of brine within the snow  
 $W_v$ : Fractional volume of water in liquid phase  
 $\chi$ : defines the Rayleigh region ( $\chi = 2\pi r / \lambda < 1$ )